1995 Annual Report

Volume 6, No. 1
July 1995

Acknowledgments

The faculty, students and staff of the Seismic Tomography Project express their sincere appreciation to the STP sponsors for their unrestricted gift support for 1995. And, special thanks to Bob Langan of Chevron for his leadership of the STP crew during the year while Professor Harris was on sabbatical. Bob's industrial and research experience was a valuable resource to the entire geophysics community at Stanford. Thanks also to Ken Bube (U. of Washington), Mike Schoenberg (Schlumberger), and Xiaofei Chen (U. of Southern California) for their contributions to this year's volume.

Table of Contents

Forward Modeling

Ray Tomography

Wave Equation Tomography & Migration

Wave Equation Tomography & Migration (con't)

CDP Imaging, Processing & Case Studies

STP

PAPER A

FAST RAY-TRACING THROUGH UNDULATING ANISOTROPIC LAYERS

Jessé Costa & Michael Schoenberg

ABSTRACT

A fast and robust scheme for two point raytracing through a 3-D piecewise homogeneous arbitrarily anisotropic medium is presented. These features are derived from a combination of the Newton-Raphson scheme and the continuation method. The algorithm performance can be useful in developing a fast traveltime inversion routine.

INTRODUCTION

In many geophysical settings it is desirable to use raytracing to get a first cut on a suitable anisotropic velocity model necessary for proper migration and/or inversion of seismic data. These data are often collected in a way such that not all source and receiver locations lie in a single vertical plane. Such a survey is called a three dimensional (3-D) survey. Modeling such a survey requires a 3-D modeling code unless the layers are all assumed to be flat (a 1-D medium) and the anisotropy is assumed to be transversely isotropic (at most) at every depth interval.

In a horizontally stratified medium each ray, from Snell's Law, has the same horizontal slowness throughout its entire length. This can be used to greatly simplifying two point raytracing in the medium. For 2-D anisotropy (e.g., transverse isotropy with a vertical symmetry axis, or orthorhombic with the vertical source-receiver plane a mirror plane of symmetry of the medium at every depth), rays remain in the source-receiver plane and the horizontal slowness, or p parameter, is the single ray parameter that must be found for any source-receiver pair (Musgrave, 1970). From this single p parameter the complete ray trajectory and the total traveltime are easily found. For 3-D anisotropy, even assuming flat layers, rays no longer lie in the source-receiver plane, yet each ray still has its unique horizontal slowness, now a horizontal vector which may be denoted by two horizontal slowness parameters, say p_x and p_y.

However, when it is necessary to allow for non-flat layer boundaries this extremely convenient property of a ray having a unique horizontal slowness is absent. Yet for the initial approach to velocity model building it is seldom desirable to resort to a full 3-D ray tracing code which can accommodate arbitrary elastic models. This is because 1) the input of an arbitrary model is awkward and time consuming, and 2) ray tracing through an arbitrary grid, even if the model is not too complicated, is relatively slow. The method presented here is a fast generalization of a flat layer code for those instances when several homogeneous layers will suffice, but when it is necessary for those layers to vary laterally, generally in three dimensions, but to still be recognizable as layers.

The method described here uses an iterative Newton-Raphson scheme (Press et al., 1990) to find the intersections of the desired ray with the non-flat layer boundaries. Our formulation is a generalization of the works of Keller & Perozzi (1983) and Docherty & Bleistein (1984) for 3-D arbitrarily anisotropic media. For this scheme to work in a robust fashion it is necessary to begin the iteration with a trial solution very close to the true solution. What we will use as a trial solution for an isolated ray is the flat layer solution. When that is not close enough we adapt a continuation method, allowing the layers to become non-flat in small increments, to make the Newton-Raphson scheme robust. Often, the objective is not to trace an isolated ray but to trace an entire suite of rays from a variety of nearby source locations to an array of closely spaced receivers. In that case, once a single ray is found through the laterally varying medium, its intersections with the layer boundaries will be used as a trial solution for the ray to the neighboring receiver, and so on. And in a similar fashion to cover all the source locations.

Thus, the assumptions for the fast 3-D ray tracing schemes presented here are as follows:

- homogeneous anisotropic elastic layers
- non-flat layer boundaries
- ray trajectory and traveltime from source to receiver in corresponding flat layered medium is known.

The ray trajectory is specified as the intersections (reflection or transmission points) of the ray with the layer boundaries since the ray traverses straight line segments between those points. Note that the corresponding flat layered medium consists of the same anisotropic layers as the non-flat layered medium but with layer boundaries consisting of horizontal planes which are best fitting to or most representative of the actual non-flat layer boundaries.

FORMULATION OF THE PROBLEM

We let our rays propagate through a set of homogeneous but arbitrarily anisotropic elastic layers separated by non-flat boundaries, the i-th boundary being specified by,

$$z = h_k + f_k(x,y) \tag{1}$$

where h_k is the depth of the corresponding best fitting flat layer boundary. Consider a particular ray consisting of $N+1$ straight ray segments, i.e., a ray which hits a layer boundary N times, with each segment a specified wave type. A ray consisting of only downward (or only upward) propagating segments would cross N different layer boundaries. In general, a ray would cross $M \leq N$ different layer boundaries. As an example of a ray trajectory for a pegleg multiple with $N=7$, even though only three different material layers are involved, see Figure 1. Note that once the source and receiver position are fixed, a ray may be specified by the function $j(i)$, $i=1,\ldots,N+1$, where j denotes the layer in which the i-th ray segment is located. For this pegleg multiple example,

$$j(1)=1 \quad j(2)=2 \quad j(3)=3 \quad j(4)=3 \quad j(5)=2 \quad j(6)=2 \quad j(7)=2 \quad j(8)=1.$$

Equivalently, the ray could also be specified by the function $k(i)$, $i = 1,...,N$, where k denotes the layer boundary crossed by the ray between the ith and $i+1$th ray segment. For this pegleg multiple example,

$$k(1) = 1 \;\; k(2) = 2 \;\; k(3) = 3 \;\; k(4) = 2 \;\; k(5) = 1 \;\; k(6) = 2 \;\; k(7) = 1 \;\; .$$

The i-th ray segment in the $j(i)$th layer is a vector connecting its endpoints, $\mathbf{x}_i - \mathbf{x}_{i-1}$. Note that $\mathbf{x}_0$ is the source point and $\mathbf{x}_{N+1}$ is the receiver point. Each ray segment has an associated slowness vector $\mathbf{p}^{(i)}$ satisfying the slowness relation $F_{j(i)}(\mathbf{p}^{(i)}) = 0$. That ray segment is parallel to group velocity $\mathbf{v}_\mathbf{g}^{(i)}$ and thus we can write,

$$\mathbf{v}_\mathbf{g}^{(i)} \tau_i = \mathbf{x}_i - \mathbf{x}_{i-1} .$$

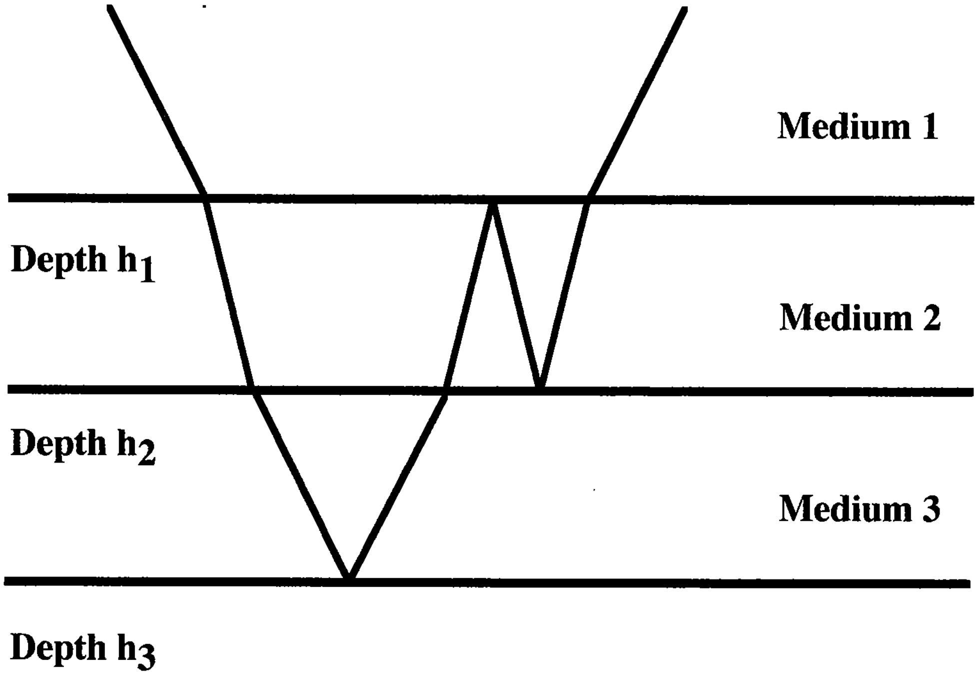

Layers: j (1, 2, 3, 4, 5, 6, 7, 8)=1, 2, 3, 3, 2, 2, 2, 1.

Intersections: k (1, 2, 3, 4, 5, 6, 7)=1, 2, 3, 2, 1, 2, 1.

Figure 1. Example of a pegleg multiple, $N = 7$.

Taking the dot product of the slowness with both sides of this equation and noting that in any anisotropic medium,

$$\mathbf{p} \cdot \mathbf{v}_\mathbf{g} \equiv 1,$$

(for example see Helbig and Schoenberg, 1987) we find that $\tau_i = \mathbf{p}^{(i)} \cdot (\mathbf{x}_i - \mathbf{x}_{i-1})$, or the traveltime for the entire ray,

$$\tau = \sum_{i=1}^{N+1} \mathbf{p}^{(i)} \cdot (\mathbf{x}_i - \mathbf{x}_{i-1}) . \tag{2}$$

Note that the group velocity for the $i-$th ray segment, and hence the $i-$th ray segment itself, $\mathbf{x}_i - \mathbf{x}_{i-1}$, is perpendicular to the slowness surface $F_{j(i)}(\mathbf{p}^{(i)}) = 0$ of that $j(i)$th material layer at the value of the slowness vector of that $i-$th ray segment.

Fermat's principle states that the traveltime τ, as a function of ray trajectory over all trajectories neighboring the true trajectory, is minimum for the true ray trajectory (Arnold, 1989). Thus we can derive non-linear equations on the parameters specifying the traveltime, i.e.,

1. the N ray boundary intersections, RBIs, of the specified ray, x_i , y_i and from (1), $z_i = h_k + f_k(x_i, y_i)$, $i = 1,\ldots,N$
2. the $N+1$ slowness vectors, $\mathbf{p}^{(i)}$, for each of the ray segments, each constrained by $F_{j(i)}(\mathbf{p}^{(i)}) = 0$, the anisotropic dispersion relation of the $j(i)$th layer,

by minimizing,

$$\begin{aligned}
\tau = {} & \mathbf{p}^{(1)} \cdot \left(\mathbf{x}_{\mathbf{h}_1} - \mathbf{x}_{\mathbf{h}_S} + \mathbf{e}_\mathbf{z} \left[h_{k(1)} + f_{k(1)}(\mathbf{x}_{\mathbf{h}_1}) - z_S \right] \right) + \lambda_1 F_{j(1)}(\mathbf{p}^{(1)}) + \\
& \sum_{i=2}^{N} \left\{ \mathbf{p}^{(1)} \cdot \left(\mathbf{x}_{\mathbf{h}_i} - \mathbf{x}_{\mathbf{h}_{i-1}} + \mathbf{e}_\mathbf{z} \left[h_{k(i)} + f_{k(i)}(\mathbf{x}_{\mathbf{h}_i}) - h_{k(i-1)} + f_{k(i-1)}(\mathbf{x}_{\mathbf{h}_{i-1}}) \right] \right) + \lambda_i F_{j(i)}(\mathbf{p}^{(i)}) \right\} + \\
& \mathbf{p}^{(N+1)} \cdot \left(\mathbf{x}_{\mathbf{h}_R} - \mathbf{x}_{\mathbf{h}_N} + \mathbf{e}_\mathbf{z} \left[z_R - h_{k(N)} - f_{k(N)}(\mathbf{x}_{\mathbf{h}_N}) \right] \right) + \lambda_{N+1} F_{j(N+1)}(\mathbf{p}^{(N+1)})
\end{aligned} \tag{3}$$

with respect to $x_i, y_i, p_x^{(i)}, p_y^{(i)}, p_z^{(i)}$, and λ_i, where $\mathbf{x}_{\mathbf{h}_i} = \mathbf{e}_x x_i + \mathbf{e}_y y_i$ is the horizontal part of the position vector to the $i-$th RBI, subscript S denotes the source point, subscript R denotes the receiver point and the λ_i, $i = 1,\ldots,N+1$ are Lagrange multipliers.

THE NON-LINEAR EQUATIONS

To find extrema of traveltime, first set the partial derivatives, $\partial\tau/\partial x_i$ and $\partial\tau/\partial y_i$ to zero yielding,

$$\left. \begin{aligned}
p_x^{(i+1)} - p_x^{(i)} + \left(p_z^{(i+1)} - p_z^{(i)} \right) \frac{\partial f_{k(i)}}{\partial x_i} &= 0 \\
p_y^{(i+1)} - p_y^{(i)} + \left(p_z^{(i+1)} - p_z^{(i)} \right) \frac{\partial f_{k(i)}}{\partial y_i} &= 0
\end{aligned} \right\} i = 1,\ldots,N . \tag{4}$$

These are expressions of Snell's Law, which says the change of slowness is normal to the boundary. For the $i-$th intersection this direction is defined by the expression $\nabla g_{k(i)}(\mathbf{x}) = \nabla_\mathbf{h} f_{k(i)}(\mathbf{x}_\mathbf{h}) - \mathbf{e}_\mathbf{z}$. Thus the cross-product,

$$\left(\mathbf{p}^{(i+1)} - \mathbf{p}^{(i)} \right) \times \left[\nabla_\mathbf{h} f_{k(i)}(\mathbf{h}_i) - \mathbf{e}_\mathbf{z} \right]$$

vanishes. Equations (4) are the x and y components of this cross-product.

Setting $\partial \tau / \partial p_x^{(i)}, \partial \tau / \partial p_y^{(i)}$ and $\partial \tau / \partial p_z^{(i)}$, $i = 1,\ldots,N+1$ to zero gives the next set of equations. First, solve for the λ_i from the $\partial \tau / \partial p_z^{(i)} = 0$ equations. Substitution of the resulting values into the $\partial \tau / \partial p_x^{(i)} = 0$ and $\partial \tau / \partial p_y^{(i)} = 0$ equations yields,

$$\begin{aligned}
&(x_1 - x_S)\frac{\partial F_{j(1)}}{\partial p_z^{(1)}} - \left[h_{k(1)} + f_{k(1)}(x_1, y_1) - z_S\right]\frac{\partial F_{j(1)}}{\partial p_x^{(1)}} = 0 \\
&(y_1 - y_S)\frac{\partial F_{j(1)}}{\partial p_z^{(1)}} - \left[h_{k(1)} + f_{k(1)}(x_1, y_1) - z_S\right]\frac{\partial F_{j(1)}}{\partial p_y^{(1)}} = 0 \\
&\left.\begin{aligned}
&(x_i - x_{i-1})\frac{\partial F_{j(i)}}{\partial p_z^{(i)}} - \left[h_{k(i)} + f_{k(i)}(x_i, y_i) - h_{k(i-1)} + f_{k(i-1)}(x_{i-1}, y_{i-1})\right]\frac{\partial F_{j(i)}}{\partial p_x^{(i)}} = 0 \\
&(y_i - y_{i-1})\frac{\partial F_{j(i)}}{\partial p_z^{(i)}} - \left[h_{k(i)} + f_{k(i)}(x_i, y_i) - h_{k(i-1)} + f_{k(i-1)}(x_{i-1}, y_{i-1})\right]\frac{\partial F_{j(i)}}{\partial p_y^{(i)}} = 0
\end{aligned}\right\} i = 2,\ldots,N \\
&(x_R - x_N)\frac{\partial F_{j(N+1)}}{\partial p_z^{(N+1)}} - \left[z_R - h_{k(1)} - f_{k(N)}(x_N, y_N)\right]\frac{\partial F_{j(N+1)}}{\partial p_x^{(N+1)}} = 0 \\
&(y_R - y_N)\frac{\partial F_{j(N+1)}}{\partial p_z^{N+(1)}} - \left[z_R - h_{k(1)} - f_{k(N)}(x_N, y_N)\right]\frac{\partial F_{j(N+1)}}{\partial p_y^{(N+1)}} = 0
\end{aligned} \tag{5}$$

Since in any layer the ray direction, given by $\mathbf{x}_i - \mathbf{x}_{i-1}$, is normal to the slowness surface, i.e., parallel to the gradient of $F_{j(i)}$ with respect to $\mathbf{p}^{(i)}$, the cross-product

$$(\mathbf{x}_i - \mathbf{x}_{i-1}) \times \nabla_{\mathbf{p}} F_{j(i)}(\mathbf{p}^{(i)})$$

vanishes. Equations (5) are the x and y components of this cross-product.

Finally, setting $\partial \tau / \partial \lambda_i$ to zero, yields the third set of equations,

$$F_{j(i)}(p_x^{(i)}, p_y^{(i)}, p_z^{(i)}) = 0, \quad i = 1,\ldots,N+1 \tag{6}$$

i.e., the slowness vectors must satisfy their respective dispersion relations.

Equations (4), (5) and (6) are $5N+3$ non-linear equations on the $5N+3$ unknowns x_i, y_i, $i = 1,\ldots,N$, and $p_x^{(i)}, p_x^{(i)}, p_x^{(i)}$, $i = 1,\ldots,N+1$.

This problem becomes two dimensional when, first, the medium is two dimensional (no variation with y and the source and receivers lie in a single plane perpendicular to the y-axis, call it the $y = 0$ plane and, secondly, the y-axis is a two-fold symmetry axis for all the material layers, i.e., the $y = 0$ plane is at least a mirror plane of symmetry for all the layers. In this case, rays stay in the $y = 0$ plane, the y component of slowness vanishes everywhere, and there is no conversion from in-plane waves (qP, qSv) to cross-plane waves (Sh) (Musgrave, 1970). In this case, the 2nd of equations (4) and the 2nd, 4th and 6th of equations (5) are identically satisfied, and (4), (5), and (6) become a set of $3N+3$ nonlinear equations on the $3N+3$ unknowns:

$$x_i, y_i,\ \ i = 1,\ldots,N, \ \ \text{and}\ \ p_x^{(i)}, p_x^{(i)}, p_x^{(i)}\ ,\ \ i = 1,\ldots,N+1$$

ITERATIVE TECHNIQUES TO SOLVE THE NON-LINEAR EQUATIONS

In either two or three dimensions the set of equations to be solved, consisting of (4), (5), and (6), is a square non-linear set of the form,

$$\Phi(\mathbf{u}) = \mathbf{0}\,, \tag{7}$$

where $\mathbf{u}$ is the solution vector consisting of the x and y coordinates of the RBI's and the slowness vectors. Let the zero'th solution be the solution for the corresponding flat layer problem, in which case the horizontal slowness is the same for all ray segments. Solving the system of equations (7) iteratively, at the j th iterate,

1. solve $\left(\nabla_{\mathbf{u}}\Phi|_{\mathbf{u}^j}\right)\Delta\mathbf{u} = -\Phi\left(\mathbf{u}^j\right)$ for $\Delta\mathbf{u}$, and then
2. update the solution vector according to $\mathbf{u}^{j+1} = \mathbf{u}^j + \Delta\mathbf{u}$.

This is the Newton-Raphson technique (Press et al., 1990) for the iterative solution of a set of non-linear equations.

If Newton-Raphson does not converge in a few iterations one can try solving it in steps. Denote the flat layer geometry by $\kappa = 0$ and the specified non-flat geometry by $\kappa = 1$. Between these cases lies a continuum of intermediary geometry's parameterized by κ, $0 \le \kappa \le 1$ for which the layer boundaries are given by,

$$z = h_k + \kappa f_k(x,y).$$

The non-linear system associated with κ is,

$$\Phi\left(\mathbf{u}_\kappa, \kappa\right) = \mathbf{0}\ ;$$

$\Phi\left(\mathbf{u}_\kappa, \kappa\right)$ may be written simply by replacing $f_k(x,y)$ in Φ by $\kappa f_k(x,y)$. We now try solving the non-flat case for some value of κ less than 1, say $1/n$, still using the $\kappa = 0$ solution as the initial trial solution. If Newton-Raphson now converges in a few iterations, then use a larger value for κ, say $2/n$, now with the solution for $\kappa = 1/n$ as the initial trial solution. The procedure continues until a solution for $\kappa = 1$ is realized, solving the desired two-point ray tracing problem. This is known as the continuation method (Keller & Perozzi, 1983; Docherty & Bleistein, 1985), and here continuation is being applied to a measure of the non-flatness of the layers. This procedure can be made quite robust and the number of iterations required at each value of κ may be kept quite low. This is because the zero'th trial solution (from the previous value of κ) may be chosen to be very close to the required solution at the present value of κ.

EXAMPLES

Often in seismic modeling, one requires traveltimes from a near surface source to a large number of closely spaced receivers, such as for modeling surface seismic or VSP traveltimes. The first ray found for flat layers could be the ray with vanishing horizontal slowness. When all the layers are at a minimum, up-down symmetric, i.e., the horizontal plane is at least a mirror plane of symmetry, that zero horizontal slowness ray is vertical. Now that ray may be used to find the ray to the same receiver location when the layers are no longer flat. If the lateral variation is large it may be necessary to use continuation to find that ray. After the first ray is found the other rays to neighboring receiver locations may be found by applying continuation to the receiver position. Thus the initial trial solution for the ray to a given receiver could naturally be the ray to the previous receiver. In this way ray trajectories and traveltimes can be rapidly built up to give almost continuous coverage, if desired.

As a three dimensional example we present the computation of rays for a walkway VSP common shot gather. The medium properties in the principal axes system are presented in the table below.

Layer	a_{11}	a_{12}	a_{13}	a_{22}	a_{23}	a_{33}	a_{44}	a_{55}	a_{66}
1	4.00	1.00	1.00	4.00	1.00	4.00	1.50	1.50	1.50
2	12.00	3.10	1.70	16.80	2.45	7.25	3.10	1.23	2.50
3	12.75	5.95	2.87	21.75	2.87	8.25	3.00	3.00	7.90
4	12.60	3.25	1.36	12.60	1.36	5.40	2.25	2.25	4.67

Table 1. Density normalized elastic moduli, at principal axes, for the model. The first layer is isotropic the second orthorhombic and the third and fourth layers are transversally isotropic.

The principal axis for the layers 2 and 4 were tilted. The orthorhombic medium in layer 2 was rotated by 45° around the Z axis and afterwards another 45° around the new X axis. The transversally isotropic medium at bottom half-space was rotated of 60° around the X axis. Figures 1 and 2 show qP rays at two different perspectives for a flat interfaces medium. Note that ray trajectories are not plane curves as they would be in the isotropic case. Figures 3 and 4 show two perspectives of the ray trajectories across a medium with the same elastic properties as before but with nonflat interfaces.

CONCLUSION

A fast ray tracing for non-flat homogeneous layers with arbitrary anisotropy was presented. The algorithm is very robust for qP-waves. It can lead to problems for quasi-shear waves around non-convex regions and near repeated roots of the slowness surface. The continuation approach can be applied to proceed from isotropic to anisotropic media and to extend results from a single source-receiver configuration to results for a full scale survey involving multiple sources and receivers. The performance of the algorithm makes it adequate for procedures that require the computation of a large number of ray trajectories, such as traveltime inversion routines.

ACKNOWLEDGMENTS

The first author would like to acknowledge the Brazilian CNPq and all the sponsors of the Seismic Tomography Project for the financial support of the first author during this year in Stanford.

REFERENCES

Arnold, V. A., 1989, **Mathematical Methods of Classical Mechanics**. New York, Springer-Verlag. 508p. (Graduate Texts in Mathematics, 60).

Docherty, P. & Bleistein, N., 1985, A fast raytracing routine for laterally inhomogeneous media: Expanded Abstracts SEG, **54**, 788-790.

Helbig, K. & Schoenberg, M., 1987, Anomalous polarization of elastic waves in transversally isotropic media. J. Acoust. Soc. Am. **81**, 1235-1245.

Keller, H. B. & Perozzi, D. J., 1983. Fast seismic raytracing. SIAM J. Appl. Math, **43,** 1402-1412

Musgrave, M. P. J., 1970. **Crystal acoustics. London**, Holden-Day. 288p.

Press, W. H., Flannery, B. P., Teukolsky, S. A.. & Vetterling, W. T., 1990, **Numerical Recipes.** Cambridge. Cambridge University Press. 702p.

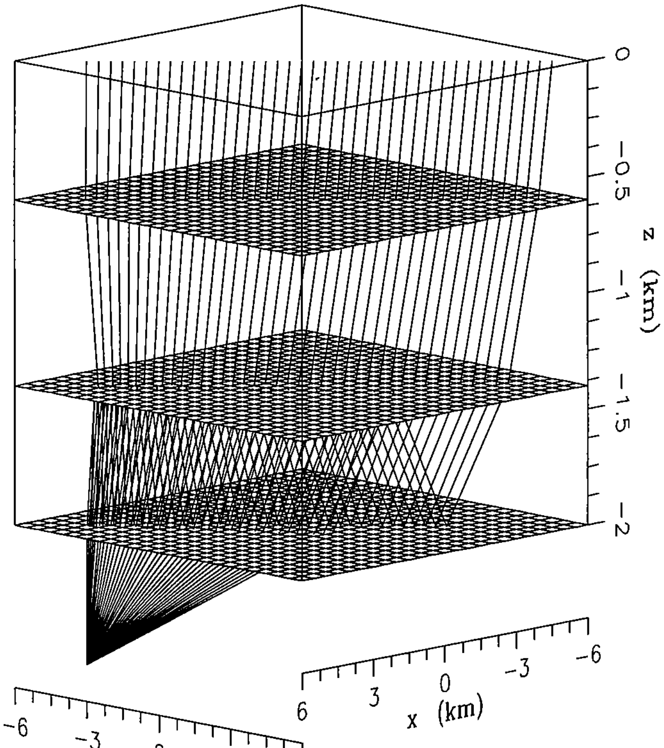

Figure 1. qP waves rays, including multiples, through a flat layered anisotropic media.

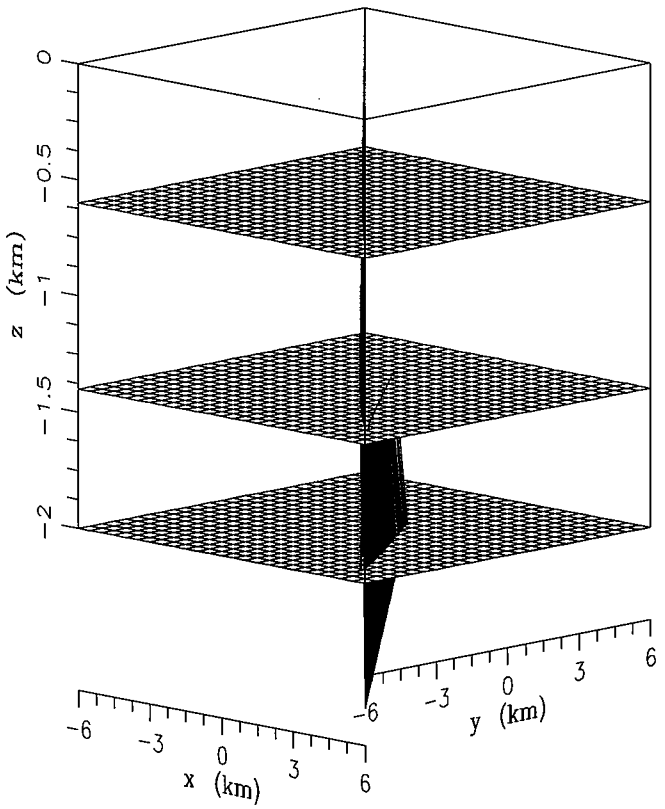

Figure 2. Another perpective for rays in figure 1. Notice that the rays are not plane curves as it should in the isotropic case.

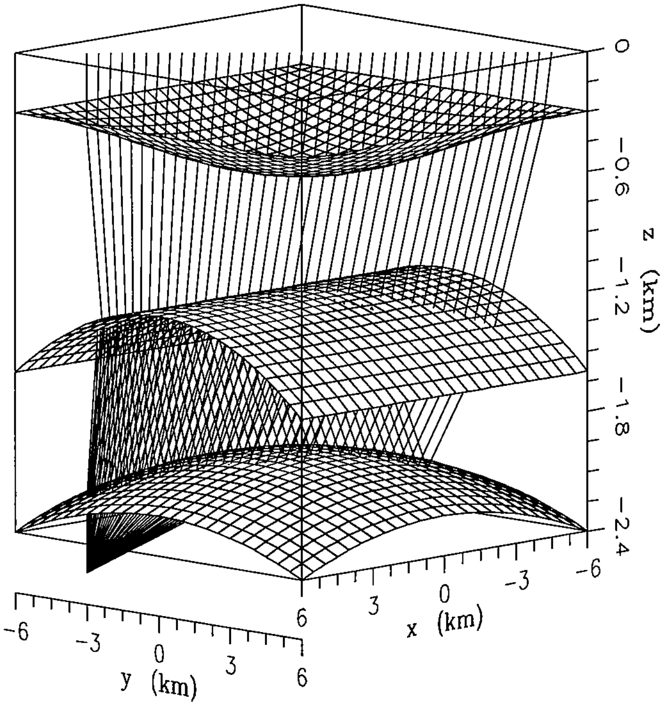

Figure 3. qP rays through a nonflat layered medium.

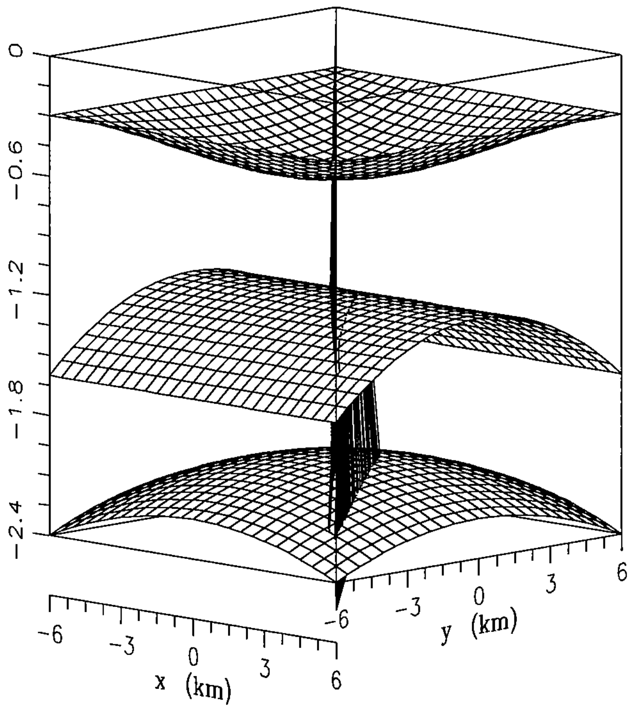

Figure 4. Another perspective for the rays in figure 3.

PAPER B

A NUMERICAL SOLUTION FOR THE SCALAR SCATTERING EQUATION USING A MOMENT METHOD WITH BILINEAR BASIS FUNCTIONS

Jerry M. Harris and Feng Yin

ABSTRACT

We present a new moment method of solving the acoustical scattering equation. We describe the formulation, the implementation, and numerical testing of the method. The main characteristic of this method is that a bilinear basis function is used instead of a pulse basis function to evaluate the Green function, total field, and scattering potential at any arbitrary point of the image region. In this way, the integral equation may be discretized to arbitrary fineness in order to increase the accuracy of the computations. From simulation tests, we find that this method is accurate and the number of unknowns can be greatly reduced compared with the pulse basis method to obtain the same accuracy. The simulation results show that the method is effective for forward modeling in the frequency domain and can be used to produce time domain seismograms with the Fourier transform.

INTRODUCTION

In recent years, several researchers have attempted wave equation tomography on field data with mixed results (Harris and Wang, 1993, Zhou and Schuster, 1993). Some used the time-domain waveform data to invert for velocity; others used the frequency domain wave field. In either domain, an estimate of the wave field in the inhomogenous medium is required; thus an expensive forward computation is required. To avoid this expense, approximations such as the Ray-Born algorithms for forward modeling have been developed (Beydoun and Mendes, 1987), and one way propagation methods have been proposed (Freit and Fleck, 1978, Martin and Flatte, 1988, Thomson and Chapman, 1989, Wu and Huang, 1992, Wu, 1994). However, methods that employ the ray approximation as the propagator can not treat "wave" phenomena in inhomogeneous media. In addition, the Born approximation is not valid for large scale or large contrast heterogeneities, and methods that employ the one-way propagation operator can not treat multi-reflection wave. In order to model wave propagation and scattering in arbitrarily heterogeneous media which are an important part in wave equation inversion, full wave modeling methods are required. There are two types of useful methods: One is to solve the differential form of the wave equation, e.g., with finite difference methods (Pratt, 1988), finite element methods (Robert and Andreas, 1992), or boundary element methods (Barhe, 1982). Another is to solve the integral equation (Richmond, 1965, Bojarski, 1971, Chew and Lu, 1993), in which the moment methods using pulse basis functions (Richmond, 1965) are widely used. Finite difference methods are especially useful for large areas. Conventional moment methods are especially useful for modeling in smaller regions. Also, the Frechet derivative required for inversion can be easily derived from the integral formulation.

In geophysics, our ultimate goal is inversion of the acoustic fields for earth properties; therefore, we choose the integral approach to forward modeling. It is known that the conventional pulse basis functions used in moment methods do not produce accurate representation for pixel sizes larger than about 0.1 wavelength. For large scale imaging problems, we must use many pixels and invert a huge matrix in order to find the wave field accurately in the inhomogenous medium. This is the main problem of the moment method. Up to now, many authors have attempted to improve this method (Johnson, 1983, Steinberg, 1993, Zhuck, 1994). For examples, some use wavelet expansions in the method of moments to solve a one-dimensional scattering problem (Steiberg and Leviatan, 1993), but up to now wavelet methods can only be applied when the domain of integration is a straight line or curved line (Steinberg and Leviatan, 1993, Wang, 1995). When the domain of integration is a 2_D region, no results have been reported. Undoubtedly that this type of method will be very complicated to implement in the 2-D case. By exploiting the property that any solution is composed of fast and slow spatial variations, i.e.., high and low frequency components, some anothers have applied multigrid methods to the moment method to solve for the slow and fast modes in the solution by using iterative solvers at a coarse and fine grids, respectively (Kalbasi and Demarst, 1993). These methods greatly complicate the computation. In addition,. by the observation that the integral equation used in the method of momen (MOM) is a convolution-type integral, the K-space method which uses FFT and the conjugate gradient method has been proposed in order to accelerate the computation and reduce the memory size requirement in solving the scattering integral equation (Bojarski, 1971, 1982, 1985, Shozo and Bojarski, 1988, Borup and Gandhi, 1984, 1985, Sarkar, Ercument, Sadasiva, 1986); but for each source, almost every parameter has to be calculated again. As we know, in seismic wave inversion, there are usually 200 sources and 200 receivers, therefore, we have to repeatedly apply this method many times. This will result in great time expense. The impedance matrix in MOM does not depend on the source and receiver positions; if we use a direct matrix method such as LU decomposition, the matrix can be used to solve for fields from multiple source positions using relatively inexpensive backsubstitutions. We can also solve for the Green's functions by putting a point source at the receiver positions and using the reciprocity principle. Therefore, the moment method or the methods of solving scattering integral equation with pulse basis function is still widely used as a forward modeling method in the wave equation inversion area (Chew and Wang, 1990; Thompson, Rodi, Cheng and Toksoz, 1992; Caorsi S., Gragnani, and Pastorino, 1993; Caorsi, et al, 1994, 1995, Moghaddam and Chew, 1993, Wang and Zheng, 1992, Slvatore, Gragnani and Pastosino, 1993). As mentioned above, in applications of the MOM to the solution of the integral equations of electromagnetic or acoustic waves, ten adjustable degrees of freedom per wavelength have been the norm even for the most benign configurations (Johnson, 1983; Herrmann, 1993). The reason most commonly given for the need to oversample is that the basis functions chosen to represent scattering sources are discontinuous or have discontinuous derivatives and consequently possess a rich high-frequency spectrum (Herrmann, 1990, 1993). In this paper, we present a new variation on the moment method that is more numerically efficient for the 2-D wave propagation in strongly heterogeneous media. In our method, we discretize the integral equation on a grid and interpolate between nodes using smooth bilinear basis functions instead of pulse basis functions. In this way, we can not only increase the accuracy of the calculation of wave field, but also reduce the number of unknowns representing the field. And as pointed out above, the Frechet derivative for non-linear wave equation inversion is very easily derived.

From the numerical simulation, we observe that bilinear elements lead to a matrix with very similar properties as pulse basis matrix. Moreover it is just as easy to set up as the pulse basis function; and the linear system is just as easy to solve as that for pulse basis functions. We can get better accuracy for same amount of work using the two methods with the same pixel size, and we can use smaller impedance matrices derived by setting the pixel size to be the wavelength divided by 6 for same accuracy as pulse method with the pixel size being the wavelength divided by 10. This great savings may enable us to use Gauss Elimination to solve linear system directly. Because the matrices derived from bilinear or pulse elements do not depend on the source and geophone position; when we apply Gauss Elimination to the matrix, we only need to do the LU factorization once, and this matrix decomposition can be used to solve for fields from multiple sources using relatively inexpensive backsubstitutions. We can also solve for the Green's functions by putting a point source at the receiver positions and using the reciprocity principle. The pulse basis method with a pixel size to obtain the same accuracy leads to a matrix which can be too large for Gauss Elimination. Therefore, the method developed here will be useful in wave field calculation in multi-source and multi-receiver system, such as cross-well imaging.

A NEW MOMENT METHOD FOR THE SCATTERING EQUATION

We restrict ourselves to the acoustic wave propagation in 2-D inhomogeneous media. In the frequency domain, we have

$$(\nabla^2 + \frac{\omega^2}{c^2(\boldsymbol{r})})u(\boldsymbol{r},\omega) = -\delta(\boldsymbol{r}-\boldsymbol{r}_s), \tag{1}$$

where, $c(\boldsymbol{r})$ is the velocity of the compression wave, $\boldsymbol{r}$ is the position vector, $\boldsymbol{r_s}$ the source position, $u(\boldsymbol{r},\omega)$ is the pressure field, and ω is the angle frequency. We define the scattering potential in terms of the contrast in velocity to be

$$M(\boldsymbol{r}) = 1 - \frac{c_o^2}{c^2(\boldsymbol{r})} \tag{2}$$

and write the total acoustic field as the sum of the incident and the scattered fields:

$$u(\boldsymbol{r}) = u^{inc}(\boldsymbol{r}) + u^{sc}(\boldsymbol{r}). \tag{3}$$

The integral equation corresponding to Eqn. (1) can be written

$$u(r) = u^{inc}(r) - k^2 \int_{\Omega} M(r')u(r',\omega)G(k|r-r'|)dr', \tag{4}$$

where $k=\omega/c_o$, Ω defines the inhomogeneous region or what we will call the object region. As shown in Figure 1, the object region is divided into R homogeneous areas, i.e., pixels, with N nodes, $\Omega = \Omega_1 \cup \Omega_2 \cdots \cup \Omega_R, \Omega_i \cap \Omega_j (i \neq j)$.

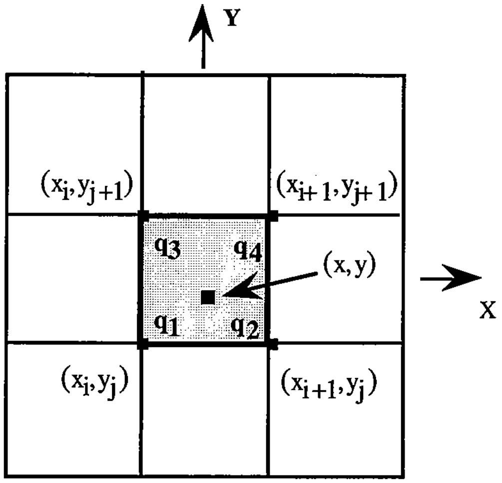

Figure 1: In the discretized form of the object region, q_1, q_2, q_3 and q_4 denote the nodes located at (x_i,y_j), (x_{i+1},y_j), (x_i,y_{j+1}) and (x_{i+1},y_{j+1}).

We then have

$$u(r) = u^{inc}(r) - k^2 \sum_{r=1}^{R} \int_{\Omega_r} M(r')u(r',\omega)G(k|r-r'|)dr'. \tag{5}$$

When r' is located in Ω_r, and the subscripted cartesian coordinates are used to denote the four nodes of the cell Ω_r as shown in Figure 1. We use (x,y) to denote a point within the cell and Δx and Δy the intervals in the x and y directions, respectively. When $x_i \le x \le x_{i+1}$, $y_j \le y \le y_{j+1}$, $(1 \le i \le M_x, 1 \le j \le M_y)$, define

$$\rho_l = \begin{cases} f_1 & l = (j-1)\times M_x + i \\ f_2 & l = (j-1)\times M_x + i + 1 \\ f_3 \quad \text{when} & l = (j-1)\times M_x + i + M_x \\ f_4 & l = (j-1)\times M_x + i + M_x + 1 \\ 0 & l = otherwise \end{cases} \tag{6}$$

where M_x, M_y are the total number of the nodes in the x and y direction, respectively.

$$f_1 = 1 - \frac{(x-x_i)}{\Delta x} - \frac{(y-y_j)}{\Delta y} - \frac{(x-x_i)(y-y_j)}{\Delta x \Delta y} \tag{7}$$

$$f_2 = \frac{(x-x_i)}{\Delta x} - \frac{(x-x_i)(y-y_j)}{\Delta x \Delta y} \tag{8}$$

$$f_3 = \frac{(y-y_j)}{\Delta y} - \frac{(x-x_i)(y-y_j)}{\Delta x \Delta y} \tag{9}$$

$$f_4 = \frac{(x-x_i)(y-y_j)}{\Delta x \Delta y} \tag{10}$$

The field quantities $M(\boldsymbol{r})$, $u(\boldsymbol{r})$ and $G(\boldsymbol{r};\boldsymbol{r}',k)$ are expanded using the basis function $\{\rho_n(x,y)\}$. We have

$$M(\boldsymbol{r})=\sum_{n=1}^{N}\rho_n\cdot M_n \tag{11}$$

$$u(\boldsymbol{r},k)=\sum_{n=1}^{N}\rho_n u_n \tag{12}$$

$$G(\boldsymbol{r};\boldsymbol{r}_j',k)=\sum_{n=1}^{N}\rho_n\cdot G_{j,n} \tag{13}$$

where N is the total number of the nodes in the object area; O_n, u_n, and $G_{j,n}$ are the values at the nodes. Substituting Eqns (11)-(13) into Eqn. (5) we obtain

$$\sum_{l=1}^{N}A_{jl}u_l+u_j=u_j^{inc}\quad(1\le j\le N) \tag{14}$$

where N is total number of the nodes,

$$A_{jl}=\sum_{r}^{R}F_{jlr} \tag{15}$$

when $n\ne j, n\ne j-1, n\ne j-M_x-1, n\ne j-M_x$, $n=r+\mathrm{int}eger(r/(M_x-1))$,, if $\mathrm{mod}(r,M_x-1)\ne 0$, $n=r+\mathrm{int}eger(r/(M_x-1))-1$, if $\mathrm{mod}(r,M_x-1)=0$, we have (see Appendix **1**)

$$F_{jlr}=B_{j,n}\delta_{l,n}+C_{j,n+1}\delta_{l,n+1}+D_{j,n+Mx}\delta_{l,n+Mx}+E_{j,n+Mx+1}\delta_{l,n+Mx+1} \tag{16}$$

$$\delta_{i,j}=\begin{cases}1 & i=j\\ 0 & \mathrm{i}\ne\mathrm{j}\end{cases} \tag{17}$$

where

$$\begin{aligned}B_{j,n}=\{&\tfrac{1}{16}Q_1(q_1)Q_2(q_1)+\tfrac{1}{48}[Q_1(q_2)Q_2(q_2)+Q_1(q_3)Q_2(q_3)+Q_1(q_2)Q_2(q_1)+\\&Q_1(q_1)Q_2(q_2)+Q_1(q_3)Q_2(q_1)+Q_1(q_1)Q_2(q_3)]+\tfrac{1}{144}[Q_1(q_4)Q_2(q_4)+\\&Q_1(q_4)Q_2(q_1)+Q_1(q_4)Q_2(q_3)+Q_1(q_1)Q_2(q_4)+Q_1(q_2)Q_2(q_3)+\\&Q_1(q_2)Q_2(q_4)+Q_1(q_3)Q_2(q_2)+Q_1(q_3)Q_2(q_4)+Q_1(q_4)Q_2(q_2)]\}\Delta x\Delta yk^2\end{aligned} \tag{18}$$

$$\begin{aligned}C_{j.n+1}=\{&\tfrac{1}{16}Q_1(q_2)Q_2(q_2)+\tfrac{1}{48}[Q_1(q_1)Q_2(q_1)+Q_1(q_4)Q_2(q_4)+Q_1(q_2)Q_2(q_1)+\\&Q_1(q_1)Q_2(q_2)+Q_1(q_4)Q_2(q_2)+Q_1(q_2)Q_2(q_4)]+\tfrac{1}{144}[Q_1(q_3)Q_2(q_3)+\\&Q_1(q_3)Q_2(q_1)+Q_1(q_1)Q_2(q_3)+Q_1(q_4)Q_2(q_1)+Q_1(q_1)Q_2(q_4)+\\&Q_1(q_2)Q_2(q_3)+Q_1(q_3)Q_2(q_2)+Q_1(q_4)Q_2(q_3)+Q_1(q_3)Q_2(q_4)]\}\Delta x\Delta y\end{aligned} \tag{19}$$

$$\begin{aligned} D_{j,n+M_x} = \{ & \tfrac{1}{16}Q_1(q_3)Q_2(q_3) + \tfrac{1}{48}[Q_1(q_1)Q_2(q_1) + Q_1(q_4)Q_2(q_4) + Q_1(q_4)Q_2(q_3) + \\ & Q_1(q_3)Q_2(q_4) + Q_1(q_3)Q_2(q_1) + Q_1(q_1)Q_2(q_3)] + \tfrac{1}{144}[Q_1(q_2)Q_2(q_2) + \\ & Q_1(q_2)Q_2(q_1) + Q_1(q_1)Q_2(q_4) + Q_1(q_2)Q_2(q_3) + Q_1(q_1)Q_2(q_2) + \\ & Q_1(q_4)Q_2(q_1) + Q_1(q_3)Q_2(q_2) + Q_1(q_4)Q_2(q_2) + Q_1(q_2)Q_2(q_4)]\}\Delta x\Delta y k^2 \end{aligned} \tag{20}$$

and

$$\begin{aligned} E_{j,n+M_x+1} = \{ & \tfrac{1}{16}Q_1(q_4)Q_2(q_4) + \tfrac{1}{48}[Q_1(q_2)Q_2(q_2) + Q_1(q_3)Q_2(q_3) + Q_1(q_2)Q_2(q_4) + \\ & Q_1(q_4)Q_2(q_3) + Q_1(q_4)Q_2(q_2) + Q_1(q_3)Q_2(q_4)] + \tfrac{1}{144}[Q_1(q_2)Q_2(q_1) + \\ & Q_1(q_1)Q_2(q_4) + Q_1(q_1)Q_2(q_2) + Q_1(q_1)Q_2(q_3) + Q_1(q_4)Q_2(q_1) + \\ & Q_1(q_3)Q_2(q_1) + Q_1(q_3)Q_2(q_2) + Q_1(q_1)Q_2(q_1) + Q_1(q_2)Q_2(q_3)]\}\Delta x\Delta y k^2 \end{aligned} \tag{21}$$

where $Q_1(q_i) = G_{j,q_i}$ and $Q_2(q_i) = M_{q_i}$.,and $R = (M_x - 1) \times (M_y - 1)$,, and the definitions of q_i are shown in Figure 1. When $n = j, n = j-1, n = j - M_x - 1, n = j - M_x$, the Green functions have a singularity, but using the same method as in the paper (Richmond, 1965) for singularity processing, we have

$$F_{jlr} = \frac{i}{2}[\pi ka H_0^{(1)}(ka) + 2i] * M_l \delta_{l,n} \tag{22}$$

where $a = \sqrt{\Delta x \cdot \Delta y / \pi}$. Thus, equation (14) can be written as

$$\Gamma \boldsymbol{U} = \boldsymbol{U}^{inc} \tag{23}$$

where $\boldsymbol{U} = (u_1, u_2, \cdots, u_N)^t, \boldsymbol{U}^{inc} = (u_1^{inc}, u_2^{inc}, \cdots, u_N^{inc})^t, \Gamma_{jl} = A_{jl},\ (j \neq l),\ \Gamma_{jl} = A_{jl} + 1.,\ (j = l)$ Therefore, the total field can be obtained by solving equation (23) and we solve the linear system (23) for $\boldsymbol{U}$ using Gaussian Elimination; we will discuss the numerical solution of (23) in the next section.

After the total field is found, the scattering field at r_m outside the object region can be expressed as

$$u_m^{sc} = -\sum_{l=1}^{N} A_{ml} M_l \tag{24}$$

where A_{ml} equals Eqn (14), and $Q_1(q_i) = G_{m,q_i}$, $Q_2(q_i) = u_{q_i}$. Therefore, the scattering field in frequency domain can be derived by Eqn (24) and the waveform of the scattering can be derived by inverse Fourier transform of the frequency domain wave field.

NUMERICAL SIMULATIONS

We used our bilinear method to calculate the scattered fields for the two models shown in Figures 2a and 3a. The velocities, along with the geometry of the source and receiver positions, are denoted in the figures. 100 sources and 100 receivers are located at x=-30 m and x=+30m at equal z-axis intervals of 1.6 m. This geometry corresponds to the crosswell imaging experiment in borehole geophysics. We compare pulse basis simulations with the bilinear basis simulations. First, we discuss the properties of the matrices derived by the two different basis functions. When we use the same size model with (Mx+1)*(My+1) nodes, then we can establish two impedance matrices for the pulse element method and bilinear element method, which we call Γ_0, $n_0 \times n_0$,, where $n_0 = Mx \times My$ for the pulse element method, and Γ, $n \times n$, where $n = (Mx+1) \times (My+1)$ for the bilinear element method. When we set the unknown number of elements in two different formulations to make $n_0 = n$, then, Γ_0 and Γ are very similar: (1) For model II, both of matrices we obtained from pulse elements and bilinear elements are very well conditioned; the condition numbers of bilinear element matrix and pulse element matrix are 4.3 and 5.8, respectively; and the matrix Γ for bilinear element is slightly better conditioned than Γ_0; and $\|\Gamma - \Gamma_0\|_2 / \|\Gamma_0\|_2 = 0.085$, which shows that the matrices are not dissimilar; and (2) the distribution of the singular values corresponding to both the largest and smallest singular values are also almost identical. Therefore, solving linear systems of the same size with Γ and Γ_0 will be of equivalent difficulty whether we use Gauss Elimination with pivoting or an iterative method like generalized minimum residual method (GMRES) (Youcef and Schultz, 1986, Walker, 1989, Navarra, 1989), which is appropriate for non-singular matrices with no special properties such as symmetry or positive definitions. Since the matrix is dense, we don't expect iterative method will be better than Gauss elimination when you can use Gauss Elimination. We find that to obtained the desired accuracy, for example, in a cross well imaging system, the matrix for bilinear is not too big to use Gauss Elimination.

In addition, one main advantage of Gauss Elimination is that once we do the LU factorization, we can solve many linear systems with same matrix and many different right hand sides, while an iterative solver will be expensive for multi-source/multi-receiver systems because for different source or receiver, the wave field must be solve independedly. Any method we can use for Γ_0 , we can also use for Γ. For the same size of cell, the moment method with bilinear basis functions get better accuracy than that with pulse basis functions To get same accuracy, the moment method with bilinear basis functions requires a smaller matrix than for the pulse basis functions, as the following numerical experiments shown

With pulse basis functions, we use 10 pixels per wavelength, while with the bilinear basis function we use only 6 nodes per wavelength. A comparison of the results is shown in Figures 2b-2f and 3b-3f.

Model I (Figure 2) consists of a rectangular block centered at x=1.6m , z=0.0 m in an otherwise homogeneous medium. We plot in Figure 2b the magnitude of the amplitude at all receivers for the source at z=0. m. If we assume that the more expensive pulse basis simulation is accurate (Johnson, 1983, Herrmann, 1993), then we find that the bilinear basis functions yield errors less than approximately 5.3 % everywhere (Figure 2b). However, the bilinear basis simulation requires less memory to store the matrix for inversion than pulse basis simulation. Therefore, it can run greatly faster than the pulse basis simulation when solving the linear system (23) for the total field in the medium. Compared with pulse basis simulation, the larger the inhomogeneous region is, the faster the bilinear simulation is. Here, the bilinear simulation is about 60% faster than the pulse basis simulation. The real and imaginary parts of the computed scattered amplitudes for the 100x100 source-receiver positions are displayed in Figures 2c and 2d for the bilinear basis functions, and in Figures 2e and 2f for the pulse basis functions. The patterns of amplitudes are obviously very similar in both simulations.

Model II is more geological in origin (Figure 3a). A line plot of the amplitude for the source at z=80m is shown in Figure 3b, where again we have error of less than about 4.8 %. The real and imaginary amplitudes of the scattered wave field are displayed in Figures 3c and 3d for the bilinear basis functions and Figures 3e and 3f for the pulse basis functions. Again, as with Model I, there is excellent similarity between the two. For inversion, we often need to know the fields everywhere in the region. In Figures 4a to 4d, we display the total field magnitude at every pixel or node on the solution grid for a source at z=80m by using the bilinear basis function moment method and the pulse moment method. This comparison illustrates the uniformity of the results for regions both near and far away form the source.

Finally, we applied the inverse Fourier transform to the frequency domain scattered wave field of both Models I and II to obtain the time domain waveforms or seismograms. These are shown in Figures 5a and 5b for the one common shot gather for Model I and II, respectively. We used a Ricker wavelet (first derivative of a Gaussian) with a 300 Hz center frequency and nodes of $\Delta x = \Delta y = 1/6 \times \lambda_{\min}$. The seismogram for Model I shows the typical hyperbolic moveout of a diffraction from a small object embedded in a homogeneous medium. The seismogram for the layered model is more complicated, exhibiting clear reflections and diffractions.

CONCLUSIONS

We described a new moment method for evaluating the wave field in inhomogeneous media. We used a bilinear basis function to discretize the acoustic integral equation and compute the area integration for each small square cell instead of approximating the pixels with circular cells everywhere as with pulse basis functions, except in the singularities. With this method, the wave field can be calculated accurately for only 6 nodes per wavelength instead of 10 pixels per wavelength with the pulse basis function. As a result, the memory requirements and execution times for numerical implementation is significantly deceased, while the errors are usually less than 6%. If there are less than 6 nodes per wavelength in the bilinear simulation, the storage and execution time can be further reduced, but the simulation precision will be decreased also. In addition, the Frechét derivative for non-linear wave equation inversion is easy to derive from our bilinear basis simulation. Numerical simulations show our method is effective and very useful in solving forward scattering problem. Although bilnear basis element have been used previously in many other application, we have demonstrated here that their application to the method of moments, where the current standard method uses pulse basis functions, leads to discrete problems which are just as easy to set up and solve as with pulse basis functions; moreover the solution with bilinear elements are much more accurate for the same level of discretization, and thus are less expensive because we can use larger pixel sizes to obtain accuracy equivalent to the standard pulse basis function method.

ACKNOWLEDGMENTS

This work was supported by the Seismic Tomography Project of Stanford University, a research consortium sponsored by companies of the oil and gas industry.

REFERENCES

Bathe, K.J., Finite Element Procedures in Engineering Analysis, Englewood Cliffs, NJ: Prentice Hall, Inc., 1982

Beydoun, W.B. and M. Mendes, Elastic ray Born l^2 migration / inversion, Geophys, J., 97, 151-160

Bojarski, N.N., K-space formulation of the electromegnetic scattering problem, Rep. AFAL-TR-71-75, AIR Force Avionics Lab., Wright-patterson Air Force Base, Ohio, March, 19971

Bojarski, N.N., The k-space formulation of the scattering problem in the time domain: An improved single propagator formulation, J. Acous. Soc. Am. 77(3), 826-831, 1985

Bojarski, N.N., The k-space formulation of the scattering problem in the time domain, J Acous Soc. AM, 72(2), 570-584, 1982

Borup, D.T., and O.P. Gandhi, Fast-Fourier-transform method for calculation of SAR distribution in finely discretized inhomogeneous models of biological bodies, IEEE Trans. Microwave Theory Tech., MIT-32, 355-360, 1984

Borup, D.T., and O.P. Gandhi, Calculation of high-resultion SAR distribution in biological bodies using the FFT algorithm and the conjugation gradient method,, IEEE Trans. Microwave Theory Tech., MIT-33, 417-419, 1985

Caorsi S., Gragnani G.L., and Pastorino M., Redundant Electromagnetic data for microwave imaging of three-dimensional dielectric objects, IEEE Transactions on Atennas and Propgation, Vol.42, No.5, 581-589, 1993.

Caorsi S. , Gragnani, G.L., Pastorino M. and Zunino G., Microwave Imaging Based on a Markov Random Field model, IEEE Transaction on Atennas and propagation, Vol. 42, No.3, 29-303, 1994

Caorsi S., Gragnani G.L., Medicina, S., Pastorino M., and Pinto, G.A., A Gibbs random fielfd-based active electromegnetic method for noninvasive diagnostics in biomedical applications, Radio Science, Vol.30, No. 1, 291-301, 1995

Chew W. C. and Cai-cheng Lu, The use of Huygens' Equivalence principle for solving the volume integral equation of scattering, IEEE Transaction on antennas and propagation, vol. 41, no.7, 897-904,1993

Chew W.C. and Y.M. Wang, Reconstruction of Two-Dimensional permittivity distribution using the Distorted Born iterative method, IEEE transactions on medical imaging, Vol. 9, No.2, 218-235, 1990

Denis F. and Basset O. and Gimenez G., Ultrasonic Transmission tomography in Refracting media: Reduction of Refraction artifacts by curved-ray techniques, IEEE Transactions on Atennas and Propgation, Vol.41, No. 1, 1993.

Feit, M. D., and Fleck, J.A. Jr., Light propagation in graded-index optical fibers: Applied Opticcs, 17, 3990-3998, 1978.

Harris, J. M and Guang Wang, Diffraction tomography for inhomogeneities in a layered background, Expanded Abstract of 63rd Annual meeting of Soiety of Exploration Geophysics, 49-52, 1993

Herrmann, G.F. and Strain S.M., Sampling method using prefiltered Band-limited Green's functions for the solution of electromagnetic integral equations, IEEE Transactions on Atennas and Propgation, Vol.41, No. 1, 20-24, 1993.

Herrmann, G.F., Note on Interpolational Basis functions in the Mothod of Moments, IEEE Transactions on Atennas and Propgation, Vol.38, No. 1, 134-137,1990.

Johnson, Steven A. and Michael L. Tracy, Inverse Scattering solution by a sinc basis, multiple source, moment method --Part I : Theory, Ultrosonic Imaging 5, 361-375, 1983

Khahil Kalbasi, and Kenneth R. Demarst, A multilevel formulation of the method of moments, IEEE Transactions on Atennas and Propgation, Vol.41, No. 5, 589-599, 1993.

LEE Robert, and Cangellaris Andreas C., A study of discretization Error in the finit element approximation of wave solutions. IEEE Transactions on Atennas and Propgation, Vol.40, No.5, 542-555, 1992.

Moghaddam, Maha , and Weng Cho Chew, Study of some practical issues in inversion with the Born Iterative method using Time-Domain Data, IEEE Transactions on Atennas and Propgation, Vol.41, No. 2, 177-184, 1993.

Martin, J.M., and Flatte, S.M., Intensity images and statistics from numerical simulation of wave propagation in 3-D radom media: Applied Optics, 27, 2111-2126, 1988

Navarra Antonio, An application of GMRES to indefinite linear problems in meteorolgy, Computer Physics Communicatios, 53, 321-327, 1989,

Zhuck, Nickolay P and Alexander G. Yarovoy, Two-dimensional scattering from an inhomogeneous dielectric cylinder embedded in a stratified medium: Case of TM polarization, IEEE Transaction on antennas and propagation, vol. 42, no.1, 1994.

Pratt, R.G., Frequency-domain elastic wave modeling by finite differences: A tool for crosshole seismic imaging, Geophysics 55: 626-623, 1990

Richmond, J.H., Scattering by a dielectric cylinder of arbitary cross section shape, IEEE Trans, Ant. Prop. 13:334-341, 1965

Sarkar Tapan K, Arvas Ercument , and Rao Sadasiva M., Application of FFT and the conjugation grdient method for the solution of electromagnetic radiation from electrically large and small conducting bodies, IEEE transactions on atennas and propagation, Vol. AP-34, No.33, 635-640,1986

Shozo Koshigoe, Bojarski, N.N., The k-space formulation of the acoustic scattering problem, J. Acoust. Sco. Am. 84(5), 1890-1893, 1988

Slvatore Caorsi, Gian Luigi Gragnani, and Matteo Pastorino, Reconstruction of Fielectric permittivity distributions in arbitrary 2-D inhomogeneous biological bodies by a multiview microwave numerical method, IEEE transactions on medical imaging, Vol. 12, No.2, 1993

Steiberg B.Z. and Leviatan Yehuda , On the use of Wavelet expansions in the method of moments, IEEE Transaction on antennas and propagation, vol. 41, no.5, 1993

Thompson, R.D, W.L.Rodi, C.H. Cheng anf M.N. Toksoz, Nonlinear Diffraction Tomography Applied to Crosshole Seismic Data, Geotomography, Vol. 2, 445-456,1992(The Proceedings of The Second SEGJ/SEG International Symposium on Geotomography)

Thomson, D.J., and Chapman, N.R., , A wide angle algorithm for the parabolic equation: J. Acoust. Soc. Am. 74, 1848-1854, 1983.

Walker F. Homer, Implementations of the GMRES method, Computer Physics Communications 53, 311-320, 1989

Wang Gaofeng, Hybrid wavelet expansion and boundary element analyssis of electromagnetic scattering from conducting objects, IEEE Transactions on Atennas and Propagation, Vol. 43, No.2, 170-178, 1995.

Wang Weiyan and Zhang Shourong, Unrelated Illumination Method for electromagnteic inverse scattering of inhomogeneous lossy dielectric bodies, IEEE Transactions on Atennas and Propgation, Vol.40, No.11, 1292-1296, 1992.

Wu, R.S., 1994, Wide-angle elastic wave one-way propagation in heterogeneous media and an elastic wave complex-screen method, J. Geophys. Res., 99, 751-766, 1994

Wu, R.S. and Huang, L.J., 1992, Scattered field calculation in heterogeneous media using phase-screen propagator, Expanded Abstracts of the technical program, SEG 62th Annual Meeting, 1289-1292.

Youcef saad and Martin H. Schultz, GMRES: A generalized minimal residual algorithm for solving nonsymmetric linear systems, SIAM J. SCI. STAT. COMPUT., Vo. 7, No. 3, 1986

Zhou Changxi and Gerard T. schuster, Waveform Inversion of Subwell velocity, Exapanded Abstract of 63rd Annual Meeting of Society of Exploration of Geophysics, 106-109, 1993.

Appendix 1

When inserting equations (11) - (13) into the integration in equation (5), we have

$$\int_{x_i}^{x_i+\Delta x}\int_{y_i}^{y_i+\Delta y} M(\mathbf{r}')G(k|\mathbf{r}-\mathbf{r}'|)U(\mathbf{r}',\omega)d\mathbf{r}' = \int_{x_i}^{x_i+\Delta x}\int_{y_i}^{y_i+\Delta y} \Big(\sum_{n=1}^{N} \rho_n M_n\Big)\cdot\Big(\sum_{n=1}^{N} \rho_n u_n\Big)\cdot\Big(\sum_{n=1}^{N} \rho_n G_n\Big)dx'dy'$$

$$= \int_{x_i}^{x_i+\Delta x}\int_{y_i}^{y_i+\Delta y} (\rho_n M_n + \rho_{n+1}M_{n+1} + \rho_{n+M_x}M_{n+M_x} + \rho_{n+M_x+1}M_{n+M_x+1})\cdot$$

$$(\rho_n G_n + \rho_{n+1}G_{n+1} + \rho_{n+M_x}G_{n+M_x} + \rho_{n+M_x+1}G_{n+M_x+1})\cdot$$

$$(\rho_n u_n + \rho_{n+1}u_{n+1} + \rho_{n+M_x}u_{n+M_x} + \rho_{n+M_x+1}u_{n+M_x+1})\, dx'dy'$$

where $n = (j-1)\cdot M_x + i$ Define
$Q_1 = G, Q_2 = M, l = q_1, l+1 = q_2, l+M_x = q_3, l+M_x+1 = q_4$, we have

$$\int_{x_i}^{x_i+\Delta x}\int_{y_i}^{y_i+\Delta y} M(\mathbf{r}')G(k|\mathbf{r}-\mathbf{r}'|)U(\mathbf{r}',\omega)d\mathbf{r}' =$$

$$\int_{x_i}^{x_i+\Delta x}\int_{y_i}^{y_i+\Delta y} [(\rho(q_1)\rho(q_1)Q_1(q_1)Q_2(q_1) + \rho(q_2)\rho(q_1)Q_1(q_2)Q_2(q_1) + \rho(q_3)\rho(q_1)Q_1(q_3)Q_2(q_1)$$

$$(\rho(q_1)Q_2(q_1) + \rho(q_2)Q_2(q_2) + \rho(q_3)Q_2(q_3) + \rho(q_4)Q_2(q_4))\cdot]$$

$$(\rho(q_1)u(q_1) + \rho(q_2)u(q_2) + \rho(q_3)u(q_3) + \rho(q_4)u(q_4))\; dx'dy'$$

$$= \int_{x_i}^{x_i+\Delta x}\int_{y_i}^{y_i+\Delta y} [(\rho(q_1)\rho(q_1)Q_1(q_1)Q_2(q_1) + \rho(q_2)\rho(q_1)Q_1(q_2)Q_2(q_1) + \rho(q_3)\rho(q_1)Q_1(q_3)Q_2(q_1)$$

$$+\rho(q_4)\rho(q_1)Q_1(q_4)Q_2(q_1))\cdot(\rho(q_1)\rho(q_2)Q_1(q_1)Q_2(q_2) + \rho(q_2)\rho(q_2)Q_1(q_2)Q_2(q_2)$$

$$+\rho(q_3)\rho(q_2)Q_1(q_3)Q_2(q_2) + \rho(q_4)\rho(q_2)Q_1(q_4)Q_2(q_2))\cdot(\rho(q_1)\rho(q_3)Q_1(q_1)Q_2(q_3)$$

$$+\rho(q_2)\rho(q_3)Q_1(q_2)Q_2(q_3) + \rho(q_3)\rho(q_3)Q_1(q_3)Q_2(q_3) + \rho(q_4)\rho(q_3)Q_1(q_4)Q_2(q_3))\cdot$$

$$(\rho(q_1)\rho(q_4)Q_1(q_1)Q_2(q_4) + \rho(q_2)\rho(q_4)Q_1(q_2)Q_2(q_4) + \rho(q_3)\rho(q_4)Q_1(q_3)Q_2(q_4)$$

$$+\rho(q_4)\rho(q_4)Q_1(q_4)Q_2(q_4))]\cdot(\rho(q_1)u(q_1) + \rho(q_2)u(q_2) + \rho(q_3)u(q_3) + \rho(q_4)u(q_4))\cdot dx'dy'$$

$$= \int_{x_i}^{x_i+\Delta x}\int_{y_i}^{y_i+\Delta y} \{[(\rho(q_1)\rho(q_1)\rho(q_1)Q_1(q_1)Q_2(q_1)+\rho(q_2)\rho(q_1)\rho(q_1)Q_1(q_2)Q_2(q_1)$$

$$+\rho(q_3)\rho(q_1)\rho(q_1)Q_1(q_3)Q_2(q_1)+\rho(q_4)\rho(q_1)\rho(q_1)Q_1(q_4)Q_2(q_1))\cdot$$

$$+\rho(q_3)\rho(q_2)\rho(q_1)Q_1(q_3)Q_2(q_2)+\rho(q_4)\rho(q_2)\rho(q_1)Q_1(q_4)Q_2(q_2))\cdot$$

$$(\rho(q_1)\rho(q_4)\rho(q_1)Q_1(q_1)Q_2(q_4)+\rho(q_2)\rho(q_4)\rho(q_1)Q_1(q_2)Q_2(q_4)$$

$$+\rho(q_3)\rho(q_4)\rho(q_1)Q_1(q_3)Q_2(q_4)+\rho(q_4)\rho(q_4)\rho(q_1)Q_1(q_4)Q_2(q_4))]\cdot u(q_1)$$

$$+[\,(\rho(q_1)\rho(q_1)\rho(q_2)Q_1(q_1)Q_2(q_1)+\rho(q_2)\rho(q_1)\rho(q_2)Q_1(q_2)Q_2(q_1)$$

$$+\rho(q_3)\rho(q_1)\rho(q_2)Q_1(q_3)Q_2(q_1)+\rho(q_4)\rho(q_1)\rho(q_2)Q_1(q_4)Q_2(q_1))\cdot$$

$$(\rho(q_1)\rho(q_2)\rho(q_2)Q_1(q_1)Q_2(q_2)+\rho(q_2)\rho(q_2)\rho(q_2)Q_1(q_2)Q_2(q_2)$$

$$+\rho(q_3)\rho(q_2)\rho(q_2)Q_1(q_3)Q_2(q_2)+\rho(q_4)\rho(q_2)\rho(q_2)Q_1(q_4)Q_2(q_2))\cdot$$

$$(\rho(q_1)\rho(q_3)\rho(q_2)Q_1(q_1)Q_2(q_3)+\rho(q_2)\rho(q_3)\rho(q_2)Q_1(q_2)Q_2(q_3)$$

$$(\rho(q_1)\rho(q_4)\rho(q_2)Q_1(q_1)Q_2(q_4)+\rho(q_2)\rho(q_4)\rho(q_2)Q_1(q_2)Q_2(q_4)$$

$$+\rho(q_3)\rho(q_4)\rho(q_2)Q_1(q_3)Q_2(q_4)+\rho(q_4)\rho(q_4)\rho(q_2)Q_1(q_4)Q_2(q_4))]\cdot u(q_2)$$

$$[\,(\rho(q_1)\rho(q_1)\rho(q_3)Q_1(q_1)Q_2(q_1)+\rho(q_2)\rho(q_1)\rho(q_3)Q_1(q_2)Q_2(q_1)$$

$$+\rho(q_3)\rho(q_1)\rho(q_3)Q_1(q_3)Q_2(q_1)+\rho(q_4)\rho(q_1)\rho(q_3)Q_1(q_4)Q_2(q_1))\cdot$$

$$(\rho(q_1)\rho(q_2)\rho(q_3)Q_1(q_1)Q_2(q_2)+\rho(q_2)\rho(q_2)\rho(q_3)Q_1(q_2)Q_2(q_2)$$

$$+\rho(q_3)\rho(q_2)\rho(q_3)Q_1(q_3)Q_2(q_2)+\rho(q_4)\rho(q_2)\rho(q_3)Q_1(q_4)Q_2(q_2))\cdot$$

$$(\rho(q_1)\rho(q_3)\rho(q_3)Q_1(q_1)Q_2(q_3)+\rho(q_2)\rho(q_3)\rho(q_3)Q_1(q_2)Q_2(q_3)$$

$$+\rho(q_3)\rho(q_3)\rho(q_3)Q_1(q_3)Q_2(q_3)+\rho(q_4)\rho(q_3)\rho(q_3)Q_1(q_4)Q_2(q_3))\cdot$$

$$(\rho(q_1)\rho(q_4)\rho(q_3)Q_1(q_1)Q_2(q_4)+\rho(q_2)\rho(q_4)\rho(q_3)Q_1(q_2)Q_2(q_4)$$

$$+\rho(q_3)\rho(q_4)\rho(q_3)Q_1(q_3)Q_2(q_4)+\rho(q_4)\rho(q_4)\rho(q_3)Q_1(q_4)Q_2(q_4))]\cdot u(q_3)$$

$$+[(\rho(q_1)\rho(q_1)\rho(q_4)Q_1(q_1)Q_2(q_1)+\rho(q_2)\rho(q_1)\rho(q_4)Q_1(q_2)Q_2(q_1)$$

$$+\rho(q_3)\rho(q_1)\rho(q_4)Q_1(q_3)Q_2(q_1)+\rho(q_4)\rho(q_1)\rho(q_4)Q_1(q_4)Q_2(q_1))\cdot$$

$$(\rho(q_1)\rho(q_2)\rho(q_4)Q_1(q_1)Q_2(q_2)+\rho(q_2)\rho(q_2)\rho(q_4)Q_1(q_2)Q_2(q_2)$$

$$+\rho(q_3)\rho(q_2)\rho(q_4)Q_1(q_3)Q_2(q_2)+\rho(q_4)\rho(q_2)\rho(q_4)Q_1(q_4)Q_2(q_2))\cdot$$

$$(\rho(q_1)\rho(q_3)\rho(q_4)Q_1(q_1)Q_2(q_3)+\rho(q_2)\rho(q_3)\rho(q_4)Q_1(q_2)Q_2(q_3)$$

$$+\rho(q_3)\rho(q_3)\rho(q_4)Q_1(q_3)Q_2(q_3)+\rho(q_4)\rho(q_3)\rho(q_4)Q_1(q_4)Q_2(q_3))\cdot$$

$$(\rho(q_1)\rho(q_4)\rho(q_4)Q_1(q_1)Q_2(q_4)+\rho(q_2)\rho(q_4)\rho(q_4)Q_1(q_2)Q_2(q_4)$$

$$+\rho(q_3)\rho(q_4)\rho(q_4)Q_1(q_3)Q_2(q_4)+\rho(q_4)\rho(q_4)\rho(q_4)Q_1(q_4)Q_2(q_4))]\cdot u(q_4)\ \}\cdot dx'dy'$$

$$=B_{q_1}u(q_1)+C_{q_2}u(q_2)+D_{q_3}u(q_3)+E_{q_4}u(q_4)$$

the defnitions of $B_{q_1}, C_{q_2}, D_{q_3}, E_{q_4}$ are shown by equations (18)-(21)

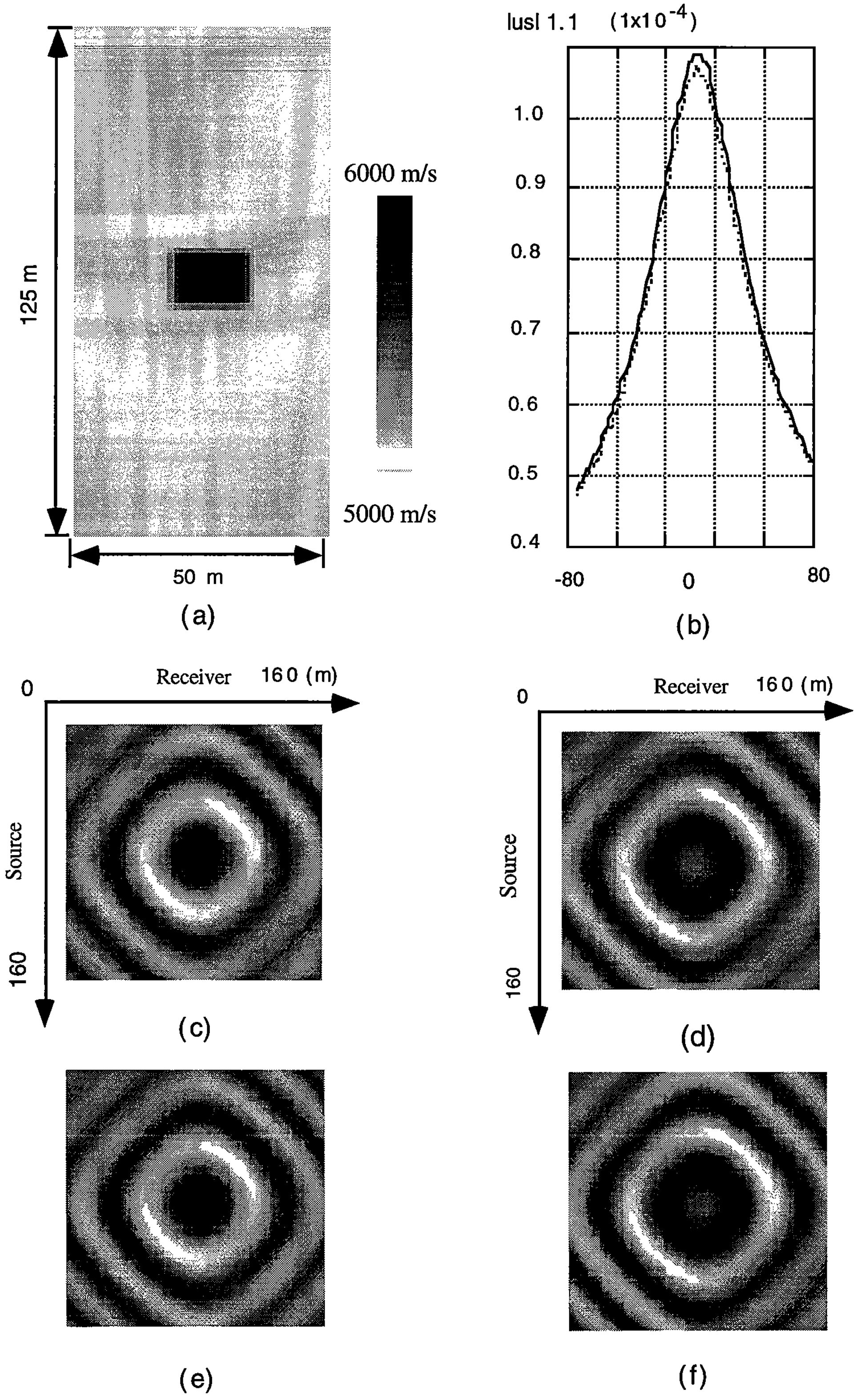

Figure 2: (a) Synthetic model I. (b) The amplitudes of the received sacattered fields for the bilinear and pulse basis functions moment methods, where dot and dense lines denote the results of the blinear and pulse basis function moments methods, respectively, and the source is located at (0,0); (c) and (d) display the real and imaginary parts of the computed scattered amplitudes for the 100 x100 source-receiver positions for the binear basis functions, the results in (e) and (f) are for the pulse basis functions.

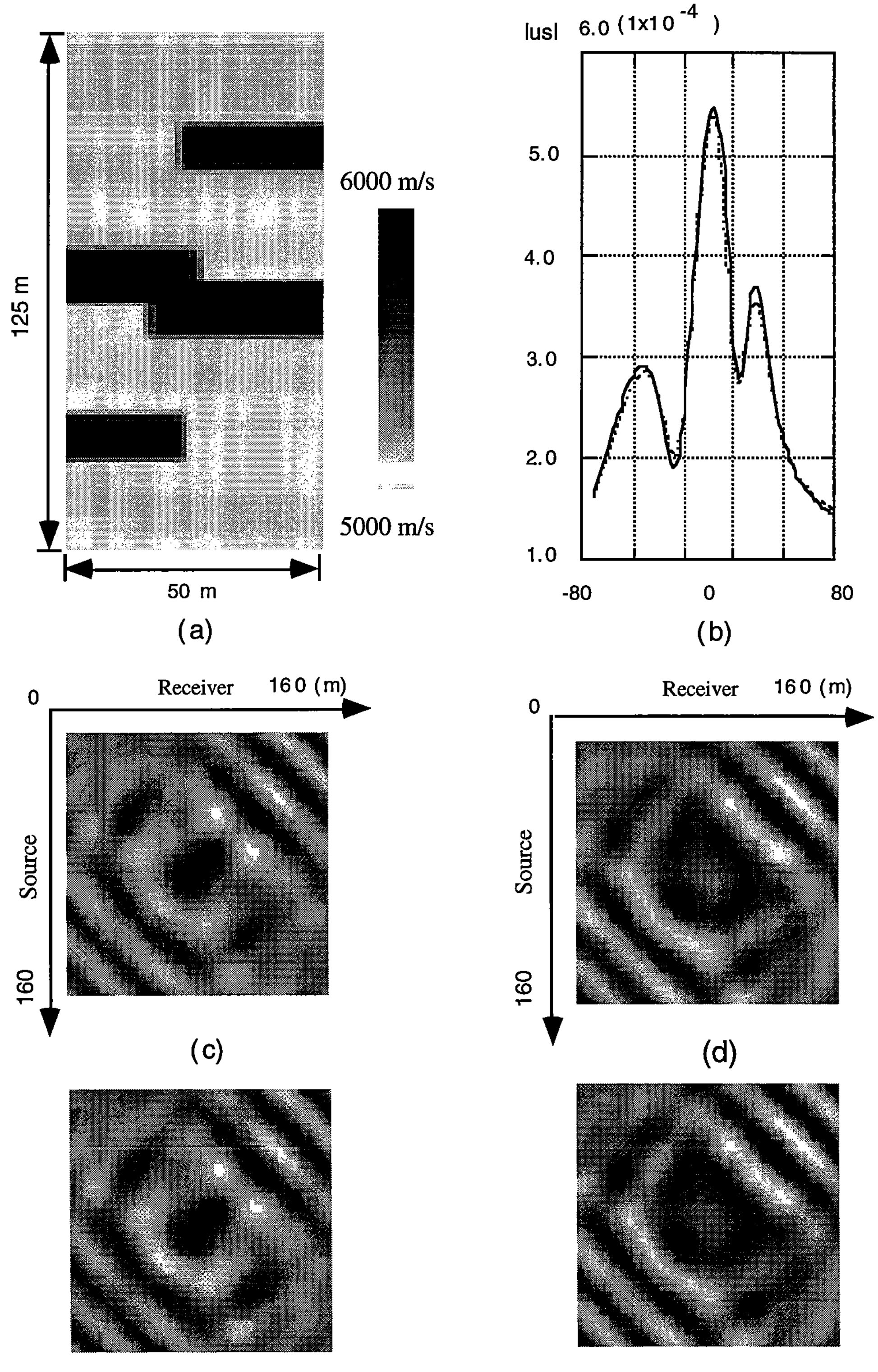

(a) (b)

(c) (d)

(e) (f)

Figure 3: (a) Synthetic model II. (b) The amplitudes of the received sacattered fields for the bilinear and pulse basis functions moment methods, where dot and dense lines denote the results of the blinear and pulse basis function moments methods, respectively, and the source is located at (0,0); (c) and (d) display the real and imaginary parts of the computed scattered amplitudes for the 100 x100 source-receiver positions for the binear basis functions, the results in (e) and (f) are for the pulse basis functions.

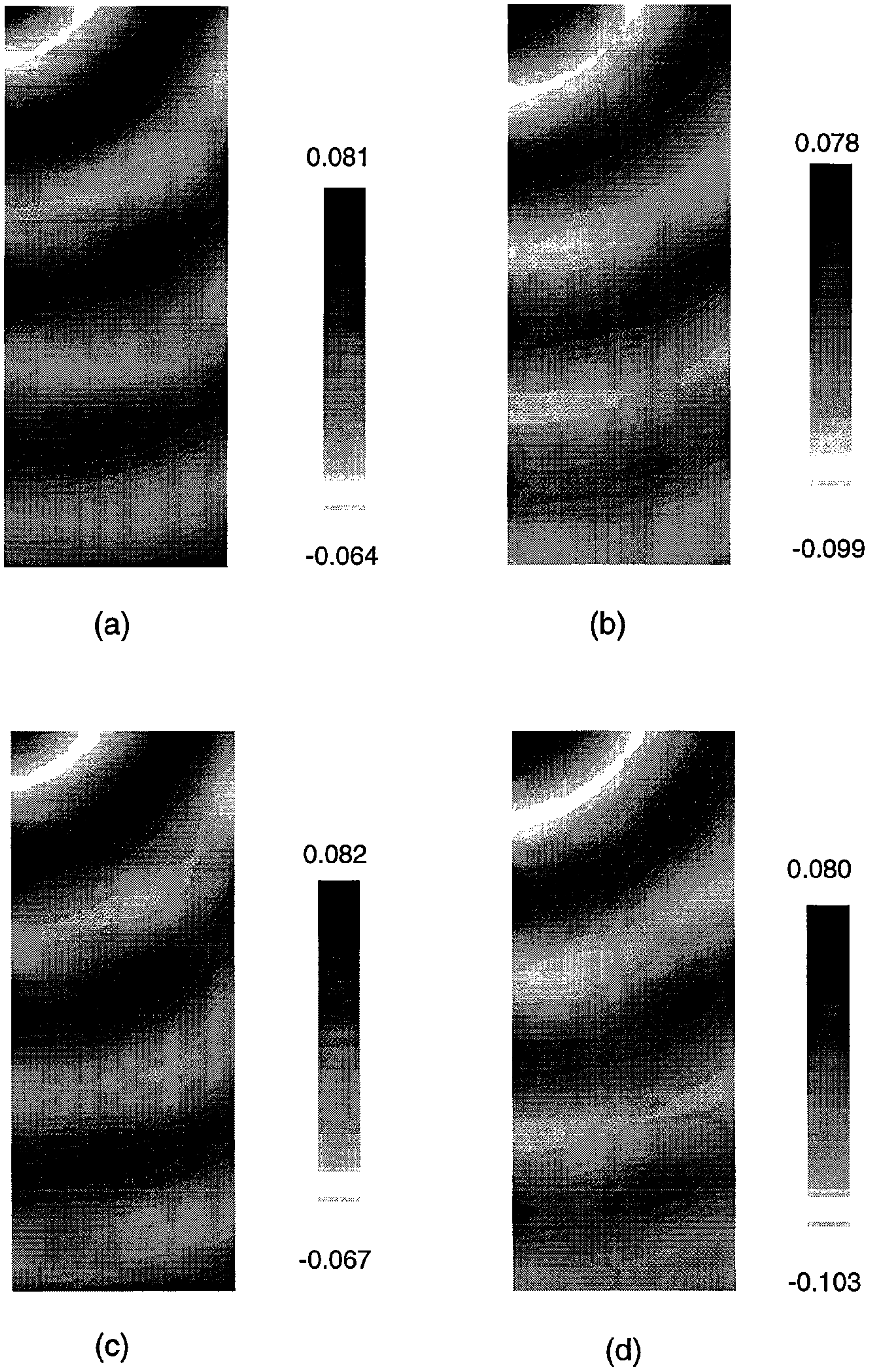

Figure 4: (a) and (b) are the real and imaginary part of the total field of model II in the object region derived by the bibinear basis function moment method, respectively; (c) and (d) are the real and imaginary part of the total field of model II in the object region derived by the pulse basis function moment method, respectively, and in the (a) -(d), theposition of the source is (-30,80).

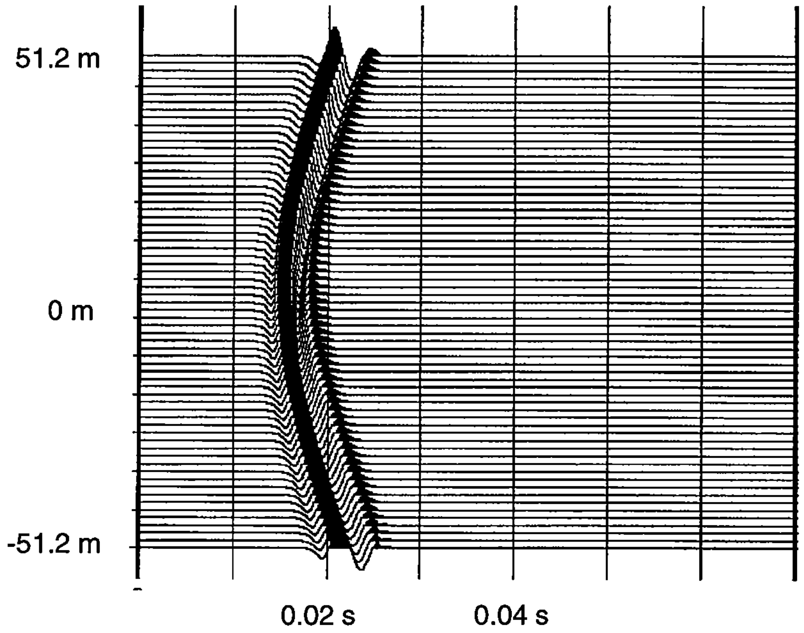

(a)

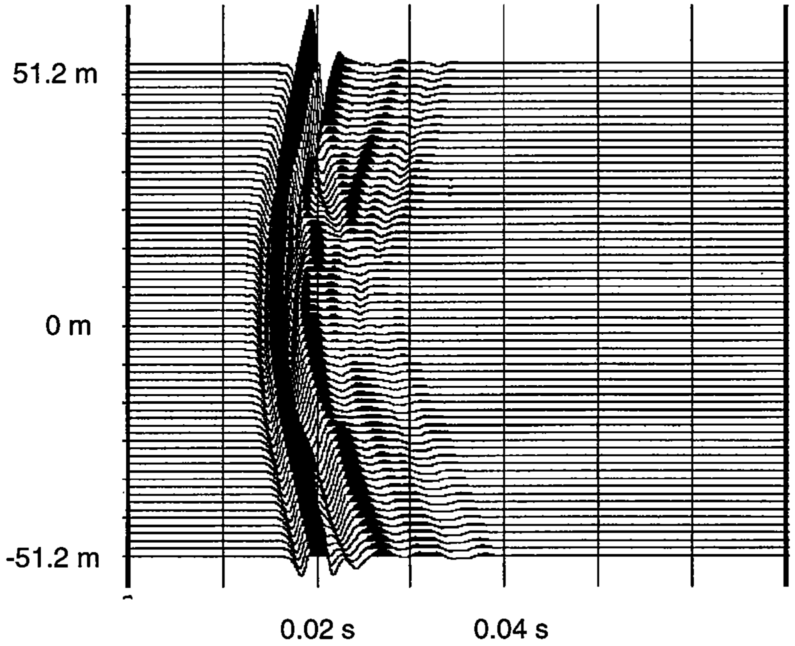

(b)

Figure 5: (a) The waveform of the scattered field by model I. (b) The waveform of the scattered field by model II

PAPER C

Synthesis Of Elastic Waves In Radially Layered Media With Horizontal structures

Youli Quan* and Xiaofei Chen**

ABSTRACT

The generalized reflection and transmission coefficients method with normal mode expansion is developed to calculate the elastic wave field for simulating energy propagation in sonic logging and the crosswell seismic data aquisition in complicated media. This method simulates models which consist of concentric cylindrical layers, and each cylindrical layer has within it horizontal layers in the *z*-direction. In the real world, the borehole casing with perforations, the source array, the open and cased boreholes embedded in layered media, etc. can be treated as this kind of model. The simulation based on this method gives reflections and transmissions, tube wave conversions generated at casing perforations and horizontal layers, the radiation pattern of a source array in a complicated borehole, and so on. This method is a semi-analytical approach. The calculation, therefore, is faster and more accurate than pure numerical methods. In this report we present five examples to show the possible applications of this approach. One of these examples is of special interest. In this example the borehole has a casing and the formation has a fault. We use this model to calculate a complete crosswell seismic data set which includes the borehole effects, reflections and scattering from the fault, tube waves, and other wave phenomena. This synthetic data set can be used to test tomography, reflection mapping and migration techniques. The computational time for this example is about 12 hours on a DEC alpha workstation.

---

* *STP, Stanford University*
** *Department of Earth Sciences, USC*

INTRODUCTION

For most borehole simulations (e.g., Tubman et al., 1984; Baker, 1984; Chen et al., 1994), a borehole is simply modeled as a series of concentric, cylindrical layers. In a real borehole, however, the medium within a cylindrical layer usually are not homogeneous, whose elastic parameters often change with depth. Pai et al. (1993) simulated the electromagnetic induction logging for this kind of models. For sonic logging problems we have to solve the elastodynamic equation in which both *P* and *S* waves are included. Therefore, the solutions for the elastic problem are more complex. For the elastic wave simulation, Bouchon (1993) presented a semi-analytical approach to use the boundary element method for a simple open borehole embedded in layered media. In this report we further develop the generalized reflection and transmission coefficients method (Chen et al., 1994) to calculate more realistic models, such as multi-layered boreholes (casing and invaded zones) embedded in multi-layered formation, faults in the formation, and perforation in a casing.

One of the objectives of this work is to calculate a complete crosswell seismic data set in which borehole effects, casing effects, tube waves, complex layers in formation, and so on, are included. Then, these synthetic data can be used to test tomography, reflection mapping and migration methods and programs.

PHYSICAL MODEL

Figure 1 shows a profile of a borehole model embedded in complex layered formation. The source is located inside the borehole, which can be a point source or finite cylinders. Receivers are located either inside or outside the borehole. This model looks complex, but it still has axially symmetric properties. Taking the advantage of this symmetry, we can derive a set of formulas to simulate the elastic wave propagation in this complex borehole-formation model.

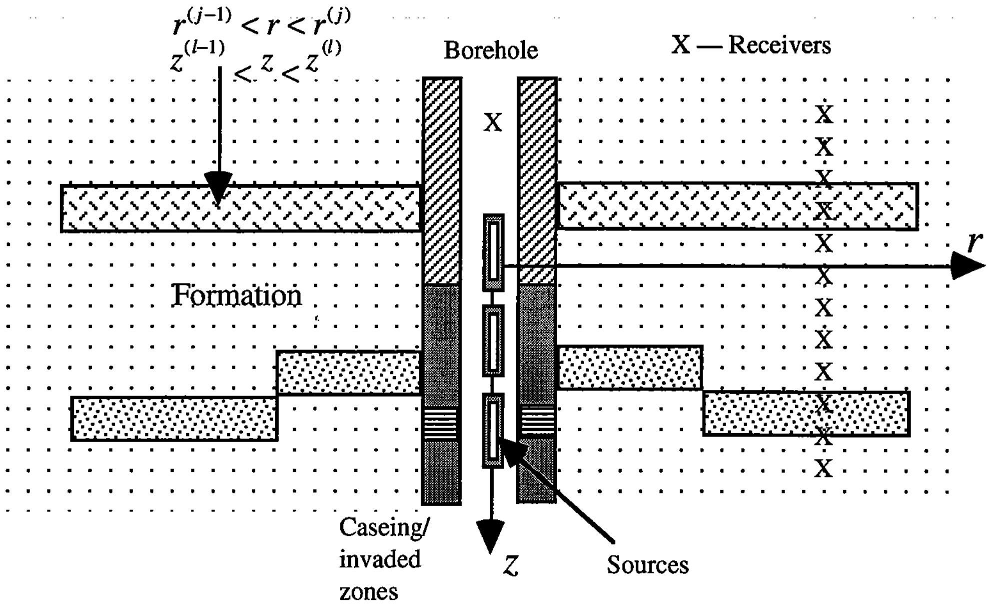

FIG. 1. A complicated borehole embedded in layered formation.

GOVERNING EQUATIONS

Since the model (see Figure 1) is independent of θ in cylindrical coordinates, we can write the displacement for the j^{th} cylindrical layer as

$$\mathbf{u}^{(j)} = \nabla\phi^{(j)} + \nabla\times(\mathbf{e}_\theta \psi^{(j)}). \tag{1}$$

The *P* wave potential $\phi^{(j)}$ and the *S* wave potential $\psi^{(j)}$ satisfy

$$\frac{\partial^2\phi^{(j)}(r,z)}{\partial r^2} + \frac{1}{r}\frac{\partial\, \phi^{(j)}(r,z)}{\partial r} + \frac{\partial^2\phi^{(j)}(r,z)}{\partial z^2} + k_\alpha^{(j)2}(z)\phi^{(j)}(r,z) = F(\omega)\frac{\delta(r)\delta(z-z_s)}{2\pi r}, \tag{2a}$$

$$\frac{\partial^2\psi^{(j)}(r,z)}{\partial r^2} + \frac{1}{r}\frac{\partial\psi^{(j)}(r,z)}{\partial r} - \frac{\psi^{(j)}(r,z)}{r^2} + \frac{\partial^2\psi^{(j)}(r,z)}{\partial z^2} + k_\beta^{(j)^2}(z)\psi^{(j)}(r,z) = 0, \tag{2b}$$

for $r^{(j-1)}<r<r^{(j)}$ (define $r^{(0)}=0$). Where, $F(\omega)$ is source function in frequency domain, z_s is the z coordinate of the source location, $k_\alpha^{(j)^2}(z) = \dfrac{\omega^2}{[\alpha^{(j)}(z)]^2}$ and $k_\beta^{(j)^2}(z) = \dfrac{\omega^2}{[\beta^{(j)}(z)]^2}$, here a and β are *P* and *S* velocities, respectively.

The potentials can be expanded by a set of eigen-functions, $\{f_n^{(j)}(z),\ g_n^{(j)}(z);\ n=1,2,\ldots,N\}$, into

$$\phi^{(j)}(r,z)=\sum_{n=1}^{2N+1}\hat{\phi}_n{}^{(j)}(r)f_n^{(j)}(z), \tag{3a}$$

$$\psi^{(j)}(r,z)=\sum_{n=1}^{2N+1}\hat{\psi}_n{}^{(j)}(r)g_n^{(j)}(z). \tag{3b}$$

where the eigen-functions $f_n^{(j)}(z)$ and $g_n^{(j)}(z)$ satisfy

$$\frac{d^2 f_n^{(j)}(z)}{dz^2}+[k_\alpha^{(j)}(z)]^2 f_n^{(j)}(z)=[\gamma_n^{(j)}]^2 f_n^{(j)}(z), \tag{4a}$$

$$\frac{d^2 g_n^{(j)}(z)}{dz^2}+[k_\beta^{(j)}(z)]^2 g_n^{(j)}(z)=[v_n^{(j)}]^2 g_n^{(j)}(z). \tag{4b}$$

$\gamma_n^{(j)}$ and $v_n^{(j)}$ are the corresponding eigen-values to be determined. Solving equations (4a) and (4b) is an eigen-value problem. Precisely, equations (4a) and (4b) should be solved simultaneously by imposing the continuity of displacement and traction at each horizontal boundary, $z=z^{(j,l)}$,within *j*th cylindrical layer. If we solve them separately, the resulting eigen-functions will not include the *P-S* and *S-P* conversions at vertical boundaries. As an approximation for the situations where these conversions are not important, we solve them separately in this report. It should be pointed out that this approximation does not affect the existance of *P-S* and *S-P* conversions at boundaries $r=r^{(j)}$. Currently we are still working on this project and trying to overcome this limitation.

The detailed procedures of solving equation (4) will be described in a later section. The solutions are:

$$f_n^{(j)}(z)=\sum_{l=1}^{2N+1}a_p^{(j)}(l,n)\exp[ik_l z], \tag{5a}$$

$$g_n^{(j)}(z)=\sum_{l=1}^{2N+1}a_s^{(j)}(l,n)\exp[ik_l z], \tag{5b}$$

where $k_l=\pi(-l-N+1)/L$ for l=1, 2,..., 2*N*+1, and *L* is the periodic length (Chen et al., 1994). Substituting equation (3) into equation (2), we obtain

$$\sum_{n=1}^{2N+1}[\frac{d^2\hat{\phi}_n^{(j)}(r)}{dr^2}+\frac{1}{r}\frac{d\hat{\phi}_n^{(j)}(r)}{dr}+(\gamma_n^{(j)})^2\phi_n^{(j)}(r)]f_n^{(j)}(z)=F(\omega)\frac{\delta(r)\delta(z-z_s)}{2\pi r}, \tag{6a}$$

$$\sum_{n=1}^{2N+1}[\frac{d^2\hat{\psi}_n^{(j)}(r)}{dr^2}+\frac{1}{r}\frac{d\hat{\psi}_n^{(j)}(r)}{dr}-\frac{\hat{\psi}_n^{(j)}(r)}{r^2}+(v_n^{(j)})^2\hat{\psi}_n^{(j)}(r)]g_n^{(j)}(z)=0. \tag{6b}$$

Considering $\int_{-L/2}^{+L/2}f_n^{(j)}(z)f_m^{(j)*}(z)dz=\delta_{nm}$ and $\int_{-L/2}^{+L/2}g_n^{(j)}(z)g_m^{(j)*}(z)dz=\delta_{nm}$, we obtain

$$\frac{d^2\hat{\phi}_n^{(j)}(r)}{dr^2}+\frac{1}{r}\frac{d\hat{\phi}_n^{(j)}(r)}{dr}+(\gamma_n^{(j)})^2\phi_n^{(j)}(r)=F(\omega)\frac{\delta(r)]f_n^{(1)*}(z_s)}{2\pi r}, \tag{7a}$$

$$\frac{d^2\hat{\psi}_n^{(j)}(r)}{dr^2}+\frac{1}{r}\frac{d\hat{\psi}_n^{(j)}(r)}{dr}-\frac{\hat{\psi}_n^{(j)}(r)}{r^2}+(v_n^{(j)})^2\hat{\psi}_n^{(j)}(r)=0, \tag{7b}$$

where "*" means conjugate. The integral limits ±*L*/2 define two artificial boundaries, which should be large enough so that the reflections from these artificial boundaries are out of the time window. The solutions of equation (7) are

$$\hat{\phi}_n^{(j)}=c_{p+}(n)H_o^{(1)}(\gamma_n^{(j)}r)+c_{p-}(n)H_o^{(2)}(\gamma_n^{(j)}r), \tag{8a}$$

$$\hat{\psi}_n^{(j)}=c_{s+}(n)H_1^{(1)}(v_n^{(j)}r)+c_{s-}(n)H_1^{(2)}(v_n^{(j)}r), \tag{8b}$$

for $j > 1$, and

$$\hat{\phi}_n^{(1)}=c(n)J_o(\gamma_n^{(1)}r)-\frac{iF(\omega)}{8\pi}f_n^{(1)*}H_o^{(1)}(\gamma_n^{(j)}r), \tag{8c}$$

$$\hat{\psi}_n^{(1)}=0, \tag{8d}$$

for $j = 1$ (fluid layer). Here, sign "+" refers to the wave going outward, and "-" refers to the wave coming inward. Coefficients $a_p^{(j)}(l,n)$ and $a_s^{(j)}(l,n)$ are orthonormal eigen-vectors corresponding to eigen-values $\gamma_n^{(j)}$ and $v_n^{(j)}$, respectively, and are given in a later section. Coefficients $c_{p\pm}$, $c_{s\pm}$, are determined by imposing boundary conditions at $r^{(j)}$, j=1,2, ..., J. Using the potentials, we obtain the displacements and stresses in the solid cylindrical layers ($j > 1$) as:

$$\begin{aligned}u_r^{(j)}(r,z)&=\frac{\partial\phi^{(j)}(r,z)}{\partial r}-\frac{\partial\psi^{(j)}(r,z)}{\partial z}\\&=\sum_{n=1}^{2N+1}[\frac{d\hat{\phi}_n^{(j)}}{dr}f_n^{(j)}(z)-\psi_n^{(j)}(r)\frac{dg_n^{(j)}}{dz}]\\&=\sum_{n=1}^{2N+1}\sum_{l=1}^{2N+1}[E_{11}^{(j)}(r;l,n)c_{p-}^{(j)}(n)+E_{12}^{(j)}(r;l,n)c_{s-}^{(j)}(n)\\&\quad+E_{13}^{(j)}(r;l,n)c_{p+}^{(j)}(n)+E_{14}^{(j)}(r;l,n)c_{s+}^{(j)}(n)]\exp(ik_lz),\end{aligned} \tag{9a}$$

$$\begin{aligned}u_z^{(j)}(r,z)&=\frac{\partial\phi^{(j)}(r,z)}{\partial z}+\frac{1}{r}\frac{\partial[r\psi^{(j)}(r,z)]}{\partial r}\\&=\sum_{n=1}^{2N+1}[\hat{\phi}_n^{(j)}(r)\frac{df_n^{(j)}}{dz}+\frac{1}{r}\frac{d(r\psi_n^{(j)})}{dr}g_n^{(j)}(z)]\\&=\sum_{n=1}^{2N+1}\sum_{l=1}^{2N+1}[E_{21}^{(j)}(r;l,n)c_{p-}^{(j)}(n)+E_{22}^{(j)}(r;l,n)c_{s-}^{(j)}(n)\\&\quad+E_{23}^{(j)}(r;l,n)c_{p+}^{(j)}(n)+E_{24}^{(j)}(r;l,n)c_{s+}^{(j)}(n)]\exp(ik_lz),\end{aligned} \tag{9b}$$

$$\sigma_r^{(j)}(r,z)=\lambda^{(j)}(z)\nabla^2\phi^{(1)}(r,z)+2\mu^{(j)}(z)[\frac{\partial^2\phi^{(j)}}{\partial r^2}-\frac{\partial^2\psi^{(j)}}{\partial r\partial z}]$$

$$=-(\lambda^{(j)}+2\mu^{(j)})k_\alpha^{(j)}(z)\phi^{(j)}(r,z)-2\mu^{(j)}[\frac{1}{r}\frac{\partial\phi^{(j)}(r,z)}{\partial r}+\frac{\partial^2\phi^{(j)}(r,z)}{\partial r^2}+\frac{\partial^2\psi}{\partial r\partial z}]$$

$$\begin{aligned}&=\sum_{n=1}^{2N+1}\sum_{l=1}^{2N+1}[E_{31}^{(j)}(r;l,n)c_{p-}^{(j)}(n)+E_{32}^{(j)}(r;l,n)c_{s-}^{(j)}(n)\\&\qquad+E_{33}^{(j)}(r;l,n)c_{p+}^{(j)}(n)+E_{34}^{(j)}(r;l,n)c_{s+}^{(j)}(n)]\exp(ik_lz)\text{'}\end{aligned}\tag{9c}$$

$$\begin{aligned}\sigma_z^{(j)}(r,z)&=\mu^{(j)}(z)\{2\frac{\partial^2\phi^{(j)}}{\partial r\partial z}+\frac{\partial}{\partial r}[\frac{1}{r}\frac{\partial(r\psi^{(j)})}{\partial r}]-\frac{\partial^2\psi^{(j)}}{\partial z^2}\}\\&=2\mu^{(j)})\{\frac{\partial^2\phi^{(j)}}{\partial r\partial z}-\frac{1}{2r}[k_\beta^{(j)}(z)]^2\psi^{(j)}-\frac{\partial^2\psi}{\partial z^2}\}\\&=\sum_{n=1}^{2N+1}\sum_{l=1}^{2N+1}[E_{41}^{(j)}(r;l,n)c_{p-}^{(j)}(n)+E_{42}^{(j)}(r;l,n)c_{s-}^{(j)}(n)\\&\qquad+E_{43}^{(j)}(r;l,n)c_{p+}^{(j)}(n)+E_{44}^{(j)}(r;l,n)c_{s+}^{(j)}(n)]\exp(ik_lz),\end{aligned}\tag{9d}$$

where $\{E_{pq}^{(j)}(r;l,n); p, q=1,2,3,4\}$ are given in the Appendix.

In the fluid-filled borehole (j=1), the displacement and stresses are:

$$\begin{aligned}u_r^{(1)}(r,z)&=\frac{\partial\phi^{(1)}(r,z)}{\partial r}\\&=\sum_{n=1}^{2N+1}\sum_{l=1}^{2N+1}[E_{11}^{(1)}(r;l,n)c_{p-}^{(1)}(n)+E_{12}^{(1)}(r;l,n)c_{p+}^{(1)}(n)]\exp(ik_lz),\end{aligned}\tag{10a}$$

$$\begin{aligned}\sigma_r^{(1)}(r,z)&=\lambda^{(1)}(z)\nabla^2\phi^{(1)}(r,z)\\&=\sum_{n=1}^{2N+1}\sum_{l=1}^{2N+1}[E_{31}^{(1)}(r;l,n)c_{p-}^{(1)}(n)+E_{32}^{(1)}(r;l,n)c_{p+}^{(1)}(n)]\exp(ik_lz),\end{aligned}\tag{10b}$$

$$\sigma_z^{(1)}(r,z)=0,\tag{10c}$$

where, $s_+(n)=\frac{i}{8\pi}F(\omega)f_n^{(1)^*}(z_s)$, and $\{E_{pq}^{(1)}(r;l,n); p=1,2,3 \text{ and } q=1,2\}$ are given in the Appendix. Unknown coefficients $c_{p\pm}^{(j)}(n)$ and $c_{s\pm}^{(j)}(n)$ are determined by imposing boundary conditions at $r=r^{(j)}, j=1, 2, ..., J$. There are totally 4x($J$+1)x(2$N$+1) unknown coefficients. The modified and generalized reflection and transmission (R/T) matrices are introduced to impose the boundary conditions.

MODIFIED R/T MATRICES

The modified R/T matrices, $\mathbf{R}_{-+}^{(j)},\mathbf{R}_{+-}^{(j)},\mathbf{T}_{+}^{(j)}$ and $\mathbf{T}_{-}^{(j)}$ at the interface $r=r^{(j)}$ are defined through relations

$$\begin{cases} \mathbf{C}_{+}^{(j+1)} = \mathbf{T}_{+}^{(j)}\mathbf{C}_{+}^{(j)} + \mathbf{R}_{-+}^{(j)}\mathbf{C}_{-}^{(j+1)} \\ \mathbf{C}_{-}^{(j)} \;= \mathbf{R}_{+-}^{(j)}\mathbf{C}_{+}^{(j)} + \mathbf{T}_{-}^{(j)}\mathbf{C}_{-}^{(j+1)} \end{cases} \tag{11a}$$

for j>1, and

$$\begin{cases} \mathbf{C}_{+}^{(2)} = \mathbf{T}_{+}^{(1)}(\mathbf{C}_{+}^{(1)} + \mathbf{s}_{+}) + \mathbf{R}_{-+}^{(1)}\mathbf{C}_{-}^{(2)} \\ \mathbf{C}_{-}^{(1)} \;= \mathbf{R}_{+-}^{(1)}(\mathbf{C}_{+}^{(1)} + \mathbf{s}_{+}) + \mathbf{T}_{-}^{(1)}\mathbf{C}_{-}^{(2)} \end{cases} \tag{11b}$$

for j=1, where $\mathbf{C}_{\pm}^{(j)} = [c_{p\pm}^{(j)}(1)\;\; c_{p\pm}^{(j)}(2)\;\; \ldots\;\; c_{p\pm}^{(j)}(2N+1)\;\; c_{s\pm}^{(j)}(1)\;\; c_{s\pm}^{(j)}(2)\;\; \ldots\;\; c_{s\pm}^{(j)}(2N+1)]^{T}$ are unknown coefficient vectors. These R/T matrices can be determined by imposing the boundary conditions at each radial boundary, $r = r^{(j)}$.

The boundary conditions for a solid-solid interface at r=$r^{(j)}$ (j>1) are:

$$u_{r}^{(j)}(r^{(j)},z) = u_{r}^{(j+1)}(r^{(j)},z), \tag{12a}$$
$$u_{z}^{(j)}(r^{(j)},z) = u_{z}^{(j+1)}(r^{(j)},z), \tag{12b}$$
$$\sigma_{r}^{(j)}(r^{(j)},z) = \sigma_{r}^{(j+1)}(r^{(j)},z), \tag{12c}$$
$$\sigma_{z}^{(j)}(r^{(j)},z) = \sigma_{z}^{(j+1)}(r^{(j)},z). \tag{12d}$$

Substituting equation (9) into equation (12) and operating $\int_{-L/2}^{+L/2} \exp(-ik_{l}z)dz$ on both sides, we obtain

$$[\mathbf{E}_{k1}^{(j)},\mathbf{E}_{k2}^{(j)}]\mathbf{C}_{-}^{(j)} + [\mathbf{E}_{k3}^{(j)},\mathbf{E}_{k4}^{(j)}]\mathbf{C}_{+}^{(j)} = [\mathbf{E}_{k1}^{(j+1)},\mathbf{E}_{k2}^{(j+1)}]\mathbf{C}_{-}^{(j+1)} + [\mathbf{E}_{k3}^{(j+1)},\mathbf{E}_{k4}^{(j+1)}]\mathbf{C}_{+}^{(j+1)}, \tag{13}$$

where k=1, 2, 3, 4. Comparing equations (11) and (13) we obtain

$$\begin{bmatrix} \mathbf{R}_{+-}^{(j)} & \mathbf{T}_{-}^{(j)} \\ \mathbf{T}_{+}^{(j)} & \mathbf{R}_{-+}^{(j)} \end{bmatrix} = \begin{bmatrix} \mathbf{E}_{11}^{(j)} & \mathbf{E}_{12}^{(j)} & -\mathbf{E}_{13}^{(j+1)} & -\mathbf{E}_{14}^{(j+1)} \\ \mathbf{E}_{21}^{(j)} & \mathbf{E}_{22}^{(j)} & -\mathbf{E}_{23}^{(j+1)} & -\mathbf{E}_{24}^{(j+1)} \\ \mathbf{E}_{31}^{(j)} & \mathbf{E}_{32}^{(j)} & -\mathbf{E}_{33}^{(j+1)} & -\mathbf{E}_{34}^{(j+1)} \\ \mathbf{E}_{41}^{(j)} & \mathbf{E}_{42}^{(j)} & -\mathbf{E}_{43}^{(j+1)} & -\mathbf{E}_{44}^{(j+1)} \end{bmatrix}^{-1} \begin{bmatrix} -\mathbf{E}_{13}^{(j)} & -\mathbf{E}_{14}^{(j)} & \mathbf{E}_{11}^{(j+1)} & \mathbf{E}_{12}^{(j+1)} \\ -\mathbf{E}_{23}^{(j)} & -\mathbf{E}_{24}^{(j)} & \mathbf{E}_{21}^{(j+1)} & \mathbf{E}_{22}^{(j+1)} \\ -\mathbf{E}_{33}^{(j)} & -\mathbf{E}_{34}^{(j)} & \mathbf{E}_{31}^{(j+1)} & \mathbf{E}_{32}^{(j+1)} \\ -\mathbf{E}_{43}^{(j)} & -\mathbf{E}_{44}^{(j)} & \mathbf{E}_{41}^{(j+1)} & \mathbf{E}_{42}^{(j+1)} \end{bmatrix}_{r=r^{(j)}}, \tag{14}$$

for j>1, where $\mathbf{T}_{+}$, $\mathbf{T}_{-}$, $\mathbf{R}_{-+}$ and $\mathbf{R}_{+-}$ are $(4N+2)$x$(4N+2)$ matrices, and $\mathbf{E}_{pq}^{(j)}$ are $(2N+1)$ x$(2N+1)$ matrices.

The boundary conditions at liquid-solid interface $r = r^{(1)}$ are

$$u_{r}^{(1)}(r^{(1)},z) = u_{r}^{(2)}(r^{(1)},z), \tag{15a}$$
$$\sigma_{r}^{(1)}(r^{(1)},z) = \sigma_{r}^{(2)}(r^{(1)},z), \tag{15b}$$
$$0 = \sigma_{z}^{(2)}(r^{(1)},z). \tag{15c}$$

Similarly, using equations (10), (11b) and (15) we obtain the modified R/T matrices for the first layer as

$$\begin{bmatrix} \mathbf{R}_{+-}^{(1)} & \mathbf{T}_{-}^{(1)} \\ \mathbf{T}_{+}^{(1)} & \mathbf{R}_{-+}^{(1)} \end{bmatrix} = \begin{bmatrix} \mathbf{E}_{11}^{(1)} & -\mathbf{E}_{13}^{(2)} & -\mathbf{E}_{14}^{(2)} \\ \mathbf{E}_{31}^{(1)} & -\mathbf{E}_{33}^{(2)} & -\mathbf{E}_{34}^{(2)} \\ \mathbf{0} & -\mathbf{E}_{43}^{(2)} & -\mathbf{E}_{44}^{(2)} \end{bmatrix}^{-1} \begin{bmatrix} -\mathbf{E}_{13}^{(1)} & \mathbf{E}_{11}^{(2)} & \mathbf{E}_{12}^{(2)} \\ -\mathbf{E}_{33}^{(1)} & \mathbf{E}_{31}^{(2)} & \mathbf{E}_{32}^{(2)} \\ \mathbf{0} & \mathbf{E}_{41}^{(2)} & \mathbf{E}_{42}^{(2)} \end{bmatrix}_{r=r^{(1)}}, \qquad (16)$$

where, $\mathbf{T}_{-}^{(1)}$, $\mathbf{T}_{+}^{(1)}$, $\mathbf{R}_{+-}^{(1)}$ and $\mathbf{R}_{-+}^{(1)}$ are (2*N*+1)x(4*N*+2), (4*N*+2)x(2*N*+1), (2*N*+1)x(2*N*+1) and (4*N*+2)x(4*N*+2) matrices, respectively.

GENERALIZED R/T MATRICES

The generalized R/T matrices $\hat{\mathbf{R}}_{+-}^{(j)}$ and $\hat{\mathbf{T}}_{+}^{(j)}$ are introduced via relations

$$\begin{cases} \mathbf{C}_{+}^{(j+1)} = \hat{\mathbf{T}}_{+}^{(j)} \mathbf{C}_{+}^{(j)} \\ \mathbf{C}_{-}^{(j)} = \hat{\mathbf{R}}_{+-}^{(j)} \mathbf{C}_{+}^{(j)} \end{cases}, \qquad (17a)$$

for *j*>1, and

$$\begin{cases} \mathbf{C}_{+}^{(2)} = \hat{\mathbf{T}}_{+}^{(1)} (\mathbf{C}_{+}^{(1)} + \mathbf{s}_{+}) \\ \mathbf{C}_{-}^{(1)} = \hat{\mathbf{R}}_{+-}^{(1)} (\mathbf{C}_{+}^{(1)} + \mathbf{s}_{+}) \end{cases} \qquad (17b)$$

for *j*=1. Substituting equation (17) into equation (12) and rearranging terms, we obtain a recursive relation

$$\begin{cases} \hat{\mathbf{T}}_{+}^{(j)} = [\mathbf{I} - \mathbf{R}_{-+}^{(j)} \hat{\mathbf{R}}_{+-}^{(j+1)}]^{-1} \mathbf{T}_{+}^{(j)} \\ \hat{\mathbf{R}}_{+-}^{(j)} = \mathbf{R}_{+-}^{(j)} + \mathbf{T}_{-}^{(j)} \hat{\mathbf{R}}_{+-}^{(j+1)} \hat{\mathbf{T}}_{+}^{(j)} \end{cases}, \qquad \text{for } j = J, J\text{-}1, \ldots, 2, 1, \qquad (18)$$

where $\mathbf{I}$ is the unit matrix, $\hat{\mathbf{R}}_{+-}^{(j)}$ and $\hat{\mathbf{T}}_{+}^{(j)}$ are (4*N*+2)x(4*N*+2) matrices for $j > 1$, $\hat{\mathbf{T}}_{+}^{(1)}$ is a (4*N*+2)x(2*N*+1) matrix, and $\hat{\mathbf{R}}_{+-}^{(1)}$ is a (2*N*+1)x(2*N*+1) matrix. In the outer most layer ($j = N+1$), there exist only outward-going waves, i.e., $\mathbf{C}_{-}^{(N+1)} = \mathbf{0}$. Therefore, the initial condition for the iteration is

$$\hat{\mathbf{R}}_{+-}^{(N+1)} = \mathbf{0}. \qquad (19)$$

Using equation (18), with initial condition (19), we can recursively calculate the generalized R/T matrices $\hat{\mathbf{R}}_{+-}^{(j)}$ and $\hat{\mathbf{T}}_{+}^{(j)}$ for all interfaces from modified R/T matrices $\mathbf{T}_{+}^{(j)}$, $\mathbf{T}_{-}^{(j)}$, $\mathbf{R}_{-+}^{(j)}$ and $\mathbf{R}_{+-}^{(j)}$ calculated by equations (14) and (16).

FINAL SOLUTIONS

Using the generalized R/T matrices we can easily obtain the coefficient vectors $\mathbf{C}_{\pm}^{(j)}$. Inside the first layer (j=1) we have

$$\mathbf{C}_{+}^{(1)} = \mathbf{C}_{-}^{(1)} \tag{20}$$

where the relation $J_o = \frac{1}{2}(H_o^{(2)} + H_o^{(1)})$ is used. Substituting (20) into (17b) yields

$$\mathbf{C}_{+}^{(1)} + \mathbf{s}_{+} = (\mathbf{I} - \mathbf{R}_{+-}^{(1)})^{-1}\mathbf{s}_{+}. \tag{21}$$

Then, substituting (21) into (17a) we have

$$\begin{cases} \mathbf{C}_{+}^{(j)} = \hat{\mathbf{T}}_{+}^{(j-1)}\hat{\mathbf{T}}_{+}^{(j-2)}\ldots\hat{\mathbf{T}}_{+}^{(1)}(\mathbf{I} - \hat{\mathbf{R}}_{+-}^{(1)})^{-1}s_{+} \\ \mathbf{C}_{-}^{(j)} = \hat{\mathbf{R}}_{+-}^{(j)}\mathbf{C}_{+}^{(j)} \end{cases}. \tag{22}$$

Once having the coefficients $\mathbf{C}_{\pm}$ we can calculate the frequency domain solutions (displacements and stresses) using equations (9) and (10). The corresponding time domain solution can be obtained by performing inverse Fourier transform.

SOLUTIONS FOR $f_n^{(j)}(z)$ and $g_n^{(j)}(z)$

In this section, we shall solve equation (4). Namely, determine $\{\gamma_n^{(j)},\ \nu_n^{(j)}\}$ appeared in equation (4) and $\{a_p^{(j)}(l,n),\ a_s^{(j)}(l,n)\}$ in equation (5). This is an eigen-value problem. Substituting equation (5) into equation (4), we have

$$\sum_{l=1}^{2N+1}\{-(k_l)^2 + [k_\alpha^{(j)}(z)]^2 - (\gamma_n^{(j)})^2\}a_p^{(j)}(l,n)\exp(ik_l z) = 0, \tag{23a}$$

$$\sum_{l=1}^{2N+1}\{-(k_l)^2 + [k_\beta^{(j)}(z)]^2 - (\nu_n^{(j)})^2\}a_s^{(j)}(l,n)\exp(ik_l z) = 0. \tag{23b}$$

Operating $\int_{-L/2}^{+L/2}\exp(-ik_m z)dz$ on equation (23), we obtain the following compact matrix equations,

$$[\mathbf{A}^{(j)} - (\gamma_n^{(j)})^2\mathbf{I}]\mathbf{a}_p^{(j)}(n) = 0, \tag{24a}$$

$$[\mathbf{B}^{(j)} - (\nu_n^{(j)})^2\mathbf{I}]\mathbf{a}_s^{(j)}(n) = 0, \tag{24b}$$

where,

$$\mathbf{a}_p^{(j)}(n) = [a_p^{(j)}(1,n), a_p^{(j)}(2,n), \ldots, a_p^{(j)}(2N+1,n)]^T,$$

$$\mathbf{a}_s^{(j)}(n) = [a_s^{(j)}(1,n), a_s^{(j)}(2,n), \ldots, a_s^{(j)}(2N+1,n)]^T,$$

$$A^{(j)}_{ml} = -(k_m)^2\delta_{lm} + \int_{-L/2}^{+L/2}[k^{(j)}_{\alpha}(z)]^2 \exp[i(k_l - k_m)z]dz, \tag{25a}$$

$$B^{(j)}_{ml} = -(k_m)^2\delta_{lm} + \int_{-L/2}^{+L/2}[k^{(j)}_{\beta}(z)]^2 \exp[i(k_l - k_m)z]dz. \tag{25b}$$

Eigen-values $(\gamma^{(j)}_n)^2$ and $(v^{(j)}_n)^2$, and their related eigen-vectors $\mathbf{a}^{(j)}_p(n)$ and $\mathbf{a}^{(j)}_s(n)$ are calculated using standard linear algebra programs. Here, $L = z_m - z_o$ is periodic length that is as the distance between two artificial boundaries.

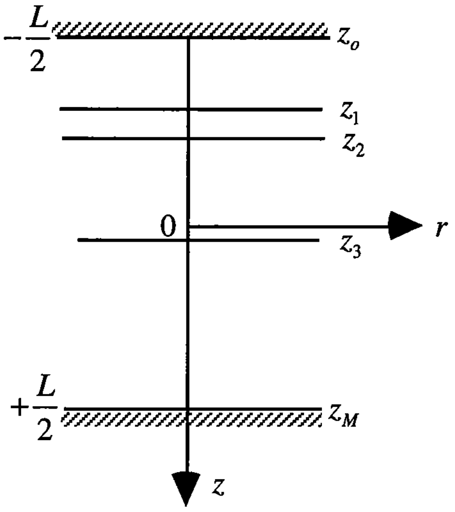

FIG. 2. A model of vertically layered media. In order to treat it as a eigen-value problem, two artificial boundaries z_O and z_N are added.

Let us consider a special case: homogeneous layer (i.e., $k^{(j)}_\alpha(z) = k^{(j)}_\alpha$, and $k^{(j)}_\beta(z) = k^{(j)}_\beta$). For this case, we have obtained the semi-analytical solution in a previous study (Chen et al., 1994). From equations (24) and (25) we simply obtain

$$(\gamma^{(j)}_n)^2 = (k^{(j)}_\alpha)^2 - k^2_n, \tag{26a}$$
$$a^{(j)}_p(l,n) = \delta_{ln}, \tag{26b}$$

and

$$(v^{(j)}_n)^2 = (k^{(j)}_\beta)^2 - k^2_n, \tag{27a}$$
$$a^{(j)}_s(l,n) = \delta_{ln}. \tag{27b}$$

Substituting these special solutions into equations (9) and (10), we obtain the identical formulas with the semi-analytic solutions of Chen et al (1994).

For the case of M vertical layers (i.e., $k^{(j)}_{\alpha_{(i)}}(z) = k^{(j)}_{\alpha_{(i)}}$ and $k^{(j)}_{\beta_{(i)}}(z) = k^{(j)}_{\beta_{(i)}}$, for $z^{(j-1)}_i < z < z^{(j)}_i$, $i = 1,2,\ldots,M$), the integral in equation (25) can be written as

$$\int_{-L/2}^{+L/2} [k_{\alpha}^{(j)}(z)]^2 e^{i(k_l-k_m)} dz = \sum_{i=1}^{M} \{(k_{\alpha_i}^{(j)})^2 e^{i(k_l-k_m)(z_{i-1}+d_i)} \frac{2\sin[(k_l-k_m)d_i]}{k_l-k_m}\}, \tag{28a}$$

$$\int_{-L/2}^{+L/2} [k_{\beta}^{(j)}(z)]^2 e^{i(k_l-k_m)} dz = \sum_{i=1}^{M} \{(k_{\beta_i}^{(j)})^2 e^{i(k_l-k_m)(z_{i-1}+d_i)} \frac{2\sin[(k_l-k_m)d_i]}{k_l-k_m}\}, \tag{28b}$$

where $d_i = (z_i - z_{i-1})/2$.

The discrete wavenumber method is used for implementation. In the numerical computation, the following rules are applied to select the parameters: $k_{\max} > \omega / \min(\beta_i^{(j)})$, $k_{\max} > \pi / \min(d_i)$, $\Delta k = \pi / L$ and $k_m = -k_{\max} + m\Delta k$, where k_{max} determine the upper limit of the summation over k in equations (9) and (10); Δk is the increment of wavenumber.

EXAMPLES

We present five examples to show the capabilities of this method. Figure 3 is the simulation of sonic logging. There is a high velocity layer in the formation. The moveout of the P and S waves is changed by the high velocity zone. This test shows that the frequency can be up to 20 KHz (the central frequency is 10KHz) in the simulation. Figures 4 – 7 are crosswell profiling examples. In these examples the seismograms are of the U_r component. Figure 4 shows the simulation of a fluid-filled open borehole. The formation has a low velocity layer which exhibits a significant influence on the wave field. The tube wave converts to P and S waves at the boundaries. The wave field within the low velocity zone is very complicated. Figure 5 gives an example of cased borehole. To simulate how a perforation in a casing creates tube conversions, we put a low velocity layer in the casing. The tube wave to P and S wave conversions clearly show up. Figure 6 is a cased borehole embedded in a multi-layered formation. There is a low velocity layer and a high velocity layer. Though the low velocity zone is only 1 m thick, its effects on the wave field can be clearly seen. Figure 7 is a common receiver gather sorted from a complete crosswell data set. There are 50 sources and 50 receivers. The source interval and receiver interval are all 2 m. The moveout of the tube wave in a common receiver gather is very different from that in a common source gather. In this example we include a cased borehole and a layer with a fault. We are going to use this synthetic data set to test tomography techniques and other inversion methods. These kinds of tests help us to understand the borehole effects on the inversion.

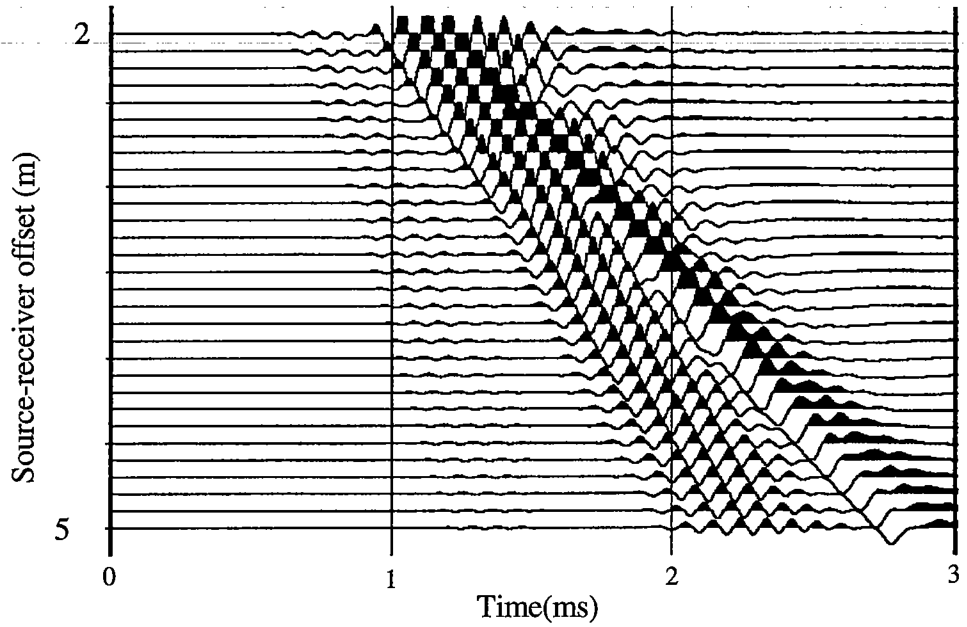

(a) Synthetic full waveform sonic log. The center frequency of the source wavelet is 10 KHz.

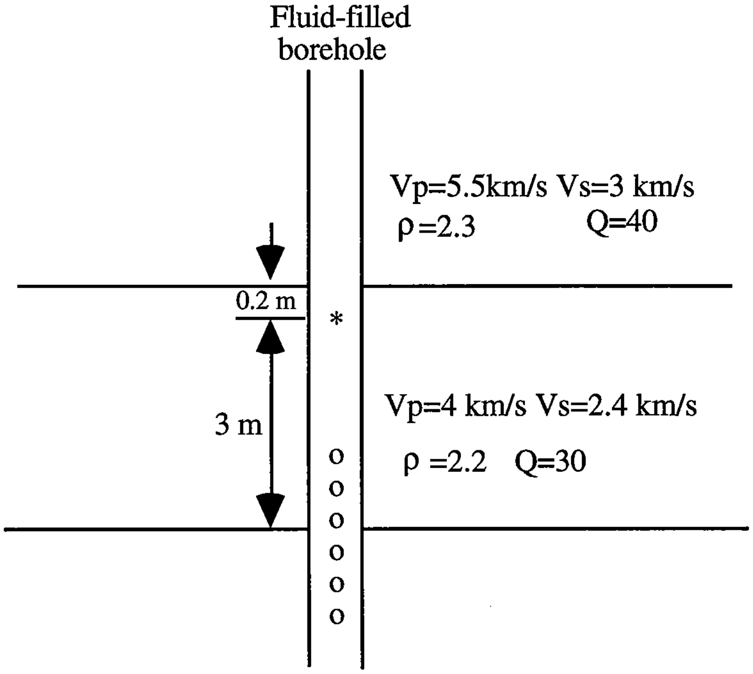

(b) Model used to calculate the sonic log shown in (a).

FIG. 3. Simulation of sonic log in a layered medium.

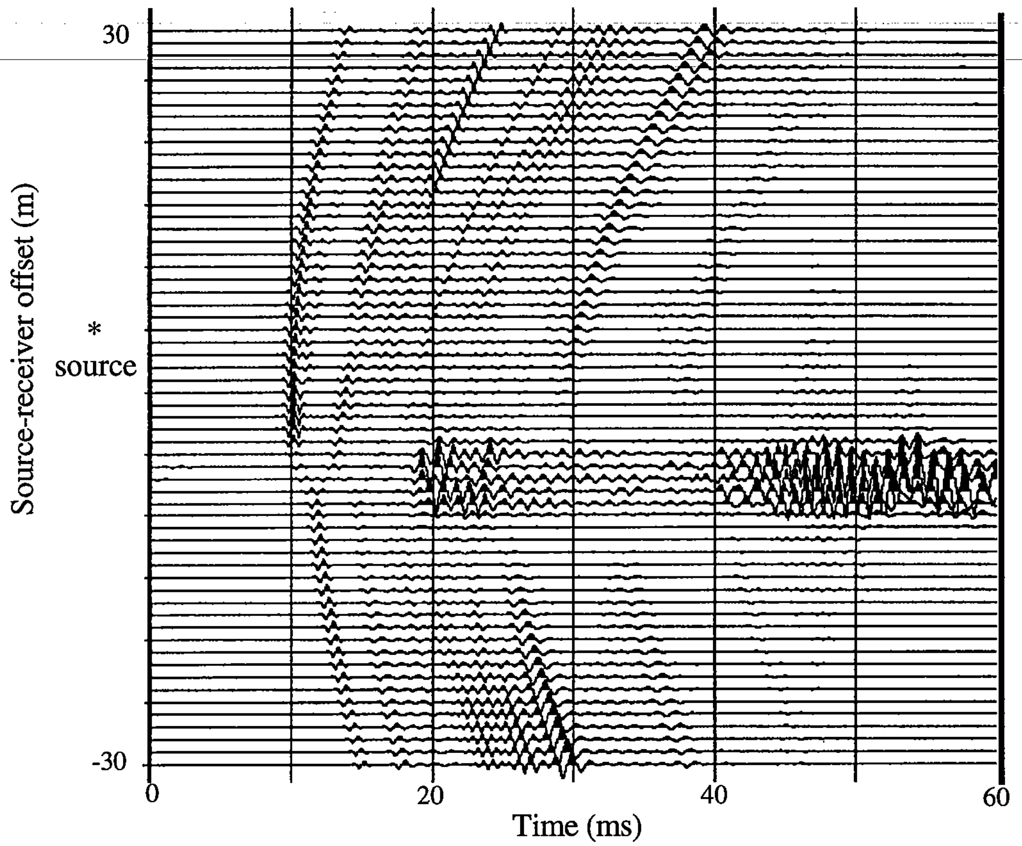

(a) A common source gather of crosswell survey using the model in (b). The center frequency of the source wavelet is 1 KHz.

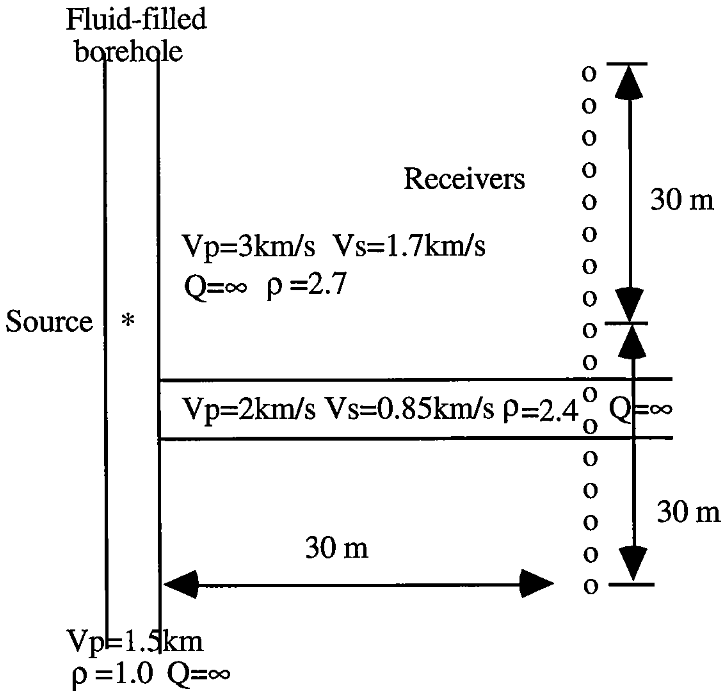

(b) model geometry and parameters

FIG. 4. Simulation of crosswell for open borehole in the formation with low velocity zone.

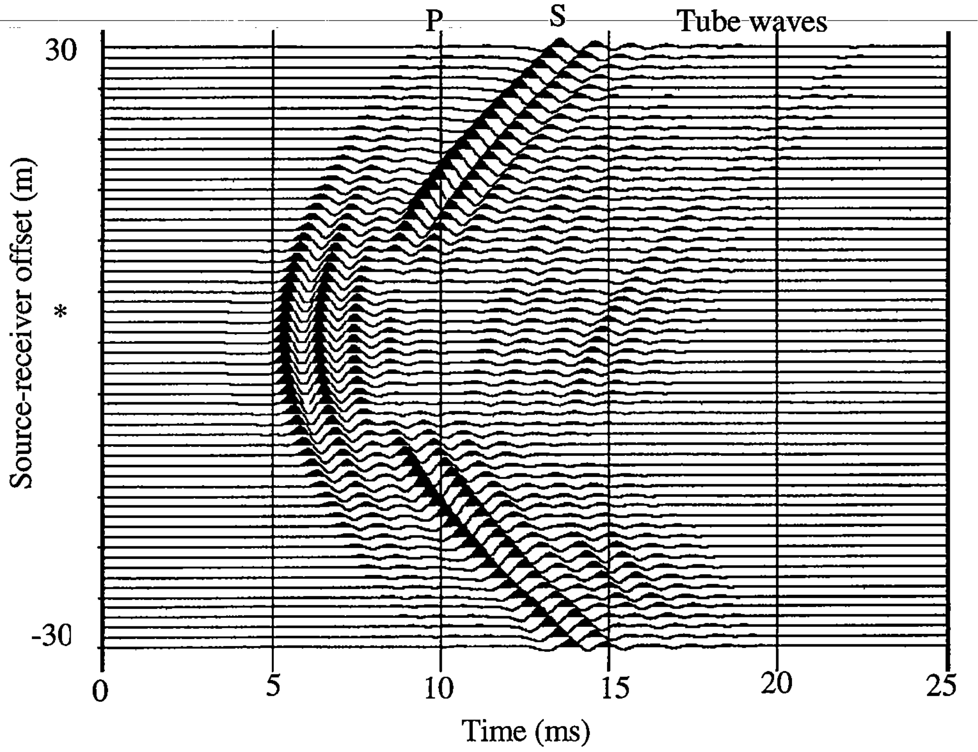

(a) Seismograms. The center frequency of the source wavelet is 1 KHz.

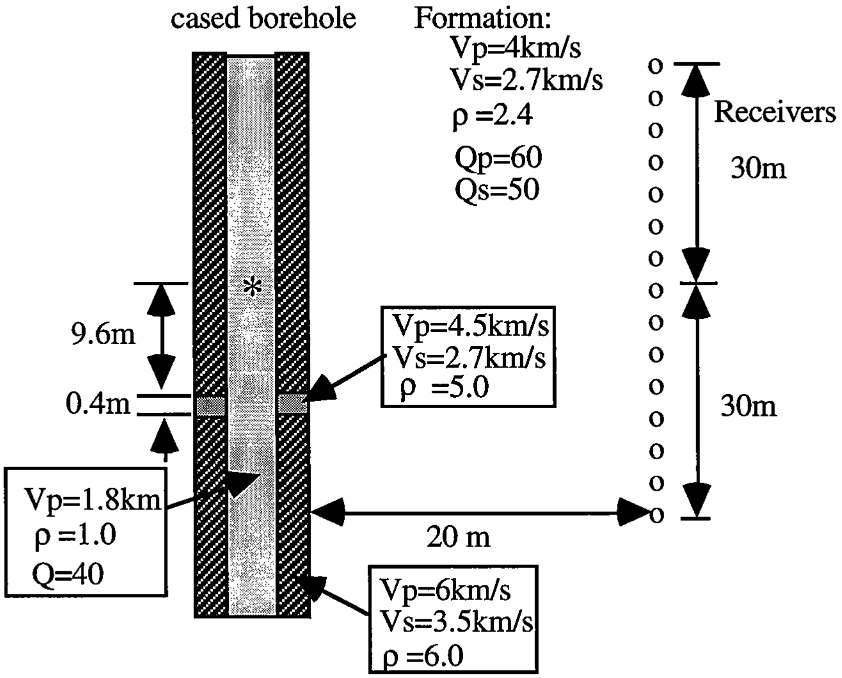

(b) Model geometry and parameters.

FIG. 5. Test on the effect of casing perforation. It can be seen that the tube wave converts to *P* and *S* waves at a perforation..

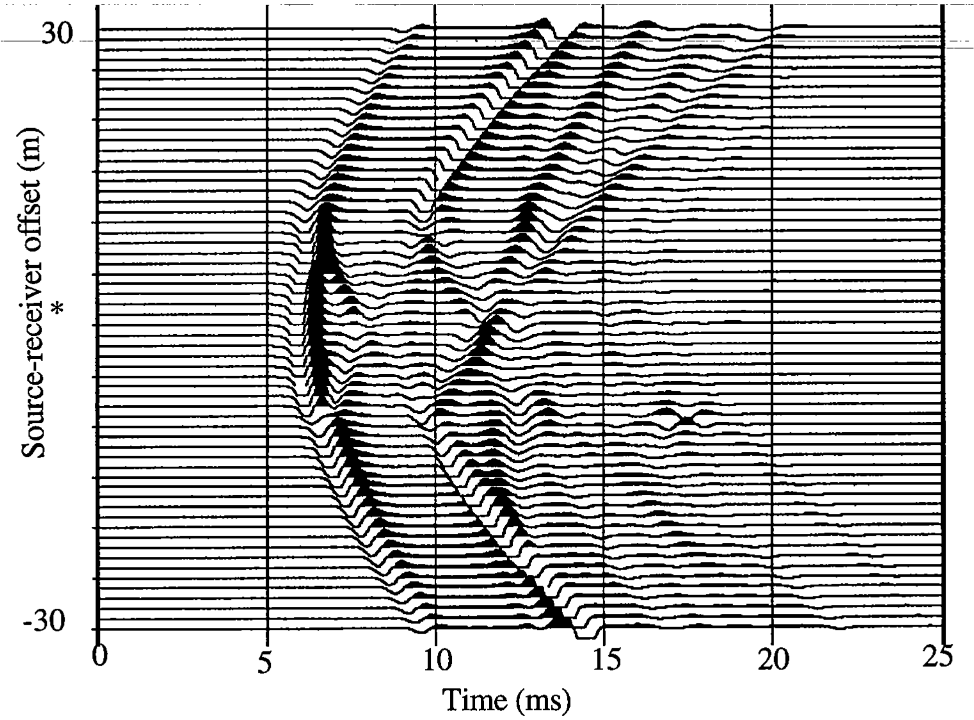

(a) Seismograms. The center frequency of the source wavelet is 1 KHz.

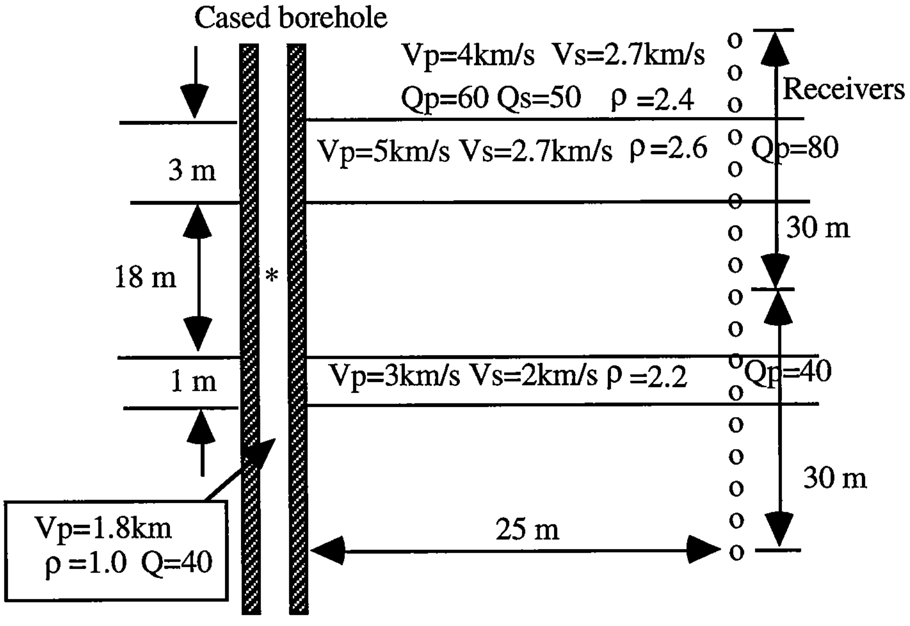

(b) Model geometry and parameters.

FIG. 6. Simulation for a cased borehole embeds in a formation with multi-layers.

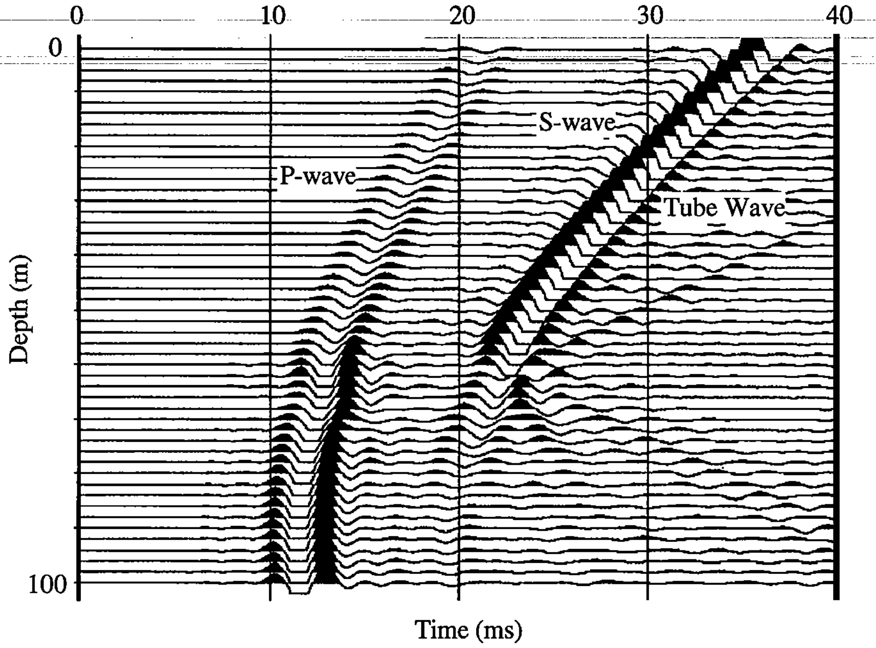

(a) seismograms. The center frequency is 300 Hz.

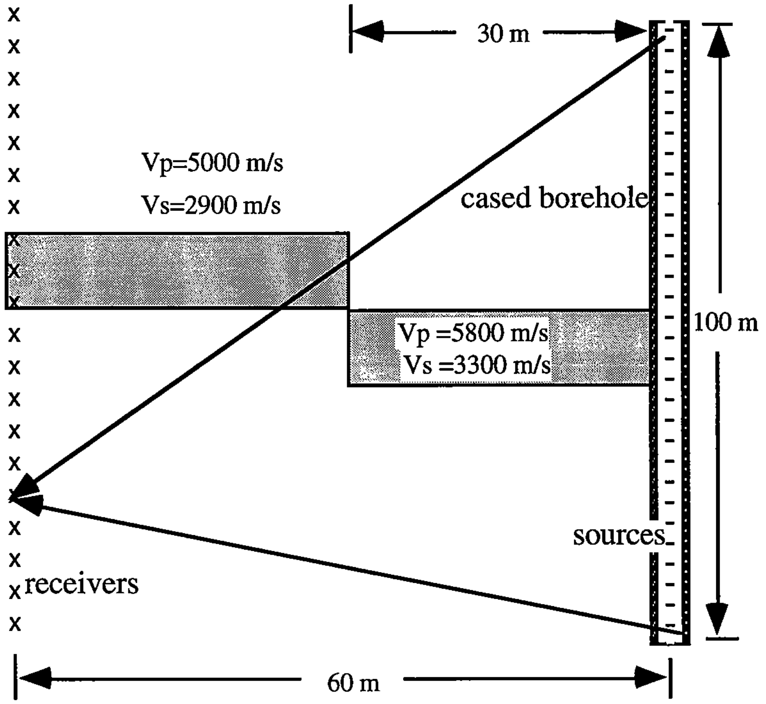

(b) Model geometry and parameters.

FIG. 7. A common receiver gather sorted from a complete synthetic crosswell data set.

CONCLUSION

We have developed a semi-analytical approach to simulate the waves in a complex borehole-formation model in which there exist both cylindrical and horizontal layers. In this approach, we first calculate the eigen-functions of horizontal layers for each cylindrical layer. Then, we expand the wave equation solutions into these eigen-functions and apply the generalized reflection and transmission coefficients method to solve the boundary problem for radial layers. Numerical examples show that this approach provides an effective tool to simulate complex models which are found in sonic logging and crosswell seismic profiling. Since we neglect the *P-S* and *S-P* conversions due to the *horizontal interfaces,* this approach is valid for the cases in which those conversions are not important. Currently, we are still working on this project, and we hope to obtain a complete solution.

REFERENCES

Baker, L., J., 1984, The effect of the invaded zone on the full wavetrain acoustic logging: Geophysics, **49**, 789.

Bouchon, M., 1993, A numerical simulation of the acoustic and elastic wavefields radiated by a source on a fluid-filled borehole embedded in layered medium: Geophysics, **58**, No. 4, 475-481.

Chen, X, Quan, Y and Harris, M. J., 1994, Seismogram synthesis for radially layered media using the generalized reflection/transmission coefficients method: Expanded Abstracts of the 64th SEG annual meeting.

Pai, D. M., Ahmad, J. and Kennedy W. D., 1993, Two-dimensional induction log modeling using a coupled-mode, multiple-reflection series method: Geophysics, **58**, No. 4, 466-474.

Tubman, K. M., Cheng, C. H. and Toksöz, M. N., 1984, Synthetic full waveform acoustic logs in cased boreholes: Geophysics, **49**, 1051-1059.

APPENDIX

For j>1 the elements E_{pq} in equation (9) are:

$$E_{11}^{(j)}(r;l,n) = -\gamma_n^{(j)} H_1^{(2)}(\gamma_n^{(j)} r) a_p^{(j)}(l,n),$$

$$E_{12}^{(j)}(r;l,n) = -ik_l H_1^{(2)}(\nu_n^{(j)} r) a_s^{(j)}(l,n),$$

$$E_{13}^{(j)}(r;l,n) = -\gamma_n^{(j)} H_1^{(1)}(\gamma_n^{(j)} r) a_p^{(j)}(l,n),$$

$$E_{14}^{(j)}(r;l,n) = -ik_l H_1^{(1)}(\nu_n^{(j)} r) a_s^{(j)}(l,n),$$

$$E_{21}^{(j)}(r;l,n) = ik_l H_o^{(2)}(\gamma_n^{(j)} r) a_p^{(j)}(l,n),$$

$$E_{22}^{(j)}(r;l,n) = \nu_n^{(j)} H_o^{(2)}(\nu_n^{(j)} r) a_s^{(j)}(l,n),$$

$$E_{23}^{(j)}(r;l,n) = ik_l H_o^{(1)}(\gamma_n^{(j)} r) a_p^{(j)}(l,n),$$

$$E_{22}^{(j)}(r;l,n) = \nu_n^{(j)} H_o^{(1)}(\nu_n^{(j)} r) a_s^{(j)}(l,n),$$

$$E_{31}^{(j)}(r;l,n) = \sum_{m=1}^{2N+1} \{[2k_m^2 H_o^{(2)}(\gamma_n^{(j)} r) + \frac{2\gamma_n^{(j)}}{r} H_1^{(2)}(\gamma_n^{(j)} r)]\mu_{lm}^{(j)} a_p^{(j)}(m,,n) \quad , \\ - \omega^2 H_o^{(2)}(\gamma_n^{(j)} r)\rho_{lm}^{(j)} a_p^{(j)}(m,n)\}$$

$$E_{32}^{(j)}(r;l,n) = \sum_{m=1}^{2N+1} [-i2k_m \nu_n^{(j)} \dot{H}_1^{(2)}(\nu_n^{(j)} r)\mu_{lm}^{(j)} a_s^{(j)}(m,n),$$

$$E_{33}^{(j)}(r;l,n) = \sum_{m=1}^{2N+1} \{[2k_m^2 H_o^{(1)}(\gamma_n^{(j)} r) + \frac{2\gamma_n^{(j)}}{r} H_1^{(2)}(\gamma_n^{(j)} r)]\mu_{lm}^{(j)} a_p^{(j)}(m,,n) \quad , \\ - \omega^2 H_o^{(1)}(\gamma_n^{(j)} r)\rho_{lm}^{(j)} a_p^{(j)}(m,n)\}$$

$$E_{34}^{(j)}(r;l,n) = \sum_{m=1}^{2N+1} [-i2k_m \nu_n^{(j)} \dot{H}_1^{(1)}(\nu_n^{(j)} r)\mu_{lm}^{(j)} a_s^{(j)}(m,n)],$$

$$E_{41}^{(j)}(r;l,n) = \sum_{m=1}^{2N+1} [-i2k_m \gamma_n^{(j)} H_1^{(2)}(\gamma_n^{(j)} r)\mu_{lm}^{(j)} a_p^{(j)}(m,n)],$$

$$E_{42}^{(j)}(r;l,n) = \sum_{m=1}^{2N+1} [2k_m^2 \mu_{lm}^{(j)} - \omega^2 \rho_{lm}^{(j)}] H_1^{(2)}(\nu_n^{(j)} r) a_s^{(j)}(m,n),$$

$$E_{43}^{(j)}(r;l,n) = \sum_{m=1}^{2N+1} [-i2k_m \gamma_n^{(j)} H_1^{(1)}(\gamma_n^{(j)} r)\mu_{lm}^{(j)} a_p^{(j)}(m,n)],$$

$$E_{44}^{(j)}(r;l,n) = \sum_{m=1}^{2N+1} [2k_m^2 \mu_{lm}^{(j)} - \omega^2 \rho_{lm}^{(j)}] H_1^{(1)}(\nu_n^{(j)} r) a_s^{(j)}(m,n),$$

where $\mu_{lm}^{(j)} = \int_{-L/2}^{+L/2} \mu^{(j)}(z) \exp[i(k_l - k_m)z]dz$ and $\rho_{lm}^{(j)} = \int_{-L/2}^{+L/2} \rho^{(j)}(z) \exp[i(k_l - k_m)z]dz$.

For j=1 the elements E_{pq} in equation (10) are:

$$E_{11}^{(1)}(r;l,n) = -\gamma_n^{(1)} H_1^{(2)}(\gamma_n^{(1)} r) a_p^{(1)}(l,n),$$

$$E_{12}^{(1)}(r;l,n) = -\gamma_n^{(1)} H_1^{(1)}(\gamma_n^{(1)} r) a_p^{(1)}(l,n),$$

$$E_{21}^{(1)}(r;l,n) = ik_l H_o^{(2)}(\gamma_n^{(1)} r) a_p^{(1)}(l,n),$$

$$E_{22}^{(j)}(r;l,n) = ik_l H_o^{(1)}(\gamma_n^{(j)} r) a_p^{(j)}(l,n),$$

$$E_{31}^{(1)}(r;l,n) = -\lambda^{(1)}(k_\alpha^{(1)})^2 H_o^{(2)}(\gamma_n^{(1)} r) a_p^{(1)}(l,n),$$

$$E_{32}^{(1)}(r;l,n) = -\lambda^{(1)}(k_\alpha^{(1)})^2 H_o^{(1)}(\gamma_n^{(1)} r) a_p^{(1)}(l,n).$$

Paper D

Normal Modes in Radially layered Media and Application to Attenuation Estimation

Youli Quan* and Xiaofei Chen**

ABSTRACT

We present an effective method to calculate the dispersion relation and eigen functions of normal modes for radially multi-layered media. These normal modes are known as the Stoneley wave, pseudo-Rayleigh waves, etc. in the acoustic logging problem. Based on this dispersion relation we derive a formula which describes the attenuation property of each mode in absorptive media. The stimulated acoustic logging technique can be used to stimulate or enhance a particular mode. We estimate the attenuation of the formation from the attenuation of the enhanced mode.

INTRODUCTION

The dispersion relation, which gives the phase velocities of normal modes, is very important for studying guided waves in acoustic logging. It has been studied by many authors, e.g., Boit (1952), Cheng and Toksöz (1981). In this work, the generalized reflection and transmission coefficients method (Chen et al., 1994; Chen, 1993; Luco and Apsel, 1983; Kennett, 1983) is developed to systematically and simultaneously determine the phase velocities and eigen functions of normal modes in radially layered media. The motivation of this work is from the stimulated mode acoustic logging method (SMAL) (Medlin and Schmitt, 1992). SMAL runs at a specific frequency to stimulate or enhance a given mode. If we know the relationship between the Q-value of a mode and the Q-value of the formation, we may estimate the formation Q-value from that mode. Cheng et al. (1982) gave a formula describing the attenuation of guided waves for a simple open borehole. In this work, a more general formula to calculate the attenuation of each normal mode for a cased borehole and other complicated boreholes is derived from the new dispersion relation. Finally, we show a numerical simulation of the SMAL method, and the attenuation estimation for the S wave.

---

* *STP, Stanford University*
** *Department of Earth Sciences, USC*

NORMAL MODES IN RADIALLY LAYERED MEDIA

The normal modes are the non-trivial solutions of the free elastodynamic equation under given boundary conditions. Starting from this point, we can derive an effective algorithm to determine the phase velocities and the corresponding eigen functions of the normal modes in radially layered media. In the acoustic logging problem, these normal modes are usually known as tube waves or guided waves.

The $k-\omega$ domain solutions of the free elastodynamic equation in a radially layered model are

$$\mathbf{U}^{(j)} = \mathbf{E}^{(j)}\mathbf{C}^{(j)}, \tag{1}$$

where j=1, 2, ..., N+1 are the index of layers, $\mathbf{U}^{(j)}$ are displacement and stress vectors, $\mathbf{E}^{(j)}$ are known matrices given in Chen et al. (1994), and $\mathbf{C}^{(j)} = [\mathbf{c}_{-}^{(j)}, \mathbf{c}_{+}^{(j)}]^{\mathrm{T}}$ are unknown coefficient vectors to be determined under given boundary conditions. Signs "+" and "-" refer to outgoing and incoming waves, respectively. $\mathbf{C}^{(j)}$ for each layer can be related by the generalized reflection/transmission matrices $\hat{\mathbf{R}}_{+-}^{(j)} / \hat{\mathbf{T}}_{+}^{(j)}$ defined in Chen et al. (1994) as follows,

$$\begin{cases} \mathbf{C}_{+}^{(j+1)} = \hat{\mathbf{T}}_{+}^{(j)}\mathbf{C}_{+}^{(j)}, & \text{(2a)} \\ \mathbf{C}_{-}^{(j)} = \hat{\mathbf{R}}_{+-}^{(j)}\mathbf{C}_{+}^{(j)} \quad . & \text{(2b)} \end{cases}$$

If the first layer is a fluid-filled borehole (the acoustic logging problem), $\mathbf{C}^{(1)} = [c_{p-}^{(1)}, c_{p+}^{(1)}]^{\mathrm{T}}$ and $\hat{\mathbf{R}}_{+-}^{(1)}$ becomes a scalar $\hat{R}_{+-}^{(1)}$. The non-singular condition at r=0 (the center of a borehole) implies

$$c_{p-}^{(1)} = c_{p+}^{(1)}. \tag{3}$$

For simplicity, we ignore the normalization factor used in Chen et al. (1994). From equation (2b) we get

$$(1-\hat{R}_{+-}^{(1)})c_{p+}^{(1)} = 0. \tag{4}$$

In order to obtain a non-trivial solution we must have $c_{p+}^{(1)} \neq 0$, which leads to

$$1-\hat{R}_{+-}^{(1)} = 0. \tag{5}$$

For a given angular frequency ω, only certain wave numbers k_n, n=1, 2, ..., $K(\omega)$, which are roots of equation (5), satisfy equation (5). These roots constitute the normal modes for certain boundary conditions. The phase velocities v_n of these modes are calculated by the relation

$$v_n = \frac{\omega}{k_n}, \qquad n=1, 2, \ldots, K(\omega). \tag{6}$$

Therefore, equation (5) is a dispersion relation whose roots correspond to the phase velocities of normal modes for a given frequency. This dispersion relation is very simple and can be easily solved.

Once we obtain the phase velocity of a normal mode, we can calculate its eigen function. According to equation (4), $c_{p+}^{(1)}$ can be any non-zero value. Without any loss of generality we set $c_{p+}^{(1)}(v_n) = 1$. Then all other coefficients are obtained by the following relations:

$$c_{p-}^{(1)}(v_n) = \hat{R}_{+-}^{(1)}(v_n),$$

and

$$\begin{cases} \mathbf{c}_{+}^{(j+1)}(v_n) = \hat{\mathbf{T}}_{+}^{(j)}(v_n)\hat{\mathbf{T}}_{+}^{(j-1)}(v_n)\ldots\hat{\mathbf{T}}_{+}^{(1)}(v_n) \\ \mathbf{c}_{-}^{(j+1)}(v_n) = \hat{\mathbf{R}}_{+-}^{(j+1)}(v_n)\mathbf{c}_{+}^{(j+1)}(v_n) \end{cases}, \quad j=1, 2, \ldots, N. \tag{7}$$

Substituting these coefficients into equation (1), we obtain the corresponding eigen functions.

Q-VALUES OF NORMAL MODES

In the above discussion, we only consider the lossless case, i.e., the Q-value for all waves is infinite. In real media the Q-value is finite, i.e., there exists attenuation. For an absorptive medium, the attenuation can be introduced via the complex velocity

$$\tilde{v}(\omega) = v(\omega)[1 - \frac{i}{2Q}] \tag{8}$$

Once the real P and S velocities (α_j, β_j) for each layer are replaced by the complex velocities $(\tilde{\alpha}_j, \tilde{\beta}_j)$, the corresponding phase velocities are complex too (i.e., roots of equation (5) become complex numbers). We assume the complex phase velocity of the n^{th} mode to be

$$\tilde{v}_n(\omega) = v_n(\omega)[1 - \frac{i}{2Q_n}], \tag{9}$$

where $v_n(\omega)$ is a real phase velocity. Then, the dispersion equation can be written as

$$1 - \hat{R}_{+-}^{(1)}[\tilde{v}_n(\omega), \tilde{\mathbf{v}}_\mathrm{p}, \tilde{\mathbf{v}}_\mathrm{s}] = 0 \tag{10}$$

where

$$\tilde{\mathbf{v}}_\mathrm{p} = (\tilde{\alpha}_1, \tilde{\alpha}_2, \ldots, \tilde{\alpha}_{N+1})$$

and

$$\tilde{\mathbf{v}}_{\mathrm{s}} = (\tilde{\beta}_1, \tilde{\beta}_2, \ldots, \tilde{\beta}_{N+1})$$

are complex P and S velocities for all layers.

Since $1/Q$ is small (usually less than 0.1), we expand $\hat{R}^{(1)}_{+-}$ about $1/Q$ as

$$\begin{aligned} \hat{R}^{(1)}_{+-}[\tilde{v}_n(\omega), \tilde{\mathbf{v}}_{\mathrm{p}}, \tilde{\mathbf{v}}_{\mathrm{s}}] = \hat{R}^{(1)}_{+-}[v_n(\omega), \mathbf{v}_{\mathrm{p}}, \mathbf{v}_{\mathrm{s}}] \\ + \sum_{j=1}^{N+1} \frac{\partial \hat{R}^{(1)}_{+-}[\tilde{v}_n(\omega), \tilde{\mathbf{v}}_{\mathrm{p}}, \tilde{\mathbf{v}}_{\mathrm{s}}]}{\partial \alpha_j} \Delta\alpha_j \\ + \sum_{j=1}^{N+1} \frac{\partial \hat{R}^{(1)}_{+-}[\tilde{v}_n(\omega), \tilde{\mathbf{v}}_{\mathrm{p}}, \tilde{\mathbf{v}}_{\mathrm{s}}]}{\partial \beta_j} \Delta\beta_j \\ + \frac{\partial \hat{R}^{(1)}_{+-}[\tilde{v}_n(\omega), \tilde{\mathbf{v}}_{\mathrm{p}}, \tilde{\mathbf{v}}_{\mathrm{s}}]}{\partial v_n} \Delta v_n + O(\frac{1}{Q^2}) \ , \end{aligned} \qquad (11)$$

where $\Delta\alpha_j = \tilde{\alpha}_j - \alpha_j = -i\alpha_j / 2Q_p$, $\Delta\beta_j = -i\beta_j / 2Q_S$ and $\Delta v_n = -iv_n / 2Q_n$. Since v_n is the phase velocity of lossless case corresponding to real velocities ($\mathbf{v}_p$, $\mathbf{v}_s$), we have

$$1 - \hat{R}^{(1)}_{+-}(\mathbf{v}_{\mathrm{p}}, \mathbf{v}_{\mathrm{s}}, v_n) = 0 . \qquad (12)$$

Substituting equation (11) into equation (10), neglecting the term $1/Q^2$ and other higher order terms, and using equation (12), we obtain the formula

$$\begin{aligned} \frac{1}{Q_n(\omega)} \cong - \sum_{j=1}^{N+1} \{ \frac{\partial \hat{R}^{(1)}_{+-}[\tilde{v}_n(\omega), \tilde{\mathbf{v}}_{\mathrm{p}}, \tilde{\mathbf{v}}_{\mathrm{s}}]}{\partial \alpha_j} \frac{\alpha_j}{v_n} \frac{1}{Q_{p_j}} + \\ \frac{\partial \hat{R}^{(1)}_{+-}[\tilde{v}_n(\omega), \tilde{\mathbf{v}}_{\mathrm{p}}, \tilde{\mathbf{v}}_{\mathrm{s}}]}{\partial \beta_j} \frac{\beta_j}{v_n} \frac{1}{Q_{S_j}} \} / \frac{\partial \hat{R}^{(1)}_{+-}[\tilde{v}_n(\omega), \tilde{\mathbf{v}}_{\mathrm{p}}, \tilde{\mathbf{v}}_{\mathrm{s}}]}{\partial v_n} \ , \end{aligned} \qquad (13)$$

which gives the relationship between the Q-value of n^{th} normal mode and the Q-values of P and S waves in all layers. Noticing that

$$- \frac{\partial \hat{R}^{(1)}_{+-}[\tilde{v}_n, \tilde{\mathbf{v}}_{\mathrm{p}}, \tilde{\mathbf{v}}_{\mathrm{s}}]}{\partial \alpha_j} \Big/ \frac{\partial \hat{R}^{(1)}_{+-}[\tilde{v}_n, \tilde{\mathbf{v}}_{\mathrm{p}}, \tilde{\mathbf{v}}_{\mathrm{s}}]}{\partial v_n} = \frac{\partial v_n}{\partial \alpha_j}$$

and

$$- \frac{\partial \hat{R}^{(1)}_{+-}[\tilde{v}_n, \tilde{\mathbf{v}}_{\mathrm{p}}, \tilde{\mathbf{v}}_{\mathrm{s}}]}{\partial \beta_j} \Big/ \frac{\partial \hat{R}^{(1)}_{+-}[\tilde{v}_n, \tilde{\mathbf{v}}_{\mathrm{p}}, \tilde{\mathbf{v}}_{\mathrm{s}}]}{\partial v_n} = \frac{\partial v_n}{\partial \beta_j} \ ,$$

we can write equation (13) in an alternative form:

$$\frac{1}{Q_n} \cong \sum_{j=1}^{N+1} \left\{ \frac{\partial v_n}{\partial \alpha_j} \frac{\alpha_j}{v_n} \frac{1}{Q_{P_j}} + \frac{\partial v_n}{\partial \beta_j} \frac{\beta_j}{v_n} \frac{1}{Q_{S_j}} \right\}. \tag{14}$$

For a simple fluid-filled open borehole, equation (14) becomes

$$\frac{1}{Q_n} \cong \frac{\partial v_n}{\partial \alpha_1} \frac{1}{Q_{P_1}} + \frac{\partial v_n}{\partial \alpha_2} \frac{1}{Q_{P_2}} + \frac{\partial v_n}{\partial \beta_2} \frac{\beta_2}{v_n} \frac{1}{Q_{S_2}}, \tag{15}$$

which is the same as in Cheng et al. (1982).

STIMULATED MODE ACOUSTIC LOGGING (SMAL)

The SMAL technique is a relatively new logging method. Some field and laboratory experiments have been done (see, e.g., Medlin and Schmitt, 1992). The SMAL method stimulates or enhances a specific mode or wave under an appropriate source frequency (or a very narrow frequency band). An excitation log obtained by running a broad band sweep reveals the wellbore response. From the response curve we find an appropriate resonant frequency to excite an interesting mode. In the following section one of the examples is on attenuation estimation from the enhanced pseudo-Rayleigh wave by SMAL. More simulations on SMAL, for example, attenuation estimation using the standing waves in a borehole, are in progress.

EXAMPLES

The dispersion relation [equation (5)], tube wave attenuation [equation (14)], and the attenuation estimation from the pseudo-Rayleigh wave are tested for three typical radially layered models (see Table 1).

Table 1. Model parameters

	Fluid	Casing or Invaded zone	Formation
Simple Borehole	r=12cm α=1.5km/s ρ=1.0	—	α=4.9km/s β=2.8km/s ρ=2.4
Cased Borehole	r=10cm α=1.5km/s ρ=1.0	r=11.5cm α=6.1km/s β=3.4km/s ρ=7.8	α=4.9km/s β=2.8km/s ρ=2.4
Invaded Borehole	r=12cm α=1.5km/s ρ=1.0	r=19cm α=3.8km/s β=2.5km/s ρ=2.2	α=4.9km/s β=2.8km/s ρ=2.4

Normal Modes

Let $d(f,k)=|1-\hat{R}^{(1)}_{+-}(f,k)|$. A plot of $d(f, k)$ vs. (f, k) is helpful to see the root distribution, and what the normal mode looks like in the $k-\omega$ domain. Figures 1-3 show plots for the three models given in Table 1. In these plots, M1, M2, ... ,etc. indicate zeros or roots of $d(f, k)$, i.e., the normal modes. M1 is the Stoneley wave, and M2, M3, ..., etc. are pseudo-Rayleigh waves. R1, R2, etc. are resonances (Schmitt and Bouchon, 1985). These resonances are only local minima, not roots. The coordinates (f, k) corresponding to modes M1, M2,..., etc. are applied to calculate phase velocities of these modes using equation (6). In the next example we use the phase velocity of the fundamental pseudo-Rayleigh wave (M2) to find its Q-value.

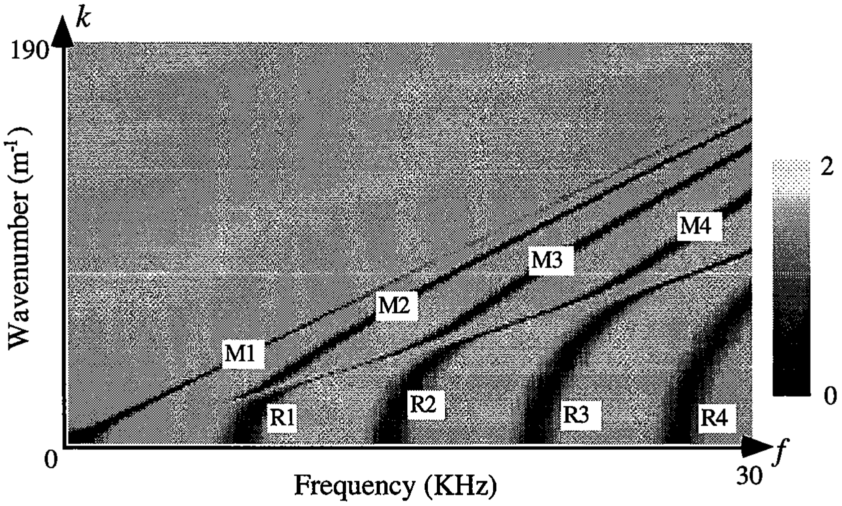

FIG. 1. A plot of the function $d(f,k)=|1-\hat{R}^{(1)}_{+-}(f,k)|$ for the *simple* open borehole.

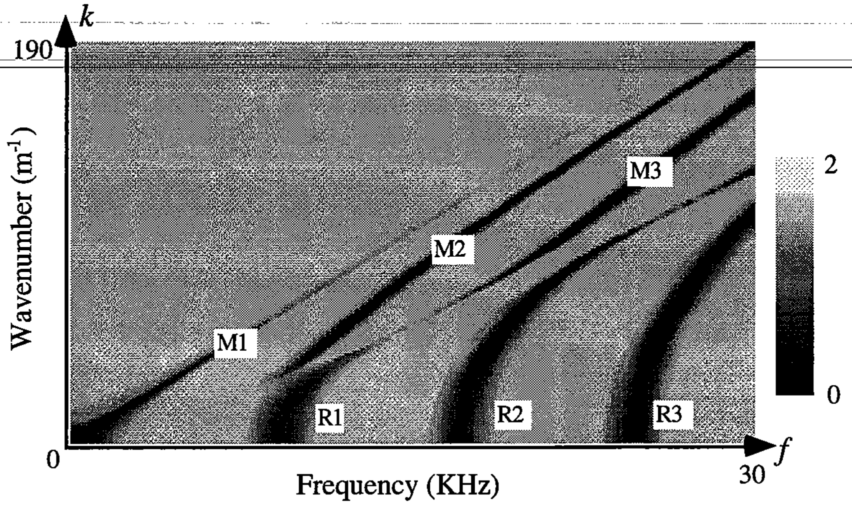

FIG. 2. A plot of the function $d(f,k) = |1 - \hat{R}^{(1)}_{+-}(f,k)|$ for the *cased* borehole.

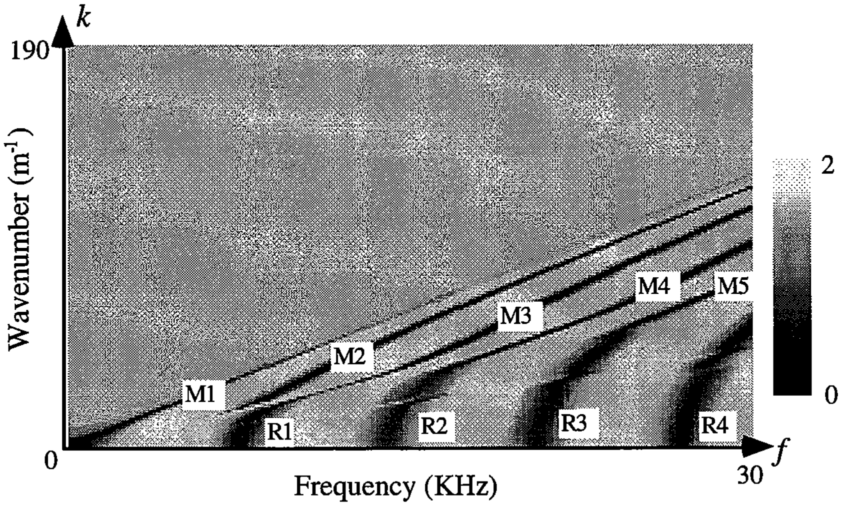

FIG. 3. A plot of function $d(f,k) = |1 - \hat{R}^{(1)}_{+-}(f,k)|$ for the borehole with an *invaded* zone.

Attenuation of the Pseudo-Rayleigh Wave (MODE M2)

The dependence of the Q_2 value of mode M2 on the Q_S-value of the S wave in the formation is shown in Figure 4 by the partition coefficient $(\partial v_n / \partial \beta)(\beta / v_n)$ [equation (14)]. It can be seen that this coefficient is sensitive to Q_S at the cutoff frequency. The next test shows how to estimate Q_S from Q_2 near the cutoff frequency for the simple borehole. Similarly, we can calculate the partition coefficients for the formation *P* wave and the fluid *P* wave. The partition coefficient for the formation *P* wave is negligible at all frequencies. The partition coefficient for the fluid *P* wave is small at the cutoff frequency, and becomes larger with increasing frequency.

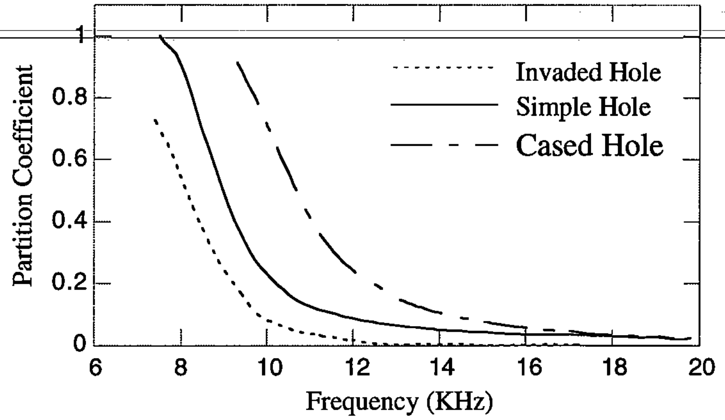

FIG. 4. Attenuation partition coefficients for the three borehole models.

Attenuation Estimation from the Pseudo-Rayleigh Wave

A linear sweep with the frequency band of 0.1-29 KHz is used as the source to calculate a synthetic excitation log (Figure 5) for the simple borehole model given in Table 1. Around *f*=9.5 Hz there is a peak on the response curve. This frequency is close to the cutoff frequency of the fundamental pseudo-Rayleigh wave. Then we run a short sweep 1.2 ms long with a frequency band of 9-9.5 KHz. This gives a SMAL log of the enhanced pseudo-Rayleigh wave, and is shown in Figure 6. Using the amplitude ratio method (Cheng et al., 1982), we find the estimated Q_{PR} =130 The given *S* wave Q_S is 80, and *Q*-values of other waves are infinite. From Figure 4 we find that the partition coefficient is about 0.45 for this case. Then, we get the estimated Q_S=60. The pseudo-Rayleigh wave is dominant in Figure 6. But other waves, e.g., the Stoneley wave, direct *P* and *S* waves are also in it, though they are very weak. This is one of the possible reasons why the estimated Q_S is smaller than the given value.

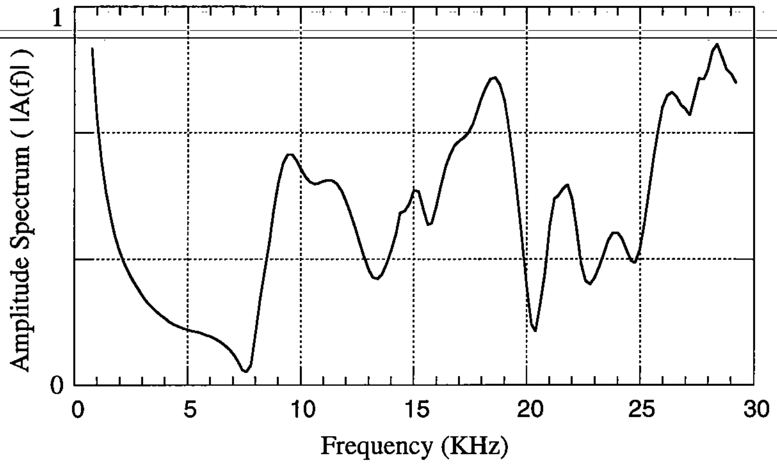

FIG. 5. Excitation log for the simple borehole.

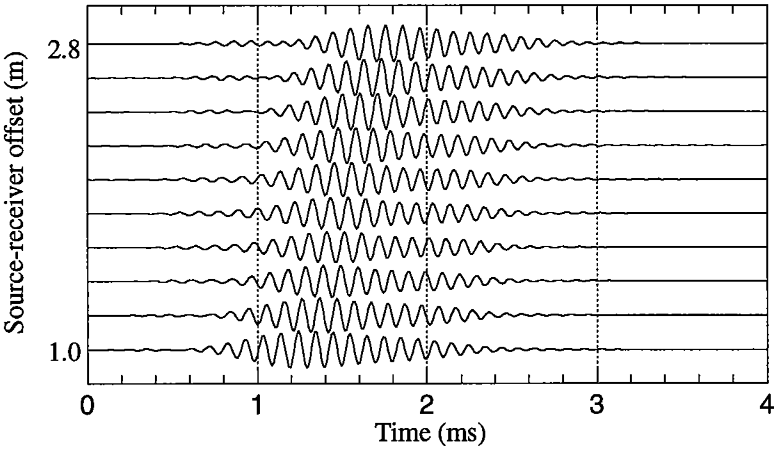

FIG. 6. The enhanced fundamental mode of the pseudo-Rayleigh wave near the cutoff frequency (9.5 KHz) for the simple borehole model.

CONCLUSIONS

A new method based on the generalized reflection and transmission coefficients is developed to calculate the phase velocities, eigen functions, and Q-values of normal modes in radially layered media. Numerical examples show that our algorithm is very efficient, and it can be applied to estimate the S -wave attenuation of the formation from the tube waves, even in a cased borehole.

REFERENCES

Boit, M. A., 1952, Propagation of elastic waves in a cylindrical bore containing a fluid: J. Appl. Physics, **23**, 997-1005.

Chen, X., Quan, Y, and Harris, J. M., 1994, Seismogram synthesis for radially multilayered media using the generalized reflection/transmission coefficients method: Expanded Abstracts of the 64th SEG annual meeting.

Chen, X., 1993, A systematic and efficient method of computing normal modes for multilayered half-space: Geophys. J. Int, **115**, 391-409.

Cheng, C. H. and Toksöz, M. N., 1981, Elastic wave propagation in a fluid-filled borehole and synthetic acoustic logs: Geophysics, **46**, No. 7, 1042-1053.

Cheng, C. H., Toksöz, M. N. and Willis, M. E., 1982, Determination of In situ attenuation from full waveform acoustic logs: J. G. R., **87**, No. B7, 5477–5484.

Kennett, B. L. N, 1983, *Seismic wave propagation in stratified media*: Cambridge University Press, New York.

Luco, J. E. and Apsel, R. J., 1983, On the Green's function for a layered half-space, Part I: Bull. Seism. Soc. Am., **73**, 909-929.

Medlin, W. L., Schmitt, D. P., 1992, Acoustic logging based on wellbore resonance: SPE 24686, the 67th Annual SPE Technical. Conference.

Schmitt, D. P. and Bouchon, 1985, Full wave acoustic logging: synthetic microseismograms and frequency-wavenumber analysis: Geophysics **50**, No. 11, 1756-1778.

PAPER E

REFLECTION AND TRANSMISSION COEFFICIENTS IN POROUS MEDIA

Xiaofei Chen ** and Youli Quan *

ABSTRACT

In this study we derive a set of exact formulas for the reflection and transmission coefficients in porous media. These formulas directly relate the amplitude of reflected waves to porous parameters, such as porosity, permeability and viscosity. If we can directly estimate porous parameters by performing AVO analysis, it is helpful for reservoir characterization and description. This work provides an effective tool for AVO in porous media. In the conventional AVO analysis, the reflection coefficient is based on *effective* velocity of a porous medium. As numerical tests, we compare the reflection coefficient calculated from our exact formulas with that using the effective velocity for different porous medium models. We find that at low frequency range two results agree very well, but at high frequency range, the solution using the effective velocity departs from the exact solution. We also assess the possible influence of the BISQ model newly developed by Dvorkin and Nur (1993) on AVO analysis. Since the BISQ model gives rise to notably smaller phase velocities at low frequency, thus it will give notably different reflection coefficients. Consequently, it will be significantly affect the results of AVO analysis.

---

* STP, Stanford University
** Department of Earth Sciences, University of Southern California

INTRODUCTION

AVO analysis of seismic reflection data is widely used to infer the presence of hydrocarbons. The conventional AVO analysis is based on such a strategy: first, one estimates the *effective* elastic parameters of a hydrocarbon reservoir using *elastic* reflection coefficient formulation; then models the reservoir as porous media and infers the porous parameters from those effective elastic parameters. Strictly speaking, this is an approximate approach to the reflection coefficient in porous media. The exact method should be based on the rigorous solutions in porous media. In this study we shall derive such an exact solution for the reflection and transmission coefficients in porous media. With these exact formulas, we can evaluate the validity and accuracy of the approximate method. Since our formulas give a direct relationship between the reflection coefficient and the porous property, we may use this relationship converting the reflection coefficient to porosity and other porous parameters under certain conditions.

This study is also a pilot work for simulation of complete wave fields in porous media. From this study we can understand how we properly propose the boundary conditions in porous media and when an exact porous solution is necessary. The modeling for vertically and/or radially layered porous media is in progress.

MODELS OF POROUS MEDIA

Biot theory (Biot, 1956a,b; 1962a,b) is the bedrock for studying the wave phenomena in porous media. Recently, Dvorkin and Nur (1993) proposed a unified model with squirt and Biot mechanisms (i.e., BISQ model). As shown by Dvorkin and Nur that at low frequency BISQ behaves differently from Biot model, at high frequency it approaches to Biot model. Figure 1 shows comparisons of the fast P-wave for these two porous medium models in the frequency range from 1 Hz to 10^{10}Hz. Here, the density of solid material is ρ_s=2.6284 g/cm^3, density of pore fluid ρ_f=1.0 g/cm^3, additional coupling density ρ_a=0.42g/cm^3, P- wave and S-wave velocities of solid material α_s =5.4497 km/s and β_s=3.2438 km/s, porosity ϕ=0.19, intrinsic permeability κ=100md and viscosity of the pore fluid η=1.0 cp. Note that the Biot's critical frequency for this case is $f_c = \dfrac{\phi\eta}{2\pi\kappa\rho_f} \approx 3\times10^5$Hz, we can clearly see that at low-frequency limit ($f << f_c$) the phase velocities of BISQ model have a smaller values than those of Biot model. At high-frequency case ($f > f_c$), however, the velocities for Biot and BISQ models tend to same value.

R/T COEFFICIENTS IN POROUS MEDIA

Let us consider two porous media wedded by a plane permeable interface. According to the acoustic theory of porous media, there are three kinds of waves in each porous medium, i.e., fast and slow P waves, and S wave. Owing to reflection and transmission effect of the interface, we have total six independent waves in each porous media, namely

$$\begin{cases} \phi_1^{(j)}(x,z,t) = p_{u1}^{(j)} e^{i(\omega t - \gamma_1^{(j)} z - kx)} + p_{d1}^{(j)} e^{i(\omega t + \gamma_1^{(j)} z - kx)}, \\ \phi_2^{(j)}(x,z,t) = p_{u2}^{(j)} e^{i(\omega t - \gamma_2^{(j)} z - kx)} + p_{d2}^{(j)} e^{i(\omega t + \gamma_2^{(j)} z - kx)}, \qquad \textit{for } j = 1,2\ . \\ \psi^{(j)}(x,z,t) = s_u^{(j)} e^{i(\omega t - \nu^{(j)} z - kx)} + s_d^{(j)} e^{i(\omega t + \nu^{(j)} z - kx)}, \end{cases} \tag{1}$$

Substituting the above potentials into following boundary conditions at interface (z=0),

(1) Continuity of total displacement (normal & shear components),
(2) Continuity of total traction (normal & shear components),
(3) Continuity of the pressure of pore fluid,
(4) Continuity of fluid motion (normal component of fluid displacement),

we obtain,

$$\mathbf{D}_{11}^{(1)}\mathbf{c}_u^{(1)} + \mathbf{D}_{12}^{(1)}\mathbf{c}_d^{(1)} = \mathbf{D}_{11}^{(2)}\mathbf{c}_u^{(2)} + \mathbf{D}_{12}^{(2)}\mathbf{c}_d^{(2)}, \tag{2a}$$

and

$$\mathbf{D}_{21}^{(1)}\mathbf{c}_u^{(1)} + \mathbf{D}_{22}^{(1)}\mathbf{c}_d^{(1)} = \mathbf{D}_{21}^{(2)}\mathbf{c}_u^{(2)} + \mathbf{D}_{22}^{(2)}\mathbf{c}_d^{(2)}, \tag{2b}$$

where, $\mathbf{c}_u^{(j)} = [p_{u1}^{(j)}, p_{u1}^{(j)}, s_u^{(j)}]^T$ and $\mathbf{c}_d^{(j)} = [p_{d1}^{(j)}, p_{d1}^{(j)}, s_d^{(j)}]^T$ (j=1,2) are coefficient vectors for up-going and down-going waves, and $\{\mathbf{D}_{mn}^{(j)},\ n,m = 1,2;\ j = 1,2\}$ are 3 by 3 matrices whose explicit expressions are given in Appendix.

The reflection and transmission coefficients are defined by the following relations,

$$\begin{cases} \mathbf{c}_u^{(1)} = \mathbf{R}_{du}\mathbf{c}_d^{(1)} + \mathbf{T}_u\mathbf{c}_u^{(2)} \\ \mathbf{c}_d^{(2)} = \mathbf{T}_d\mathbf{c}_d^{(1)} + \mathbf{R}_{ud}\mathbf{c}_u^{(2)} \end{cases}, \tag{3}$$

where, $\mathbf{R}_{du}$, $\mathbf{T}_u$, $\mathbf{T}_d$ and $\mathbf{R}_{ud}$ are all 3 by 3 matrices which have the following form

$$\mathbf{X} = \begin{bmatrix} X^{P_1P_1} & X^{P_1P_2} & X^{P_1S} \\ X^{P_2P_1} & X^{P_2P_2} & X^{P_2S} \\ X^{SP_1} & X^{SP_2} & X^{SS} \end{bmatrix}. \tag{4}$$

By comparing equation (2) with (3) we can obtain the following exact expression of reflection and transmission coefficients in porous media,

$$\begin{bmatrix} \mathbf{R}_{du} & \mathbf{T}_u \\ \mathbf{T}_d & \mathbf{R}_{ud} \end{bmatrix} = \begin{bmatrix} \mathbf{D}_{11}^{(1)} & -\mathbf{D}_{12}^{(2)} \\ \mathbf{D}_{21}^{(1)} & -\mathbf{D}_{22}^{(2)} \end{bmatrix}^{-1} \begin{bmatrix} \mathbf{D}_{11}^{(2)} & -\mathbf{D}_{12}^{(1)} \\ \mathbf{D}_{21}^{(2)} & -\mathbf{D}_{22}^{(1)} \end{bmatrix}. \tag{5}$$

NUMERICAL EXAMPLES

Let us first compare the our exact solution with effective elastic P-P (precisely speaking, should be fast P to fast P) reflection coefficients for Biot model for water, oil and gas saturated porous media, respectively. The upper and lower media are shale and sandstone, whose elastic and porous parameters are $\rho_s^{(1)}$=2.6774 g/cm^3, $\alpha_s^{(1)}$ =4.7877 km/s, $\beta_s^{(1)}$=2.52 km/s, $\phi^{(1)}$=0.16, $\kappa^{(1)}$=0.0014 md, and $\rho_a^{(1)}$ =0.38 g/cm^3 for shale, and $\rho_s^{(2)}$=2.6284 g/cm^3, $\alpha_s^{(2)}$ =5.4497 km/s, $\beta_s^{(2)}$=3.2438 km/s, $\phi^{(2)}$=0.19, $\kappa^{(2)}$=100 md, and $\rho_a^{(2)}$=0.42 g/cm^3 for sandstone. The properties of pore fluids are ρ_{water} =1.0 g/cm^3, ρ_{gas} =0.14 g/cm^3, ρ_{oil}=0.88 g/cm^3, η_{water}=1.0 cp, η_{gas}=0.022 cp and η_{oil}=180 cp. The comparisons for f=100 Hz shown in Figure 2 are for water, oil and gas saturated cases, respectively. Here, the solid lines stand for the exact solutions and dashed lines for effective elastic ones. We find that for this frequency our exact solutions agree excellently with the effective elastic ones. Figure 3 shows the comparisons of reflection with vertical incidence (i.e., θ=0) in the frequency range of 1Hz to 10^8Hz, and the corresponding distributions of *effective* elastic velocities of P wave (fast P wave) and S wave in the same frequency range. We can see that the departure of the effective elastic solution from the exact one in porous media occurs from the Biot's critical frequency.

Using our exact reflection coefficient formula of porous media, we can directly relate the reflection coefficient to the porous parameters (e.g., porosity, permeability, fluid density and viscosity, etc.). Figure 4 shows the distributions of reflection coefficients with vertical incidence (θ=0) for various porosities and permeabilities, respectively.

As shown in Figure 1(b) those phase velocities of BISQ model depart from those of Biot model at low frequency limit, and converge to same value at high frequency limit. Therefore, we expect that the resulting reflection coefficients of BISQ model will be different from those of Biot model at low frequency, and become same as those of Biot model at high frequency limit. Since the AVO analysis is a low frequency problem, the discrepancy of phase velocities between Biot and BISQ models will lead to the difference of reflection coefficients between these two models, consequently will affect the AVO analysis. We could also directly relate the reflection coefficient of BISQ model to the porous parameters of the saturated porous media, but our computer code doses not run through yet at this moment, and we are still working on this problem.

DISCUSSIONS AND CONCLUSIONS

We have rigorously derived an exact formula for computing the reflection and transmission coefficients in porous media, and verified its validity by comparing with the effective elastic solution (i.e., conventional solution). Using this exact formula we can directly relate the reflection coefficients to the parameters of porous media, such as porosity, permeability, fluid density and viscosity, etc.). Therefore, this new exact solution of porous media may be useful for AVO analysis. The BISQ model (Dvorkin and Nur, 1993), on the other hand, gives rise to notably smaller phase velocities at low frequency, thus it will give notably different reflection coefficients. Consequently, it will be significantly affect the results of AVO analysis.

According to our numerical results shown above, we find that at high frequency ($f > f_c$) the effective elastic solution departs from the exact solution of porous media. Thus, in well-logging analysis where the characteristic frequency is near the Biot's critical frequency, we need to use the exact solution of porous media rather than the effective elastic solution. Next, we shall apply our rigorous method to the study of full waveform logging in radially layered media.

REFERENCES

Biot, M. A., 1956a, Theory of propagation of elastic waves in a fluid-saturated porous solid. I. Low-frequency range: J. Acoust. Soc. Am., **28**, 168-178.

Biot, M. A., 1956a, Theory of propagation of elastic waves in a fluid-saturated porous solid. II. Higher-frequency range: J. Acoust. Soc. Am., **28**, 179-191.

Biot, M. A., 1962a, Mechanics of deformation and acoustic propagation in porous media: J. Appl. Phys., **33**, 1482-1498.

Biot, M. A., 1962b, Generalized theory of acoustic propagation in porous dissipative media: J. Acoust. Soc. Am., **34**, 1254-1264.

Dvorkin, J. and Nur, A., 1993, Dynamic poroelasticity: a unified model with the squirt and Biot mechanism, Geophysics, **58**, 524-533.

Paillet, F. L. and Cheng, C. H., 1993, *Acoustic waves in boreholes*, CRC Press.

Schmitt, D. P. , Bouchon, M. and Bonnet, G., 1988, Full-waveform synthetic acoustic logs in radially semi-infinite saturated porous media, Geophysics, **53**, 807-823.

APPENDIX

Those 3x3 matrices in equation (2), $\{\mathbf{D}^{(j)}_{mn},\ n,m=1,2;\ j=1,2\}$, are defined as,

$$\mathbf{D}^{(j)}_{nm}=\begin{bmatrix} a^{(j)}_{3(n-1)+1,3(m-1)+1} & a^{(j)}_{3(n-1)+1,3(m-1)+2} & a^{(j)}_{3(n-1)+1,3(m-1)+3} \\ a^{(j)}_{3(n-1)+2,3(m-1)+1} & a^{(j)}_{3(n-1)+2,3(m-1)+2} & a^{(j)}_{3(n-1)+2,3(m-1)+3} \\ a^{(j)}_{3(n-1)+3,3(m-1)+1} & a^{(j)}_{3(n-1)+3,3(m-1)+2} & a^{(j)}_{3(n-1)+3,3(m-1)+3} \end{bmatrix} \quad \text{for } j=1,2,$$

where,

$$a^{(j)}_{11}=a^{(j)}_{14}=\alpha^{(j)}_1 k,$$

$$a^{(j)}_{12}=a^{(j)}_{15}=\alpha^{(j)}_2 k,$$

$$a^{(j)}_{13}=-a^{(j)}_{16}=\alpha^{(j)}_3 v^{(j)},$$

$$a^{(j)}_{21}=-a^{(j)}_{24}=-\alpha^{(j)}_1\gamma^{(j)}_1,$$

$$a^{(j)}_{22}=-a^{(j)}_{25}=-\alpha^{(j)}_2\gamma^{(j)}_2,$$

$$a_{23}^{(j)} = a_{26}^{(j)} = \alpha_3^{(j)} k,$$

$$a_{31}^{(j)} = -a_{34}^{(j)} = 2\gamma_1^{(j)} N^{(j)} k,$$

$$a_{32}^{(j)} = -a_{35}^{(j)} = 2\gamma_2^{(j)} N^{(j)} k,$$

$$a_{33}^{(j)} = -a_{36}^{(j)} = \alpha_3^{(j)} N^{(j)} [(v^{(j)})^2 - k^2],$$

$$a_{41}^{(j)} = a_{44}^{(j)} = -\{2N^{(j)}(\gamma_1^{(j)})^2 + [F^{(j)} + G^{(j)} + (T^{(j)} + G^{(j)})C_1^{(j)}](k_{p1}^{(j)})^2\},$$

$$a_{42}^{(j)} = a_{45}^{(j)} = -\{2N^{(j)}(\gamma_2^{(j)})^2 + [F^{(j)} + G^{(j)} + (T^{(j)} + G^{(j)})C_2^{(j)}](k_{p2}^{(j)})^2\},$$

$$a_{43}^{(j)} = -a_{46}^{(j)} = 2k\alpha_3^{(j)} N^{(j)} v^{(j)},$$

$$a_{51}^{(j)} = a_{54}^{(j)} = -(G^{(j)} + T^{(j)} C_1^{(j)})(k_{p1}^{(j)})^2 / \phi^{(j)},$$

$$a_{52}^{(j)} = a_{55}^{(j)} = -(G^{(j)} + T^{(j)} C_2^{(j)})(k_{p2}^{(j)})^2 / \phi^{(j)},$$

$$a_{53}^{(j)} = a_{56}^{(j)} = 0,$$

$$a_{61}^{(j)} = -a_{64}^{(j)} = -C_1^{(j)} \gamma_1^{(j)},$$

$$a_{62}^{(j)} = -a_{65}^{(j)} = -C_2^{(j)} \gamma_2^{(j)},$$

$$a_{63}^{(j)} = a_{66}^{(j)} = \chi^{(j)} k,$$

$$\alpha_{1,2}^{(j)} = 1 - \phi^{(j)} + \phi^{(j)} C_{1,2}^{(j)},$$

$$\alpha_3^{(j)} = 1 - \phi^{(j)} + \phi^{(j)} \chi^{(j)},$$

$$v^{(j)} = \sqrt{(k_s^{(j)})^2 - k^2},$$

$$\gamma_{1,2}^{(j)} = \sqrt{(k_{p1,2}^{(j)})^2 - k^2},$$

$$k_{p1,2}^{(j)} = \omega / V_{p1,2}^{(j)},$$

and

$$k_s^{(j)} = \omega / V_s^{(j)}.$$

Where, the $C_{1,2}^{(j)}$, $\chi^{(j)}$, $F^{(j)}$, $N^{(j)}$, $G^{(j)}$ and $T^{(j)}$ have same definitions as those in Paillet and Cheng (1993).

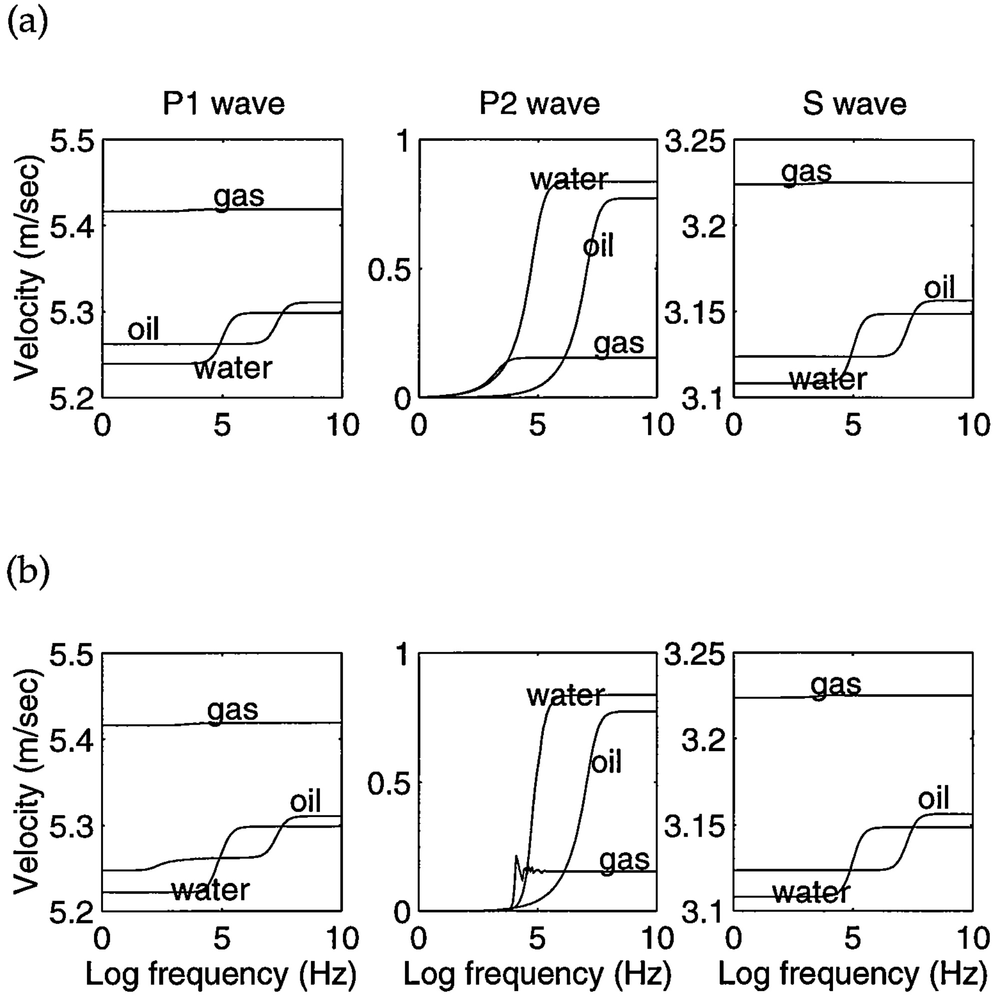

Figure 1. Phase velocities for saturated sandstone. (a) Phase velocities of Biot model; (b) phase velocities of BISQ model (Dvorkin and Nur, 1993).

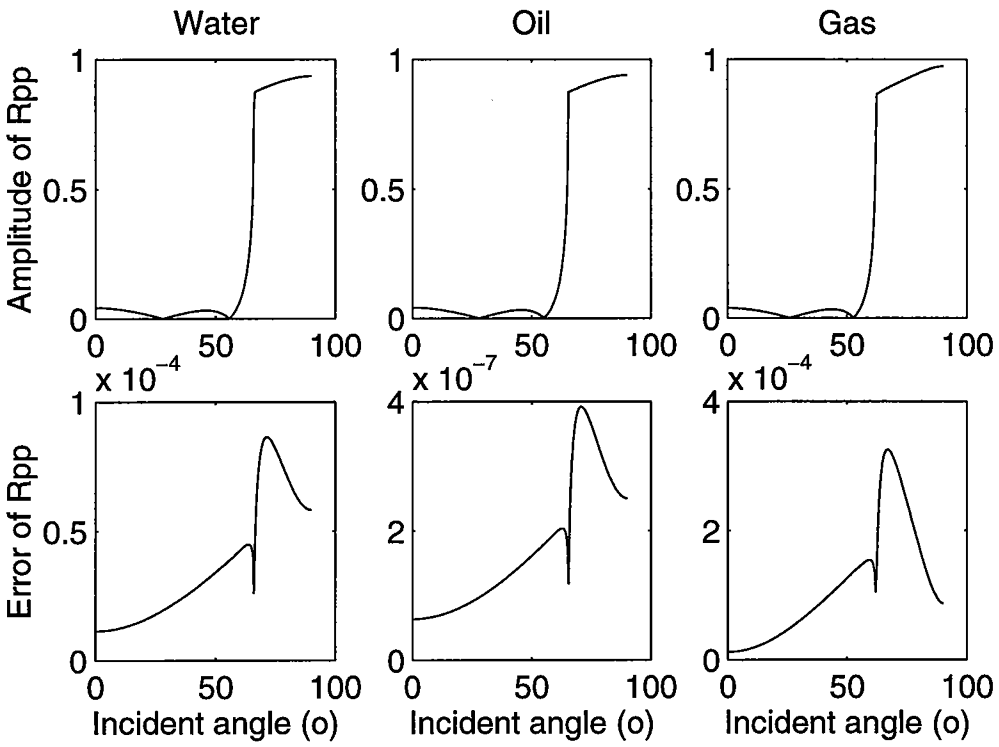

Figure 2. Comparisons of reflection coefficients of porous media between the exact solutions (solid lines) and effective elastic solutions (dashed lines) for different pore fluids. Here f=100 Hz.

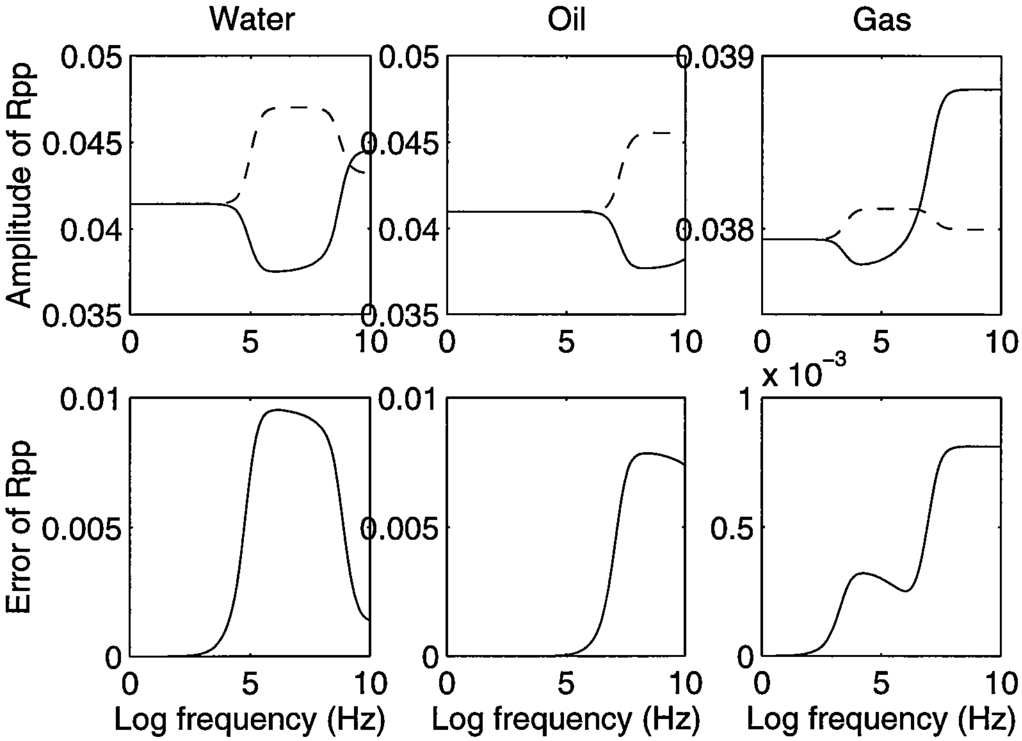

Figure 3. Comparisons of exact solutions (solid lines) with effective elastic solution of vertical incidence over a frequency range from 1Hz to 10^{10} Hz.

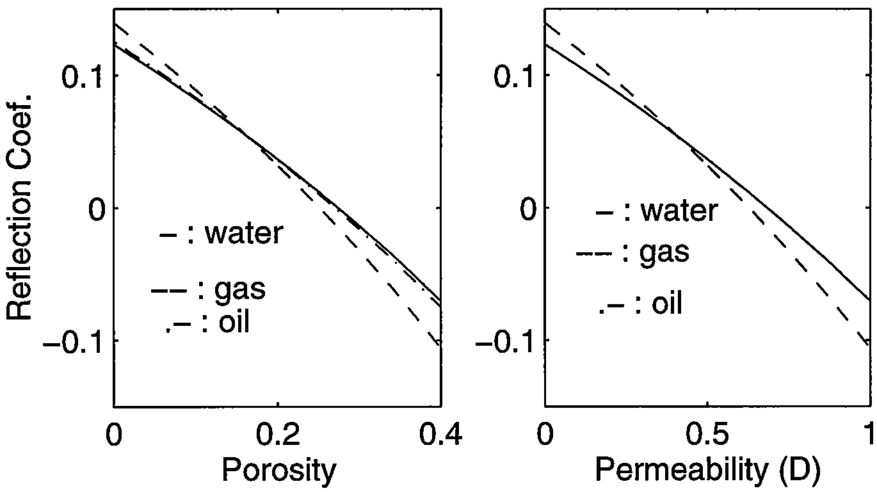

Figure 4. Relationships of reflection coefficients with the porosity and permeability. Where, the solid, dashed and dot-dashed lines denote, respectively, the water, gas and oil saturated porous media.

TRAVELTIME TOMOGRAPHY IN ANISOTROPIC MEDIA

Jessé Costa

ABSTRACT

A stable reconstruction of anisotropic models from crosswell transmitted traveltimes is formulated and validated on synthetic data sets. The model is monoclinic and the symmetry plane is coincident with the acquisition plane. No approximation is used for the slowness surfaces and the raytracing is consistent with the model. The problem is ill-conditioned in consequence of the data type, *P*- and/or *S*-wave traveltimes, and the limited angular coverage provided by crosswell acquisition geometry. To recover meaningful results, regularization constraints are imposed requiring minimum anisotropy and inhomogeneity. Additional regularization is achieved controlling the scale of inhomogeneities allowed by parameterizing the model using nodes instead of cells. Application to the McElroy data set produced a virtually isotropic model.

INTRODUCTION

The broad angular ray coverage provided by crosswell surveys makes these experiments more sensitive to the occurrence of anisotropy than surface seismic experiments. The determination of the effective anisotropy at the crosswell frequency band has two important applications. Velocity models more consistent with traveltimes can improve the quality and likelihood of acoustic images. Besides, since effective anisotropy reflect patterns of inhomogeneities at scales much smaller than the dominant acoustic energy wavelength (Schoenberg & Muir, 1989), it can be potentially correlated, through geologic and petrophysical information, to the permo-porosity properties.

We present a stable algorithm to the reconstruction of anisotropic velocity models from traveltimes of q*P*- and/or q*S*v- transmitted waves. Previous approaches to this problem assumed approximations to the slowness surfaces. Cerveny (1982) derived the Frechét derivatives for traveltime inversion around an isotropic background. Chapman & Pratt (1992) and Pratt et al. (1993) investigated the limits of reconstruction for weak anisotropic models. Michelena et al. (1995) used the double-elliptical approximation (Dellinger et al., 1993) for transversally anisotropic models to justify the inversion of elliptical models in 1.5-D and posterior estimation of TI parameters. Costa et al. (1993) considered the inversion of 1-D transversally isotropic models and obtained an anelliptical model for the Devine data set.

We discuss the traveltime inversion for monoclinic models. The tomographic problem is formulated for arbitrary anisotropic slowness models and solved through linear iterations. The problem is then specialized to monoclinic models with a symmetry plane coincident with the acquisition plane. The limits of resolution of q*P*- and q*S*v-wave data are investigated and the subsets of parameters resolved by each data set are derived. The limited aperture of the crosswell experiment and the available data types, q*P*-and/or q*S*-waves, determine the nonuniqueness of the solutions, therefore defining an ill-posed problem (Menke, 1984). To obtain stable solutions, hopefully with geological meaning, the solutions are constrained through three regularizing functionals (Menke, 1984). The first, functionl minimizes anisotropy in the solution. The other two, requiring solutions with minimum vertical and horizontal gradients, enforces homogeneity. The weight of the constraints on the solution decreases during the iterations following the continuation method proposed by Bube & Langan (1994). Additional regularization is obtained controlling the scale of heterogeneities by parameterizing the model using nodes (Harris, 1993). This algorithm is validated on synthetic data sets. The joint inversion of McElroy *P*- and *S*-wave transmitted traveltimes produced a virtually isotropic model.

THEORY

Model Parameterization

The traveltime of acoustic waves through an anisotropic elastic medium, under the framework of ray theory, is completely determined by the slowness surfaces at each point in the medium (Arnold, 1989). Besides the slowness surfaces obtained for anisotropic elastic medium from wave equation through plane wave (Musgrave, 1970) or asymptotic expansions (Cerveny, 1972), several approximations have been used in geophysics. The weak anisotropy approximation (Thomsen, 1986) was used by Stewart (1988). Chapman & Pratt (1992) also assume weak anisotropy. Michelena (1995) recovered transversally isotropic elastic parameters through traveltime inversion for elliptical models based on the double-elliptical approximation (Dellinger et al., 1993). We assume that the slowness surfaces in every point in the medium are defined by a dispersion relation in the form,

$$\mathrm{F}(\mathbf{s},\mathbf{x}) = \mathrm{F}(\mathbf{s},\eta(\mathbf{x})) = 0 \quad , \tag{1}$$

where, $\mathbf{x}$ is the position, $\mathbf{s}$ is slowness and η is the tensor of parameters defining the slowness surface. In order to trace rays through a model and set up the inversion problem we need a finite parameterization to $\eta(\mathbf{x})$. We use tensor products (DeBoor, 1978),

$$\eta(\mathbf{x}) = \sum_{i=1}^{nx}\sum_{j=1}^{nz}\eta_{ij}B_i(x-x_i)B_j(z-z_j) \quad , \tag{2}$$

where, η_{ij} is the tensor of parameters at $\mathbf{x}_{ij} \equiv (x_i,z_j)$, over a rectangular grid $n_x \times n_z$, B_i are the interpolation basis functions and $\mathbf{x} \equiv (x,z)$ is the position. Right now we are utilizing bilinear interpolation, but B-splines are being implemented.

Forward Modeling

The raypath connecting two points through a heterogeneous anisotropic medium is defined by the Fermat's Principle, which states that the traveltime is stationary along the ray trajectory in phase space, in this case, the extended space of position and slowness $(\mathbf{x},\mathbf{s})$. In mathematical language, the variation of the traveltime functional,

$$\tau = \int_{\mathbf{x}_0}^{\mathbf{x}_1} \mathbf{s}\cdot d\mathbf{x} \quad ,$$

subject to, (3)

$$\mathrm{F}(\mathbf{x},\mathbf{s}) = 0 \quad ,$$

should vanish along the ray. The solution of this variational problem results in the system of ordinary differential equations that governs the raypath and the slowness along the ray (Arnold, 1989),

$$\begin{aligned} \frac{d\mathbf{x}}{d\gamma} &= \lambda \nabla_{\mathbf{s}} F \ , \\ \frac{d\mathbf{s}}{d\gamma} &= -\lambda \nabla_{\mathbf{x}} F \ , \end{aligned} \tag{4}$$

where γ and λ depend on the specific parameterization for the raypath, for example, traveltime or path length. Two other equations are added to (4), one to integrate traveltime and another to integrate the dispersion relation (1) along the ray. This last equation is used to monitor the accuracy of the raytracing system. The resulting system of differential equations, using path length, *l*, as parameterization, is

$$\begin{aligned} \frac{d\mathbf{x}}{dl} &= \frac{\operatorname{sign}(\mathbf{s}\cdot\nabla_{\mathbf{s}}F)}{\|\nabla_{\mathbf{s}}F\|}\nabla_{\mathbf{s}}F \ , \\ \frac{d\mathbf{s}}{dl} &= -\frac{\operatorname{sign}(\mathbf{s}\cdot\nabla_{\mathbf{s}}F)}{\|\nabla_{\mathbf{s}}F\|}\nabla_{\mathbf{x}}F \ , \\ \frac{d\tau}{dl} &= \frac{\operatorname{sign}(\mathbf{s}\cdot\nabla_{\mathbf{s}}F)}{\|\nabla_{\mathbf{s}}F\|}\mathbf{s}\cdot\nabla_{\mathbf{s}}F \ , \\ \frac{dS}{dl} &= F \ , \end{aligned} \tag{5}$$

with initial conditions,

$$\begin{aligned} &\mathbf{x}(l=0) = \mathbf{x}_0 \ , \\ &F(\mathbf{x}_0, \mathbf{s}(l=0)) = 0 \ , \\ &\tau(l=0) = 0 \ , \\ &S(l=0) = 1 \ . \end{aligned} \tag{6}$$

This system is integrated using fourth order Runge-Kutta with controlled step size (Press et al., 1990). This integration scheme is accurate although more computationally expensive than fixed step size integration.

The two point raytracing is solved using the shooting method. We use an implementation developed by Robert Langan (personal comm.). An initial fan of rays with broad aperture is shot. If the desired end point is bracket by the fan, the algorithm performs a secant method search to find the required raypath. Otherwise, the fan is refined until it either brackets the end point or until it exceeds the maximum number of iterations allowed. This procedure is very robust and can capture multiple raypaths, in this case the raypath with minimum traveltime is used in the inversion.

Inverse Problem - Linearization

The reconstruction of $\eta(\mathbf{x})$ from crosswell traveltimes measurements is a nonlinear problem. The raypath depends on $\eta(\mathbf{x})$. One approach is to linearize the problem, computing the Fréchet derivative of the functional (3), and to proceed iteratively. Because traveltime along the ray is stationary, the time error resulting from the integration along a nearby, but erroneous raypath, distant from the actual ray by a small parameter of order ε, is of order ε^2. Thus when computing first order traveltime perturbations relative to changes in the parameters, $\delta\eta^p$, to first order in ε, from (3), traveltime does not vary with perturbation of the raypath, but only due to the perturbations in slowness. Thus one can write,

$$\delta\tau = \int_{ray} \sum_{i=1}^{N} \delta\eta^p \mathbf{s},_{\eta^p} .\mathbf{x}' d\gamma \tag{7}$$

where the comma indicates partial derivatives, $\mathbf{x}' \equiv d\mathbf{x}/d\gamma$, and η^p represent the N_p components of the parameters tensor that defines the slowness surfaces. The total derivative of the dispersion relation (1) with respect to any particular η^p at any point $\mathbf{x}$ along the ray must vanish, i.e.,

$$\frac{d\mathrm{F}}{d\eta^p} = \mathrm{F},_{\eta^p} + \mathbf{s},_{\eta^p} \cdot \nabla_{\mathbf{s}} \mathrm{F} = 0 \tag{8}$$

From (4), $\mathbf{x}' = \lambda \nabla_{\mathbf{s}} \mathrm{F}$, substituting into the above equation gives,

$$\mathbf{s},_{\eta^p} \cdot \mathbf{x}' = -\lambda \mathrm{F},_{\eta^p} \quad , \tag{9}$$

and further substitution in (7), yields the result,

$$\delta\tau = -\int_{ray} \lambda \sum_{i=1}^{N} \mathrm{F},_{\eta^p} \delta\eta_i d\gamma \quad . \tag{10}$$

Therefore, the derivative of the traveltime relative to η_{ij}^p for a model parameterized in the form (2), using the length along the ray as the integration variable, is given by,

$$\tau,_{\eta_j^p} = -\int_{ray} \frac{\mathrm{sign}(\mathbf{s}.\nabla_{\mathbf{s}} \mathrm{F})}{\| \nabla_{\mathbf{s}} \mathrm{F} \|} \mathrm{F},_{\eta_j^p} B_i(x - x_i) B_j(z - z_j) dl \quad . \tag{11}$$

The determination of η_{ij} from a set of N_d measured traveltimes, τ_k^o, is performed iteratively. Starting from an initial model, $\eta = \lfloor \eta_{ij} \rfloor$, the raypath and the corresponding traveltime is computed for each source-receiver pair. The computed traveltimes, τ_k^c, yield a set of residuals, $\delta\tau_k$, that are approximated to first order by perturbations in the model parameters, $\delta\eta_{ij}^p$ by,

$$\delta\tau_k = \tau_k^o - \tau_k^c(\eta_{ij}^p) \approx \sum_i \sum_j \sum_p \tau,_{\eta_{ij}^p} \delta\eta_{ij}^p \quad , \tag{12}$$

a set of N_d equations in $n_x \times n_z \times N_p$ unknowns, $\partial\eta^r_{ij}$. After solving (12), the model is updated and the iteration repeated until the residual norm reaches a required tolerance level. In crosswell applications the system (12) is usually highly overdetermined, with N_d much greater than the number of unknowns, and the solution is obtained by least squares (Menke, 1984). However, although overdetermined, the linear system (12) is in general ill-conditioned (Lawson & Hanson, 1974). For tomography using isotropic models, this is due to the limited ray coverage provided by crosswell acquisition geometry (Spakman & Nolet,1988). The reconstruction of anisotropic models is even more unstable as discussed below.

Inverse Problem -Reconstruction Limits for Monoclinic Media

The most complex anisotropic model we consider is monoclinic with a vertical plane of mirror symmetry, plane X-Z, coincident with the acquisition plane. This model is the most general consistent with the 2-D nature of crosswell surveys. The tensor of density normalized elastic moduli for this model, in condensed notation (Musgrave, 1970), is

$$a_{IJ} = \begin{bmatrix} a_{11} & a_{12} & a_{13} & 0 & a_{15} & 0 \\ a_{12} & a_{22} & a_{23} & 0 & a_{25} & 0 \\ a_{13} & a_{23} & a_{33} & 0 & a_{35} & 0 \\ 0 & 0 & 0 & a_{44} & 0 & a_{46} \\ a_{15} & a_{25} & a_{35} & 0 & a_{55} & 0 \\ 0 & 0 & 0 & a_{46} & 0 & a_{66} \end{bmatrix} . \tag{13}$$

For a medium whose elastic properties vary slowly with respect to the wavelength, the general dispersion relation which the slowness must satisfy at any point **x** (Musgrave, 1970) is

$$\mathrm{F}(\mathbf{x},\mathbf{s}) = \left| a_{ijkl}(\mathbf{x}) s_j s_l - \delta_{ik} \right| = 0 \ , \tag{14}$$

where, $a_{ijkl} \equiv c_{ijkl} / \rho$, is the density normalized elastic stiffness moduli, in indicial notation. At the symmetry plane of a monoclinic medium, represented by (13), the expression (14) can be factored in the form,

$$\mathrm{F}(\mathbf{s}) \equiv \mathrm{F}(s_1, s_3) = \mathrm{F}_{\mathrm{qP-qSv}}(\mathbf{s}) \times \mathrm{F}_{\mathrm{SH}}(\mathbf{s}) = 0 \ , \tag{15}$$

where,

$$\mathrm{F}_{\mathrm{SH}}(\mathbf{s}) = a_{66} s_1^2 + 2a_{46} s_1 s_3 + a_{44} s_3^2 - 1 = 0 \ , \tag{16}$$

and

$$\begin{aligned} \mathrm{F}_{\mathrm{qP-qSv}}(\mathbf{s}) = {} & (a_{11}s_1^2 + a_{55}s_3^2 + 2a_{15}s_1s_3 - 1)(a_{55}s_1^2 + a_{33}s_3^2 + 2a_{35}s_1s_3 - 1) - \\ & [(a_{15}s_1^2 + a_{35}s_3^2 + 2(a_{13} + a_{55})s_1s_3]^2 = 0 \end{aligned} . \tag{17}$$

The relation F_{SH} controls the slowness of *S*h-waves, i.e., waves with polarization perpendicular to the plane of propagation. The slowness of waves polarized along the symmetry plane, q*P*- and q*S*v-waves, are governed by (17). Since we are interested in q*P*- and q*S*v-waves inthe crosswellexperiment the slownesses considered from now on satisfy the dispersion relation (17). Consequently, the traveltimes of the q*P*- and q*S*v-waves that propagate along the symmetry plane of a monoclinic medium depend only on a_{11}, a_{13}, a_{15} , a_{33} , a_{35} , a_{55}. Our goal is therefore the reconstruction of these parameters in the region between the wells.

Equation (10) shows that the Fréchet derivatives of traveltime with respect to the dispersion relation parameters differ only by the derivatives of the dispersion relation itself with respect to η^{ν}. Thus, these derivatives controls the resolution of each parameter. First we investigate the limits of reconstruction of q*P*- and q*S*v-waves separately. To do this we introduce the following parameterization (Costa et al., 1993),

$$\begin{aligned}
\eta_1 &\equiv C = \frac{a_{11}+a_{33}}{2} \ , \\
\eta_2 &\equiv c = a_{55} \ , \\
\eta_3 &\equiv D = \frac{a_{11}-a_{33}}{2} \ , \\
\eta_4 &\equiv \Delta = \frac{C-(a_{13}+2a_{55})}{2} \ , \\
\eta_5 &\equiv \psi = \frac{a_{15}+a_{35}}{2} \ , \\
\eta_6 &\equiv \varphi = \frac{a_{15}-a_{35}}{2} \ .
\end{aligned} \tag{18}$$

For an isotropic medium the only nonzero parameters are C and c, in this case, the square of *P*- and *S*-wave velocities respectively. The dispersion relation (17) takes the form,

$$\begin{aligned}
\mathrm{F} = &\left[(C+D)s_1^2 + cs_3^2 + 2(\psi+\varphi)s_1s_3 - 1\right]\times\left[cs_1^2 + (C-D)s_3^2 + 2(\psi-\varphi)s_1s_3 - 1\right] - \\
&\left[(\psi+\varphi)s_1^2 + (\psi-\varphi)s_3^2 + (C-c-2\Delta)s_1s_3\right]^2 = 0
\end{aligned} \quad ,(19)$$

and the derivatives in (10) are,

$$\begin{aligned}
\mathrm{F},_C &= s^4\left[c + \Delta\sin^2 2\theta - \varphi\sin 4\theta - 1/s^2\right] \ , \\
\mathrm{F},_c &= s^4\left[C + D\cos 2\theta - \Delta\sin^2 2\theta + 2\psi\sin 2\theta + \varphi\sin 4\theta - 1/s^2\right] \ , \\
\mathrm{F},_D &= s^4\left[c\cos 2\theta - \frac{D}{2}\sin^2 2\theta + \frac{\psi}{2}\sin 4\theta - \varphi\sin 2\theta - 1/s^2\right] \ ,
\end{aligned} \tag{20}$$

$$F,_{\Delta} = s^4\left[2\psi\sin 2\theta + \varphi\sin 4\theta + (C - c - 2\Delta)\sin^2 2\theta\right] ,$$

$$F,_{\psi} = s^4\left[\frac{D}{2}\sin 4\theta - 2\psi\cos^2 2\theta - 2\varphi\cos 2\theta - 2(\Delta + c)\sin 2\theta - 2\sin 2\theta / s^2\right] ,$$

$$F,_{\varphi} = -s^4\left[D\sin 2\theta + (C - c - \Delta)\sin 4\theta + 2\psi\cos 2\theta + 2\varphi + 2\sin 2\theta / s^2\right] ,$$

where, $s = \sqrt{s_1^2 + s_3^2}$, and, $\theta = \mathrm{tg}^{-1}\left(\frac{s_3}{s_1}\right)$, is the slowness direction.

These partial derivatives can be interpreted using the weak anisotropy approximation discussed in Appendix A,

$$\begin{aligned} F_{qP_a}(\mathrm{s}) &\equiv \left[C + D\cos 2\theta - \Delta\sin^2 2\theta + 2\psi\sin 2\theta + \varphi\sin 4\theta - 1/s^2\right] = 0 \ , \\ F_{qSv_a}(\mathrm{s}) &\equiv \left[c + \Delta\sin^2 2\theta - \varphi\sin 4\theta - 1/s^2\right] = 0 \ . \end{aligned} \qquad (21)$$

Comparing (21) and (20) we notice that,

$$F,_{C} = s^4 F_{qSv_a} \quad \text{and} \quad F,_{c} = s^4 F_{qP_a} \qquad (22)$$

Thus,

- since, $F,_c$ is approximately zero for q*P*-waves, perturbations on this parameter cannot be recovered from q*P*-traveltimes irrespective of the angular ray coverage, at least in the f weak anisotropy limit.
- similarly, since $F,_C$ is almost zero q*S*v-waves so perturbations δC cannot be resolved from q*S*v-wave traveltimes.
- and, since the weak approximation for q*S*v-waves do not depend to first order on D and ψ, these parameter are poorly determined from q*S*v-wave traveltimes.

A related but somewhat weaker form of these results shows that only perturbations on a_{11}, a_{33} e $(a_{13} + 2a_{55})$ can be recovered from q*P*- traveltime data assuming weak anisotropy was described by Chapman & Pratt (1992).

Figure 1.a and 1.b are plots of the q*P*- and q*S*v-wave slowness curves and their corresponding weak anisotropy approximations for a medium with $D/C = 33\%$, $\Delta/C = 15\%$, $\psi = 0$ and $\varphi = 0$, i.e., a non-weak anisotropic medium. These plots indicate that, for values of anisotropy plausible for geologic materials, q*P*-traveltimes do not carry information on c and q*S*v-wave traveltimes do not depend on C, irrespective to the ray angular coverage through the medium. Another way of visualizing these results is by looking at the graphs of the dispersion relation (17) with respect to the parameters given by (18). These graphs are shown in Figures 2 and 3 for q*P*- and q*S*v-waves respectively.

These conclusions have implications as to the set up of the tomographic reconstruction for anisotropic models. One approach is to assume weak anisotropy and use the dispersion relations (21) for q*P*- and/or q*S*v-waves. As indicated by Figures 1.a and 1.b, these approximations are worse at the angular interval between 30° and 60°. In this work we do not use weak anisotropy and we assume that q*P*- and q*S*v-wave traveltimes are available.

Inverse Problem - Preconditioning

Another feature seen in Figures 2 and 3 is the strong angular dependence of the Fréchet derivatives. Thus, to obtain a stable reconstruction of anisotropic models a broad angular coverage is required throughout the medium. Unfortunately this coverage cannot be achieved in all regions of the model in crosswell surveys. The unavoidable limited aperture reduces the resolution and yields nonunique solution. This fact is translated numerically by the ill-conditioning of the tomographic system (12). To explicitly take into account the limited angular ray coverage and try to attenuate its dangerous effects the following parameterization is considered,

$$\begin{aligned}
s_1^{-2} &\equiv s_{qP_a}^{-2}(0°) = C + D \ , \\
s_2^{-2} &\equiv s_{qP_a}^{-2}(30°) = C + \frac{D}{2} - \frac{3\Delta}{4} + \frac{\sqrt{3}}{2}(\,2\psi + \varphi) \, , \\
s_3^{-2} &\equiv s_{qP_a}^{-2}(-30°) = C + \frac{D}{2} - \frac{3\Delta}{4} - \frac{\sqrt{3}}{2}(\,2\psi + \varphi) \ , \\
s_4^{-2} &\equiv s_{qS_a}^{-2}(30°) = c + \frac{3\Delta}{4} - \frac{\sqrt{3}\varphi}{2} \ , \\
s_5^{-2} &\equiv s_{qS_a}^{-2}(-30°) = c + \frac{3\Delta}{4} + \frac{\sqrt{3}\varphi}{2} , \\
s_6^{-2} &\equiv s_{qS_a}^{-2}(0°) = c \ .
\end{aligned} \qquad (23)$$

The motivation for the introduction of this parameterization is the preconditioning the tomographic system (12), since these parameters are associated with a limited angular sector of the slowness curves. To investigate the effect of this parameterization, the condition number (Lawson & Hanson, 1974) of the system (12) was computed for different values of angular ray coverage for two parameterizations defined by (18) and (23) respectively. The matrix of the tomographic system using *P*- and *S*v-wave traveltimes was computed for a homogeneous isotropic model with receivers placed in a circle around a source at 1° interval. The condition number for this matrix was computed using MATLAB. The results are shown in Table 1.

Angular Coverage	Parameters I	Parameters II
-90° - 90°	23.0072	13.7800
-60° - 60°	79.4686	16.2778
-30° - 30°	779.5074	129.3789

Table 1. Condition number of the tomographic system as a function of angular ray coverage. Parameters I are given by equations (18) and parameters II by equations (23).

This results show that parameterization II, equations (23), improves the condition number of the tomographic system. Although this result holds rigorously only for weak anisotropic models, since we linearized the problem around an isotropic model, we use this parameterization for the inversion qP- and qSv-wave traveltimes.

Inverse Problem - Regularization

The considerations above on the condition number of the tomographic system has a local character. The global resolution properties of the system (12) also depends strongly on the scale of heterogeneities allowed in the model. For isotropic models these aspects are discussed by Bube & Resnick (1984) and Spakman & Nolet (1988) who point out the low horizontal resolution of crosswell traveltime tomography. Michelena (1993), discussing the trade off of anisotropy and heterogeneity for elliptical models, shows that horizontal and high frequency variations in the vertical component of the slowness are poorly determined. These results indicate the importance of adding prior information on the scale of heterogeneities allowed in the model for regularizing inversion. Parameterizing the model in the form (2) improves the flexibility for controlling the scale of heterogeneities allowed. Since the tomographic problem is ill-posed, for all the reasons discussed above, we need to introduce regularization constraints (Menke, 1984). We use three regularizing functionals. The first requires that deviations from isotropy to be minimized. The other two penalize horizontal and vertical variations and therefore constrain against heterogeneity. The regularized problem takes the form,

$$\text{Minimize } \| \tau_{obs} - \tau_{calc}(\eta) \|_2^2 \; + \; \lambda_1^2 \, \| \mathbf{D}_{\mathrm{iso}} \eta \|_2^2 \; + \; \lambda_2^2 \, \| \mathbf{D}_{\mathrm{x}} \eta \| \; + \; \lambda_3^2 \, \| \mathbf{D}_{\mathrm{z}} \eta \| \; , \tag{24}$$

where, τ_{obs}, is the measured traveltimes, τ_{calc} are the traveltimes through the model η and $\mathbf{D}_{\mathrm{iso}}$, $\mathbf{D}_{\mathrm{x}}$, $\mathbf{D}_{\mathrm{z}}$ are first order finite difference operators that measure the variations in the model with respect to isotropy, horizontal, and vertical variations of the parameters respectively. The penalty parameters λ_1, λ_2 and λ_3 control the weight of each functional on the solutions with respect to fitting the data. The linearization of (24) yields the regularized tomographic system,

$$\begin{aligned} \mathbf{A}\delta\eta &= \delta\tau \, , \\ \lambda_1 \mathbf{D}_{\mathrm{iso}} \delta\eta &= -\lambda_1 \mathbf{D}_{\mathrm{iso}} \eta \, , \\ \lambda_2 \mathbf{D}_{\mathrm{x}} \delta\eta &= -\lambda_2 \mathbf{D}_{\mathrm{x}} \eta \, , \\ \lambda_3 \mathbf{D}_{\mathrm{z}} \delta\eta &= -\lambda_3 \mathbf{D}_{\mathrm{z}} \eta \, . \end{aligned} \tag{25}$$

The first set of equations corresponds to the system (12). At each iteration this linear system is solved using the conjugate gradient method for least squares (Spakman & Nolet, 1988).

Inverse Problem -Continuation Method

Equations (24) and (25) show that the parameters λ_1, λ_2 and λ_3 control the effectiveness of the regularization on the solution. The values of these parameters relative to the norm of the **A** matrix control the trade off between fitting the data and obeying the regularization constraints. In the continuation method (Bube & Langan, 1994), starting from high values relative to the Frobenius norm of **A** matrix, the penalty terms are slowly relaxed over the iterations producing a family of solutions associated with the corresponding values of λ_1, λ_2 and λ_3. For each particular values of the penalty terms the linear iterations are performed until the norm of residuals in (25) does not decrease by a significant amount, this constitutes one step in the continuation method. Afterwards λ_1, λ_2 and λ_3 are decreased and the continuation step repeated. These continuation iterations proceed until the instabilities in (25) produce models so rough that the two point raytracing breaks down. A particular solution can then be singled out observing the trade off between fitting the data and obeying the regularization constraints.

APPLICATION TO SYNTHETIC DATA SETS

The algorithm was validated on two synthetic data sets. The synthetic models are based on the McElroy sonic log. One is isotropic and the other has anisotropy in one layer. The traveltimes for *P*- and *S*-waves were obtained using an eikonal finite difference approach for the isotropic model and the raytracing described in this paper for the anisotropic model. To try to mimic actual conditions data with a vertical offset less than 30 ft were masked. This is because the peizoelectric source radiation pattern do not generate *S*-waves in this direction. This also helps to minimize artifacts due to head waves that can occur in real data. The acquisition geometry is the same, the well distance is 200 ft and sources and receivers are spaced every 5 ft. These two data sets were inverted for a monoclinic model with 2x91 nodes distributed regularly every 5 ft in each well. The initial model is isotropic and homogeneous with Vp = 18.2 kft/s and Vs = 10.4 kft/s. The initial values of the penalty parameters λ_1, λ_2 and λ_3 relative to the Frobenius norm of the tomographic system (12) were 3, 3 and 0.75 respectively, therefore isotropic layered solutions are heavily weighted at the beginning of iterations. After each continuation step the penalty terms are divided by $\sqrt{10}$. The inversion results for the isotropic model data set, after 9 continuation steps, are shown in Figures 4 and 5. These plots show the velocities corresponding to the slowness parameters s_1 , s_2 , s_3, s_4, s_5 and s_6. The inverted model fits the data with an rms error of 16 microseconds. Figures 6 and 7 show the results after 10 continuation steps. The inversion results for the anisotropic model data set are shown in Figures 6 and 7, after 10 continuation steps. The inverted model fits the data with rms error of 20 microseconds. The artifacts near sharp boundaries are probably due to the use of bilinear interpolation which produces discontinuities in the gradient thus violating the assumptions of our raytracing. The inversion results for these synthetic data sets indicate that the algorithm proposed is stable, at least for the scale of heterogeneities allowed in these models.

APPLICATION TO MCELROY DATA SET

The next step was to apply the algorithm to the McElroy data set. The details of the acquisition can be found in Harris et al. (1995). The well head distance is 184 ft. Source and receiver positions were corrected to account for well deviations following Harris (1993). Due to memory limitation only a subset of 83 sources and 80 receivers were used. Data with vertical offset less than 30 ft were masked since the source radiation pattern does generate strong *S*v-waves (Van Schaack et al., 1995) at this interval and to avoid possible artifacts due to *P*-wave headwaves.

The data were inverted for a monoclinic model with 2x91 nodes discretized on a rectangular grid with 200 ft horizontal spacing and 5 ft vertical. The initial model was the same one used for the synthetic data sets with Vp = 18.2 kft/s and Vs = 10.4 kft/s. The penalty terms λ_1, λ_2 and λ_3 start with values 3, 3 and 0.75 respectively, relative to the Frobenius norm of the tomographic matrix in (12). After each continuation step these parameter are divided by $\sqrt{10}$. The profiles of the velocities corresponding to the parameters in (23), after 8 continuation steps, are shown in Figures 8 and 9. The depths have been changed for presentation purposes. This model fits the data with an rms error of less than 150 microseconds for P-wave traveltimes and 300 microseconds for S-wave traveltimes, which is approximately equal to the picking error.

Figures 8 and 9 show that the inverted model does not present significant anisotropy. The differences between the profiles near sharp boundaries are probably due to the use of bilinear interpolation as pointed out earlier. Therefore, these results indicate that an isotropic medium is consistent with the McElroy data set. This result differs from Michelena et al. (1995) who obtained an anisotropic model for McElroy. About this we can only point out some differences favoring our approach. We think that the joint inversion of qP- and qS-wave traveltimes is a better constrained problem when inverting for anisotropic models. We also used a larger aperture since we were not constrained by the elliptical approximation. Finally, smooth models are more robust for traveltime tomography.

CONCLUSIONS

The reconstruction of anisotropic models from qP- and/or qSv-wave traveltimes was discussed. The resolution limits for the reconstruction of monoclinic media were derived and the effects of limited angular ray coverage were taken explicitly into account. The model was parameterized using nodes which permitted a flexible way to handle the trade off between anisotropy and heterogeneities. An accurate forward modeling raytracing code, consistent with the node parameterization, was developed which allows us to approach the nonlinear problem of tomographic reconstructions through linear iterations. The regularization of the tomographic system, through the minimization of anisotropy and heterogeneity on the solution, yields a stable algorithm, which was validated on synthetic data sets. The joint inversion of McElroy P- and S-wave traveltimes resulted in a virtually isotropic model.

The formulation presented is general and thereby any approximation for the slowness curves can be easily be included. The next steps in this project includes the extension of this approach to reflection traveltime tomography together with Mark Van Schaack. The reflection trajectories increase the ray angular coverage therefore reducing the null space of the tomographic system. The investigation of better ways to take advantage of the node parameterization as *a priori information* constraints is also a topic for future investigation.

ACKNOWLEDGMENTS

The field data were picked and edited by Mark Van Schaack. The first author strongly acknowledges Mark for his friendship and the great synergetic interaction in the work during this year. We also acknowledge Bob Langan and Ken Bube for sharing with us their continuation method code. Thanks to the Brazilian CNPq and all the sponsors of the Stanford Tomography Project that supported the first author this year in Stanford.

REFERENCES

Arnold, V. A., 1989, **Mathematical Methods of Classical Mechanics**. New York, Springer-Verlag. 508p. (Graduate Texts in Mathematics, 60).

Bube, K. P. & Langan, R. T., 1994, A continuation approach to regularization for traveltime tomography: Expanded Abstracts, SEG, **64**, 980-983.

Bube, K. P. & Resnick, J. R., 1984, Well-determined and poorly-determined features in seismic tomography: Expanded Abstracts, SEG, **54**, 717-719.

Cerveny, V., 1972, Seismic rays and ray intensities in inhomogeneous anisotropic media: Geophys. J. Roy. Astr. Soc., **29**, 1-13.

Cerveny, V., 1982, Direct and inverse kinematic problem for inhomogeneous anisotropic media-linearization approach: Contr. Geophys. Inst. Slov. Acad. Sci., **13**, 127-133.

Chapman, C. H. & Pratt, R.G., 1992, Traveltime tomography in anisotropic media. I-theory: Geophys. J. Int., **109**, 1-19.

Costa, J. C., Miller, D. Schoenberg, M., 1993, Ray tracing and tomography in anisotropic layered media-theory and practice, with application to Devine data set: Scientific Report Schlumberger Cambridge Research.

Costa, J. C., 1993, Modelagem sísmica e inversão na presença de anisotropia: Tese de Doutoramento. Depto. de Geofísica, UFPa.

Dellinger, J., Muir, F. & Karrenbach, M., 1993, Anelliptic approximations for TI media: J. Seismic Expl., **2**, 23-40.

Harris, J. M., 1993, Lattice parameterization for tomography: STP Annual Report, 4(1). Paper E.

Harris, J. M., Nolen-Hoeksema, R. C., Langan, R. T., Van Schaack, M., Lazaratos, S. K., & Rector III, J. W., High-resolution crosswell imaging of a west Texas carbonate reservoir: Part I - Project summary and interpretation: Geophysics, **60**, 667-681.

Helbig, K. & Schoenberg, M., 1987, Anomalous polarization of elastic waves in transversally isotropic media: J.Acoust. Soc. Am., **81**, 1235-1245

Menke, W., 1984, **Geophysical data analysis: discrete inverse theory**: New York, Academic Press. 206p.

Michelena, R. J.,1993, Anisotropic traveltime tomography: Ph.D thesis, Stanford University.

Michelena, R. J.,1995, Crosswell tomographic estimation of elastic constants in transversely isotropic media: Geophysics, **60**, 774-783.

Miller, D. & Chapman, C.H., 1991, Incontrovertible evidence of anisotropy in crosswell data: Expanded Abstracts, SEG, **61**, 825-828.

Musgrave, J. P., 1970, **Crystal acoustics**. Lodon, Holden-Day.288p.

Press, W.H, Flannery, B. P., Teukolsky, S. A. & Vetterling, W.T., 1990, **Numerical Recipes**. Cambridge. Cambridge University Press. 702p.

Van Schaack, M. A., Harris, J. M., Rector III, J. W. & Lazaratos, S. K., 1995, High-resolution crosswell imaging of a west Texas carbonate reservoir: Part 4-reflection imaging: Geophysics, **60**, 602-691.

Spakman, W. & Nolet, G., 1988, Imaging algorithms, accuracy and resolution in delay time tomography: In: **Mathematical Geophysics**. Editors: Vlaar, N.J. Nolet, G. Wortel, M.J.R. & Cloetingh, S.A.P.L. Dordretcht, D. Reidel Publishing Company. 407p.

Stewart, R. R., 1988, An algebraic reconstruction technique for weakly anisotropic velocity: Geophysics, **53**, 1613-1615.

Thomsen, L., 1986, Weak elastic anisotropy: Geophysics, **51**, 1954-1966.

APPENDIX A

APPROXIMATE SLOWNESS CURVES

Consider a arbitrary rotation in the plane X-Z, forming an angle α with respect to the X axis; the parameters (18) are transformed according to,

$$\begin{aligned} C' &= C - \Delta\sin^2 2\alpha + \varphi\sin 4\alpha \ , \\ D' &= D\cos 2\alpha + 2\psi\sin 2\alpha \ , \\ \Delta' &= \Delta\cos 4\alpha - \varphi\sin 4\alpha \ , \\ \psi' &= \psi\cos 2\alpha + \frac{D}{2}\sin 2\alpha \ , \\ \varphi' &= \varphi\cos 4\alpha - \frac{\Delta}{2}\sin 4\alpha \ , \\ c' &= c + \Delta\sin^2 2\alpha - \varphi\sin 4\alpha \, . \end{aligned} \tag{A-1}$$

For transversally isotropic media with symmetry axis in the plane or if the plane is coincident with the symmetry planes of an orthorhombic medium it is always possible to find a coordinate system such that ψ' and φ' vanish. In this system of principal axes the dispersion relation (19) takes the form

$$(s^{-2})^2 - (C + D\cos 2\theta + c)s^{-2} + c(C + D\cos 2\theta) + [(C-c)\Delta - \Delta^2 - \frac{D^2}{4}]\sin^2 2\theta = 0 \ , \tag{A-2}$$

a quadratic equation in s^{-2} (where s is the magnitude of the slowness vector) with coefficients that are functions of θ, the phase angle. The dispersion relation can be exactly factored (with an elliptical slowness curve for q*P*-waves and a circular q*S*v-wave slowness curve) if the quantity,

$$E^2 \equiv (a_{11} - a_{55})(a_{11} - a_{55}) - (a_{11} - a_{55})^2 = 4(C-c)\Delta - 4\Delta^2 - D^2 \ , \tag{A-3}$$

is equal to zero (Helbig & Schoenberg, 1987). Solving (A-2) gives q*P*- and q*S*v-waves,

$$s^{-2} = \frac{C + D\cos 2\theta + c}{2} \pm \sqrt{\left(\frac{C + D\cos 2\theta - c}{2}\right)^2 - \frac{E^2}{4}\sin^2 2\theta} \ . \tag{A-4}$$

Expanding these solutions in powers of the anisotropy parameters, D and Δ, and neglecting terms of order $O[D/(C-c), \Delta/(C-c), D\Delta/(c-c]$, yield the simple expressions for phase slowness,

$$s_{qP_a}^{-2} \approx C + D\cos 2\theta - \Delta\sin^2 2\theta \ , \qquad s_{qS_a}^{-2} \approx c + \Delta\sin^2 2\theta \ . \tag{A-5}$$

which reconverted to a coordinate system noncoincident with the principal axes takes the form of (21).

The anellipticity parameter ε_A (Costa et al., 1993) (a nondimensional version of E^2, normalized so that $Max\ \varepsilon_A = 1$), becomes proportional to Δ in the weak approximation:

$$\varepsilon_A \equiv \frac{E^2}{(a_{11}-a_{55})(a_{33}-a_{55})} = \frac{4(C-c)\Delta - 4\Delta^2 - D^2}{(C-c)^2 - D^2} \approx \frac{4\Delta}{(C-c)} \quad . \tag{A-6}$$

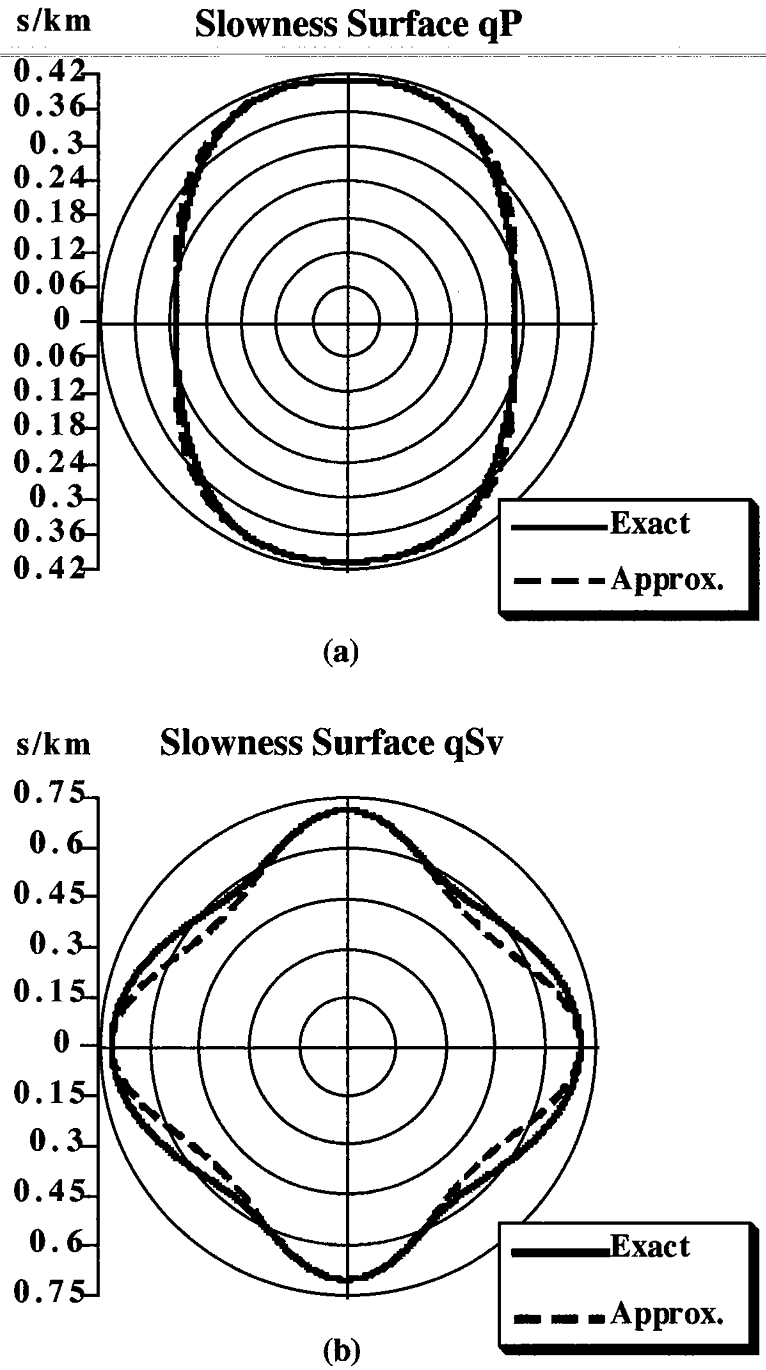

(a)

(b)

Figure 1: Slowness curves for q*P*- and q*S*v-waves and their corresponding weak anisotropy approximations calculated for a medium with parameters set as follows: $D/C = 33\%$, $\Delta/C = 15\%$ and $c/C = 2/9$. Even for this non-weak anisotropic medium the approximations are accurate, especially for the q*P*-wave slowness curve.

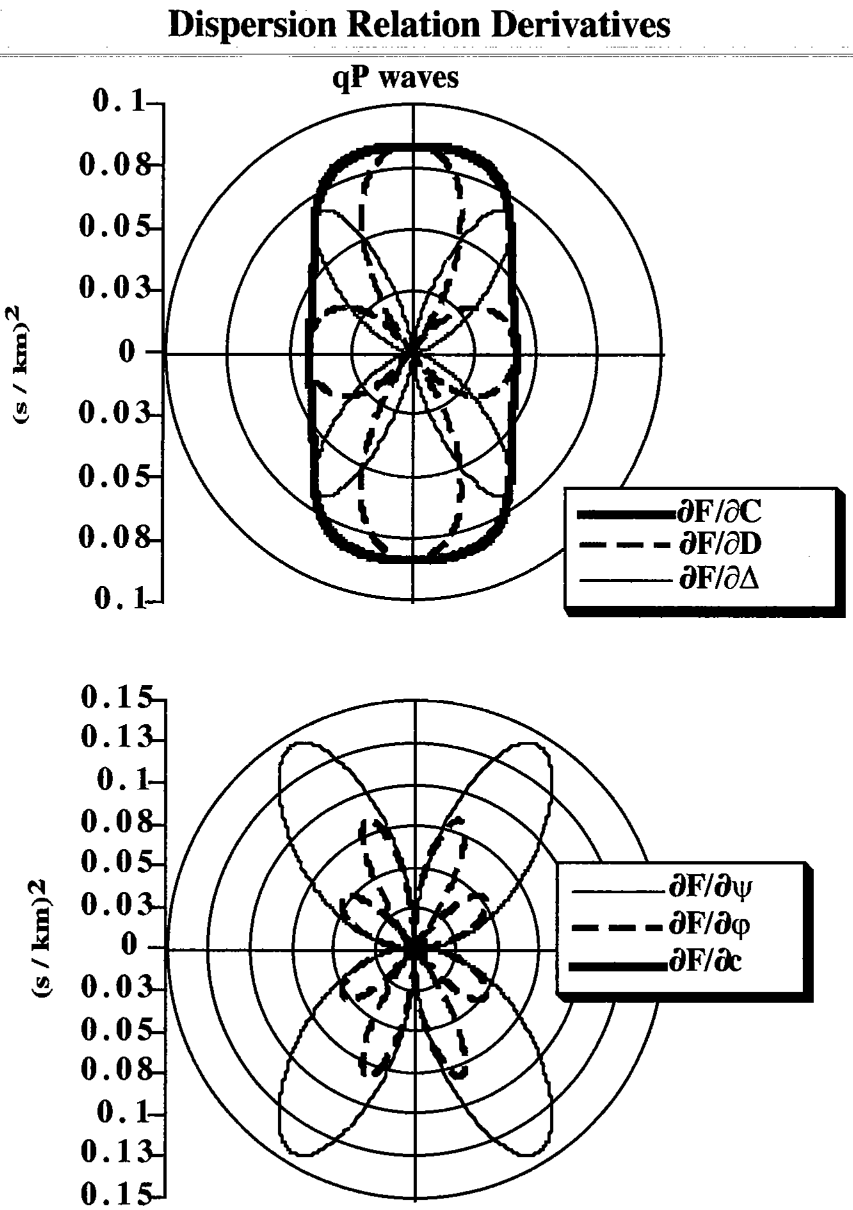

Figure 2: Derivatives of the dispersion relation with respect to the parameters (18) for q*P*-waves (equation 19) for the medium shown in Figure 1. The derivative $\partial F/\partial c$ can be neglected with respect to the others, even for this non weak anisotropic medium, indicating that this parameter cannot be recovered from q*P*-traveltimes.

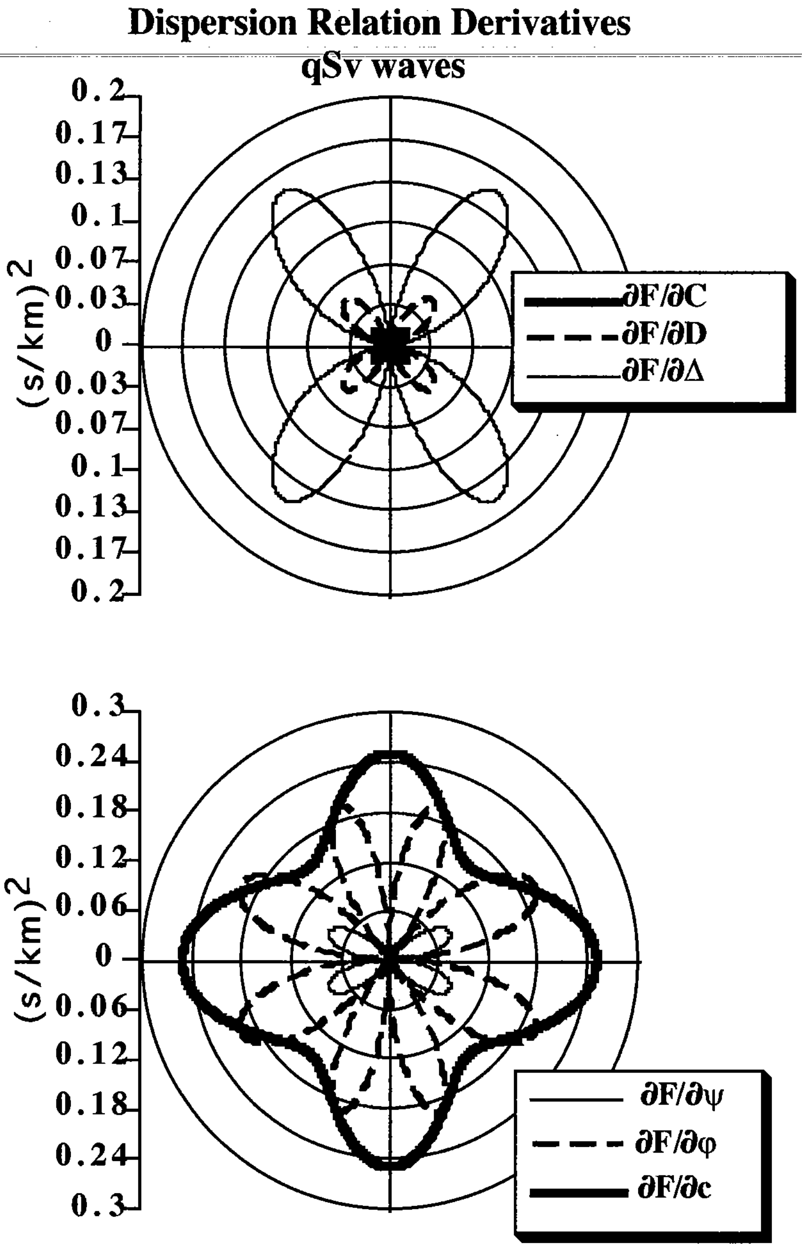

Figure 3: Derivatives of the dispersion relation for qSv-waves, equation (19), for the model shown in Figure 1. Notice that $\partial F/\partial C$ can be neglected with respect to the other derivatives indicating that this parameter cannot be recovered from qSv-wave traveltimes.

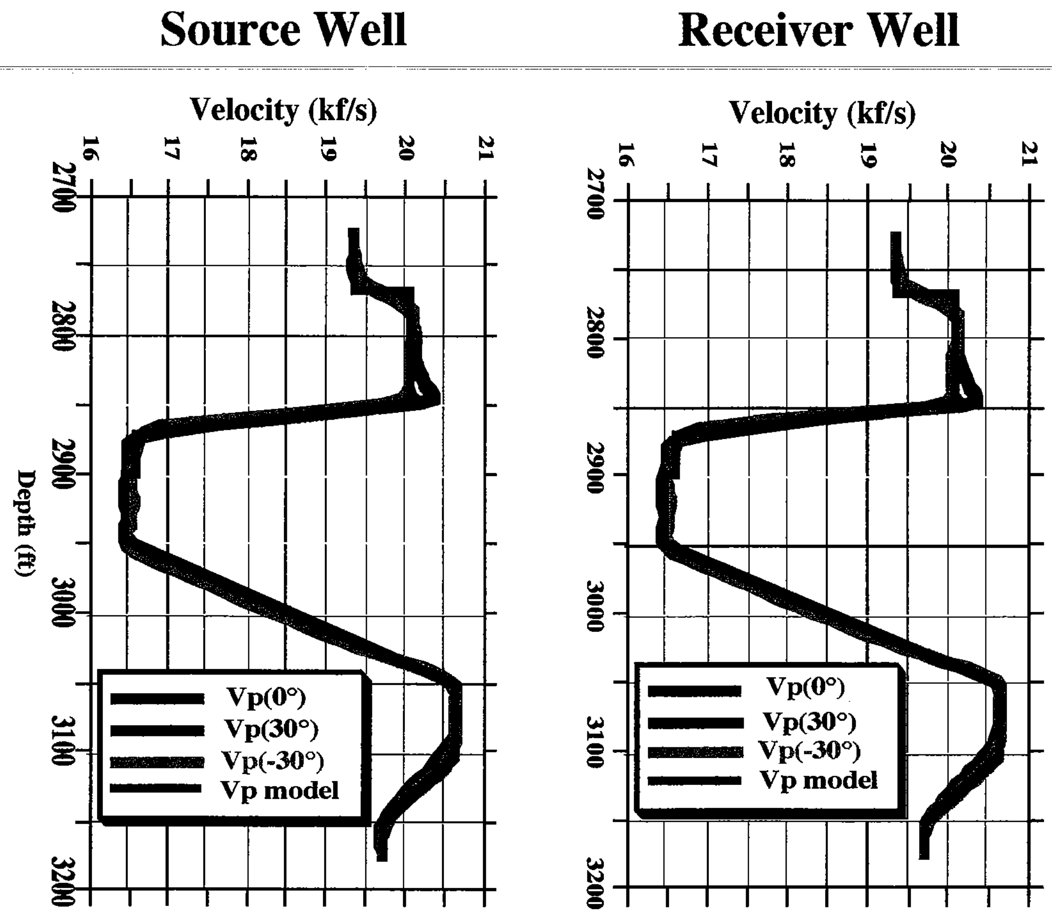

Figure 4: Profile of q*P*-velocity parameters, equation (23), after the inversion of the synthetic data set.

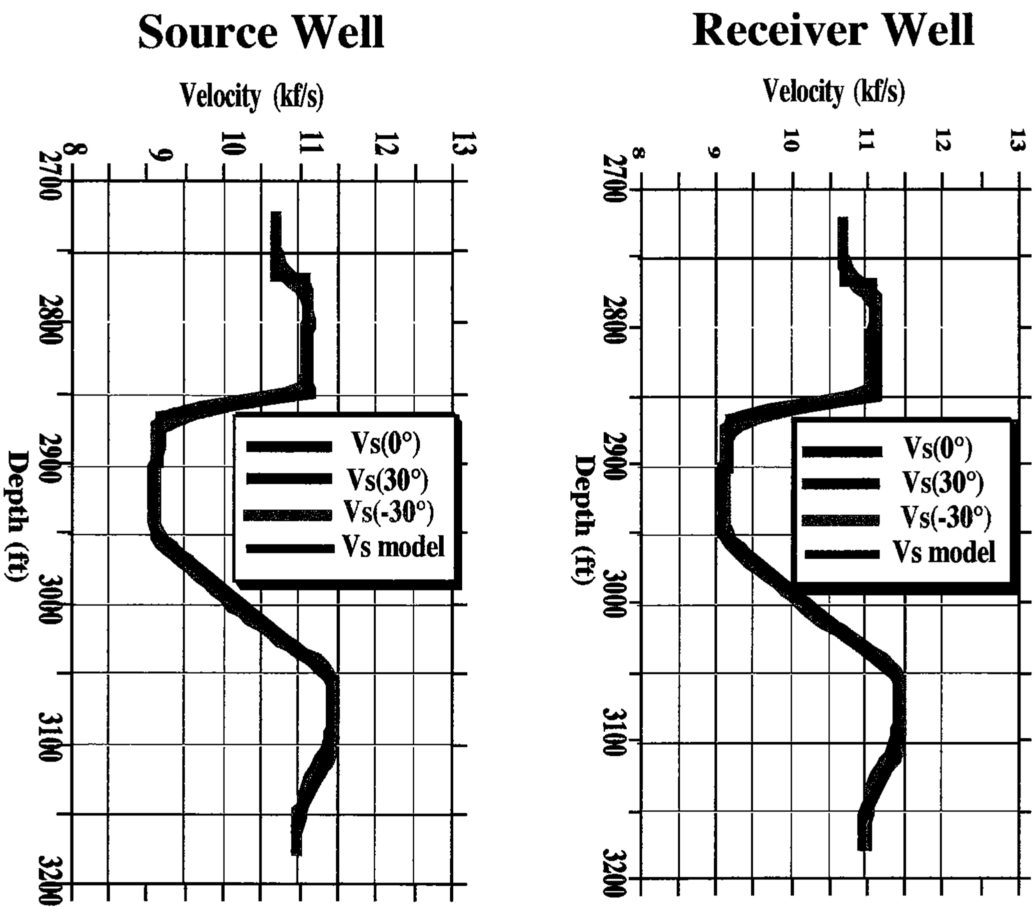

Figure 5: Profile of qSv-wave velocity parameters, equation (23), after the inversion of synthetic the data set.

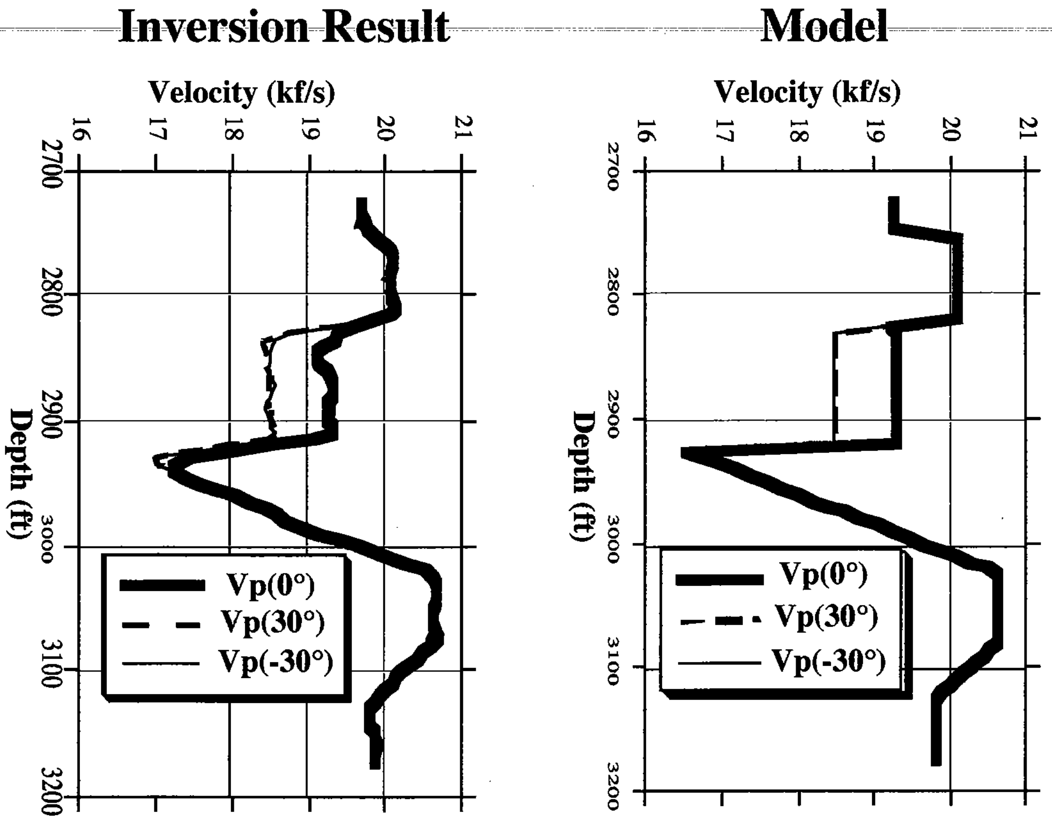

Figure 6: Profile of q*P*-velocity parameters, equation (23), after inversion of synthetic data set.

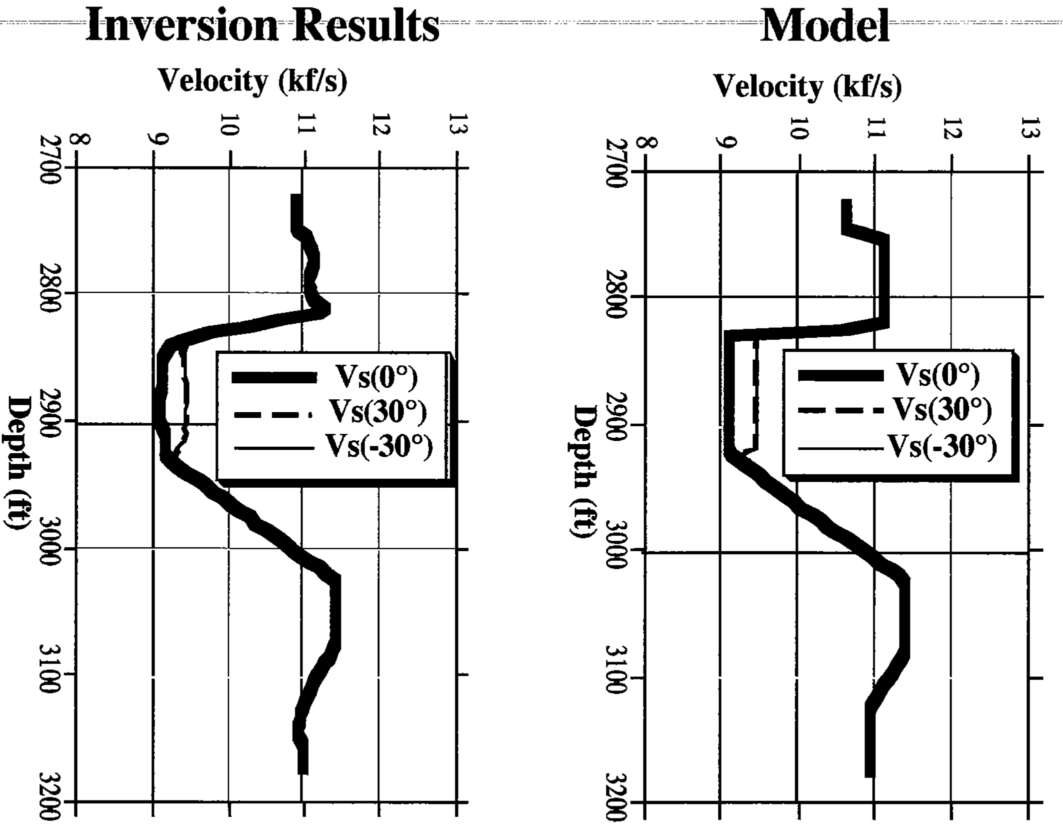

Figure 7: Profiles of the q*S*v-wave velocity parameters, equation (23), after the inversion of the synthetic data set.

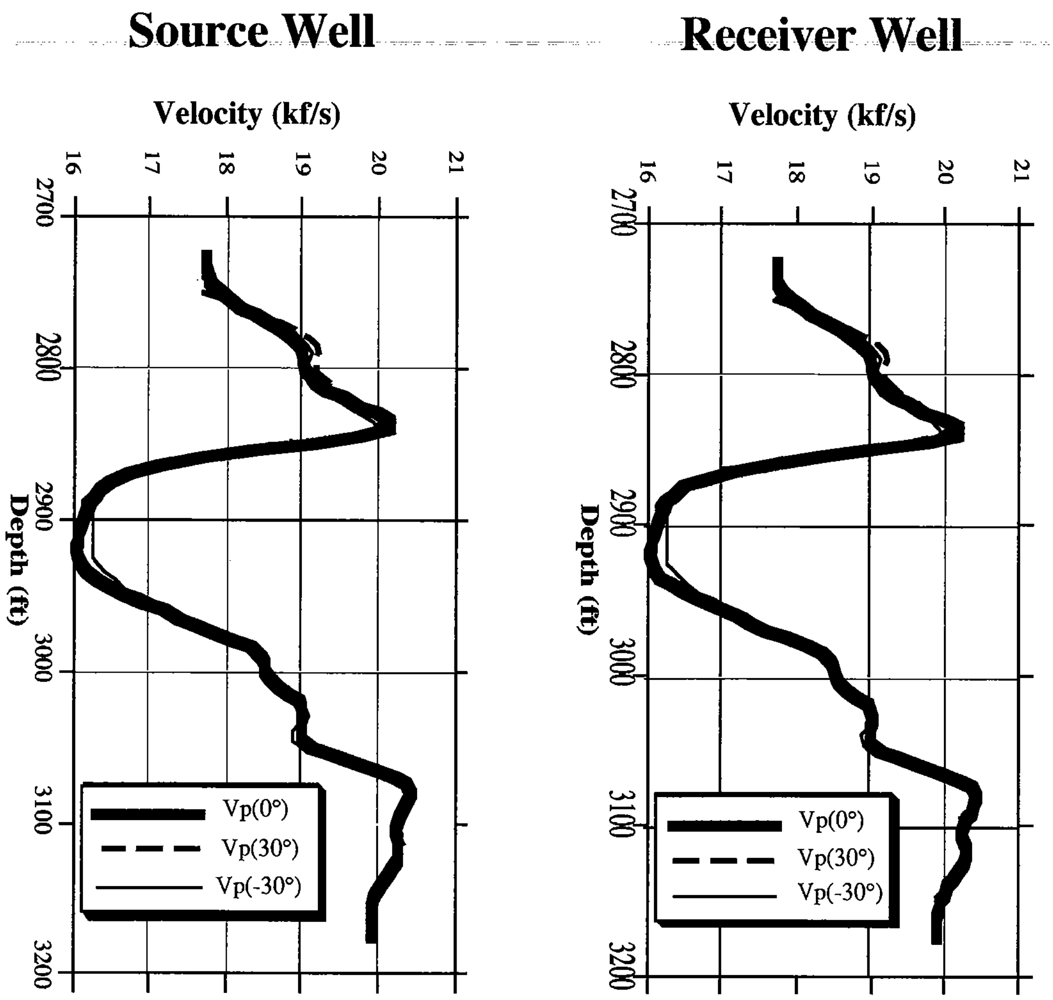

Figure 8: q*P*- velocity parameters, equation (23), after joint inversion of *P*- and *S*v-wave McElroy traveltimes.

PAPER G

CROSSWELL TRAVELTIME TOMOGRAPHY USING DIRECT AND REFLECTED ARRIVALS: PART 1: THEORY AND IMPLEMENTATION

Mark A. Van Schaack

ABSTRACT

In past STP consortia meetings I have outlined several approaches for integrating crosswell reflection imaging and traveltime tomography. The basis of these approaches has been to obtain reflection traveltimes from the processed wavefield data and to invert these traveltimes simultaneously with direct arrival traveltimes. In all these approaches I assumed the reflector depths were known or were solved through an iterative method of successive approximations using traveltime tomography and XSP-CDP mapping. This year I have modified my scheme for Crosswell Reflection Traveltime Tomography (CRTT) so that the 2-D velocity field and reflector depths are solved for simultaneously in a single traveltime inversion.

I present my inversion scheme in two papers. In this paper, Part 1, I discuss the theory and implementation of a combined direct and reflected arrival traveltime inversion. In Part 2, found in the next paper, I present several synthetic examples of this combined inversion and a field example using data collected from the McElroy field in west Texas.

INTRODUCTION

In previous years I have described methods for integrating traveltime tomography and reflection imaging (Van Schaack, 1994; Van Schaack and Lazaratos, 1993). The basis of these methods has been to extract traveltimes from the reflection events and to invert those simultaneously with direct arrival traveltimes to obtain a velocity model which is consistent with both. One fundamental shortcoming of these methods is that the depths of the reflectors, a function of offset between wells, are assumed to be known in the traveltime inversion. Unfortunately the actual reflector depths are never known *a priori* and the reflector depths used in these inversion have been only estimates.

One approach for obtaining better estimates of the reflector depths is to use interpretations of the crosswell reflection image to update the depths (Van Schaack, 1994). This requires an iterative approach of traveltime tomography with reflector depth estimates and XSP-CDP mapping using the new velocity field to obtain better estimates. Unfortunately, the traveltime tomography and XSP-CDP mapping must be repeated for each iteration making this scheme inefficient.

I have revised my approach to CRTT to explicitly solve for reflector depths in the inversion of direct and reflected arrival traveltimes. Reflector depths have been shown to be well resolved in synthetic studies using typical crosswell acquisition geometries (Bube and

Langan, 1995). In fact, these synthetic studies predict errors in reflector depths on the order of only *inches*. I have confirmed this prediction with several synthetic studies discussed in Part 2 found in the next paper.

In this paper I describe the theory and implementation of my combined direct and reflected arrival traveltime inversion program where I simultaneously solve for a 2-D velocity field and reflector depths. I begin with a description of the basic theory and setup of the inverse problem followed by a more specific discussion of the parameterizations used in my inversion code. Next, I describe the forward modeling used in the inversion: raytracing and traveltime calculations. Finally, I discuss the details of the solution of the combined direct and reflected arrival traveltime inversion.

DIRECT AND REFLECTED ARRIVAL INVERSION: BASIC THEORY

Seismic traveltime tomography is typically a non-linear problem due to large variations of velocity within the Earth. Traveltime tomography is non-linear in the sense that the velocity field is required to calculate the raypaths which are used to solve for the velocity field. One procedure used to solve the non-linear tomography problem is the Gauss-Newton method (Marquardt, 1963). In the Gauss-Newton method the non-linear problem is linearized by using an initial estimate of the model parameters. The solution of the linearized problem is an updated estimate of the model parameters. This procedure is performed in an iterative fashion until some convergence criteria is finally reached; usually convergence is assumed when the difference between the updated solution and the initial estimate becomes negligible.

To describe how reflection traveltimes and reflector depths are added to the tomography problem I will focus on a single linearized step:

$$\mathbf{A}\,\mathbf{x} = \mathbf{t} \tag{1}$$

where **A** is the traveltime derivative matrix, **x** is the vector of model parameters, and **t** is the vector of observed traveltimes. The dimensions of **A** are m x n, where m is the number of traveltime observations and n is the number of parameters being calculated. Usually the matrix **A** is overdetermined so the problem is solved using least squares or some other norm. Also, since an estimate of **x** is used to define **A**, the problem typically is defined in terms of residual traveltimes ($\Delta\mathbf{t}$) and perturbations to the parameters ($\Delta\mathbf{x}$). To keep the explanations simple I limit the discussion in this section to the setup of Eqn. 1. Later in this paper I describe the solution of the actual inverse problem.

The exact form of **A** and **x** are related to how the model is parameterized. In order to be more specific about the setup of matrix **A** I use a simple model parameterization. One of the simplest ways to parameterize the slowness model is as rectangular constant slowness (1/velocity) cells. Figure 1 shows a simple numbering scheme for this constant slowness parameterization and how the values are stored in vector **x**. The values of matrix **A** are the derivatives of traveltime with respect to the model parameters, in this case slowness only. Each row of **A** corresponds to an individual raypath of a source-receiver pair. Each column in that row contains the contribution of a particular cell to the traveltime of that raypath. Only cells crossed by a ray have non-zero traveltime derivatives in the constant slowness cell parameterization and the value of the traveltime derivative is the length of the ray in that cell.

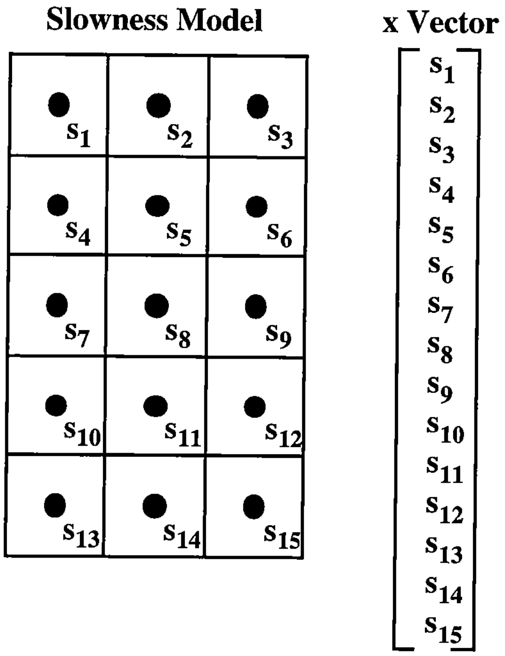

Figure 1: A simple parameterization of the slowness model and how it is stored as a vector. The slowness is defined for each node which is located in the center of the constant slowness cell.

Direct Arrival Traveltime Tomography

Direct arrival traveltime tomography is the most common method of processing cross-well data. Typically the only parameters being determined are the slowness (1/velocity) values of the model. By substituting **s** (slowness) for **x** we can rewrite Eqn. 1 as:

$$\mathbf{A}\,\mathbf{s} = \mathbf{t} \tag{2}$$

The number of elements in **s** equals the number of slowness elements (n) in the model and the number of elements in **t** (m) equals the number of traveltime observations.

Expressing Eqn. 2 in matrix form further clarifies the setup of the problem:

$$\begin{bmatrix} \frac{\partial t_1}{\partial s_1} & \frac{\partial t_1}{\partial s_2} & \frac{\partial t_1}{\partial s_3} & \cdots & \frac{\partial t_1}{\partial s_m} \\ \frac{\partial t_2}{\partial s_1} & \frac{\partial t_2}{\partial s_2} & \frac{\partial t_2}{\partial s_3} & \cdots & \frac{\partial t_2}{\partial s_m} \\ \cdots & \cdots & \cdots & \cdots & \cdots \\ \frac{\partial t_n}{\partial s_1} & \frac{\partial t_n}{\partial s_2} & \frac{\partial t_n}{\partial s_3} & \cdots & \frac{\partial t_n}{\partial s_m} \end{bmatrix} \begin{bmatrix} s_1 \\ s_2 \\ s_3 \\ \cdots \\ s_m \end{bmatrix} = \begin{bmatrix} t_1 \\ t_2 \\ \cdots \\ t_n \end{bmatrix} \tag{3}$$

From the system of equations shown in Eqn. 3 the linear equations corresponding to the various source-receiver traveltime observation can be more easily seen. The variable $\partial t_i / \partial s_j$ is the length of raypath i in cell j. The unknown s_j is the slowness of the j'th cell and t_i is the traveltime observation corresponding to the i'th raypath. Each single equation in the system of equations corresponds to a single traveltime observation. For example, the first raypath, seen in row 1 of the **A** matrix, defines the linear equation

$$\frac{\partial t_1}{\partial s_1} s_1 + \frac{\partial t_1}{\partial s_2} s_2 + \frac{\partial t_1}{\partial s_3} s_3 + \ldots + \frac{\partial t_1}{\partial s_m} s_m = t_1 \tag{4}$$

Now that the setup of direct arrival traveltime tomography has been defined I will describe how reflection traveltimes can be added to the inversion.

Combined Direct & Reflected Arrival Tomography

In my past implementations of CRTT I assume the locations of the reflectors are known so the only parameters solved for in the inversion are the model slowness values. The addition of the reflection traveltime data to the inversion in this case is very simple. No parameters are added to the **x** vector so **s** = **x** as in Eqns. 2 & 3. The only change is the addition of a row to **A** and **t** for each reflection traveltime and its associated raypath. Since the reflector location is known the only parameters that can influence the reflection traveltime are the slowness values of the cells through which the raypath passes. So, for each reflection traveltime, a linear equation in the form of Eqn. 4 can be added to the linear system of equations. Once the linear system is defined the inversion can be performed in the same manner as if only direct arrivals were being used.

To solve for model slowness and reflector depths simultaneously both **A** and **x** must be modified. Although I use a more general description of the reflectors in the CRTT program I use flat reflectors in this discussion to describe how Eqns. 3 & 4 are modified. Flat reflectors can be fully described by one parameter, depth. I use the notation Zr_j to signify the depth of reflector r_j. For each reflector that traveltime picks are available an additional parameter is added to **x**. Corresponding to each parameter added to **x**, an additional column is added to **A**. In Eqn.5 I show one way to modify the linear set of equations shown in Eqn. 3 to include reflection traveltimes and solutions for reflector depths.

The **A** matrix in Eqn. 5 has been assembled with rows related to direct arrival traveltimes placed in the top part and rows related to reflected arrival traveltimes placed in the bottom part. A new term has been introduced in the **A** matrix, $\partial t_i / \partial Zr_j$. This term is the derivative of the traveltime with respect to changes in the reflector depth. In Eqn. 5 I assume a parameterization where slowness and reflector depths are decoupled. For this reason $\partial t_i / \partial Zr_j$ is always zero for direct arrival raypaths. I also ignore raypaths which contain more than one reflection so there is only one non-zero reflector derivative for each reflected raypath.

$$\begin{array}{r|cccccccc|}
 & \frac{\partial t_1}{\partial s_1} & \frac{\partial t_1}{\partial s_2} & \frac{\partial t_1}{\partial s_3} & \cdots & \frac{\partial t_1}{\partial s_m} & 0 & \cdots & 0 \\
\text{Direct arrival raypaths} & \cdots & \cdots & \cdots & \cdots & \cdots & 0 & \cdots & 0 \\
 & \frac{\partial t_{n1}}{\partial s_1} & \frac{\partial t_{n1}}{\partial s_2} & \frac{\partial t_{n1}}{\partial s_3} & \cdots & \frac{\partial t_{n1}}{\partial s_m} & 0 & \cdots & 0 \\
 & \frac{\partial t_{n2}}{\partial s_1} & \frac{\partial t_{n2}}{\partial s_2} & \frac{\partial t_{n2}}{\partial s_3} & \cdots & \frac{\partial t_{n2}}{\partial s_m} & \frac{\partial t_{n2}}{\partial Zr_1} & \cdots & 0 \\
\text{Reflected arrival raypaths} & \cdots & \cdots & \cdots & \cdots & \cdots & \cdots & \cdots & \cdots \\
 & \frac{\partial t_n}{\partial s_1} & \frac{\partial t_n}{\partial s_2} & \frac{\partial t_n}{\partial s_3} & \cdots & \frac{\partial t_n}{\partial s_m} & 0 & \cdots & \frac{\partial t_n}{\partial Zr_r}
\end{array}
\begin{bmatrix} s_1 \\ s_2 \\ s_3 \\ \cdots \\ s_m \\ Zr_1 \\ \cdots \\ Zr_r \end{bmatrix}
=
\begin{bmatrix} t_1 \\ \cdots \\ t_{n1} \\ t_{n2} \\ \cdots \\ t_n \end{bmatrix}
\qquad (5)$$

Summary of Basic Theory

In this section I have described the basic setup of a linear set of equations for direct arrival tomography and combined direct and reflected arrival tomography. The exact setup depends on the parameterization used in the inversion and on any regularization added to the system. In the next several sections I describe in detail the parameterization and regularization used in my inversion code and the approach I use for solving the non-linear inversion problem.

PARAMETERIZATION OF THE MODEL

A number of issues influence the choices made in parameterizing the CRTT inversion. One issue is accuracy. For example, describing velocity as a 1-D function of depth leads to inversion errors for data sets collected in areas where lateral velocity variations are present. Parameterizing the problem allowing velocity to vary in 2-D may reduce inversion errors but leads to the issue of problem size. Invariably, increasing the number of parameters used to define the model will increase the size of the inversion. Potentially this may lead to a problem which is overparameterized. In addition, a large inverse problem may exceed the capacity of the computer hardware in the areas of memory or speed.

In my current CRTT program I have focused most heavily on parameterizing the model to accommodate the features found in STP data sets and the limitations of STP computer hardware. The primary features I have attempted to accommodate in the current version of my traveltime inversion are:

- 2-D isotropic velocity variations
- Deviated source and receiver wells
- Dipping, non-linear, and/or discontinuous reflector interfaces

In later versions I hope to accommodate additional parameters such as anisotropy and depth statics.

Slowness

In my current version of CRTT I parameterize the model using constant slowness cells. I do this for two reasons: to maintain simplicity and to minimize memory requirements. Simplicity is maintained since the inverse problem is defined using the setup shown in Eqn. 5. The traveltime derivative, $\partial t_i / \partial s_j$, can be calculated in a straightforward manner using this parameterization since it is simply the length of the i'th ray in the j'th cell.

The primary reason I use the constant slowness cell parameterization is that the amount of RAM memory required to solve the inverse problem is minimized. This reduction in memory results from the way the **A** matrix is stored. Any one ray will only intersect a small number of cells in the slowness model. Rather than wasting space storing all the zero traveltime derivatives the **A** matrix is preserved in a compact form where only the non-zero traveltimes derivatives are stored. For example, a horizontal ray traveling from one side to the other through the Fig. 1 model would have 12 zero and 3 non-zero traveltime derivatives. Only the 3 non-zero derivatives (and their indices) need be saved.

Another useful way to parameterize the slowness model is by using nodes similar to those in Fig. 1 but using them to define the value of the slowness at the corners of a cell. By interpreting the slowness within the cell this parameterization yields a continuous function of slowness in 2-D. One advantage of a continuous function of slowness is that it is much more stable in which to trace rays. Unfortunately, the memory requirements using this parameterization are approximately double those using the constant slowness cell parameterization. This increase results from the more complex traveltime derivatives that result from this parameterization. Instead of the 3 non-zero derivatives saved in our previous example we would be required to save 6 traveltime derivatives. This is because the slowness at any point in the model is a function of at least 3 nodes.

While the constant slowness cell parameterization requires much less memory to store the **A** matrix it poses a problem of how to trace rays through it effectively. I explain later in this paper the details of the raytracing and traveltime calculations. It should be restated that the primary reason I use the constant slowness cell parameterization in the inverse problem is to reduce memory requirements. Currently I am solving problems in synthetic models of approximately 650 ft x 1000 ft using 10 foot cells. Using approximately 60,000 direct and reflected arrival traveltimes results in a problem that requires almost 100 Mb of memory. The almost negligible errors found in the results of the synthetic studies detailed in Part 2 of my next paper suggest that the constant slowness cell parameterization is sufficiently accurate for these problems. Doubling the size of these problems by using a more accurate model parameterization would make them too large to solve using STP computers.

Reflectors

In the basic theory section of this paper I outlined the setup of the linearized inverse problem. This setup included solutions for reflector location defining the reflectors using a single parameter, depth. Unfortunately, this parameterization limits our model to simple flat reflectors. In my CRTT inversion code I have implemented a more general description of the reflectors. Each reflector is defined at a constant interwell interval across the slowness model. The interval between defined reflector locations is a variable set by the user.

Between defined reflector locations the reflector is described using a cubic spline curve. The advantage of using the cubic spline curve is that the 1st derivative of depth with respect to interwell offset is continuous. This improves the ability of the raytracer to link source and receivers for reflected raypaths.

Discontinuous reflectors are handled as independent reflecting horizons. The starting estimate for each reflecting horizon where traveltime picks are obtained is flat, continuous, and ranges from one side of the slowness model to the other. The actual extent of the reflector is determined following the inversion and is based on the ray coverage along the reflector. This approach for handling a discontinuous reflector does not provide any information about how the discontinuous reflector segments may be associated with each other. As with surface seismic imaging, determining fault locations and throw would be done in the interpretation phase.

FORWARD MODELING — RAYTRACING & TRAVELTIMES

I use an initial value raytracer and solve the two-point problem using an iterative approach. One drawback of the discrete constant slowness cell parametrization of the model is that it suggests raytracing by launching rays and calculating changes in trajectory at cell boundaries using Snell's Law. The resulting rays tend to be undesirable since they can make sharp changes in trajectory at each cell boundary which is unphysical in light of the assumptions made in justifying the use of ray theory in the first place. Unfortunately, as mentioned previously, parameterizing the slowness model using gradients leads to inverse problems which are too large to solve. To overcome this dilemma I have adopted a hybrid parameterization of slowness. An alternative to this approach would have been to limit the number of reflectors used in any given inversion.

I implement my hybrid parametrization of slowness starting with a model where slowness values are defined at node points on an evenly spaced grid. This gridding scheme is identical to that shown in Fig. 1. The difference is in how the value of slowness between nodes is allowed to vary. For raytracing, where better results are obtained with a continuous slowness field, I interpolate the slownesses as needed using bilinear interpolation. To calculate traveltimes and the traveltime derivatives required to set up the inverse problem I assume each node defines the center of a constant slowness cell.

While this hybrid scheme might seem fatally inconsistent, it roughly parallels the philosophy used in straight ray tomography. In straight ray tomography the calculation of the raypaths and the discretization of the slowness field (for purposes of setting up the inverse problem) are completely decoupled. Likewise, in this hybrid parameterization I obtain the most reliable raypaths using the best parameterization and then, ignoring the origin of the raypaths, use them in a model parameterization ideal for the inverse problem. Results of synthetic tests are presented in the next paper which support my opinion that this hybrid approach of model parameterization is effective and sufficiently accurate to obtain good results.

Initial Value Raytracing

I use a modified version of the initial value raytracer described by Harris (1992). This raytracer calculates raypaths in smoothly varying heterogeneous media. Raytracing is performed in a piece-wise fashion using the Runge-Kutta method to solve the ordinary differential equations defining the raypath.

I have modified the original code described by Harris to obtain slightly better performance. The original version calculates the slowness gradient at each point along the raypath from interpolated slowness values. To improve speed and efficiency I calculate the slowness gradient in the x and z directions at each node point prior to raytracing. I then obtain the gradient when required by interpolating the precalculated gradients. Bilinear interpolation is used both to interpolate slowness values to calculate the gradients and to interpolate the gradients themselves.

Calculating Reflected Raypaths

Reflected raypaths are calculated using the same initial value raytracing code as direct raypaths. Raypaths are calculated first for all direct arrivals then for all reflected arrivals, each reflector in turn. To obtain a reflected raypath for a particular reflector the ray is initially launched in the same fashion as a direct ray. The ray is monitored as it is calculated step by step until it crosses the reflecting horizon.

Once the ray crosses the reflecting horizon I calculate the exact reflection point. The reflection point calculation uses an iterative approach. First points on the reflector are obtained using the cubic spline approximation which bracket the possible intersection point. The reflector is assumed to be linear between these points and an intersection point with the raypath is found. This intersection point is used to calculate a new point on the reflector which replaces one of the two previous reflector points so the possible reflection point remains bracketed. This routine is performed iteratively until the intersection point is found to a user-defined tolerance.

The intersection point of the ray and the reflector is used to calculate the local incidence angle of the ray on the reflector. This angle is computed using the local raypath trajectory and a derivative function of the cubic spline curve to determine the local reflector dip. From this information a reflected trajectory is computed and the ray is re-launched. The ray then proceeds until it intersects the well or leaves the model.

The Two-Point Problem

The two-point problem is solved using a standard iterative approach which is a derivation of a code described by Langan et al. (1985). Rays are traced by receiver gather from receiver to source. I do this partly for philosophical reasons, to parallel the acquisition method, and partly to aid the calculation of traveltime residuals.

The first step in solving the two-point problem is to shoot a reference fan for the receiver gather under consideration. The rays are shot so as to provide a relatively uniform coverage at the source well. For each source-receiver pair for which a raypath is desired the algorithm finds rays from the reference fan which bracket the pair. Attempts are made to connect the source and receiver using the reference fan data as a starting point and a derivative-based search algorithm. Rays are shot from receiver to source until a ray is "captured" within a user defined "capture tolerance" or until a user-specified number of iterations is reached and the process is aborted.

It is possible to find more than one pair of reference rays bracketing the source. This will occur when triplications are present. To discriminate between these various rays the user sets a flag indicating whether rays of minimum traveltime or minimum path length are desired. A minimum path length raypath corresponds to the "energetic" direct arrival ray. The minimum traveltime raypath corresponds to the "first arrrival" raypath which may be associated with a head wave. Raypaths for all possible source-receiver combinations are calculated and the desired path is stored.

Calculating Traveltimes and Traveltime Derivatives

Once the raypath is obtained its traveltime is calculated using the constant slowness cell parameterization. The traveltime of raypath i, t_i, is calculated using this equation,

$$t_i = \sum_{j=1}^{m} l_{ij} s_j \tag{6}$$

In Eqn. 6 l_{ij} is the length of the i'th ray in the j'th cell and s_j is the slowness of the j'th cell.

The traveltime derivative, $\partial t_i / \partial s_j$, for the constant slowness cell parameterization is simply the length of the ray in the cell, l_{ij} from Eqn. 6. I currently use an estimate of this which is accurate to 1/10 of a foot. To obtain this estimate I resample the ray in 1/10 ft increments and count the number of segment endpoints which fall in each cell. The advantage of this approximation is speed and simplicity.

Calculating Reflector Depth Derivatives

Traveltime derivatives with respect to the reflector depth parameters, $\partial t_i / \partial Zr_j$, are calculated within the raytracing process. To calculate these derivatives I use the procedure derived by Bishop et al. (1985) with a modification to handle both upgoing and downgoing reflections. The expression for the traveltime depth derivative of reflector parameter j when the reflection point, (x_R, z_R), is located (in offset) between $x(r_j)$ and $x(r_{j-1})$ is

$$\frac{\partial t_i}{\partial Zr_j} = 2s(x_R, z_R)\cos\beta\cos\theta\left(\frac{x_R - x(r_{j-1})}{x(r_j) - x(r_{j-1})}\right) \tag{7}$$

In this equation, $s(x_R, z_R)$ is the local slowness at the reflection point, β is the dip of the reflector from the horizontal, and θ is the local angle of incidence of the raypath on the reflector.

SOLVING THE INVERSE PROBLEM

To solve the tomographic inverse problem I use a continuation approach described by Bube and Langan (1994). The basis of this approach is to add regularization to the inverse problem in the form of smoothing penalty terms. The non-linear system of equations is then solved with penalty weights fixed using the Gauss-Newton (G-N) method. After the non-linear problem is solved the penalty weights are relaxed and the non-linear problem is solved again. This procedure is repeated until an optimum solution is reached. In this approach a "continuation step" refers to the solution of a non-linear problem through a series of linearized steps while holding the smoothing penalties constant. A "G-N step" is the solution of a single linearized system of equations within the larger continuation step.

There are several advantages to this approach. One is that it provides regularization to the inverse problem. A second, related advantage, is that the optimum weights for the regularization do not need to be known *a priori.* A range of weights is run during the inversion so that initial iterations are dominated by the smoothing terms and later inversions are dominated by the data. Although a wide variety of smoothing terms are possible I have found, like Bube and Langan (1994), that penalty terms for the horizontal and vertical first spatial derivatives of slowness work well. Additionally, in my inversion, I have found that I must add a smoothing penalty term for the second derivative of the reflector depth with respect to offset. In the next sections I will further discuss the details of these penalty terms.

Regularization — Slowness Field

In my crosswell inversion I use smoothing penalty terms for horizontal and vertical spatial derivatives of slowness in the same manner as Bube and Langan (1994). Typically I weight the horizontal derivatives about four times heavier than the vertical derivatives although this is a user-defined variable. This preferential weighting is consistent with the lower resolution of the typical crosswell inversion in the horizontal direction. Also, there is typically less lateral variation in slowness than vertical variation in many geologic settings.

Regularization — Reflector Geometries

Because I allow the possibility of reflectors which do not extend completely from one well to the other there must be regularization added to the solution of the reflector depths. The main reason regularization is required is because of the cubic spline parameterization of the reflectors. If, for example, a reflector only extends half way between the wells only about half of the reflection depth derivatives for that reflector will be non-zero. The reflector depth parameters for which the depth derivatives are always zero lie in the null space of the model. The least-squares solver used in my program will not provide any perturbations to those parameters.

In a CRTT inversion containing discontinuous reflectors there will exist adjacent reflector points where one is updated during the inversion and the other remain unmodified since it lies in the null space of the inversion. The unfortunate side effect of this is that the cubic spline solution across this discontinuity will vary wildly. Even worse, these wild variations will not be confined to the area of the discontinuity. Once a reflector geometry acquires these sharp oscillations it becomes difficult to link rays through this reflector.

To solve this problem I have added a smoothing penalty term to the inversion to minimize second derivative variations of the reflector depth with respect to horizontal offset. The effect of this penalty term on discontinuous reflectors is to preserve the slope of the reflector when no other information is present. Like the smoothing penalty terms applied to the slowness field, I decrease the weight of this reflector penalty term at the beginning of each continuation step. I have found in synthetic examples shown in my next paper that the weight of the reflector second derivative penalty term need not be very strong to maintain the stability of the reflector solutions.

Problem Setup

The least-squares solution of the linearized G-N step is the minimum of

$$\|\mathbf{A}\delta\mathbf{x}-\delta\mathbf{t}\|^2+\mathrm{c}_h\|\mathbf{D}_h\mathbf{x}\|^2+\mathrm{c}_v\|\mathbf{D}_v\mathbf{x}\|^2+\mathrm{c}_z\|\mathbf{D}_z\mathbf{x}\|^2 \tag{8}$$

In Eqn. 8, **A** is the matrix of derivatives of the traveltime with respect to each of the parameters of the model. In this case, **A** contains derivatives of traveltimes with respect to the slowness in each cell and derivatives of traveltime with respect to the depth of the reflectors. The vector $\delta\mathbf{t}$ contains the traveltime residuals, e.g. the differences between traveltimes calculated using the starting model $\mathbf{x}^k$ and traveltimes observed in the experiment:

$$\delta\mathbf{t} = \mathbf{t}(\mathbf{x}^k)-\mathbf{t}_{obs} \tag{9}$$

The Eqn. 9 the vector, $\delta\mathbf{x}$, is the perturbation to the starting model $\mathbf{x}^k$ required to minimize Eqn. 8. The result of the *k*'th G-N step is the $k+1$'th updated model, $\mathbf{x}^{k+1}$, where

$$\mathbf{x}^{k+1} = \mathbf{x}^k+\delta\mathbf{x} \tag{10}$$

The remaining terms in Eqn. 8 are the smoothing penalty terms. The constants c_j are the weights of the various penalty terms relaxed prior to the beginning of each new continuations step. The matrix operators $\mathbf{D}_j$ are used to calculate the derivatives used in the smoothing penalties and are constant through the entire inversion.

The final version of the linearized system of equations solved in the CRTT inversion is

$$\begin{bmatrix} \cdots & \dfrac{\partial t_i}{\partial s_j} & \cdots & 0 \\ \cdots & \dfrac{\partial t_i}{\partial s_j} & \cdots & \dfrac{\partial t_i}{\partial Zr_k} \\ \cdots & \sqrt{\mathrm{c}_h}\mathbf{D}_h & \cdots & 0 \\ \cdots & \sqrt{\mathrm{c}_v}\mathbf{D}_v & \cdots & 0 \\ \cdots & 0 & \cdots & \sqrt{\mathrm{c}_z}\mathbf{D}_z \end{bmatrix} \begin{bmatrix} \cdots \\ \delta s_m \\ \cdots \\ \delta Zr_r \end{bmatrix} = \begin{bmatrix} \delta t_{dir} \\ \delta t_{ref} \\ \sqrt{\mathrm{c}_h}\mathbf{D}_h(s_m-\mathrm{C}_{start}) \\ \sqrt{\mathrm{c}_v}\mathbf{D}_v(s_m-\mathrm{C}_{start}) \\ -\sqrt{\mathrm{c}_z}\mathbf{D}_z Zr_r \end{bmatrix} \tag{11}$$

In Eqn. 11 the constant C_{start} provides the user the ability to drive the derivatives toward an input slowness model or towards flatness (when C_{start} is homogeneous). I typically initialize C_{start} to be homogeneous and equal the average slowness of the data set.

I have broken up the **A** matrix into 5 distinct parts in Eqn. 11. Each distinct part of **A** is designated by a row. The first row represents derivatives related to direct arrivals only. Notice in the first row that the derivatives of traveltime with respect to reflector depths are zero as you would expect for non-reflected raypaths. The second row represents all reflected arrival raypaths which have both slowness and depth derivatives. The next three rows are the smoothing penalty terms.

Finally, to keep the penalty terms properly balanced they are normalized by the Frobenius norm of subsets of the **A** matrix. The values c_h and c_v are calculated by taking the current penalty weight and scaling it by the square of the Frobenius norm of the traveltime derivatives with respect to slowness. The value c_z is scaled by the square of the Frobenius norm of the traveltime derivatives with respect to depth.

CONCLUSIONS

In this paper I present an approach to reflection and direct arrival traveltime tomography. This approach solves for a 2-D isotropic slowness model and reflector depths parameterized using cubic splines. The slowness model and reflector depths are calculated by minimizing the difference between both direct arrival traveltimes and reflected arrival traveltimes to selected reflectors, and traveltimes calculated tracing rays through the model.

The CRTT program described in this paper uses a continuation approach for solving the non-linear tomography problem. Smoothing penalty terms are added to the inversion providing regularization for both the slowness and reflector solutions. The inverse problem is solved in a series of continuation steps where the smoothing penalty terms are slowly relaxed. Each continuation step consists of a number of linearized Gauss-Newton steps solving the non-linear inverse problem while the weights of the smoothing penalty terms are held constant. Solutions of early continuation steps provide a smooth slowness model and nearly linear reflectors. In later solutions the slowness model is allowed more 2-D variations while the reflectors are allowed to model increasingly non-linear fluctuations.

In this paper I have provided the background theory of a combined direct and reflected arrival traveltime inversion and details of my implementation of this theory. In my next paper I provide the results of several synthetic studies and one field data study.

ACKNOWLEDGEMENTS

I would like to thank Ken Bube and Robert Langan for providing me with their traveltime inversion code and helpful guidance. I would also like to thank Jesse Costa for his invaluable assistance in providing me insights to the inversion process. I would finally like to thank Jerry Harris and the sponsors of the STP consortia for providing support for this work

REFERENCES

Bishop, T. N., Bube, K. P., Cutler, R. T., Langan, R. T., Love, P. L., Resnick, J. R., Shuey, R. T., Spindler, D. A., and Wyld, H. W., 1985, Tomographic determination of velocity and depth in laterally varying media: Geophysics, **50**, 903–923.

Bube, B. P., and Langan, R. T., 1995, Resolution of crosswell tomography with transmitted and reflected traveltimes: STP-**6**, Paper I.

Harris, J. M., 1992, Initial value raytracing in smoothly varying heterogeneous media: STP-**3**, Paper I.

Langan, R.T., Lerche, I., and Cutler, R.T., 1985, Tracing of rays through an heterogeneous media: Am accurate and efficient procedure: Geophysics, **50**, September.

Lazaratos, S. K., 1993, Cross-well reflection imaging: Ph.D. thesis, Stanford University.

Lazaratos, S. K., Harris, J. M., Rector, J. W., and Van Schaack, M. A., 1995, High-resolution crosswell imaging of a west Texas carbonate reservoir: Part 4—Reflection imaging: Geophysics, **60**, 702–711.

Marquardt, D. W., 1963, An algorithm for least-squares estimation of non-linear parameters: Soc. of Industr. Appl. Math., **11**, 431–441.

Van Schaack, M. A. and Lazaratos, S. K., 1993, An approach to interval velocity analysis for crosswell reflection imaging using reflection traveltimes: STP-**4**, Paper F.

Van Schaack, M. A., 1994, Integrated crosswell imaging: Reflection tomography—Synthetic examples: STP-**5**, Paper A.

CROSSWELL TRAVELTIME TOMOGRAPHY USING DIRECT AND REFLECTED ARRIVALS: PART 2: EXAMPLES

Mark A. Van Schaack

ABSTRACT

The predicted resolution of reflector depth for an inversion of crosswell seismic data using direct and reflected traveling data is *several inches*. This prediction is for a survey with an acquisition geometry similar to the ~180 ft McElroy data set. The predicted reflector resolution for an inversion of data collected in a ~600 ft survey is 0.5-2.5 ft. I have run combined direct and reflected arrival traveltime tomography on 3 synthetic surveys and 1 field data survey and have obtained results very near to these theoretical predictions.

Resolution of reflector depths is very high in the crosswell traveltime inversion while velocity resolution remains mediocre. The extent to which reflector depths can be recovered suggests that direct and reflected arrival tomography may be an ideal tool for obtaining a velocity model and reflector geometries suitable for accurately mapping crosswell reflection data.

INTRODUCTION

In my first paper, Crosswell Traveltime Tomography using Direct and Reflected Arrivals—Part 1: Theory and Implementation, I presented an approach for using direct and reflected arrival traveltimes to solve for a 2-D slowness field and reflector depths simultaneously. While the potential of surface seismic reflection tomography has been heavily studied in the recent past, (Bishop et al., 1985; Ivansson, 1986; Stork, 1988; Bube et al., 1989) little work has been done in the area of crosswell reflection tomography. Partly this is because it has been only recently that reflections have been successfully extracted from crosswell data (Lazaratos, 1993; Lazaratos et al., 1995).

Calnan and Schuster (1989) compared direct arrival and combined direct and reflected arrival tomography in a theoretical study. This study was performed using straight rays, horizontal reflectors, and vertical boreholes. The conclusion of this study was that the primary benefit of direct and reflected arrival tomography was that it could yield a finer velocity resolution than allowed by direct arrival tomography.

More recently, resolution analyses were performed by Bube and Langan (1995) using acquisition parameters based on the 1991 and 1993 McElroy Reservoir Geosciences Project experiments (Harris et al., 1995). The motivation of these analyses was to obtain information on how well reflector depths and velocity might be resolved in a combined direct and reflected arrival inversion. Two synthetic problems were formulated: one based on the ~180 ft McElroy profile, and the other based on the ~600 ft profile. An extraordinary result of these studies was that estimated errors in reflector depths were only a *few inches* for the 180 ft survey and 0.5–2.5 ft for the 600 ft survey. Another observation, consistent with those made in surface seismic tomography, was that good resolution of reflector depths could be expected in spite of mediocre velocity resolution.

In this paper I present the results of several combined direct and reflected arrival inversions. I primarily focus on the ability of these inversions to recover reflector depths accurately in these studies. Two of my synthetic studies are designed to test the ability of my program to handle nonlinear reflectors and discontinuous reflectors. In the last study I invert an *S*-wave direct and reflected arrival traveltime data set collected from the McElroy 188 ft offset profile. To aid the analysis of the field inversion I have created a synthetic data set using many of the field experiment's parameters and a velocity model with a structure similar to the field geology. I invert this data set using identical parameters as the field data set inversion.

FORWARD MODELING OF SYNTHETIC DATA SETS

The synthetic data sets found in this paper were all calculated using an eikonal-based forward modeling program that I have developed. This modeler uses a derivation of the finite-difference scheme introduced by Mo (1994). There are several advantages to using this approach to create synthetic crosswell reflection data sets. One advantage is that no raytracing or raypaths are required, making it very fast. Another advantage is that reflection traveltimes can be calculated very easily for arbitrary reflection surfaces. Another useful feature, related to the studies contained in this paper, is that this forward modeling program is different from the raytracer used in the tomography program. Other than both programs being based on ray theory, their approaches to calculating traveltimes are quite different. This should provide a better test of the effectiveness of the direct and reflected arrival tomography code.

Calculating Direct Arrival Traveltimes

Calculating direct arrival traveltimes is accomplished in one step using the finite-difference eikonal code. For each receiver location, a traveltime map is generated (I prefer "shooting" from receiver to source). Receiver to source traveltimes are read from the traveltime map location which coincides with the source. Bilinear interpolation is used when the source location does not reside on a grid node. The traveltimes are recorded for all source locations after which the code increments to the next receiver location. All receivers are "shot" in turn until the entire direct arrival traveltime data set has been acquired

Calculating Reflected Arrival Traveltimes

The first step in calculating reflection traveltimes is to compute traveltime maps for the source and receiver of interest. These source and receiver maps are then added together to create a single traveltime map. A fundamental characteristic of the combined map is that the traveltime stored at each node is the total traveltime from the source, to the node, and to the receiver. Once the combined traveltime map has been obtained, reflection traveltimes can be extracted from it.

The next step is to interpolate the reflector locations within the image area at a fine interval. Reflectors are defined by their depths recorded at several points across the image. The location of the reflector between these defined points is determined using a cubic spline interpolation method. This method is identical to that used in the raytracer described in my previous paper. It is necessary to interpolate the reflector position since it may be defined with as few as two points. The interpolation is usually done at the same interval as the image's node spacing in the x direction.

Once the reflector coordinates are defined, traveltimes are interpolated from the combined traveltime map for each of the points along the reflector. The reflection traveltime from source, to that reflector, and to the receiver, is simply the minimum traveltime along the reflector. Potentially the reflection point does not occur within the bounds of the image if the minimum traveltime is found at a reflector endpoint. When this occurs I record a null value for the source-receiver-reflector combination.

Reflection traveltimes can be found for any number of reflectors for the source-receiver combination used to create the combined traveltime map. To minimize computations I calculate reflection traveltimes for all reflectors before calculating a traveltime map for the next source-receiver pair. A NOTE ON EFFICIENCY: If sufficient computer memory exists traveltime maps for all source and receiver locations can be calculated beforehand. From this collection of maps a combined map can be created for any source-receiver combination simply by adding the appropriate source and receiver maps.

SYNTHETIC STUDY #1

The primary goal of the first synthetic study is to test the ability of direct and reflected arrival tomography to recover the geometries of straight and curved reflectors. I have created a simple model, shown in Figure 1, consisting of 3 layers and 4 reflectors. The layers are constant velocity although a mild 2-D filter has been run over the model to smooth the interfaces slightly.

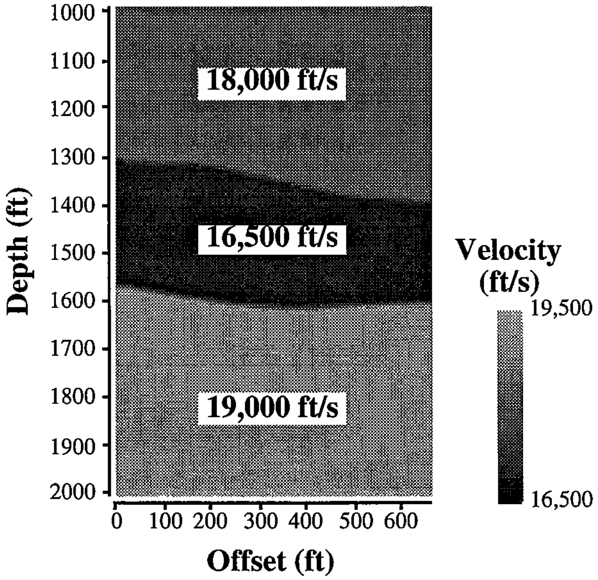

Figure 1: This figure shows the velocity distribution of model #1. The reflectors are defined by a cubic spline curve calculated from 8 evenly spaced points across the model.

The reflector definitions are shown in Table 1. As previously mentioned, the forward modeler interpolates between the defined reflector points using a cubic spline. In this example the top and bottom reflectors are linear and horizontal and reflectors 2 & 3 are curved, seen graphically in Fig. 1.

TABLE 1. Synthetic model #1 reflectors

Offset (ft)	**0.0**	**94.29**	**188.57**	**282.86**	**377.14**	**471.43**	**565.71**	**660.0**
Reflector 1	1003.0	1003.0	1003.0	1003.0	1003.0	1003.0	1003.0	1003.0
Reflector 2	1302.0	1310.0	1315.0	1335.0	1355.0	1375.0	1385.0	1392.0
Reflector 3	1569.0	1584.0	1600.0	1610.0	1615.0	1610.0	1607.0	1604.0
Reflector 4	1998.0	1998.0	1998.0	1998.0	1998.0	1998.0	1998.0	1998.0

Synthetic Study #1: Acquisition Geometry and Data Specifications

The synthetic survey is designed with 201 sources and 201 receivers spaced every 5.0 ft along the sides of the model shown in Fig. 1. The range of the sources and receivers is from 1000.0–2000.0 ft and the distance between the source and receiver wells is 660.0 ft. Direct and reflected arrival traveltimes were initially calculated for all source-receiver-reflector combinations in the forward modeling. In order to create a data set more closely resembling one that might come from the field, I edited these traveltimes by setting unlikely combinations to zero.

To prepare the direct arrival data set I zeroed traveltimes for source-receiver pairs at near and far offsets. Near offset traveltimes are often thought to be unreliable in field data sets due to head waves. For this test I muted traveltimes if the source and receiver were within 75 ft of each other in depth, approximately $\pm 6.5°$ about the horizontal. I also muted traveltimes with a source/receiver offset greater than ~940 ft, $\pm 55.0°$, in part to reduce the size of the inversion problem, and in part because far offset traveltimes can be difficult to pick.

There are several observations which I have used to edit the synthetic reflected arrival traveltimes. One is that reflections are most visible in processed ~600 ft offset surveys for angles of incidence ranging from approximately 40-65° (Lazaratos, 1993; Lazaratos, personal comm.). Another observation is that it is difficult to pick traveltimes of a single reflector for both up and downgoing reflections reliably. I edited reflection traveltimes on the basis of upgoing or downgoing, and for a range of Common Depth Point (CDP) elevations chosen to keep the incidence angles of the rays approximately 40-65°. In crosswell experiments the CDP elevation of a source/receiver pair is

$$\mathbf{CDP}_{\mathrm{elev}} = \frac{\mathbf{ELEV}_{\mathrm{rec}} + \mathbf{ELEV}_{\mathrm{sou}}}{2.0} \tag{1}$$

In Table 2 I indicate the edited non-zero reflected arrival traveltimes based on the direction of the reflection and the CDP range.

TABLE 2. Specifications of Example 1 reflection traveltime data

	Direction	CDP Range (ft)	# Traveltimes
Reflector 1	downgoing	1187.0–1390.0	6887
Reflector 2	downgoing	1500.0–1702.0	6456
Reflector 3	upgoing	1217.0–1421.0	6239
Reflector 4	upgoing	1609.0–1812.0	6501

Synthetic Study #1: Inversion and Results

I ran a direct and reflected arrival inversion on the synthetic data set starting with a homogeneous slowness model and flat reflectors defined by 8 nodes at 1000.0, 1347.0 1586.0, and 2000.0 ft. I set the initial horizontal smoothing penalty weight equal to the traveltime data weight and the vertical smoothing penalty to1/4th of the horizontal value. The initial value of the reflector second derivative smoothing penalty weight was 1/100th the horizontal weight at the beginning of the inversion. The horizontal and vertical smoothing penalty terms were relaxed an order of magnitude every 4 continuation steps and the reflector penalty term was relaxed an order of magnitude every 2 continuation steps.

The ideal, or "best", answer of this inversion is the result of continuation step 12. By this step the horizontal penalty term, the strongest of the three, has only 4% of the weight of the traveltime data. Traveltime residuals are ~58μs root-mean-square (rms) for the 24,327 reflected rays and ~28μs rms for the 33,993 direct arrival rays. Figure 2 shows the results of the velocity tomogram.The velocity tomogram recovers the homogeneous nature of the 3 zones reasonably well. The curved nature of the interfaces bounding the low velocity central layer is also seen in the tomogram although the interfaces themselves are a somewhat blurred.

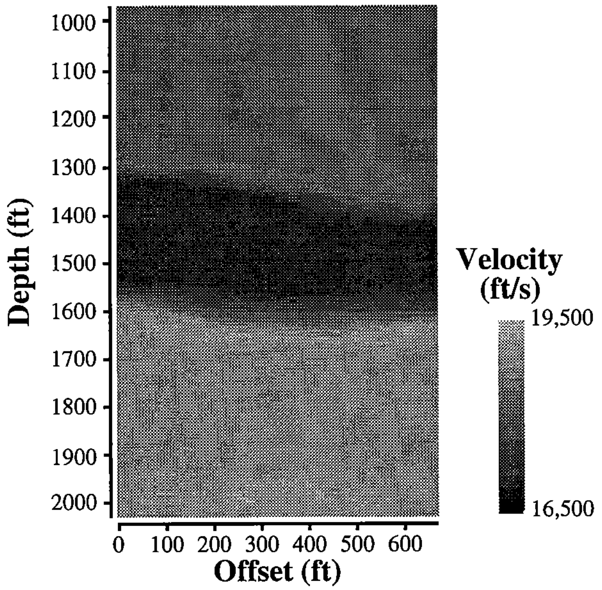

Figure 2: The velocity tomogram resulting from 12 continuation steps of a combined direct and reflected arrival traveltime inversion. Compare this result with the original velocity model used to create the synthetic data seen in Fig. 1.

The recovered reflector parameters, shown inTable 3, have distinctly higher resolution. Unfortunately, a direct comparison cannot be made between the parameters seen in Table 3 and those listed in Table 1. In spite of the fact that 8 parameters are used for each reflector description there is a slight difference in the offsets in the two parameter sets which can be noted across the top of each table. The difference is because the tomogram is 670.0 ft across while the source-receiver offset is 660.0 ft. The raytracer used in the inversion program requires the sources (on the right side of the model) to lie *within* the model so an extra pixel was added to the right of the model for the inversion.

TABLE 3. Example 1 reflector depth inversion results

Offset (ft)	**0.0**	**95.7**	**191.4**	**287.1**	**382.8**	**478.6**	**574.3**	**670.0**
Reflector 1	1002.7	1002.3	1002.1	1002.6	1002.8	1002.9	1002.8	1003.0
Reflector 2	1301.4	1308.9	1315.3	1334.8	1354.6	1373.9	1383.8	1392.3
Reflector 3	1569.7	1586.6	1603.1	1613.1	1617.9	1612.7	1609.4	1603.9
Reflector 4	1998.0	1998.5	1998.9	1998.5	1998.4	1998.5	1998.3	1998.0

While the errors in depth due to the slightly different offset are small, increasing from left to right, a more direct comparison of the recovered reflector depths and the model values has been assembled in Table 4. The recovered reflector depths seen in Table 3 have been interpolated using the cubic spline definition to the same offset values as the model.

The range of errors in the recovered reflector depths seen in Table 4 is -2.3–3.1 ft. The rms error of the recovered reflector depths is 1.4 ft. These errors basically confirm the theoretical predictions of Bube and Langan (1995) for a 600 ft tomographic inversion. This resolution of reflector depth seems quite remarkable considering the 10.0 ft constant slowness cell parameterization. The primary source of errors are reflectors 2 and 3. The calculated location of reflector 2 is uniformly shallow while reflector 3 is uniformly deep. This is a result of the direction of the reflection raypaths with respect to velocity contrast.

TABLE 4. Resampled* reflector depth inversion results and synthetic model #1 reflector depths

Offset (ft)	**0.0**	**94.29**	**188.57**	**282.86**	**377.14**	**471.43**	**565.71**	**660.0**
Ref.1 model	1003.0	1003.0	1003.0	1003.0	1003.0	1003.0	1003.0	1003.0
Ref.1 result*	1002.7	1002.3	1002.1	1002.6	1002.7	1002.9	1002.8	1002.9
Ref.2 model	1302.0	1310.0	1315.0	1335.0	1355.0	1375.0	1385.0	1392.0
Ref.2 result*	1301.4	1308.8	1315.0	1333.8	1353.4	1372.7	1383.2	1391.2
Ref.3 model	1569.0	1584.0	1600.0	1610.0	1615.0	1610.0	1607.0	1604.0
Ref.3 result*	1569.7	1586.3	1602.7	1612.7	1617.9	1613.1	1609.7	1604.7
Ref.4 model	1998.0	1998.0	1998.0	1998.0	1998.0	1998.0	1998.0	1998.0
Ref.4 result*	1998.0	1998.5	1998.9	1998.5	1998.4	1998.5	1998.3	1998.0

*The reflector inversion results have been interpolated using a cubic spline interpolation to obtain reflector depths for the same reflector x offsets as the original model so that a direct comparison can be made.

Reflection traveltimes obtained from reflector 3 are for upgoing raypaths. The ability of the inversion routine to locate exactly a reflector defined by a sharp interface is related to the ability of the inversion to define the interface itself. Since the velocity gradient in the vertical direction is somewhat smooth the reflector must be shifted slightly to compensate for the gradient. In the case of reflector 3, a low velocity zone overlies a high velocity zone and the raypaths travel primarily through low velocities. The smooth gradient causes the raypaths to travel through velocities which are a little too high near the reflector. This results in a calculated traveltime which is too low if the reflector is properly located. To compensate for this the reflector is shifted down slightly to lengthen the raypaths and increase the traveltimes. The same reflector would be shifted up slightly if the model consisted of a high velocity zone overlying a low velocity zone. This same reasoning applies to reflector 2 except that the direction of the correction is opposite since the location of this reflector is calculated using downgoing rays.

SYNTHETIC STUDY #2

I designed the second example to test the ability of the direct and reflected arrival traveltime inversion to recover reflector geometries when the reflectors are discontinuous. The model used to generate the direct and reflected arrival traveltimes is shown in Figure 3. This model includes 5 dipping layers that have been thrown offset by a steeply-dipping normal fault. I have also included a low velocity layer near the bottom of the model with a velocity contrast across the fault. This situation is designed to mimic a possible field experiment where the target exists near the bottom of the survey. This is a situation where traditional direct arrival tomography has poor lateral resolution.

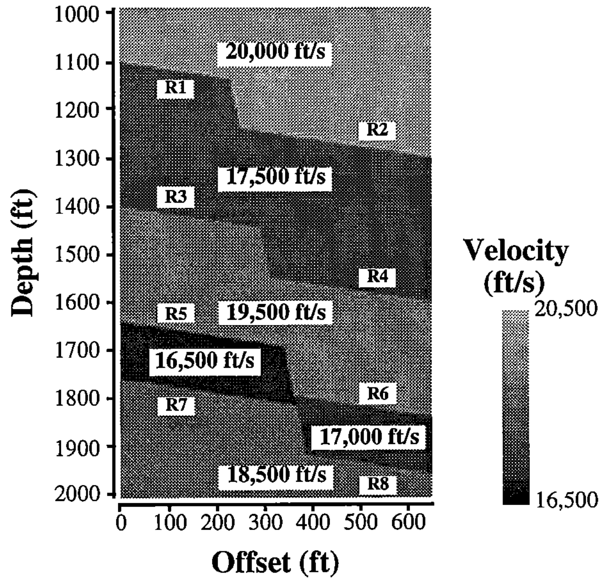

Figure 3: Velocity model used to generate traveltime data for synthetic study #2. Reflectors are numbered from top to bottom. Discontinuous reflectors are defined by the individual segments. Reflector depths can be found in Table 5.

The dimensions of the model shown in Fig. 3 are identical to those of the first synthetic model (Fig. 1) except that the new model is 650.0 ft across rather than 660.0 ft. The interfaces are linear, except at the fault point, and dip uniformly at 8.75° from the receiver well to the source well. Each reflector can be completely described by the point at which it intersect a well and the point it intersects the fault. The broken reflectors have been numbered separately to maintain a consistency with the inversion routine which solves for the broken pieces of a discontinuous reflector as separate individual reflectors. The geometries of the reflectors are given in Table 5.

TABLE 5. Synthetic model #2 reflector data

	Receiver Well intersection depth (ft)	Fault Plane intersection point x,z (ft)	Source Well intersection depth (ft)
Reflector 1	1100.0	227.0, 1134.9	null
Reflector 2	null	247.6, 1238.1	1300.0
Reflector 3	1400.0	288.9, 1444.4	null
Reflector 4	null	309.5, 1547.6	1600.0
Reflector 5	1640.0	338.4, 1692.1	null
Reflector 6	null	359.0, 1795.2	1840.0
Reflector 7	1760.0	363.2, 1815.9	null
Reflector 8	null	383.8, 1919.0	1960.0

Synthetic Study #2: Acquisition Geometry and Data Specifications

The source and receiver acquisition geometry of synthetic survey #2 is almost identical to that of survey #1 except that the source-receiver offset is 650.0 ft. There are 201x201 sources and receivers spaced evenly every 5.0 ft from 1000.0–2000.0 ft. As with survey #1, traveltimes were initially calculated for all source-receiver-reflector combinations and then edited to provide a more realistic traveltime data set. Direct arrival traveltimes have been prepared in a slightly different manner in this example. All near offset direct arrival traveltimes have been kept for the inversion. Far offset traveltimes are limited to ±50.0°, about 775 ft in offset. Reflected traveltime arrivals have been edited in much the same way as in the Study #1. The reflection data for each reflector are edited to include traveltimes of either upgoing or downgoing events. The traveltimes are further edited to provide a reasonable range of incidence angles. Table 6 provides information on the traveltimes used for the various reflectors.

TABLE 6. Specifications of Example 2 reflection traveltime data

	Direction	# Traveltimes
Reflector 1	downgoing	1495
Reflector 2	downgoing	6976
Reflector 3	downgoing	3841
Reflector 4	upgoing	4091
Reflector 5	upgoing	5290
Reflector 6	upgoing	5060
Reflector 7	upgoing	6471
Reflector 8	upgoing	2811

Synthetic Study #2: Inversion and Results

I ran a direct and reflected arrival inversion on synthetic data set #2 starting with a homogeneous model with 10.0 ft cells and flat reflectors each defined by 34 nodes. The initial reflector depths for reflectors 1-8 respectively were: 1090.0, 1290.0, 1395.0, 1610.0, 1755.0, 1850.0, 1870.0, and 1970.0 ft. Since part of the information desired from the inversion is an estimate of the reflector extent the reflectors were parameterized using a higher number of nodes. From the final result, the segments of each reflector that are subject to reflections are interpreted to define the reflector extent.

The initial values of the smoothing penalties weights in this inversion differ slightly from the values used in Study #1. Like Study #1, the initial weight of the horizontal smoothing penalty equals the weight of the traveltime data and the vertical smoothing penalty weight is 1/4th of the horizontal weight the entire inversion. But, in this inversion, the initial reflector second derivative smoothing penalty weight *equals* the horizontal weight. The reflector smoothing was initialized at a higher value in this example to help stabilize the larger number of nodes used to define each reflector. Another difference in this inversion is that *all* smoothing penalty terms were relaxed an order of magnitude every 4 continuation steps.

The ideal, or "best", answer is the result of continuation step 10. Traveltime residuals are ~108μs rms for the 33,884 reflected rays and ~120μs rms for the 37,873 direct arrival rays. Note in this example that the direct arrival traveltime residuals are slightly higher than the reflected arrival residuals. This result is due to an increased ratio of reflected traveltimes to direct arrival traveltimes and the inclusion of near-offset direct-arrival traveltimes which themselves have higher residuals.

The final tomogram is shown in Figure 4. Note that the resolution is somewhat low and similar to the result of Study #1. Although the resolution is low the existence of a fault can be seen clearly, especially at the bottom of the image. The different velocities of the thin layer near the bottom can also be identified in the image.

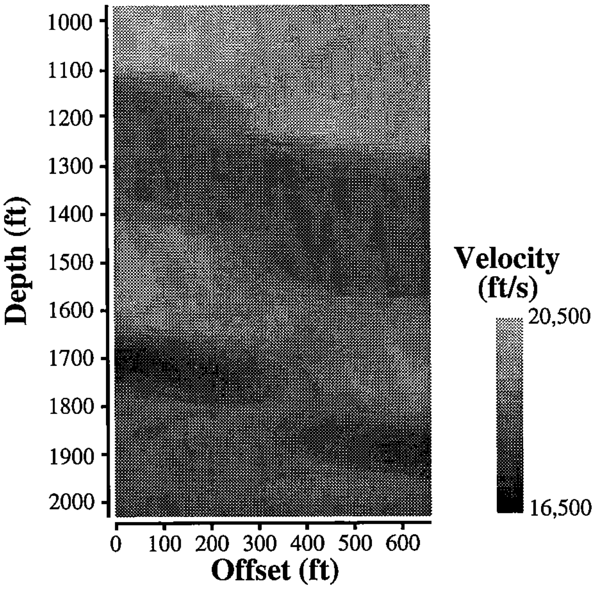

Figure 4: The resulting velocity tomogram obtained after 10 continuation steps of a combined direct and reflected arrival traveltime inversion. This result should be compared to the velocity model shown in Fig. 3 which was used to generate the traveltime data.

The reflector depth results obtained in this example are interpreted in a slightly different manner than in Study #1 although the inversions are run in much the same way. The lateral extent of the reflectors is never known *a priori* so each reflector is initially assumed to extend all the way across the model. After the inversion is complete an estimate of the lateral extent of the reflectors can be recovered based on the raypath coverage of each reflector segment. By using 34 nodes to describe the reflectors across the 660.0 ft model the distance between nodes is 20.0 ft. The coverage is maintained by keeping track of the number of non-zero derivatives of each reflector depth parameter. In this inversion the average number of non-zero derivatives for all reflector parameters is 490.6. I have set the cutoff for the number of non-zero parameters to qualify a segment as being "covered" as 6. This cutoff value affects only 6 reflector segments. To aid in the visualization of the reflector recovery I have plotted the "covered" reflector solutions in Figure 5 as an overlay to the original model.

Figure 5 shows that direct and reflected arrival traveltime inversion locates the reflectors fairly well in depth and also in extent. The largest errors in depth appear in reflector 1, 2, 7, and 8. A similar mispositioning phenomena to that seen in Study #1 can be seen. Reflectors 1 and 2, determined by downgoing reflections, with a high velocity layer overlying a low velocity layer, are too shallow just like reflector 2 in Study #1. Reflectors 7 and 8, determined by upgoing reflectors, with a low velocity layer overlying a high velocity layer, are too deep just like reflector 3 of the first study. The magnitude of the errors is a bit larger this time though.

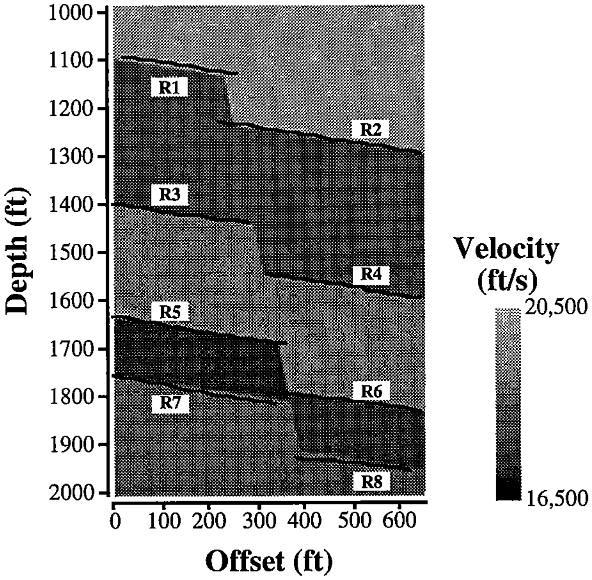

Figure 5: The reflector depth locations obtained from the traveltime inversion plotted on top of the original velocity model used to generate the synthetic data. The reflectors are actually defined across the entire velocity image but only reflector parameters with a significant number of non-zero depth derivatives have been plotted.

To provide a graphic display of the reflector depth errors they have been plotted in Figure 6. The extent of the reflector depth errors is from about -10–12 ft, a bit larger than found in the previous example. Note that largest errors occur in reflectors near the top and bottom of the image. There are several possible explanations to be investigated at a later date. First, the top and bottom layers are covered by relatively few direct arrival raypaths. This may make it more difficult to calculate a sharp velocity gradient at these interfaces. Second, this inversion ran only 10 continuation steps before it became unstable. This means the smoothing penalty terms are still relatively strong compared to Study #1, preventing sharp velocity gradients. Finally, the forward modeler used to calculate the direct arrival traveltimes is more prone to errors near sharp, nearly-horizontal interfaces. It may be that there are significant errors in these traveltimes preventing the inversion from correctly calculating the sharp interfaces.

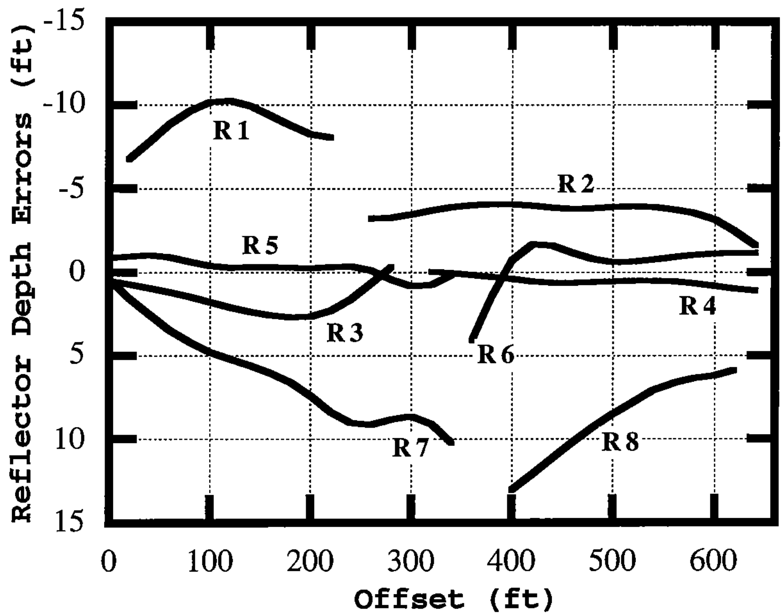

Figure 6: The difference between the reflector depths obtained from the traveltime inversion and the actual model depths shown if Fig. 5. Note that the largest errors are in the reflector depths near the top and bottom of the model.

COMBINED STUDY #3

Combined study #3 consists of a field data traveltime inversion and a synthetic data traveltime inversion. The field data set is from the McElroy Reservoir Geosciences Project (MRGP) (Harris et al., 1995). Reflected and direct arrival *S*-wave traveltimes have been collected from the near offset (~188 ft) survey between wells McElroy 1202 and McElroy 1068. The data used are actually a subset of the entire data set to keep the traveltime inversion problem within the capabilities of the computer hardware.

The synthetic part of this study is designed to parallel the field inversion in processing, source/receiver acquisition geometry, and model characteristics. The goal is to obtain an estimate of the resolution of the field survey by studying the results of an inversion on a synthetic data set. The synthetic data are calculated using a velocity model containing many of the features of the field geology. Figure 7 shows the model used to create the synthetic data. This model is based on a smoothed version of the receiver well (McElroy 1202) *S*-

wave sonic log, seen on either side of the model in Fig. 7, and information on the reflector geometries at the McElroy site.

The geometries of the reflectors at the McElroy site are based on an interpretation of the traveltime picks and the crosswell reflection image (Lazaratos et al., 1995). To interpret reflector geometries from the field data set requires reflection traveltimes for reflectors R1–R9, seen in Fig. 7, and the direct arrival traveltimes. The intersection of the direct and reflected arrivals provides an estimate of the intersection of the reflecting horizons and the wells. An analysis of the crosswell reflection image shows that although the picked reflectors are dipping to various degrees that they are basically linear. The reflectors used in the design of the synthetic model, shown in Fig. 7, reflect these observations.

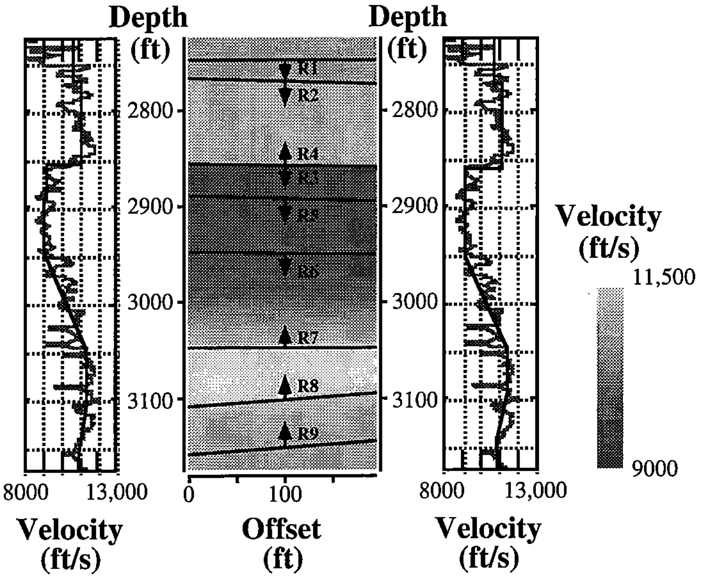

Figure 7: The synthetic model used in Study #3. The simple velocity profile is an approximation of the receiver well S-wave sonic log. The velocity profile on the right side is perturbed to reflect the change in reflector depths across the model. The location and nature of these reflectors is believed to reflect the geology at the McElroy site. Arrows on the reflectors indicate the nature (upgoing or downgoing) of the reflected arrival traveltime picks obtained from the field data set. The synthetic traveltime picks were edited to include picks for the same source-receiver-reflector combinations as the field data set.

Table 7 provides details of the reflector geometries for the synthetic model. Since the reflectors are linear they can be completely defined by their intersection points with the wells. The primary difference between the setup of the field and synthetic survey is that the well deviations of the field survey were not used to create the synthetic model. In the synthetic model the wells are assumed to be vertical with an offset of 195.0 ft. Note that reflectors 3 and 4 are identical in location. They are defined as separate reflectors to remain consistent with the field data inversion.

In field data, traveltimes may be picked for an event that can be seen in both upgoing and downgoing data sets. For a series of closely spaced reflectors the shape of the upgoing and downgoing reflections may differ by more than a phase reversal. This potential difference in phase results in traveltime picks that correspond to slightly different depths in the correct velocity field. In other words, the peak of an upgoing reflection may not exactly correspond in depth to the trough of a downgoing reflection when mapped. Another similar potential problem can occur even if a strong reflection is isolated, meaning that upgoing and downgoing reflections *should* differ by a simple phase reversal. In this case the separate processing of the upgoing and downgoing data sets may introduce phase shifts in the data which mimic the interference error. Rather than trying to monitor and correct this problem the upgoing and downgoing events are inverted as separate reflectors.

TABLE 7. Synthetic model #3 well intersection depths

	Receiver Well intersection depth (ft)	Source Well intersection depth (ft)
Reflector 1	2746.0	2748.5
Reflector 2	2767.5	2772.5
Reflector 3	2855.0	2860.0
Reflector 4	2855.0	2860.0
Reflector 5	2890.0	2895.0
Reflector 6	2947.5	2952.5
Reflector 7	3048.5	3048.5
Reflector 8	3107.0	3092.0
Reflector 9	3157.5	3142.5

Combined Study #3: Acquisition Geometry and Data Specifications

As previously mentioned, the synthetic data are edited to have non-zero traveltimes for the same source-receiver-reflector combinations as the field data set. So the primary difference in the data sets should be in the well configurations, the field data set having deviated wells and the synthetic data set having vertical wells. The surveys consist of 162 sources from 2745.0–3147.5 ft by 167 receivers located from 2745.0–3160.0 ft, every 2.5 ft.

S-waves are not produced by the piezoelectric source at near offsets and the minimum offset for which direct arrival traveltimes are available is about 55 ft. Direct arrival traveltimes have been collected for all larger offsets. Reflection traveltimes were picked manually from the field data set from wavefield data in the CDP domain. Prior to reflection traveltime picking, the data are processed as 2 separate data sets to enhance the S-wave reflections from upgoing and downgoing events. Table 8 provides information about the reflection traveltime picks.

TABLE 8. Field and synthetic reflection traveltime coverage

	Direction	# Traveltimes
Reflector 1	downgoing	4392
Reflector 2	downgoing	4275
Reflector 3	downgoing	4940
Reflector 4	upgoing	783

TABLE 8. Field and synthetic reflection traveltime coverage

	Direction	# Traveltimes
Reflector 5	downgoing	2664
Reflector 6	downgoing	3872
Reflector 7	upgoing	6399
Reflector 8	upgoing	4264
Reflector 9	upgoing	4203

Combined Study #3: Inversion

The inversions of both synthetic and field data were run using identical processing parameters. Direct arrival traveltimes were limited to a ±65.0° aperture, equivalent to approximately 420 ft in offset. At the beginning of the inversion the weights of the second derivative reflector smoothing penalty and the horizontal smoothing penalty were set equal the weight of the traveltime data while the vertical smoothing weight was 1/8th the weight of the horizontal smoothing. The penalty weights were relaxed at a rate of one order of magnitude every 4 continuation steps.

The initial slowness model used in both inversions is homogeneous and equal the average slowness of the direct arrival traveltimes (of the field data set). The cell size of the slowness model is 5.0 ft by 5.0 ft. The reflectors are defined with 21 nodes each, equal to 10.0 ft between nodes. Like Study 1 and Study 2, the inversions were started with flat reflectors. The starting depths for reflectors 1-9 respectively are: 2750.0, 2770.0, 2860.0, 2855.0, 2890.0, 2950.0, 3050.0, 3100.0, and 3150.0.

Combined Study #3: Synthetic Data Results

The results of the 12th continuation step of the synthetic data inversion are optimal for a direct comparison with the field data inversion. Traveltime residuals are ~24μs rms for the 35,237 reflected rays and ~18μs rms for the 20,163 direct arrival rays. These residuals are very near the resolution of the code used to calculate the traveltimes of the raypaths. The velocity tomogram, shown in Figure 8 shows the simple features of the velocity model with few artifacts.

The calculated reflector depths have a range of errors of -1.27–0.73 ft and an rms depth error of 0.54 ft, ~6.5 *inches*. This result confirms the theoretical estimate of Bube and Langan for a ~180 ft crosswell profile. Table 9 provides an abbreviated listing of the inversion results along with the model parameters. Every other parameter in offset (11 out of 21) is shown in this listing. One observation that can be made from data in Table 9 is that the largest depth errors occur in reflectors 3 and 4. These reflectors occur at the interface of two zones with a high velocity contrast. The slow layer lies beneath the fast layer.

The errors in reflectors 3 and 4 are exactly of the type that was previously discussed in Studies 1 and 2. Reflector 3, determined by downgoing reflections in the slower material, is slightly shallow over its entire length. Reflector 4, determined by upgoing reflections in the faster layer, is *also* shallow. This is the situation predicted but not observed in Studies 1 and 2. Due to the velocity gradient in the vicinity of the correct reflector location, the upgoing reflected ray travels through slow material near the interface. The increase in traveltime caused by the slow material forces the reflector up, so that the raypath is shortened and the traveltime is compensated.

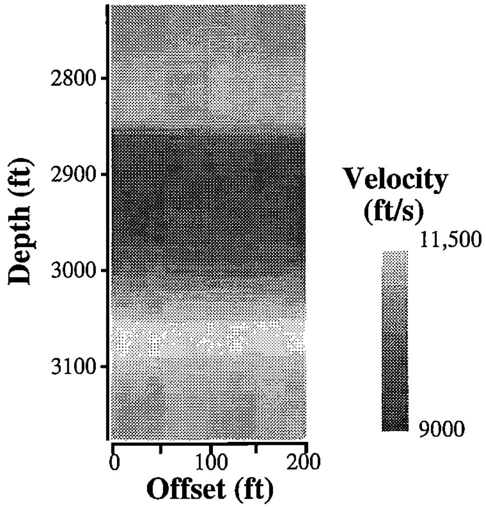

Figure 8: The tomogram result of the 12th continuation step of the synthetic data inversion. The rms error of the 55,400 direct and reflected traveltimes used in this inversion is 20.3 µs. This tomogram can be compared with the model used to generate the synthetic data shown in Fig. 7.

TABLE 9. Synthetic model #3 and synthetic inversion reflector depths

Offset (ft)	0.0	20.0	40.0	60.0	80.0	100.0	120.0	140.0	160.0	180.0	200.0
R1 model	2746.0	2746.3	2746.5	2746.8	2747.0	2747.3	2747.5	2747.8	2748.1	2748.3	2748.6
R1 result	2745.9	2746.0	2746.1	2746.3	2746.5	2746.9	2747.2	2747.6	2747.9	2748.2	2748.5
R2 model	2767.5	2768.0	2768.5	2769.0	2769.6	2770.1	2770.6	2771.1	2771.6	2772.1	2772.6
R2 result	2767.6	2768.1	2768.6	2769.1	2769.6	2770.1	2770.7	2771.3	2771.9	2772.4	2772.7
R3 model	2855.0	2855.5	2856.0	2856.5	2857.1	2857.6	2858.1	2858.6	2859.1	2859.6	2860.1
R3 result	2854.5	2854.7	2855.1	2855.5	2855.9	2856.3	2856.8	2857.5	2858.1	2858.8	2859.5
R4 model	2855.0	2855.5	2856.0	2856.5	2857.1	2857.6	2858.1	2858.6	2859.1	2859.6	2860.1
R4 result	2854.2	2854.7	2855.1	2855.6	2856.1	2856.5	2857.0	2857.6	2858.1	2858.7	2859.3
R5 model	2890.0	2890.5	2891.0	2891.5	2892.1	2892.6	2893.1	2893.6	2894.1	2894.6	2895.1
R5 result	2889.9	2890.5	2891.1	2891.7	2892.3	2892.7	2893.2	2893.6	2894.1	2894.5	2894.9
R6 model	2947.5	2948.0	2948.5	2949.0	2949.6	2950.1	2950.6	2951.1	2951.6	2952.1	2952.6
R6 result	2947.5	2948.0	2948.5	2949.0	2949.4	2949.9	2950.5	2951.0	2951.5	2952.0	2952.5
R7 model	3048.0	3048.0	3048.0	3048.0	3048.0	3048.0	3048.0	3048.0	3048.0	3048.0	3048.0
R7 result	3048.5	3048.5	3048.5	3048.5	3048.5	3048.4	3048.4	3048.5	3048.5	3048.5	3048.7
R8 model	3107.0	3105.5	3103.9	3102.4	3100.8	3099.3	3097.8	3096.2	3094.7	3093.2	3091.6
R8 result	3107.0	3105.5	3103.9	3102.4	3100.9	3099.3	3097.7	3096.2	3094.6	3093.1	3091.7
R9 model	3157.0	3155.5	3153.9	3152.4	3150.8	3149.3	3147.8	3146.2	3144.7	3143.2	3141.6
R9 result	3157.6	3156.1	3154.6	3153.0	3151.4	3149.8	3148.3	3146.7	3145.2	3143.7	3142.3

COMBINED STUDY #3: FIELD DATA RESULTS

The best answer in the tomographic inversion of the McElroy *S*-wave field data is the result of continuation step 12. Traveltime residuals are ~108μs rms for the 35,680 reflected rays and ~65μs rms for the 20,114 direct arrival rays. The combined rms error is ~95μs. The velocity tomogram from continuation step 12 is shown in Figure 9. The tomogram shows quite a bit more lateral variation than seen in the synthetic study. In the low velocity zone in the middle of the image the slower regions are concentrated towards the edge of the model.

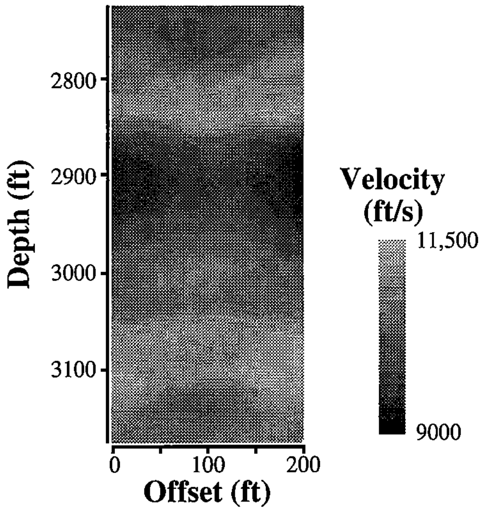

Figure 9: The *S*-wave velocity tomogram from the McElroy field data set created using direct and reflected traveltime arrivals. This tomogram is the result of the 12th continuation step. The overall traveltime residual is ~95 μs rms for the 55,794 traveltimes used in this inversion.

The reflector depths obtained in the inversion are plotted over an *S*-wave crosswell reflection image in Figure 10. The calculated reflectors match the structure seen in the reflection image in a general way but several reflectors are distinctly non-linear. In particular, reflectors 1 and 7 drift a fair amount compared to the image. Several other reflectors are a bit more linear. Reflectors 3 and 4, located at about 2850 ft, almost exactly overlay each other and follow the moveout of the reflection image quite closely.

Compared to the almost perfect recovery of the reflector depths in the synthetic example the mild disagreement between the calculated reflector geometries and the reflection structure seen in the crosswell reflection image (Fig. 10) is interesting. This disagreement suggests that some other parameter may be affecting the inversion. There are several different possibilities to be studied: errors in the traveltime picking, well deviation errors, timing errors, or velocity anisotropy.

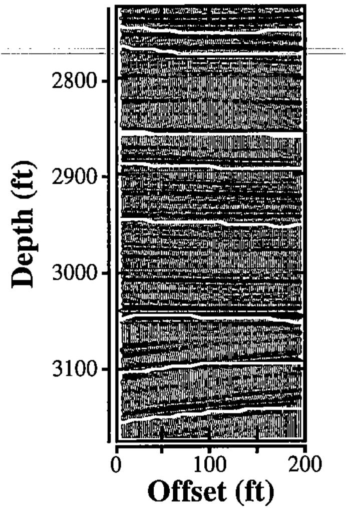

Figure 10: The reflector solutions of the direct and reflected arrival traveltime inversion plotted over the S-wave crosswell reflection image (Lazaratos, 1995).

CONCLUSIONS

The results of the combined direct and reflected arrival traveltimes inversions shown in this paper support the theoretical predictions that reflector locations are well resolved in crosswell data. In a synthetic example designed around the McElroy 188 ft. offset survey, reflector depths were recovered with an rms error of 6.5 *inches* . This survey and other, larger offset surveys, achieved a resolution in reflector depths very close to the values predicted by theoretical studies done by Bube and Langan (1995).

The field data example, an S-wave data set from the McElroy Reservoir Geosciences Project, produced results that were also quite promising. While the reflector geometries calculated using the traveltime inversion had some differences compared to the crosswell reflection image created from the same data, at least one major feature was recovered quite well. The unconformity, located at ~3050 ft, can be seen quite easily in the calculated reflector depths.

The success of these inversions opens a wide range of related areas to study. The next step is to determine the effectiveness of using combined direct and reflected arrival traveltime tomography as a velocity analysis tool for reflection imaging. Currently, obtaining an effective velocity model and reflector geometries for VSP-CDP mapping is the most labor intensive of the imaging steps. Planned future research is to develop a mapping algorithm that uses the velocity image and reflector geometries provided by the traveltime inversion to map the wavefield data directly.

ACKNOWLEDGEMENTS

I would like to thank Ken Bube and Robert Langan for providing me with their traveltime inversion code and helpful guidance. I would also like to thank Jesse Costa for his invaluable assistance in providing me insights to the inversion process. I would finally like to thank Jerry Harris and the sponsors of the STP consortia for providing support for this work

REFERENCES

Bishop, T. N., Bube, K. P., Cutler, R. T., Langan, R. T., Love, P. L., Resnick, J. R., Shuey, R. T., Spindler, D. A., and Wyld, H. W., 1985, Tomographic determination of velocity and depth in laterally varying media: Geophysics, **50**, 903–923.

Bube, B. P., Langan, R. T., and Resnick, J. R., 1989, Unique determination of reflector depths in seismic reflection tomography: 59th Ann. Internat. Mtg., Soc. Expl. Geophys., Expanded Abstracts, 918–921.

Bube, B. P., and Langan, R. T., 1995, Resolution of crosswell tomography with transmitted and reflected traveltimes: STP-**6**, Paper I

Calnan, C., and Schuster, G. T., 1989, Reflection + Transmission Crosswell Tomography: 59th Ann. Internat. Mtg., Soc. Expl. Geophys., Expanded Abstracts, 908–911.

Harris, J. M., Nolen-Hoeksema, R. C., Rector, J. W., Lazaratos, S. K., and Van Schaack, M. A., 1995, High-resolution crosswell imaging of a west Texas carbonate reservoir: Part 1—Project summary and interpretation: Geophysics, **60**, 667–681.

Ivansson, S., 1986, Some remarks concerning seismic reflection tomography and velocity analysis: Geophys. J. R. Astr. Soc., **87**, 539–557.

Lazaratos, S. K., 1993, Cross-well reflection imaging: Ph.D. thesis, Stanford University.

Lazaratos, S. K., Harris, J. M., Rector, J. W., and Van Schaack, M. A., 1995, High-resolution crosswell imaging of a west Texas carbonate reservoir: Part 4—Reflection imaging: Geophysics, **60**, 702–711.

Stork, C., 1988, Ray trace tomographic velocity analysis of surface seismic reflection data: Ph.D. Thesis, Calif. Inst. of Technology.

PAPER I

RESOLUTION OF CROSSWELL TOMOGRAPHY WITH TRANSMISSION AND REFLECTION TRAVELTIMES

K. P. Bube[‡] **and R. T. Langan**

ABSTRACT

Transmission traveltimes alone in crosswell tomography are insufficient to determine the slowness field between the wells accurately. Horizontal smearing is common. In many crosswell data sets, traveltimes from reflections can also be picked. We study here the effect that including these reflected traveltimes has on the resolution of both the slowness field and the reflector depth. When reflected traveltimes are used, more unknown parameters need to be introduced to solve for the position of the reflectors. We compute the diagonal elements of the resolution matrix for two realistic crosswell geometries based upon the acquisition parameters used in the McElroy crosswell field experiment. We compare the resolution when no reflections are used, when upgoing reflections only are used, and when both upgoing and downgoing reflections are used. Our results indicate that the reflector positions are very well determined, so these new unknowns can be determined from the new traveltime data. Including reflection traveltimes improves the resolution of the slowness field somewhat, particularly near the reflectors.

INTRODUCTION

In crosswell seismic tomography, transmission traveltimes from shot locations in one well to receiver locations in another well are measured, and the goal is to determine the slowness field (reciprocal of wavespeed or velocity) between the wells. Unfortunately, transmission traveltimes alone are insufficient to determine the slowness field accurately (Menke, 1984; Bregman, 1986; Bregman *et al.*, 1989; Calnan and Schuster, 1989, 1990; Langan and Bube, 1995). The most poorly determined features in crosswell transmission tomography are horizontally zero-mean, vertically homogeneous perturbations of a slowness field ("stripes"); these slowness perturbations cause little or no perturbation in the traveltimes, so they are difficult to recover from traveltime data alone. Stated less formally, in general the horizontal location of features in the slowness model is poorly determined by the traveltime data.

A number of approaches have been used to augment the transmission traveltimes with other data in order to obtain an improved estimate of the slowness field. Wavefield inversion has been coupled to traveltime inversion (Luo and Schuster, 1991). There has been much recent interest in using reflections in crosswell seismic data to estimate the slowness field, both in wavefield imaging and for augmenting transmission traveltimes with reflection traveltimes (Calnan and Schuster, 1989, 1990; Stewart and Marchisio, 1991; Lazaratos, 1993; Lazaratos *et al.*, 1992, 1993). We focus here on the effect of including reflection traveltimes together with transmission traveltimes in crosswell tomography.

[‡] Department of Mathematics, University of Washington

Calnan and Schuster (1989, 1990) proposed combining transmission traveltimes with reflection traveltimes in tomography to obtain some improvement in the resolution of the slowness field. In their analyses, it appears that they fixed the reflector depths while solving for the slowness field, rather than solving for both the reflector depths and the slowness field simultaneously. It should be noted that they did this work before the first high quality reflection image was produced by Lazaratos *et al.* (1992) and it was not even known at the time whether one could "pick" reflection events in prestack or post-stack data.

The purpose of our study is to analyze the effect that adding reflection traveltimes has on the resolution of slownesses *and* reflector depths in crosswell tomography. A key issue is whether the addition of more unknowns (the reflector positions) damages the potential gain of adding more information (the reflection traveltimes). We examine the diagonal elements of the resolution matrix for a selected series of linearized problems in order to address this question.

THE RESOLUTION MATRIX

One way to study the ability of the traveltimes to resolve features of the model is to study the derivative matrix $\underline{\mathbf{A}}$ of traveltimes with respect to model parameters at a particular background model. This matrix tells us how perturbations in the background model change the traveltimes. We choose a background model with constant slowness and a single flat reflector. Even though the background model is constant, the slowness field (a function of x and z) and the reflector depth (a function of x) have complete freedom (up to the level of discretization) in the possible perturbations.

The choice of a constant background model forces symmetry on the problem which we hope brings out worst-case behavior for conditions where we have good raypath coverage over most of the region. On can easily envision complicated models whereby the ray coverage is either locally sparse or mostly parallel, such that the resolution problems are quite different from the ones posed here.

The resolution matrix of $\underline{\mathbf{A}}$ can be described in terms of its singular value decomposition, $\underline{\mathbf{A}} = \underline{\mathbf{U}}\,\underline{\Sigma}\,\underline{\mathbf{V}}^{\mathrm{T}}$, where $\underline{\mathbf{U}}$ and $\underline{\mathbf{V}}$ are orthogonal matrices and $\underline{\Sigma}$ is a diagonal matrix whose diagonal elements are the singular values of $\underline{\mathbf{A}}$: $\sigma_1 \geq \sigma_2 \geq \ldots \geq \sigma_n \geq 0$. The columns of $\underline{\mathbf{V}}$ are the singular vectors in the model space. For a given noise level, and a choice of a minimum signal-to-noise ratio (e.g., 1), a cutoff l in the index of the singular values can be chosen so that whenever $j > l$, the expected signal-to-noise ratio for the coefficient of the j^{th} column of $\underline{\mathbf{V}}$ (in the solution of the linearized problem) is less than the chosen minimum. Let $\underline{\mathbf{V}}_l$ be the matrix consisting of the first l columns of $\underline{\mathbf{V}}$. The resolution matrix (for this noise level) is

$$\underline{\mathbf{R}} = \underline{\mathbf{V}}_l\,\underline{\mathbf{V}}_l^{\mathrm{T}}.$$

The diagonal elements of $\underline{\mathbf{R}}$ can be shown to satisfy $0 \leq r_{ii} \leq 1$. If $l = n$ (so no columns are dropped), $\underline{\mathbf{R}} = \underline{\mathbf{I}}$. In general, the closer r_{ii} is to 1, the better the resolution of the i^{th} model parameter.

RESOLUTION STUDIES

We formulated two sets of synthetic problems for study based upon two crosswell experiments in the McElroy Field, one set based upon a 180-ft spacing between wells, and the other based on a 600-ft spacing between wells. Both synthetic studies used source and receiver geometries similar to the actual field experiments.

Tables 1 and 2 summarize the parameters of the problems we investigated. We traced rays through a constant slowness model between all appropriate source and receiver locations. A reflector was placed at a depth of 2900 ft, approximately the midline of the 100-ft thick reservoir. We calculated the traveltime derivatives from ray tracing, and then computed the derivative matrix $\underline{\mathbf{A}}$ and the resolution matrix $\underline{\mathbf{R}}$ (for a given noise level).

Note that the reflector position is independent of the slowness structure. We have found that this decoupling is essential in order to obtain the best resolution possible in studies where surface seismic data are used to resolve reflector depths with traveltime tomography (Bube *et al.*, 1995). Another observation we have made with surface seismic data is that one must be careful not to *underparametrize* the slowness field as well in order to resolve reflector depths accurately--if a proposed simplification of slowness structure in the model is not justified by what is present in the real world, errors associated with an oversimplification of the slowness field are forced to create errors in the reflector depth. Even though one may not be able to resolve accurately the complicated slowness structure, this freedom must be present in the slowness model. The interesting result is that one has to avoid both overparametrizing *and* underparametrizing the slowness model!

We computed three raypath coverages for each well spacing; *transmitted* rays only, *transmitted* rays plus *upwardly reflected* rays, and *transmitted* plus *upwardly reflected* rays plus *downwardly reflected* rays. We based the singular value cutoff for the computation of resolution diagonals upon an assumed noise level. For the 185-ft well spacing a 1% noise level was chosen, which is equivalent to about 0.15 msec error (slightly greater than the 0.1 msec sample interval). For the 600-ft well spacing a 2% noise level was chosen, equivalent to about 0.9 msec error. Too fine a grid spacing can strongly affect this analysis due to overparametrization. We chose a grid spacing of 10 ft for the narrow profile and 20 ft for the wide profile. In both profiles this corresponds to four times the source and receiver spacing, which is normally great enough to prevent spatial aliasing of the slowness field (Bube and Resnick, 1984; Bube *et al.*, 1985).

The contour plots of the resolution diagonals for slowness are shown if Figures 1 and 2, which correspond to the 180-ft profile and the 600-ft profile, respectively. The magnitude of the contour values indicates what fraction of a perturbation to the constant background will be recovered at each grid point location. A value of 0.8 is generally considered good. Lower values usually mean there will be considerable smearing of the image.

Figure 1A shows that for a 10-ft grid spacing and a 1% noise level, and using the transmitted data only, we should expect good slowness resolution on the 180-ft profile through the central half of the acquisition area. Note that there will be some degradation just below the reservoir interval of 2850 ft to 2950 ft. The addition of a reflector and upgoing reflected events (Figure 1B) substantially improves the slowness resolution for a zone about 75-ft thick just above the reflector. There is also a slight improvement in slowness resolution just below the central part of the reflector. The further addition of downgoing reflections (Figure 1C) improves the slowness resolution below the central partof the reflector in a zone about 50 ft thick vertically. Note that the raypath coverage for the downgoing reflections is not as extensive as the upgoing raypath coverage (Table 1).

The resolution diagonals for the reflector depth parameters all exceed 0.993 for the 180-ft profile. After scaling slowness and reflector depth appropriately (because their units are different), an estimate for the errors predicted for the reflector depths yields a value of only a few inches. Therefore, the reflector depths are well determined in this example.

Figure 2A shows that for a 20-ft grid spacing and 2% noise level, we will get slightly poorer slowness resolution on the 600-ft profile. In particular, the slowness resolution is considerably poorer in the lower portion of the reservoir. The addition of upgoing reflections from a reflector at 2900 ft (Figure 2B) improves the resolution substantially. The addition of downgoing reflections (Figure 2C) only slightly improves the slowness resolution below the reflector. Note that there are fewer than 4000 downgoing reflected rays out of total of about 60,000 (Table 2). This explains in part the minimal impact of the downgoing reflections.

The resolution diagonals for the reflector depths all exceed 0.975 for the 600-ft profiles, leading to an estimate of a maximum error in the reflector depth parameters on the order of 0.5 ft to 2.5 ft. One can expect good resolution of the reflector depths, in spite of the somewhat mediocre slowness resolution.

CONCLUSIONS

We have performed a resolution analysis for two realistic crosswell geometries by computing the diagonals of the resolution matrix. The addition of reflection traveltimes to the transmission traveltimes adds more parameters to be determined (the reflector depth parameters). Fortunately, even when reflections from only one side of the reflector are used, the reflector depths are very well determined. Thus, crosswell transmission and reflection tomography should put the reflectors in the right place, *even if there are still errors in the slowness field.* As we noted, decoupling the reflector position from the slowness structure is probably critical for this conclusion to be valid, as is the degree of parametrization of the slowness field. Including reflection traveltimes improves the resolution of the slowness field, particularly near the reflector (on the same side as the reflections). Including reflection traveltimes from several reflectors should further improve the slowness resolution.

The potential application of transmission plus reflection traveltime tomography would be in situations where one wants to know the precise structure of selected reflection events in a reflection image. Although a reflection image obtained by migration or VSP-CDP mapping may be well focused, the actual geometric structure of the reflections may be subtly distorted due to errors in the velocity model used in the time-to-depth conversion. Traveltime tomography, when applied to both transmitted and reflected events, should provide superior depth resolution of these selected reflection events. A potential side benefit would be a more accurate velocity model.

A second potential application is in trying to obtain improved slowness images for larger well spacings when they raypath coverage is less than ideal. The improved angular coverage that the reflections provide will improve the slowness resolution somewhat, particularly near the selected reflectors.

Van Schaack (this volume) has implemented a transmission plus reflection traveltime tomography method and tested it on both synthetic data and field data. His preliminary results support the conclusions of our study.

REFERENCES

Bishop, T. N., Bube, K. P., Cutler, T. T., Langan, R. T., Love, P. L., Resnick, J. R., Shuey, R. T., Spindler, D. A., and Wyld, H. W., 1985, Tomographic determination of velocity and depth in laterally varying media, *Geophysics*, **50**, 903-923.

Bregman, N. D., 1986, *Tomographic inversion of crosshole seismic data*, Ph. D. Thesis, Univ. of Toronto.

Bregman, N. D., 1989, Crosshole seismic tomography, *Geophysics*, **54**, 200-215.

Bube, K. P., 1995, Uniqueness of reflector depths and characterization of the slowness null space in linearized seismic reflection tomography, *SIAM J. Appl. Math.*, 55, 255-266.

Bube, K. P., Jovanovich, D. B., Langan, R. T., Resnick, J. R., Shuey, R. T., and Spindler, 1985, Well-determined and poorly-determined features in seismic reflection tomography, Part II, *Technical Program, 55th Annual SEG Meeting*, Society of Exploration Geophysicists, Tulsa, OK, 608-610.

Bube, K. P., Langan, R. T., and Resnick, J. R., 1989, Unique determination of reflector depths in seismic reflection tomography, *Technical Program, 59th Annual SEG Meeting*, Society of Exploration Geophysicists, Tulsa, OK, 918-921.

Bube, K. P., Langan, R. T., and Resnick, J. R., 1995, Theoretical and numerical issues in the determination of reflector depths in seismic reflection tomography, to appear in the *J. Geophys. Res.*

Bube, K. P., and Resnick, J. R., 1984, Well-determined and poorly-determined features in seismic reflection tomography, *Technical Program, 54th Annual SEG Meeting*, Society of Exploration Geophysicists, Tulsa, OK, 49-51.

Calnan, C. J., and Schuster, G. T., 1989, Reflection + transmission crosswell tomography, *Technical Program, 59th Annual SEG Meeting*, Society of Exploration Geophysicists, Tulsa, OK, 908-911.

Calnan, C. J., and Schuster, G. T., 1990, Reflection + transmission crosswell tomography, University of Utah Tomography Development Project, 1989 Annual Report, 290-331.

Lazaratos, S. K., 1993, *Crosswell reflection imaging*, Ph. D. Dissertation, Stanford Univ.

Lazaratos, S. K., Rector III, J. W., Harris, J. M., and Van Schaack, M. A., 1992, High resolution crosswell imaging of a West Texas carbonate reservoir: Part 4: Reflection Imaging, *Technical Program, 62nd Annual SEG Meeting*, Society of Exploration Geophysicists, Tulsa, OK, 49-51.

Lazaratos, S. K., Rector III, J. W., Harris, J. M., and Van Schaack, M. A., 1993, High-resolution crosswell reflection imaging: Potential and technical difficulties, *Geophysics*, **58**, 1270-1280.

Langan, R. T., and Bube, K. P., 1995, A resolution analysis of crosswell seismic tomography, to appear in *Mathematical Methods in Seismic Inversion*, W. Symes (ed.), The Society of Industrial and Applied Mathematics Series on Frontiers in Applied Mathematics.

Luo, Y., and Schuster, G. T., 1991, Wave equation traveltime inversion, *Geophysics*, **56**, 645-653.

Menke, W., 1984, The resolving power of cross-borehole tomography, *Geophys. Res. Let.*, **11**, 105-108.

Stewart, R. R., and Marchisio, G., 1991, Crosswell seismic imaging using reflections, *Technical Program, 61st Annual SEG Meeting*, Society of Exploration Geophysicists, Tulsa, OK, 375-378.

Stork, C., 1988, *Ray trace tomographic velocity analysis of surface seismic reflection data*, Ph. D. Dissertation, Calif. Inst. of Tech.

Stork, C., 1992, Singular value decomposition of the velocity-depth trade-off, Part 2, High-resolution analysis of a generic model, *Geophysics*, **57**, 933-943.

Table 1. Parameters Governing The Analysis For The 180-ft Well Spacing

Ray Pattern for Inversion	Sources	Receivers	Rays	Grid Spacing	Unknowns	Noise Level	S.V. Cut*	Figure
Transmitted Rays Only	240 @ 2.5 ft	240 @ 2.5 ft	57,600	10 ft	1,159	1%	337	1A
Trans. + Upgoing Reflections	240 @ 2.5 ft	240 @ 2.5 ft	77,200	10 ft	1,178	1%	325	1B
Trans. + Upgoing + Downgoing	240 @ 2.5 ft	240 @ 2.5 ft	87,200	10 ft	1,178	1%	323	1C

*Singular Vectors Cut Off

Table 2. Parameters Governing The Analysis For The 600-ft Well Spacing

Ray Pattern for Inversion	Sources	Receivers	Rays	Grid Spacing	Unknowns	Noise Level	S.V. Cut*	Figure
Transmitted Rays Only	200 @ 5.0 ft	200 @ 5.0 ft	40,000	20 ft	1,581	2%	816	2A
Trans. + Upgoing Reflections	200 @ 5.0 ft	200 @ 5.0 ft	59,600	20 ft	1,611	2%	776	2B
Trans. + Upgoing + Downgoing	200 @ 5.0 ft	200 @ 5.0 ft	63,200	20 ft	1,611	2%	766	2C

*Singular Vectors Cut Off

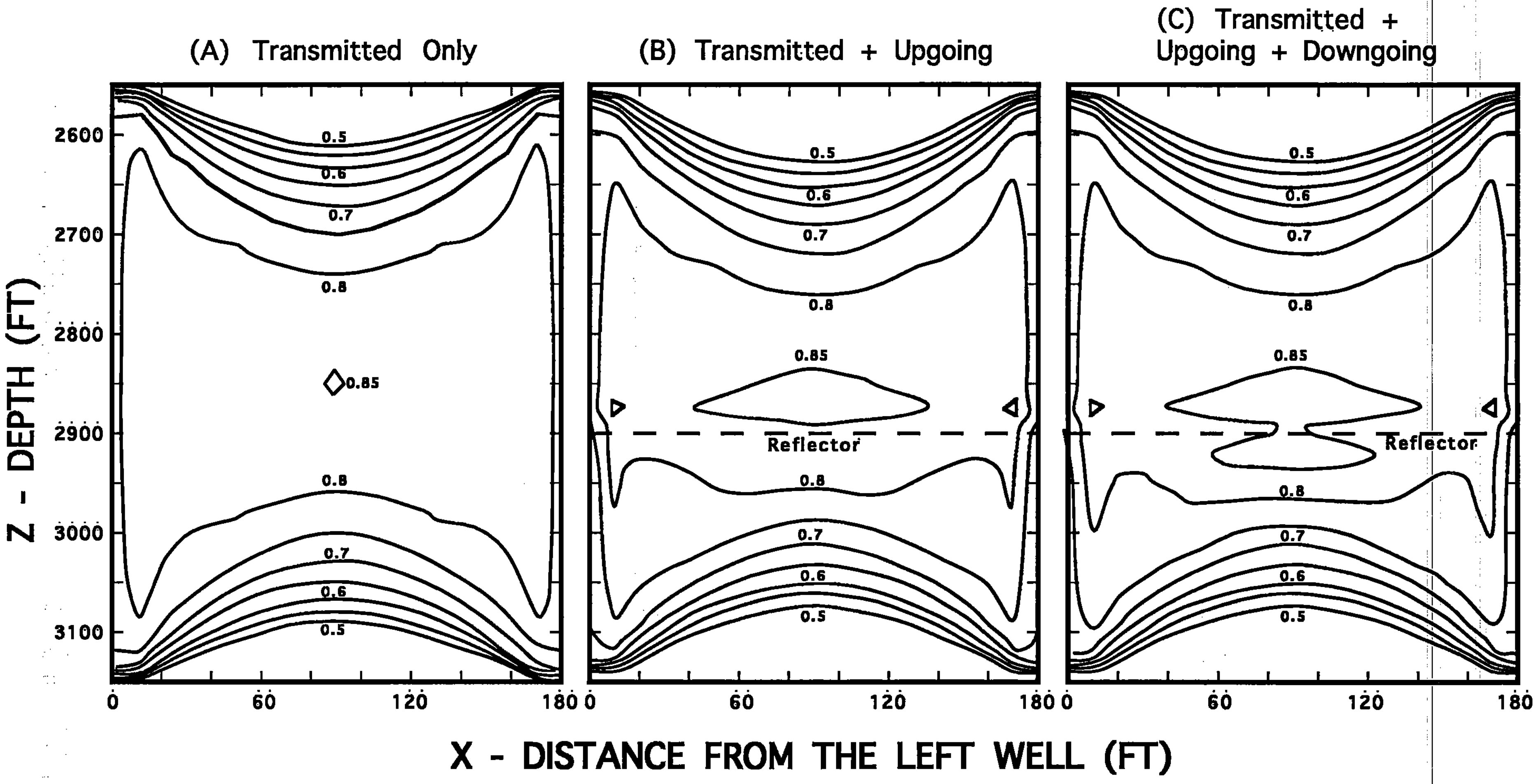

Figure 1. Contoured resolution diagonals for a 180-ft crosswell profile. Three cases are shown: (a) transmitted raypaths only, (b) transmitted plus upwardly reflected raypaths, and (c) transmitted plus upwardly plus downwardly reflected raypaths. These resolution diagonals indicate how good the slowness resolution will be between the wells for a given acquisition geometry, model parametrization, and noise level. A value of 1.0 would indicate perfect recovery of the slowness information at a given point. Lesser values indicate poorer recovery and subsequent smearing (usually) of the image about the neighboring grid points.

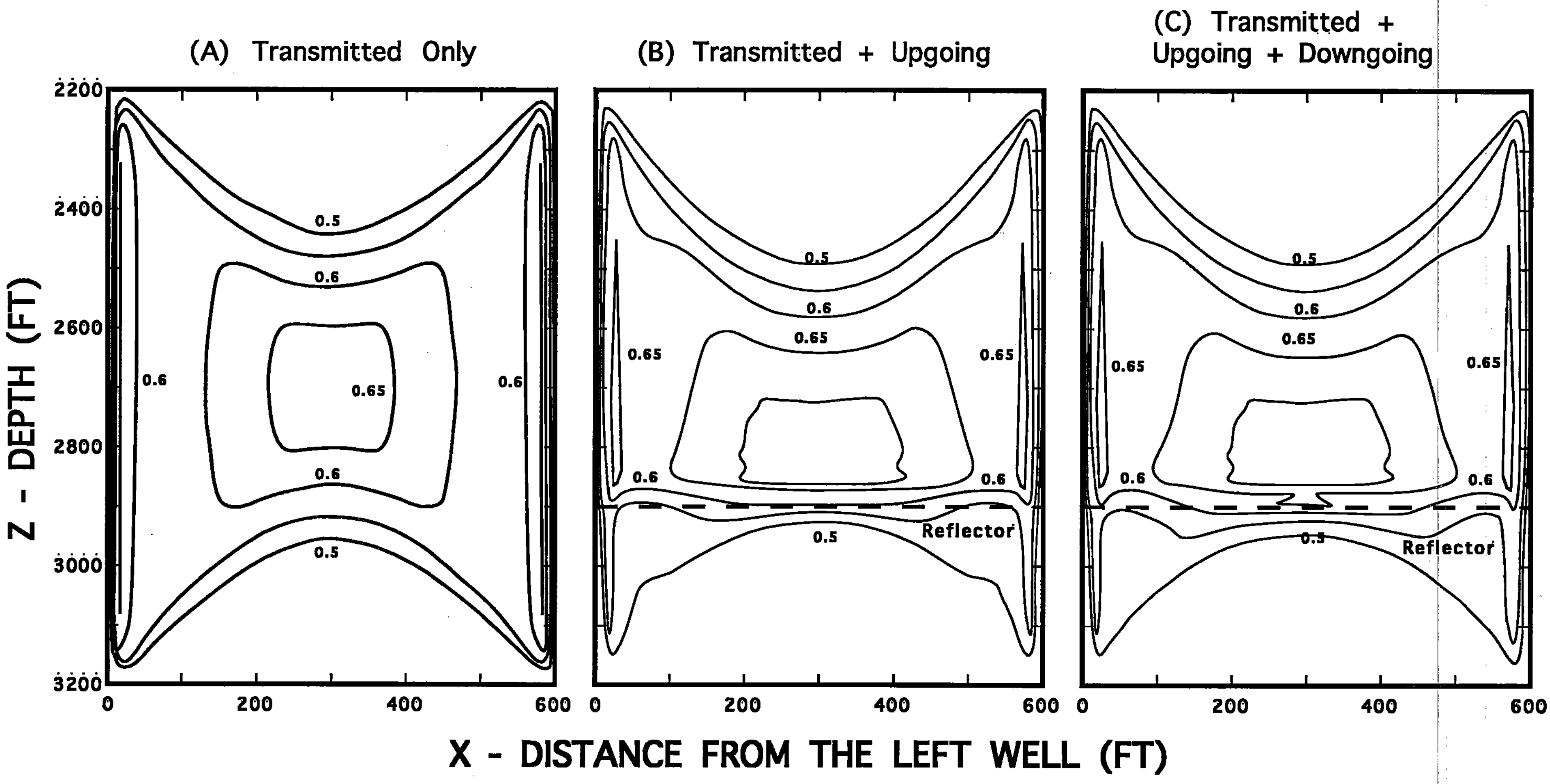

Figure 2. Contoured resolution diagonals for a 600-ft crosswell profile. Three cases are shown: (a) transmitted raypaths only, (b) transmitted plus upwardly reflected raypaths, and (c) transmitted plus upwardly plus downwardly reflected raypaths. These resolution diagonals indicate how good the slowness resolution will be between the wells for a given acquisition geometry, model parametrization, and noise level. A value of 1.0 would indicate perfect recovery of the slowness information at a given point. Lesser values indicate poorer recovery and subsequent smearing (usually) of the image about the neighboring grid points.

PAPER J

WAVE EQUATION TOMOGRAPHY WITH PHASE CORRECTION FROM THE FIRST ARRIVAL TRAVELTIMES

Feng Yin

SUMMARY

We use the first arrival traveltime to correct the phase distortion in a nonlinear wave equation inversion scheme. This improves the precision of tomographic reconstruction of a velocity structure with large variations and helps solve the ill-posed problem of wave equation inversion. When the variation of the velocity distribution is large, general non-linear wave equation inversions are very ill-posed and for such strong nonlinear we can not obtain a correct inversion. One of main reasons is that the calculated and observed phase of the wavefield differs greatly if the initial model is far from the true model. This leads to highly mismatched phase between the calculated and the observed wave field. The phase mismatch is even more pronounced if a high operating frequency is employed in order to increase resolution. To address this problem, we use the first arrival to "demodulate" the wave field in the frequency domain with a goal of restoring the phase of wave field. Then we minimize a objective function consisting of so called "demodulated" wave field to solve wave equation inversion problem. In this way, we find that the inversion is much improved, and when the velocity perturbation in a complicated model reaches 35%, we can still obtain a good inversion. A computer simulation shows that our method is a very robust for acoustical wave inversion with good reconstruction precision.

INTRODUCTION

Many wave equation tomography methods have been proposed. Some use Born or Rytov approximation (Harris, 1987, Harris and Wang, 1995, Wu and Toksöz, 1987). Others use the non-linear iterative inversion theory to solve wave equation inversion problem, and develop the inversion method in frequency domain (Pratt and Worthington, 1990, Harris and Yin, 1993) or in time domain (Tarantola etal, 1990,, Luo and Schuster, 1990). But when the variation of velocity is large, all of these methods face a challenge due to the intrinsic non-linearity and ill-posed nature of the problem of wave equation inversion. One reason is the large phase mismatch between the calculated and observed wave fields when the variation of the velocity of wave propagation in the media is large: suppose the observed phase is $\Phi^o = \Phi_0^o + \Delta\Phi^o$, where $\Phi_0^o = \omega t^o$, and t^o is the first arrival traveltime observed from the waveform; and, the calculated phase is $\Phi^c = \Phi_0^c + \Delta\Phi^c$, where $\Phi_0^c = \omega t^c$, and t^c is the first arrival traveltime from the synthetic waveform. If the difference $t^o - t^c$ between observed and calculated first arrival of an event is 0.001 second, and if we use the wave field with 500 Hz to invert for velocity, the phase difference will be larger than π , and located outside the range $(-\pi/2, \pi/2)$. Moreover, the higher the operating frequency, the more serious the phase mismatch will be. Therefore, it is very difficult to get satisfactory results form wave equation tomography. In order to address this non-linear and ill-posed problem in wave equation tomography, we use the first arrival traveltime to make a phase correction or "demodulate" the wave field in frequency domain. Then, we use the general non-linear inversion method to minimize the objective function which contains the demodulated wave field. The phase difference between the observed and calculated wave fields after demodulation will be $\Delta\Phi^o - \Delta\Phi^c$ instead of the original $(\Phi_0^o - \Phi_0^c) + (\Delta\Phi^o - \Delta\Phi^c)$ in all iterative inversion from starting to the end. We match $(\Phi_0^o - \Phi_0^c)$ first, then, $(\Phi_0^o - \Phi_0^c) + (\Delta\Phi^o - \Delta\Phi^c)$. In addition, we can see in the next section that the first arrival phase is employed as a implicit matching condition in our algorithm. In this way, the phase mismatch problem can be resolved in each iterative step of the inversion.

The paper is organized as follows, the problem of wave equation inversion method and its solution are described in the theory and method section. Then, we apply our method to the crosswell geometry to conduct a forward and inverse simulation. We compare the inversion results using the new method and old inversion method in the numerical test section. We find that a complicated model with 35% velocity perturbation can be reconstructed very well by our new method while standard nonlinear inversion method in frequency domain has failed. We believe that the method we propose here will be useful when applied to real data. The general idea proposed in this paper can be extended to inversion in the time domain case.

THEORY AND METHOD OF WAVE EQUATION INVERSION WITH PHASE CORRECTION

Let us revisit the general inversion method in the frequency domain and check its solution first. We know that the goal in the non-linear inversion is to minimize the objective function

$$Q(\boldsymbol{m}) = J(\boldsymbol{m}) + \alpha H(\boldsymbol{m}) \longrightarrow min \tag{1}$$

Where $J(\boldsymbol{m}) = \sum_{g=1}^{G} \sum_{s=1}^{S} \| U^o(\omega) - U^c(\omega) \|_2$, and $U^o(\omega)$ and $U^c(\omega)$ are the observed and calculated wave fields in the frequency domain, H is a smoothing operator, and $\boldsymbol{m}$ is a model vector, G and S are total number of the receiver and source, the turning parameter α regulates the amount of smoothing versus the fit to the data of the model. Suppose that we have a waveform $u(t)$ in time domain, if we apply the Fourier transform to the waveform $u(t)$, then we have $U(\omega) = \mathrm{F}\ (u(t))$, where F denotes Fourier transform. If the signal were shifted to $u_1(t) = u(t + t_0)$, then we have $U_1(\omega) = e^{j\omega t_0} U(\omega)$. We here call $U_1(\omega)$ a "demodulated" signal of $U(\omega)$ in frequency domain. We can see the oscillation of $U(\omega)$ is much quicker than $U_1(\omega)$. The fact is illustrated in Figures (1)-(4). Suppose we have a time domain signal $u(t)$ as shown in Figure (1) with a frequency band of (0,500) Hz. Then the spectrum of it can be derived by Fourier transform, which is shown in Figure (2). From Figure (2), we can see, if we want to match this spectrum, we much have good initial model so that the waveform is very close to the original one; otherwise, the iterative inversion will probably be divergent. But if we shift the signal to $u(t + t_0)$ as shown in Figure (3), then we obtain the spectrum of the signal $u(t + t_0)$ as shown in Figure (4). By comparing Figure (2) with Figure (4), it is obvious that the oscillation of the spectrum in Figure (2) is much stronger than that shown in Figure (4). Therefore, the inversion implemented in the domain as shown in Figure (4) is much easier than that as shown in Figure (2). So we believe that the non-linear problem in the demodulated domain easier than before.

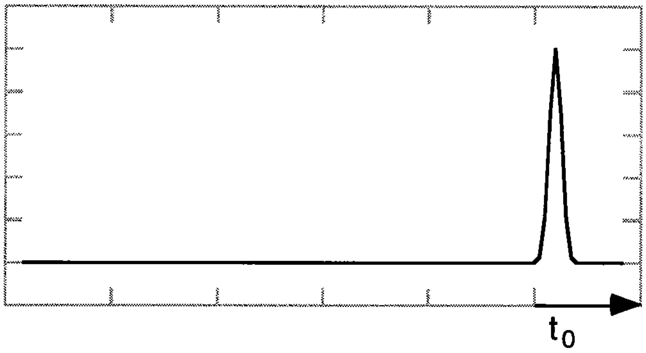

Figure 1: A time domain signal u(t)

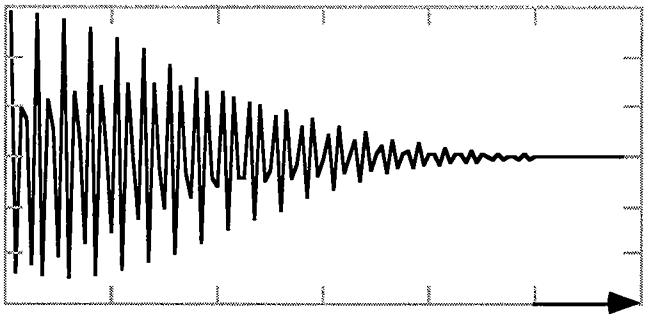

Figure 2: The real part of the spectrum of u(t)

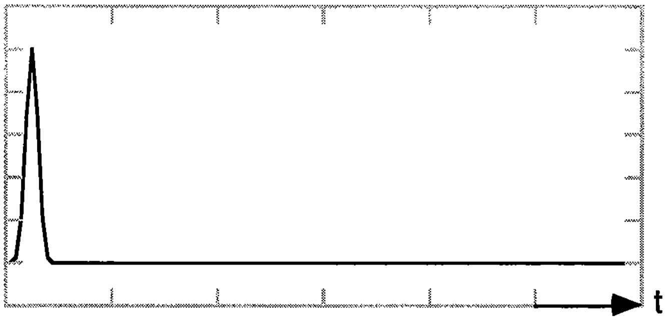

Figure 3: The time domain signal of u(t+t_0)

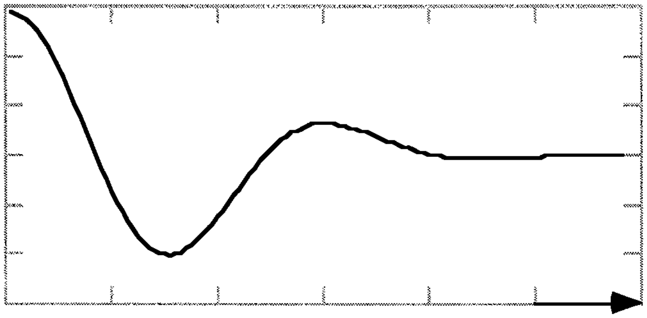

Figure 4: The real part of spectrum of u(t+t0)

Therefore, we have the suggestion that the inversion will be better inversion by matching the demodulated waveform rather than the original waveform. According to nonlinear inversion theory, we establish a new object function as follows:

$$Q(\boldsymbol{m}) = J(\boldsymbol{m}) + \alpha H(\boldsymbol{m})$$

$$= \sum_{g=1}^{G} \sum_{s=1}^{S} \| U_d^o(\omega) - U_d^c(\omega) \|_2 + \alpha H(\boldsymbol{m}) \longrightarrow min \tag{2}$$

where $U_d^o(\omega) = \mathrm{F}\ (u^0(t+t_0))$, and $U_d^c = \mathrm{F}\ (u^c(t+t_c))$, F denotes the Fourier transform, and subscript (superscribpt) o , c and d represent the observed and calculated wave field data and the demodulated in frequency domain, respecttively. In this paper, we restrict ourselves to inversion for velocity using acoustical wave equation. Therefore, we use the following integral equation

$$U(r,\omega) = -k^2 \iint_{\Omega} U_t(r', r_s, \omega) m(r') G(k|r' - r|) dr' \tag{3}$$

where $U(r,\omega)$ are the scattering field in the background media with velocity V_0, $U_t(r,\omega)$ is the total pressure field in the media with velocity V, ω is the angular frequency, $m(r) = 1 - \frac{V^2}{V_0^2}$, $k = \frac{\omega}{V_0}$, and $G(k|r - r'|)$ is the Green's function in the background media. The total field in equation (3) can be solved by the moment method (Harris and Yin, 1993) or finite difference method in frequency domain (Pratt and Worthington, 1990). So we have $U_d^o(\omega) = e^{j\omega t_o} U^o(\omega)$ and $U_d^c(\omega) = e^{j\omega t_c} U^c(\omega)$.

Therefore, by using the iterative inversion shown below to invert for model $\boldsymbol{m}(r)$, we have

$$\boldsymbol{m}^{(q+1)} = \boldsymbol{m}^{(q)} + \delta \boldsymbol{m}^{(q)} \tag{4}$$

$$\delta \boldsymbol{m}^{(q)} = x_1 \vec{e}_1 + x_2 \vec{e}_2 + x_3 \vec{e}_3 \tag{5}$$

where

$$(\vec{e}_1)_i = (\frac{\partial J}{\partial \boldsymbol{m}})_i,\ (\vec{e}_2)_i = (\frac{\partial H}{\partial \boldsymbol{m}})_i,\ (\vec{e}_3)_i = \sum_j (\frac{\partial^2 J}{\partial m_i \partial m_j} \frac{\partial Q}{\partial m_j}) \tag{6}$$

and from equation (2), we have

$$(\frac{\partial J}{\partial \boldsymbol{m}})_i = \sum_{g}^{G} \sum_{s}^{S} R[e^{-j\omega t^c} (-j\omega \frac{\partial t^c}{\partial m_i} U^c + \frac{\partial U^c}{\partial m_i})] \cdot R(e^{-j\omega t^c} U^c - U_d^o)$$

$$+ I[e^{-j\omega t^c} (-j\omega \frac{\partial t^c}{\partial m_i} U^c + \frac{\partial U^c}{\partial m_i})] \cdot I(e^{-j\omega t^c} U^c - U_d^o) \tag{7}$$

$$
\begin{aligned}
&(\frac{\partial^2 J}{\partial m_i \partial m_j}) = \\
&\sum_g^G \sum_s^S R[e^{-j\omega t^c}(-j\omega \frac{\partial t^c}{\partial m_i} U^c + \frac{\partial U^c}{\partial m_i})] \cdot R[e^{-j\omega t^c}(-j\omega \frac{\partial t^c}{\partial m_i} U^c + \frac{\partial U^c}{\partial m_i})] \\
&I[e^{-j\omega t^c}(-j\omega \frac{\partial t^c}{\partial m_i} U^c + \frac{\partial U^c}{\partial m_i})] \cdot I[e^{-j\omega t^c}(-j\omega \frac{\partial t^c}{\partial m_i} U^c + \frac{\partial U^c}{\partial m_i})]
\end{aligned}
\tag{8}
$$

From equation (3) , we have

$$
\frac{\partial U^c}{\partial m_i} = -k^2 U_t^c(\omega, r', r_s) G(k|r - r'|) \Delta s_i,\ r' \subset \Delta s_i \tag{9}
$$

where Δs_i is the area of i-th pixel and $\frac{\partial t^c}{\partial m_i}$ can be derived by variable methods. Under the ray approximation, we have

$$
\frac{\partial t^c}{\partial m_i} = -\frac{\Delta l_i V_i}{2V_0^2} \tag{10}
$$

where Δl_i and V_i are ray length and velocity in i-th cell. The coefficients $x_i (1 \le i \le 3)$ can be derived by the method described in the paper (Harris and Yin, 1993).

From equation (7), we see that there are two derivatives making contribution to the Frechet derivative of object function, one is the derivative of first arrival to the model, another is the derivative of total field to the model. Therefore, the phase of first arrival is used as a implicit constraint condition which should be matched in all iterative steps, that is, the variation of the first arrival phase is also employed to correct the current model. Thus, this will be helpful for the iterative procedure to be convergent to the true model. So the inversion steps can be summarized as follows:

1. pick the first arrival time from the sacttering waveform *u(t);*
2. shift the waveform $u(t+t_0)$;
3. transform $u(t+t_0)$ to $U_d^o(\omega)$;
4. calculate searching directions e_1, e_2, e_3;
5. updating the model using equation (4);
6. if $Q(m) \le \varepsilon,\ \varepsilon$, stop iterative inversion, otherwise, go to 4.

INVERSION RESULTS USING SIMULATION DATA

Figure (5) and (6) are two synthetic models. In Figure (5), there is a two layer perturbation. Figure (6) is a more complicated model. The velocity in each region is shown. The minimum velocity is 5000 m/s, the maximum 6750 m/s, and the range of the variation is 35%. In the forward calculation, the image region is divided into 20×50 pixels, where the width of each pixel is 2.5 m. In the frequency we use is 200 Hz. The experiment consists of 50 sources and receivers spaced at intervals of 2.5 m apart. We use moment method to produce the observed wave field. Figure (7) and Figure (8) are the tomography reconstruction results of the model (5) and model (6) by the demodulation method presented herein,. The starting models are constant with a velocity of 5000 m/s. Figure (9) and Figure (10) are the tomography reconstruction of the model (5) and model

(6) by minimizing equation (1) using the standard nonlinear method, in which the starting models are also constant with a velocity of 5000 m/s .

CONCLUSIONS

We put forward a new wave equation iterative tomography method, in which the first arrival traveltime is used to "demodulate" the wave field in frequency domain to reach the goal of resolving the large phase mismatch between the observed and calculated wave fields. Then the velocity is inverted by minimizing a new objective function which describes the mismatch between the observed "demodulated" wave field and corresponding calculated data below a threshold determined by the errors in the observation. In addition, in our algorithm, the first arrival phase is automatically used as a implicit constraint condition to help the algorithm to be convergent to the true model. Through this way, we can avoid the ambiquity problem of the phase between the observed and calculated wave field and obtain a robust wave equation inversion method. The computer simulation results show that when the perturbation of the velocity is as large as 35%, our inversion method still works while the old nonlinear inversion has already failed.

ACKNOWLEDGMENTS

The work is supported by the Seismic Tomography Project of Stanford University, a research consortium sponsored by companies of the oil and gas industry. The first author would like to thank Youli Quan for some useful discussion with him and Mark Van Shaack and Jesse Costa for their help in calculating the first arrival in the waveform.

REFERENCES

Harris, J.M. and G.Y. Wang, 1993, Diffraction tomography in a layered background medium, 63rd Annual Internal SEG Meeting, Expanded Abstract , .49-52

Harris, J.M., 1987, Diffraction tomography with arrays of discrete source and receivers: IEEE trans., GE-25, 448-455.

Harris, J.M., and Feng Yin, 1993, Nonlinear multi-frequency wave equation tomography, 63rd Annual Internal SEG Meeting, Expanded Abstract , 988-991.

Luo, Y. and Schuster, G.T., 1990, Wave equation traveltime plus waveform inversion, 60th Ann. Inter. Mtg of SEG, Expanded Abstracts, 1223-1225. and P.921.

Prott, R.G., and Worthington, M.H., 1990, Inverse theory applied to multi-source cross-hole tomography, part 1: Acoustical wave equation method: Geophys. Prosp., 38, 287-310

Tarantola, A. etal, 1990, Nonlinear inversion of seismogram, state of the art, 60th Annual Internal SEG meeting, 1193-1198

Wu, R. S., and Toksoz, M.N., 1987, Diffraction tomography and multisource holography applied to seismic imaging: Geophysics, 52, 11-25

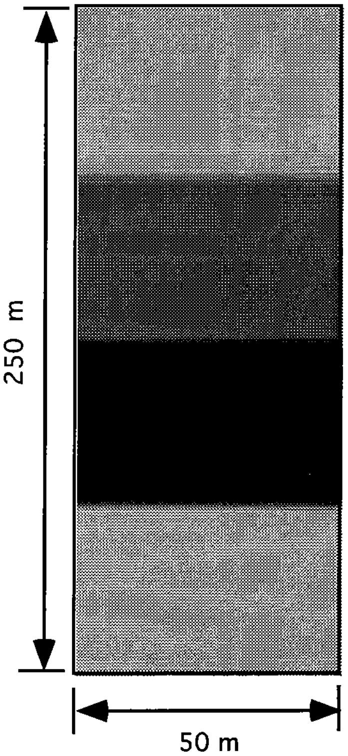

(a)

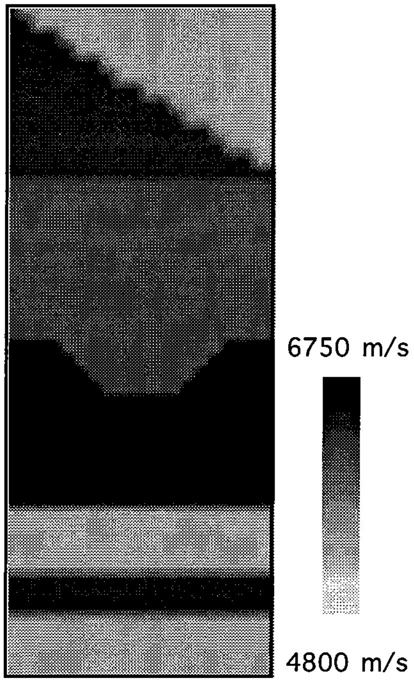

(b)

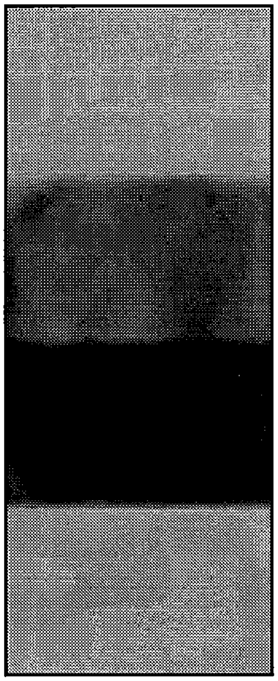

(c)

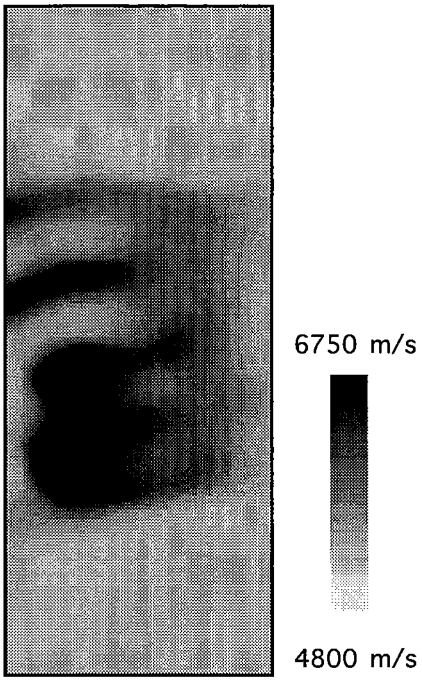

(d)

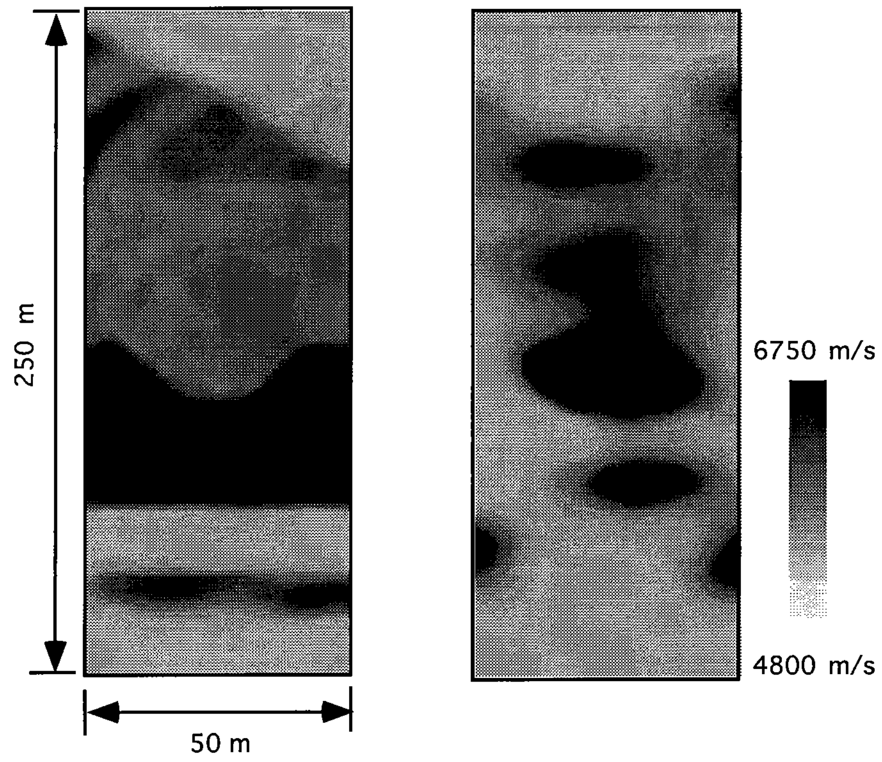

(e) (f)

PAPER K

ACOUSTIC WAVE EQUATION TOMOGRAPHY USING A NEW MOMENT METHOD

Feng Yin and Jerry M. Harris

ABSTRACT

We review a new moment method of solving the acoustical scattering equation, and then apply this method to non-linear wave equation tomography. We describe the formulation, the implementaion, and numerical testing of the method. The main characteristic of this method is that a bilinear basis function is used instead of a pulse basis function to evaluate the Green function, total field, and scattering potential at any arbitray point of the image region. In this way, the integral equation may be discretized to arbitrary fineness in order to increase the accuracy of the computations. From simulation tests, we find that this method is accurate and the number of inversion unknowns can be greatly reduced. We utilize this method in solving a non-linear wave equation inverse problem.

INTRODUCTION

In recent years, some researchers made effort to apply the wave equation tomography to real data with mixed results. Some used the time-domain waveform data to invert for velocity; others used the frequency domain wave field. In frequency domain methods, the wave field in the inhomogenous media is required. There are two types of the methods useful for obtaining this wave field. One is to solve the wave equation in its derivative form, e.g., finite differences (Pratt, 1988), or boundary element methods (Barhe, 1982). Another is to solve the scattering integral equation, e.g., moment method using pulse basis function (Richmond, 1965). The moment method is especially useful for modeling the wave field in a local region of interest rather than a larger area as in finite difference methods. And with the moment method, the Frechet derivative for inversion is easy to derive.

However, it is known that pulse basis functions do not produce accurate representation with the method of moments for pixel sizes larger than about 0.1 wavelength. Therefore, for large scale imaging problems, we must invert a huge matrix in order to find the wave field in the inhomogenous media. This is the main problem of the moment method. Therefore, up to now, there are many authors who are attempting to improve this method (Johnson, 1983, Steinberg, 1993, Zhuck, 1994). To develop a more efficient numerical solution for the 2-D wave propagation in the inhomogeneous media, we develop a new variations on the moment method. In our method, we discretize the integral equation using bilinear basis functions instead of pulse basis functions.. In this way, we can not only increase the accuracy of the calculation of wave field, but also reduce the number of pixels representing the field. And from this method, the Frechet derivative for non-linear wave equation inversion is easy to derive. Then we apply this method to non-linear wave equation inversion and test the validity of the method.

A NEW MOMENT METHOD FOR SOLVING SCATTERING EQUATION

In this paper, we restrict ourselves to the acoustic wave propagation in 2-D inhomogeneous media..In the frequency domain, we have:

$$(\nabla^2 + \frac{\omega^2}{c^2(\boldsymbol{r})})u(\boldsymbol{r},\omega) = -\delta(\boldsymbol{r}-\boldsymbol{r}_s) \tag{1}$$

where, $c(\boldsymbol{r})$ is the velocity of the compressional wave, **r** is the position vector, $u(\boldsymbol{r},\omega)$ is the pressure, and ω is the angle frequency. Let us define

$$M(\boldsymbol{r}) = 1 - \frac{c_0^2}{c^2(\boldsymbol{r})} \tag{2}$$

and let

$$u(\boldsymbol{r}) = u^i(\boldsymbol{r}) + u^s(\boldsymbol{r}), \tag{3}$$

then the integral equation corresponding to Eqn. (1) can be written

$$u(\boldsymbol{r}) = u^i(\boldsymbol{r}) - k^2 \int_{\Omega} M(\boldsymbol{r}')u(\boldsymbol{r}',\omega)G(k|\boldsymbol{r}-\boldsymbol{r}'|)d\boldsymbol{r}' \tag{4}$$

where $k = \omega/c_0$, Ω is the object region. As shown in Figure 1, the object region is divided into L_a pixels with N nodes, that is, $\Omega = \Omega_1 \cup \Omega_2 \cdots \cup \Omega_{L_a}, \Omega_i \cup \Omega_j (i \neq j)$.

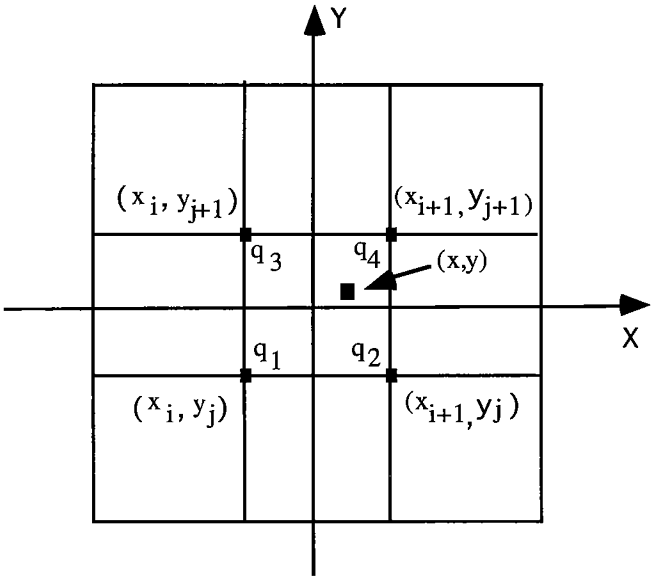

Figure 1: The discretized form of the object region. $q_1,q_2.q_3$ and q_4 denote the nodes (x_i,y_j), (x_{i+1},y_j), (x_i,y_{j+1}) and (x_{i+1},y_{j+1})

We then have

$$u(\boldsymbol{r}) = u^i(\boldsymbol{r}) - k^2 \sum_{i=1}^{L_a} \int_{\Omega_i} M(\boldsymbol{r}')u(\boldsymbol{r}',\omega)G(k|\boldsymbol{r}-\boldsymbol{r}'|)d\boldsymbol{r}'. \tag{5}$$

When $\boldsymbol{r}'$ is located in Ω_i, (xi,yj),(xi+1,yj),(xi,yj+1),(xi+1,yj+1) are used to denote the four nodes of the cell Ω_i as shown in Figure 1. We use (x,y) to denote a point within the cell; Δx and Δy are the intervals of x and y directions, respectively. When $x_i \le x \le x_{i+1}$, $y_i \le y \le y_{i+1}$, define

$$\rho_{ip} = \begin{cases} f_1 & ip = (j-1)\times mx + i \\ f_2 & ip = (j-1)\times mx + i + 1 \\ f_3 \quad \text{when} & ip = (j-1)\times mx + i + mx \\ f_4 & ip = (j-1)\times mx + i + mx + 1 \\ 0 & ip = others \end{cases} \tag{6}$$

where mx is the total numbers of the nodes in the x direction.

$$f_1 = 1 - \frac{(x-x_i)}{\Delta x} - \frac{(y-y_i)}{\Delta y} - \frac{(x-x_i)(y-y_j)}{\Delta x \Delta y} \tag{7}$$

$$f_2 = \frac{(x-x_i)}{\Delta x} - \frac{(x-x_i)(y-y_j)}{\Delta x \Delta y} \tag{8}$$

$$f_3 = \frac{(y-y_i)}{\Delta y} - \frac{(x-x_i)(y-y_j)}{\Delta x \Delta y} \tag{9}$$

$$f_4 = \frac{(x-x_i)(y-y_j)}{\Delta x \Delta y} \tag{10}$$

$M(\boldsymbol{r})$, $u(\boldsymbol{r})$ and $G(\boldsymbol{r};\boldsymbol{r}',k)$ are expanded using the basis function $\{\rho_{ip}(x,y)\}$. We have

$$M(\boldsymbol{r}) = \sum_{l=1}^{N} \rho_l \cdot M_l \tag{11}$$

$$u(\boldsymbol{r},k) = \sum_{n=1}^{N} \rho_n u_n \tag{12}$$

$$G(\boldsymbol{r};\boldsymbol{r}',k) = \sum_{m=1}^{N} \rho_m \cdot G_m \tag{13}$$

where N is the total number of the nodes in the object area; O_l,, u_n, and G_m represent the value of $M(\boldsymbol{r})$ at the lth node, $u(\boldsymbol{r},k)$ at nth node, and $G(\boldsymbol{r};\boldsymbol{r}')$ at mth node in row order, respectively.

For the sake of simplicity, q1, q2, q3 and q4 are used to represent the nodes $(x_i, y_j), (x_{i+1}, y_j), (x_i, y_{j+1})$ and (x_{i+1}, y_{j+1}), respectively. Integrating Eqns (11)-(13) into equation (4), we obtain

$$\sum_{l=1}^{N} A_{jl} u_l = u_l^i \tag{14}$$

where N is total number of the nodes, and when $l \neq j, l \neq j-1, l \neq j-mx-1$, $l \neq j-mx-2$, and

$$A_{jl} = -k^2 (B_l H^{(1)}_{l,La+1} + C_l H^{(2)}_{l,2} H^{(1)}_{l,La-2} + D_l H^{(2)}_{l,mx-1} H^{(1)}_{l,L_a-mx-1} + E_l H^{(2)}_{l,mx-2}) \tag{15}$$

In above equation

$$H^{(1)}_{l,l'} = \begin{cases} 1 & l < l' \\ 0 & l \geq l' \end{cases} \tag{16}$$

$$H^{(2)}_{l,l'} = \begin{cases} 0 & l < l' \\ 1 & l \geq l' \end{cases} \tag{17}$$

$$\begin{aligned} B_l = \{ & \tfrac{1}{16} Q_1(q_1) Q_2(q_1) + \tfrac{1}{48} [Q_1(q_2) Q_2(q_2) + Q_1(q_3) Q_2(q_3) + Q_1(q_2) Q_2(q_1) + \\ & Q_1(q_1) Q_2(q_2) + Q_1(q_3) Q_2(q_1) + Q_1(q_1) Q_2(q_3)] + \tfrac{1}{144} [Q_1(q_4) Q_2(q_4) + \\ & Q_1(q_4) Q_2(q_1) + Q_1(q_4) Q_2(q_3) + Q_1(q_1) Q_2(q_4) + Q_1(q_2) Q_2(q_3) + \\ & Q_1(q_2) Q_2(q_4) + Q_1(q_3) Q_2(q_2) + Q_1(q_3) Q_2(q_4) + Q_1(q_4) Q_2(q_2)] \} \Delta x \Delta y \end{aligned} \tag{18}$$

$$\begin{aligned} C_l = \{ & \tfrac{1}{16} Q_1(q_2) Q_2(q_2) + \tfrac{1}{48} [Q_1(q_1) Q_2(q_1) + Q_1(q_4) Q_2(q_4) + Q_1(q_2) Q_2(q_1) + \\ & Q_1(q_1) Q_2(q_2) + Q_1(q_4) Q_2(q_2) + Q_1(q_2) Q_2(q_4)] + \tfrac{1}{144} [Q_1(q_3) Q_2(q_3) + \\ & Q_1(q_3) Q_2(q_1) + Q_1(q_1) Q_2(q_3) + Q_1(q_4) Q_2(q_1) + Q_1(q_1) Q_2(q_4) + \\ & Q_1(q_2) Q_2(q_3) + Q_1(q_3) Q_2(q_2) + Q_1(q_4) Q_2(q_3) + Q_1(q_3) Q_2(q_4)] \} \Delta x \Delta y \end{aligned} \tag{19}$$

$$\begin{aligned} D_l = \{ & \tfrac{1}{16} Q_1(q_3) Q_2(q_3) + \tfrac{1}{48} [Q_1(q_1) Q_2(q_1) + Q_1(q_4) Q_2(q_4) + Q_1(q_4) Q_2(q_3) + \\ & Q_1(q_3) Q_2(q_4) + Q_1(q_3) Q_2(q_1) + Q_1(q_1) Q_2(q_3)] + \tfrac{1}{144} [Q_1(q_2) Q_2(q_2) + \\ & Q_1(q_2) Q_2(q_1) + Q_1(q_1) Q_2(q_4) + Q_1(q_2) Q_2(q_3) + Q_1(q_1) Q_2(q_2) + \\ & Q_1(q_4) Q_2(q_1) + Q_1(q_3) Q_2(q_2) + Q_1(q_4) Q_2(q_2) + Q_1(q_2) Q_2(q_4)] \} \Delta x \Delta y \end{aligned} \tag{20}$$

and

$$E_l = \{\tfrac{1}{16}Q_1(q_4)Q_2(q_4) + \tfrac{1}{48}[Q_1(q_2)Q_2(q_2) + Q_1(q_3)Q_2(q_3) + Q_1(q_2)Q_2(q_4) + Q_1(q_4)Q_2(q_3) + Q_1(q_4)Q_2(q_2) + Q_1(q_3)Q_2(q_4)] + \tfrac{1}{144}[Q_1(q_2)Q_2(q_1) + Q_1(q_1)Q_2(q_4) + Q_1(q_1)Q_2(q_2) + Q_1(q_1)Q_2(q_3) + Q_1(q_4)Q_2(q_1) + Q_1(q_3)Q_2(q_1) + Q_1(q_3)Q_2(q_2) + Q_1(q_1)Q_2(q_1) + Q_1(q_2)Q_2(q_3)]\}\Delta x\Delta y \tag{21}$$

where $Q_1(q_i) = G_{q_i}$ and $Q_2(q_i) = M_{q_i}$ .when $(l = j, l = j-1, l = j-mx-1, l = j-mx-2)$

$$A_{jl} = \frac{i}{2}[\pi ka H_0^{(1)}(ka) + 2i] * M_l \tag{22}$$

where a=$\sqrt{\Delta x \cdot \Delta y / \pi}$. Thus, equation (14) can be written as

$$\boldsymbol{AU} = \boldsymbol{U}^i \tag{23}$$

where $\boldsymbol{U} = (u_1, u_2, \cdots, u_N)^t, \boldsymbol{U}^i = (u_1^i, u_2^i, \cdots, u_N^i)^t$, Therefore, the total field can be obtained by solving equation (23), we have

$$\boldsymbol{U} = \boldsymbol{A}^{-1}\boldsymbol{U}^i \tag{24}$$

After the total field is solved, the scattering field at r_m outside the object region can be expressed as

$$u_m^s = \sum_{l=1}^{N} A_{ml} M_l \tag{25}$$

where A_{ml} equals to equation (14), and $Q_1(q_i) = G(q_i), Q_2(q_i) = u(q_i)$. Therefore, the scattering field in frequency domain can be derived by equation (24) and the waveform of the scattering can be derived by applying inverse Fourier transform to the wave field in the fequency domain.

APPLICATION TO NON-LINEAR WAVE EQUATION INVERSION

Suppose now that the observed wave field is $U^0(\mathbf{r}_s, \mathbf{r}_s, \omega)$ $(1 \le s \le S, 1 \le g \le G)$. We wish to use these observed data to determine a model M=$(m_1, m_2, \cdots, m_N)$ from which the corresponding calculated wave field matches the observed wave field. Therefore, we should have a measure of fit, that is, we should establish a measure for assessing the degree of mismatch between the observed data and the synthetic data. We choose the squared L2 norm of the observed and calculated data. That is, our goal is to minimize the function

$$J(M) = \tfrac{1}{2}\sum_{s}^{S}\sum_{g}^{G} \| U^o(r_s, r_g, \omega) - U^c(r_s, r_g, \omega) \|^2 = \text{minimum} \tag{26}$$

where U^o and U^c are measured field data and calculated field data, respectively. The wave equation inverse problem in crosswell geometry is not only nonlinear, but extremely non unique, that is, ill-posed. In order to derive a stable solution of the inverse problem and prevent unrealistic behavior of the model parameters, we impose a form of regularization on Eqn. (26) as follows:

$$Q(\mathbf{M}) = \tfrac{1}{2}\sum_{s}^{S}\sum_{g}^{G} \| U^{o}(r_s, r_g, \omega) - U^{c}(r_s, r_g, \omega) \|^2 + \lambda H(\mathbf{M}) = \text{minimum} \tag{27}$$

where H(M) is the regularization term, e.g., a smoothing operator. Then, we use a steepest gradient method, conjugate gradients to solve (27). Eqn. (27) is quadratic, therefore, not only the first derivative, but also the second derivative is required. A subspace method (Kennet, etc., 1987, Skilling, et al, 1987) in which the Hessian matrix is used will be utilized to solve Eqn. (27).

In the subspace method, the current model is updated by a small model perturbation which is determined in a small subspace, that is

$$\mathbf{M}^{(q+1)} = \mathbf{M}^{(q)} + \Delta\mathbf{M}^{(q)} \tag{28}$$

$$\Delta\mathbf{M}^{(q)} = x_1\mathbf{e}_1 + x_2\mathbf{e}_2 + x_3\mathbf{e}_3 \tag{29}$$

where $\mathbf{e}_1, \mathbf{e}_2$ and $\mathbf{e}_3$ are the basis of the subspace, and they are

$$(\mathbf{e}_1)_i = \frac{\partial J}{\partial m_i},\ (\mathbf{e}_2)_i = \frac{\partial H}{\partial m_i},\ (\mathbf{e}_3)_i = \sum_k \frac{\partial^2 J}{\partial m_i \partial m_k}\frac{\partial Q}{\partial m_k} \tag{30}$$

and x_1, x_2 and x_3 can be determined by the subspace method (Skilling,1984, Kennet, et al, 1987).

We can see that one of main points of the inversion step is the calculation of the Frechét derivative and the second derivative of the quadratic function. After the wave fields are calculated in the current background media, the total wave field at receiver array can be derived by equation (25):

$$U\ (\mathbf{r}_s, \mathbf{r}_g, \omega) = U^i(\mathbf{r}_s, \mathbf{r}_g, \omega) + \sum_j A_{ji} m_i \ \ (j = 1, \cdots, G \cdot S) \tag{31}$$

The Frechét derivative for inversion and the second derivative of the objective function can be easily expressed as

$$\frac{\partial J}{\partial m_i} = \sum_{l}^{SGL} R(A_{li}) \cdot \left[R(U_l^c) - R(U_l^o) \right] + I(A_{li}) \cdot \left[I(U_l^c) - I(U_l^o) \right] \tag{32}$$

$$\frac{\partial^2 J}{\partial m_i \partial m_k} = \sum_{l}^{SGL} [R(A_{li}) \cdot R(A_{lk}) + I(A_{li}) \cdot R(A_{lk})] \tag{33}$$

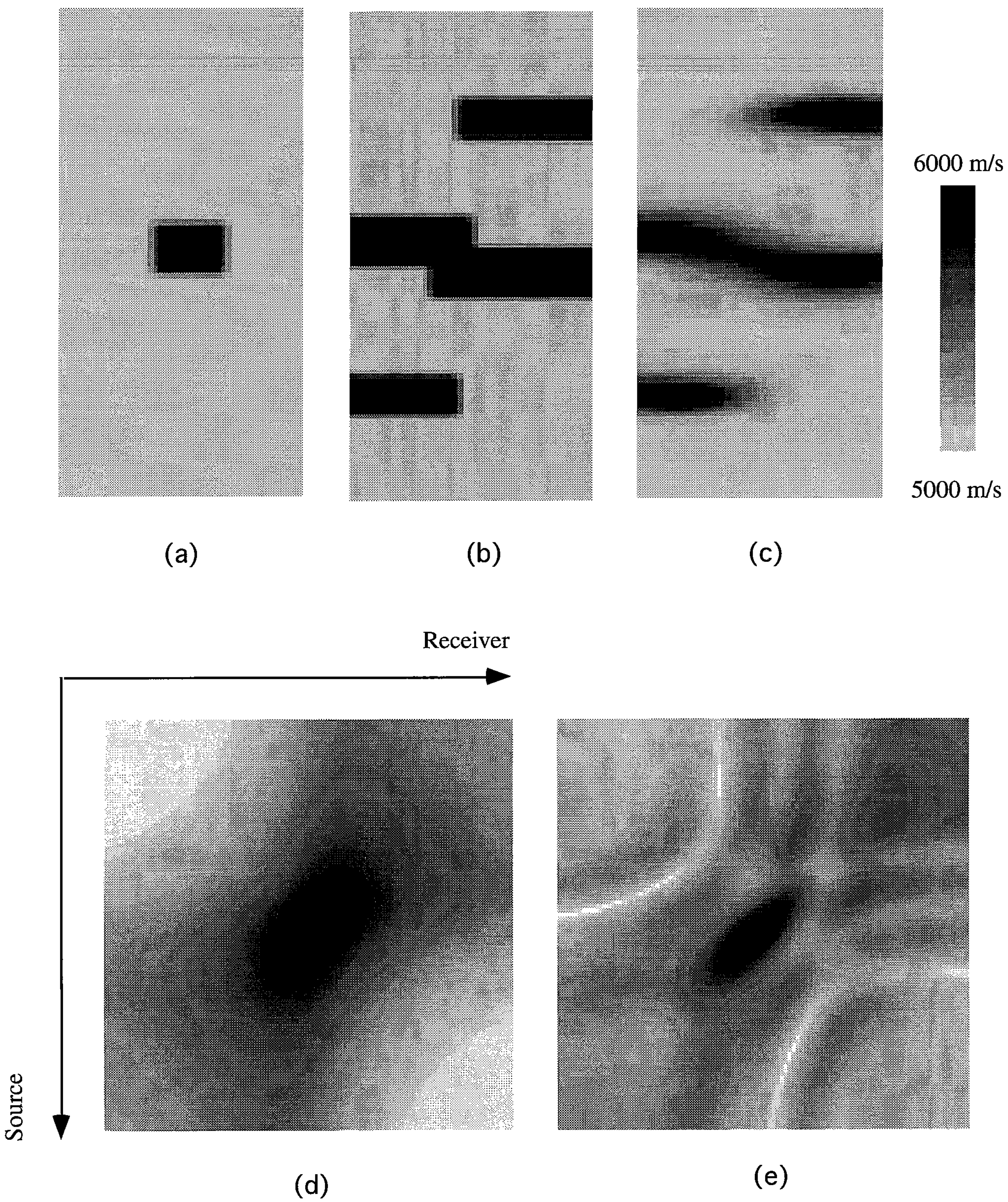

Figure 2. (a) Synthetic model I. (b) Synthetic model II. (c) Reconstructed result of model II. (d) Amplitude of scattered field of model I. (e) Amplitude of scattered field of model II

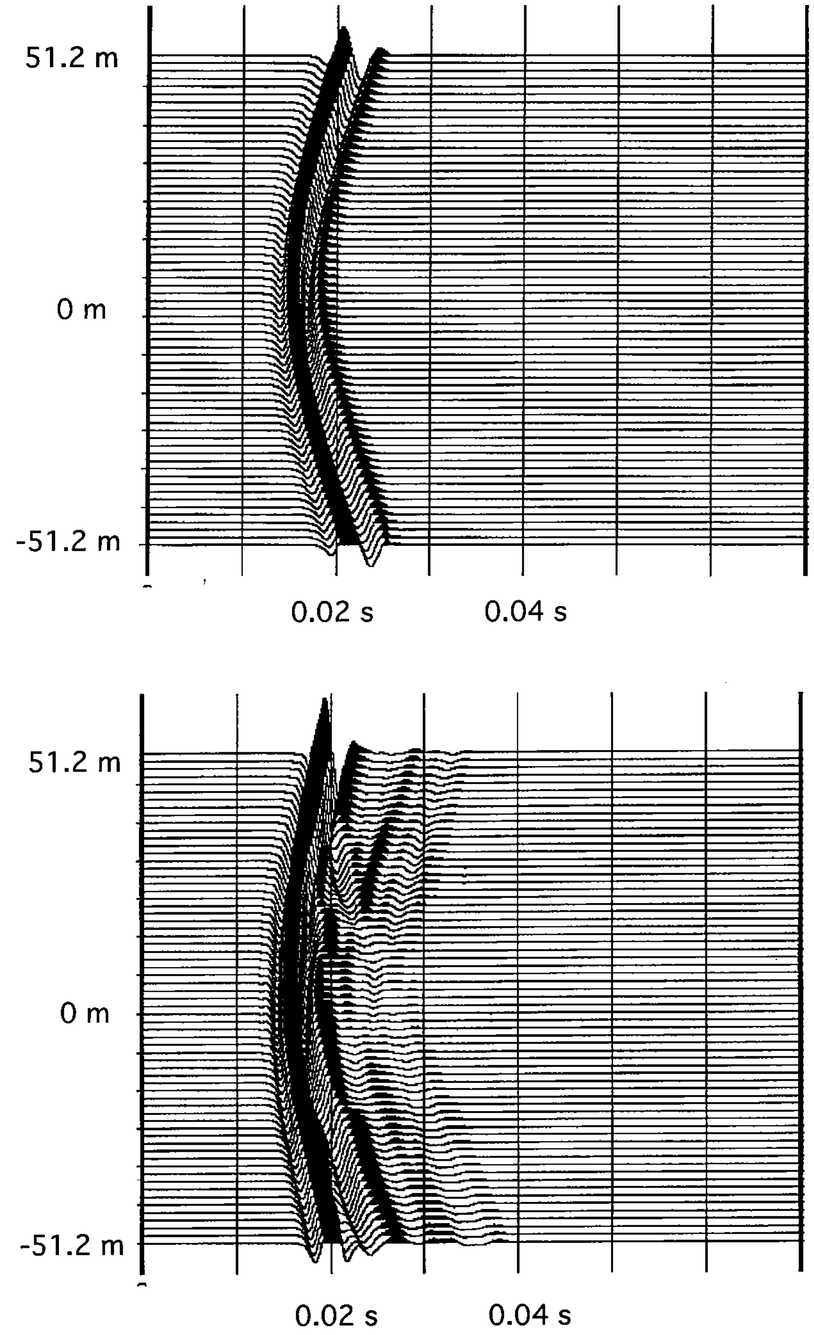

Figure 3: (a) The waveform of the scattered field by model I. (b) The waveform of the scattered field by model II

where R and I means taking real part and imaginary part. S, G, and L are the total number of the discrete sources, receivers, and frequencies, and up-script c and o mean the calculated and measured value.

Because analytical formulas for the Frechét derivative can be obtained for our numerical method, we use them to invert the model by non-linear iterative methods of

Eqns. (29). This is one of the advantages of using the integral equation over the differential equation.

NUMERICAL SIMULATIONS

Figures 2 (a) and (b) are two models for forward calculation. The velocities are denoted in the pictures. We locate 100 sources at x=-30 m in equal depth Δs=1.6 m, and put 100 receivers at x=+30 m in equal depth Δr=1.6 m. Figures 2 (c) and (d) are the amplitudes of the scattering wave field corresponding to the models using out moment method. In order to test our method effectively, we also applied this forward method to the nonlinear wave equation inversion, figure 2 (e) is the reconstructed result by our moment inversion method. Finally, we applied inverse Fourire transform to the scattering field in frequency domain to obtain the waveform of the scattering field. Figures 3 (a) and (b) are the scattering waveforms of one common shot gather where a ricker wavelet of 300 Hz center frequency is used and the $\Delta x = \Delta y = 1/6$ $\Delta x = \Delta y = 1/6 \times \lambda_{\min}$.

CONCLUSIONS

We reviewed a new moment method for evaluating the wave field in the inhomogeneous media in this paper. With this method, the wave field not only can be calculated accurately when there are 6 nodes per wavelength instead of 10 pixels per wavelength with the pulse basis function. Also, the Frechet derivative is easy to derive for non-linear wave equation inversion. Computer simulations show our method is effective and very useful in solving both forward and inverse problems.

ACKNOWLEDGMENTS

This work is supported by the Seismic Tomography Project of Stanford University, a research consortium sponsored by companies of the oil and gas industry.

REFERENCES

Bathe, K.J., Finite Element Procedures in Engineering Analysis, Englewood Cliffs, NJ: Prentice Hall, Inc., 1982

Ben Zion and Yehuda Leviatan, On the use of Wavelet Expansions in the method of moments, IEEE Transaction on antennas and propagation, vol. 41, no.5, 1993

Nickolay P. Zhuck and Alexander G. Yarovoy, Two-dimensional scattering from an inhomogeneous dielectric cylinder embedded in a stratified medium: Case of TM polarization, IEEE Transaction on antennas and propagation, vol. 42, no.1, 1994.

Pratt, R.G., Frequency-domain elastic wave modeling by finite differences: A tool for crosshole seismic imaging, Geophysics 55: 626-623, 1990

Richmond, J.H., Scattering by a dielectric cylinder of arbitary cross section shape, IEEE Trans, Ant. Prop. 13:334-341, 1965

Steven A. Johnson and Michael L. Tracy, Inverse Scattering solution by a sinc basis, multiple source, moment method --Part I : Theory, Ultrosonic Imaging 5, 361-375, 1983

Weng Chow Chew and Cai-cheng Lu, The use of Huygens' Equivalence principle for solving the volume integral equation of scattering, IEEE Transaction on antennas and propagation, vol. 41, no.7, 897-904,1993

PAPER L

A STUDY OF ACOUSTIC WAVE EQUATION TOMOGRAPHY APPLIED TO ANELASTIC SYNTHETIC DATA THAT INCLUDES BOREHOLE EFFECTS

Feng Yin and Youli Quan

ABSTRACT

In order to understand the inversion property of wave equation tomography when it is applied to real data, we used a synthetic elastic wave field with attenuation to better simulate the real wave field recorded in real cross well experiments. We used the simulation method described in the paper (Quan, Chen, and Harris, 1995). However, we apply our *acoustical* wave equation tomography method in the frequency domain to this synthetic data set to study the inversion properties, for example, its robustness, the relationship between artifact and noise (e.g., S wave, converted wave, etc.) in the wavefield, borehole effects on the inversion, etc.. This work shows that the resolution of acoustical equation tomography is higher than traveltime tomography as predicated by the theory, and the artifacts in the image can be controlled in an acceptable way if we can accurately extract the scattered field. We believe that the borehole elastic wave modeling method (Quan, et al, 1995) is very useful for testing the inversion property of acoustic wave equation tomography before it is applied to a real dataset.

INTRODUCTION

Acoustical wave equation tomography methods for cross well imaging have been studied for many years. Presently, they are being applied to real data (Harris and Wang, 1993, Song et al., 1995, Zhou, et al, 1995). But the real data usually are recorded in the anelastic media between cased boreholes. When we apply the acoustic wave equation tomography methods to this kind of data, it is hard for us to understand the properties of our simplified model based on our acoustic wave equation when it is applied to real data usually involving S waves, converted waves, casing effects, and radiation patterns, etc. Therefore, we wish to apply acoustical wave equation tomography to the synthetic elastic wave field with attenuation in cased boreholes before we apply them to real data. The literature is limited in this area. The possible reasons are that the methods which are able to simulate the wave field recorded in two dimensional inhomogenous anelastic media between cased boreholes have not been well developed. Fortunately, a method which can simulate the wave field in radially layered media with horizontal structures between cross well with casing has been developed in this year (Quan, Chen and Harris, 1995). Therefore, we can utilize this method to produce the synthetic elastic wave field with attenuation between cased borehole, and apply our acoustic wave equation tomography method to the synthetic dataset to test its inversion properties. Then we can analyze the factors which affect the quality of our imaging method: its robustness, the relationship between inversion artifacts and noise in the wavefield, the error of estimating source function, borehole effects on the inversion, etc.

We first studied the application of acoustic wave equation tomography to the anelastic synthetic data without wavefield separation. We also tested the accuracy and robustness of the codes for elastic forward modeling. We found that it is possible to apply wave equation tomography to the elastic wave field and the inversion artifacts can be controlled to an acceptable level if we can accurately obtain the scattered wave field. The resolution is much higher than travel time tomography. The results show that the method and code for elastic waves modeling in radially layered media with horizontal structure is very useful and helpful for testing the inversion property of the wave equation tomography based on the acoustical equation.

THE TEST OF WAVE EQUATION TOMOGRAPHY APPLIED TO ANELASTIC SYNTHETIC DATA

1. Wave Field Imaging and Travel Time Tomography method

The imaging method we used is based on the acoustical equation in the frequency domain. We have

$$(\nabla^2 + \frac{\omega^2}{c^2(\boldsymbol{r})})U_t(\boldsymbol{r},\omega) = -\delta(\boldsymbol{r} - \boldsymbol{r}_s) \tag{1}$$

where, $c(\boldsymbol{r})$ is the velocity of the compression wave, $\boldsymbol{r}$ is the position vector, $\boldsymbol{r}_s$ the source position, $U_t(\boldsymbol{r},\omega)$ is the pressure field, and ω is the angle frequency. The scattered wave field is expressed as

$$U(r_s,r_g) = -\omega^2 \iint dxG(\boldsymbol{r},\boldsymbol{r}_g,\omega)O(\boldsymbol{r})U_t(\boldsymbol{r},\boldsymbol{r}_s,\omega)d\boldsymbol{r} \tag{2}$$

where $O(\boldsymbol{r}) = \frac{2\delta v(\boldsymbol{r})}{v(\boldsymbol{r})}$, $U(r_s,r_g)$ is the measured scattered field. The goal of the inversion can be reached by minimizing a representative objective function. In this paper an l_2 norm of the data residuals is used as the objective function. Then the gradient direction can be used in iterative optimization methods to minimize the objective function (Harris and Yin, 1994).

The gradient of the objective function $Q(\boldsymbol{m})$ with respect to the model space $\boldsymbol{m}$ can be derived as

$$g = \frac{1}{2}\frac{\partial Q}{\partial m} = -\frac{2\omega 2}{v(r)^3}\sum_{s,g}[G(r,r_g,\omega) * U_t(r,r_s,\omega)]^* \delta U(r_s,r_g,\omega) \tag{3}$$

The simplest way for updating the current model can be obtained from

$$v_{i+1} = v_i + \beta * \delta v \tag{4}$$

where δv = g, and β is a damping factor.

In the travel time tomography, the method we used is the combination algorithm of ART and SIRT.

2. Numerical Experimental setup and results

Figure 1(a) shows the cross-well imaging system, including a cased borehole filled with water. Between the wells, there is a 2-D inhomogeneous body with a fault embedded in a homogeneous background with a P wave velocity of 5000 m/s, S wave velocity of 2900 m/s ,and a Q value of 300. The P wave velocity of the inhomogeneous body is 5800 m/s and the S wave velocity is 3300 m/s, and the Q value is 300. The model used for forward modeling and imaging is shown by Figure 1(b). The cased well contains 51 sources and the other well is the receiver well which contains 51 receivers. The vertical spacing of the source and receiver is 2 meters. The distance between the source and receiver well is 60 meters. We use the method and codes described in another paper (Quan, Chen and Harris, 1995) to produce a synthetic elastic wave field recorded in the horizontal direction, which is the total field. Then we remove the inhomogeneous body and produce a synthetic wave field recorded in the horizontal direction, which is the incident field. We derive the scattered field by subtracting the incident field from the total field.

We transformed the waveforms from the time domain to the frequency domain from the numerical synthetic scattered dataset to obtain the wave field in frequency domain. The figure 1(c) shows the real part of the scattered wave field in the frequency domain with frequency of 300 Hz in which the x direction is receiver line and z direction are source line. Then we picked one source gather from the synthetic seismogram datasets. Figures 2 (a), (b) and (c) are one source gather of the seismograms of the total field, the incident field, and the scattered field, respectively.

Then, we used the imaging methods described in the section (2) to conduct wave field imaging and travel time tomography. The reconstruction of the object in the slowness map are shown in figure 3, in which the figure 3(a) is the reconstructed result using one frequency of 300 Hz; figure 3(b) is the result using 5 frequencies at 233, 266, 299, 332, 365 Hz together; figure 3(c) is the travel time tomogram using the combination algorithm of ART and SIRT. From the imaging result and test, we derived following conclusions.

CONCLUSIONS

We have studied the application of acoustical wave equation tomography to the elastic wave field with attenuation in a simple model including a well with casing. With this simply model, we find that the artifacts due to converted wave and S wave and tube wave can be controlled under an acceptable level if we can derive an accurate scattering wave field. The resolution of wave equation tomography is much higher than travel time tomography as predication by theory analysis. The results show that the method and codes used to simulate the elastic wave with attenuation are helpful to test the property of our wave equation tomography before they are applied to real data. In the future, we will continue to test various factors which will affect the quality of the tomogram. This include the error of extracting the scattered wave field, error of estimating the source function, radiation pattern effect in more complicated models. We will continue to develop more accurate and fast acoustical modeling method, for arbitrary 2 dimensional inhomogeneous media to be used in acoustical wave equation tomography

ACKNOWLEDGMENTS

The work is supported by the Seismic Tomography Project of Stanford University, a research consortium sponsored by companies of the oil and gas industry. We would like to thank Nicholas Smalley for his help in editing this report.

REFERENCES

Harris Jerry M. and Gang Wang, Diffraction tomography for inhomogeneities in a layered background, Expanded Abstract of 63rd Anuual meeting of SEG, 49-52, 1993.

Harris Jerry M. and Feng Yin, Nonlinear multi-frequency wave equation tomography, Expanded Abstract of 64rd Anuual meeting of SEG, 988-991, 1994.

Quan Youli, Xiaofei Chen and Jerry M. Harris, Synthetics of elastic waves in radially layered media with horizontal structures, STP report 95 in this volume.

Song Z.M. and P. R. Williamson, and R.G. Pratt, Frequency-domain acoustical-wave modeling and inversion of crosshole data, Part2 - Inversion method, synthetic experiments, and real data results, Geophysics, 796-809, 1995

Zhou C., W. Cai, Y. Luo, G.T., Schuster, and S. Hassanzadeh, Acoustical wave equation traveltime and waveform inversion of crosshole seismic data, 765-773, Geophysics, Vol. 60, No. 3, 1995

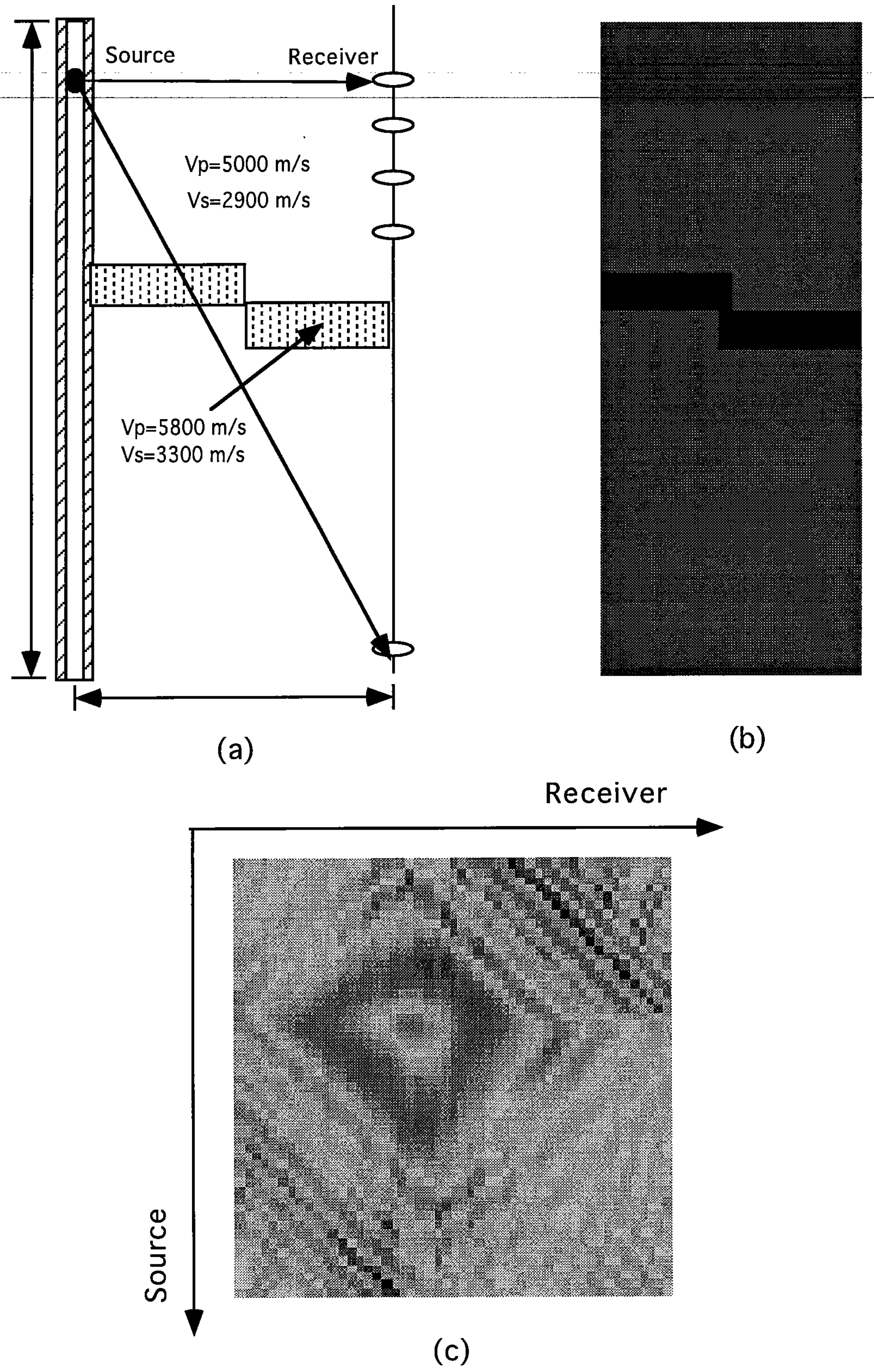

Figure 1 (a) The Cross well numerical experiment Geometry
(b) A fault Model for numerical test
(c) Scattering wave field in frequency domain

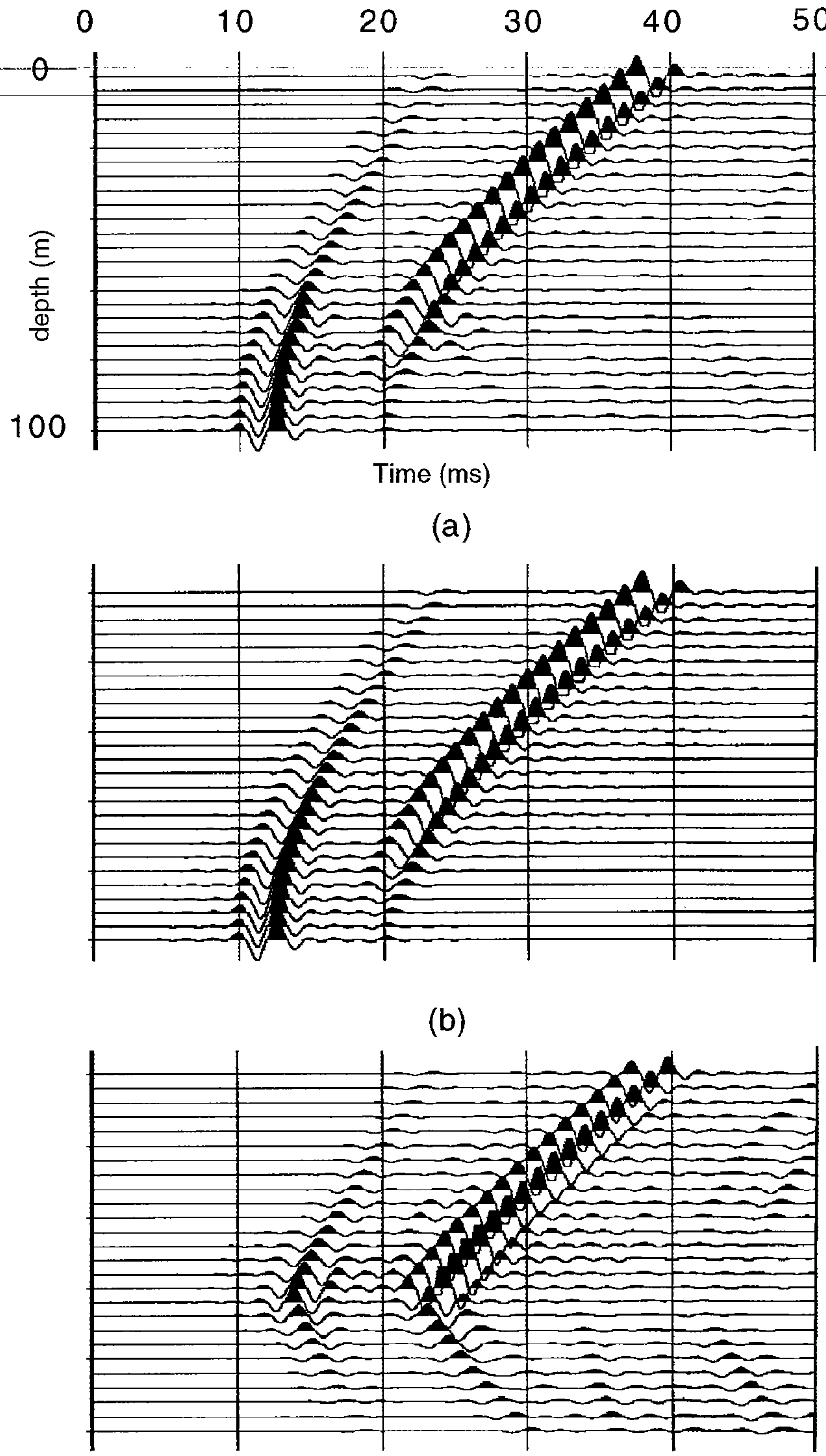

(a)

(b)

(c)

Figure 2: (a) One source gether of the elastic total wave field in cross well geometry shown by Figure 1
(b) One source gether of the elastic incident wave field
(c) One source gether of the elastic scattering field

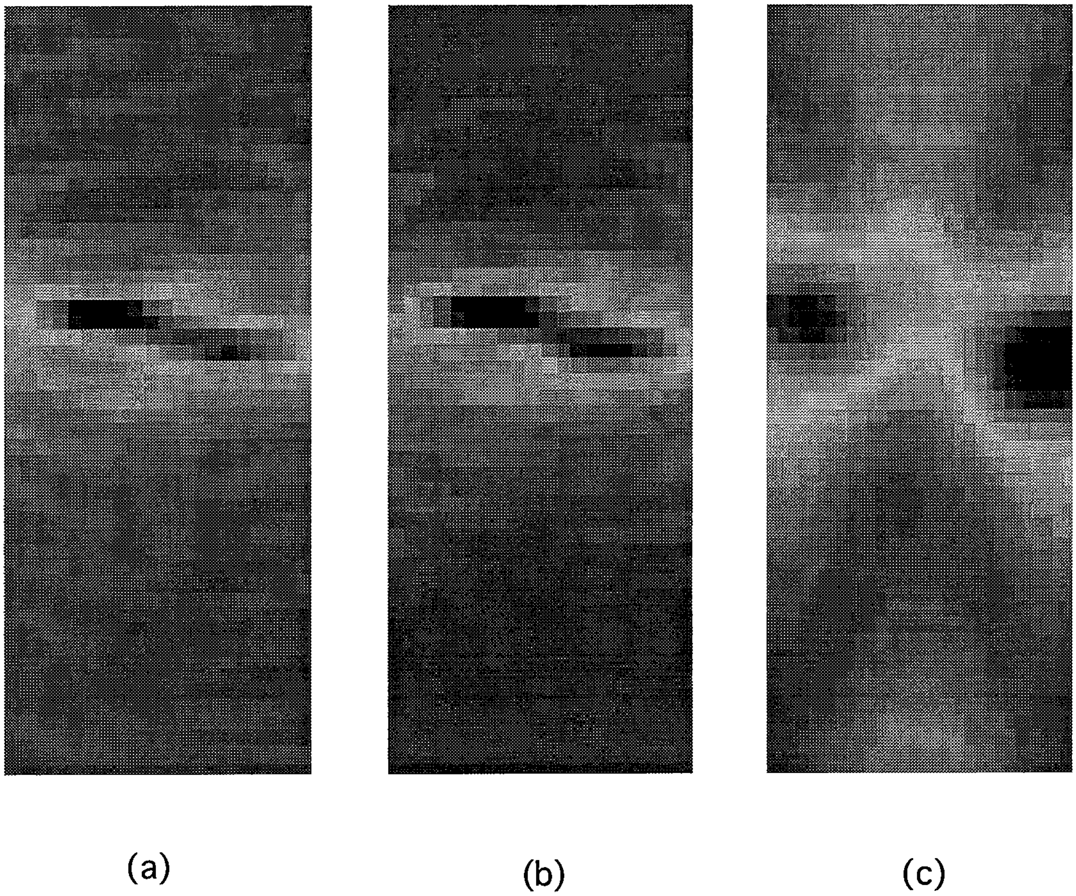

Figure 3: (a) Wave Field Backpropagation Imaging using scattering sfield shown by Figure 1 (c), the frequency = 300 Hz

(b) Wave field backpropagation imaging using multi-frequencies wave field, the frequency band is 233 - 365 Hz.

(c) Travel Time tomography derived by ART and SIRT together in which the iterations of ART and SIRT are 30, 40, respectively

Paper M

DIFFRACTION TOMOGRAPHY OF STRONGLY SCATTERING MEDIUM
PART I: USING PHASE EXTRAPOLATION

Guan Y. Wang

ABSTRACT

The existing diffraction tomographic techniques are mainly based on the Born approximation. Such methods are simple to implement but do not work well in a strongly scattering medium. We re-exam the widely used inverse scattering model and develop a formulation to include multiple scattering by estimating the scattered field inside the medium with the Fourier phase extrapolation technique. The method works well in the situation where the variation of the propagation speed due to inhomogeneity is small. The yield algorithm is the same as conventional diffraction tomography with the Born approximation. However, the individual diffraction projection of the scattering spectrum is obtained by solving the Toeplitz recursive equation in the transform domain.

INTRODUCTION

Diffraction tomography is used to reconstruct, from the observed scattered field, the spatial distribution of appropriate parameters in a medium. In its common form, diffraction tomography is formulated as an approximate inversion of the Helmholtz equation with a spatially varying coefficient. The inversion is accomplished in practice by first transforming the Helmholtz equation into an inhomogeneous one with constant coefficients. Two transformations leading to two different approximate inversions have been most commonly used, i.e., the Born and Rytov transformations (Devaney, 1984; Harris, 1987). See Appendix A for a summary about the Born approximation. These techniques substantially simplify the inversion problem and all for computational advantages of fast Fourier transform processing. The appealing feature of these methods is the fact that the inversion algorithms are non-iterative and computationally efficient. However, computational efficiency and algorithmic simplicity are accompanied by limitations on the ranges of validity for these methods.

The objective of this study is to reformulate the basic diffraction tomography algorithms to include the effects of multiple scattering. Therefore, the diffraction tomography methods will be able to work in strongly inhomogeneous medium. To take account the multiple scattering, the total field in the integral kennel is estimated by phase extrapolation or other techniques. In this paper, we present a formulation in which the total field is estimated with the Fourier phase extrapolation and the individual diffraction projection of the scattering spectrum from the receiver gather. This is obtained by solving the Toeplitz recursive equation. Once the spectrum of the object is obtained, the object function is reconstructed by the inverse Fourier transform.

TIME HARMONIC SOLUTIONS

Fourier integral techniques provide the most powerful method of analysis of wave propagation problems. By use of superposition it is possible to express a wave pulse as a superposition in frequency space of harmonic motions.

$$(\nabla^2 + k^2)\phi(r) = v(r)\psi(r), \qquad (1)$$

where ψ and ϕ are the total and scattered fields respectively. $k = \omega / v_0$ and $v = k^2 o(r)$. Notice that ω is angular frequency, v_0 the background velocity and o the strength of scatterer. The solution to equation (1) can be expressed as Lippmann-Schwinger integral equation,

$$\psi(r) = \varphi(r) + \int dr'\, G(r - r')v(r')\psi(r'). \qquad (2)$$

The asymptotic form of the wave function is

$$\psi(r) \to \varphi(r) + f(k,k')\frac{\exp(ikr)}{r}$$

$$f(k,k') = -\int dr'\, e^{-ik'\cdot r} v(r')\psi(r')$$

the coefficient f(k,k') of the outgoing wave is usually called the scattering amplitude. Notice that the scattering amplitude f(k,k') depends on the energy of the relative motion, the angle between the vector k and k', and the scattering potential. To calculate the scattering amplitude, it is necessary to know the solution of equation (2).

SPECTRUM REPRESENTATION

Equation (2) can be rewritten as two parts

$$\varphi(g,s) = -\int G(g,r)v(r)G(r,s)d^2r - \int G(g,r)v(r)\varphi(r,s)d^2r. \qquad (3)$$

The second term on the right hand of the equation (3) is the multiple scattering term which is responsible for the nonlinear effects of the interaction between scattered and multiple scattering waves, as indicated in figure 1.

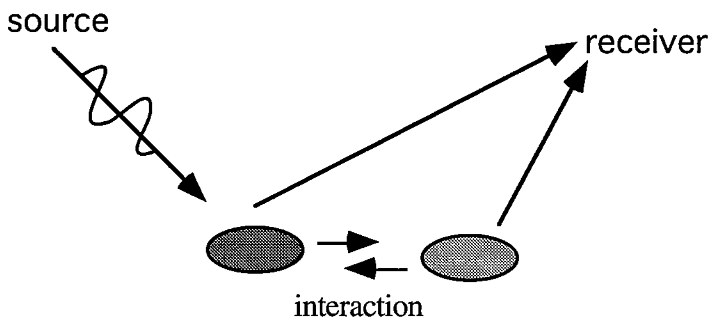

Figure 1. Illustration of scattering and multiple scattering.

For two dimensional problem, the Green's function in equation (3) is the first kind and zero order Hankel function, i.e.

$$G(r,s)=\frac{i}{4}H_0^{(1)}(k|r-s|),\ \text{and}\ \ G(g,r)=\frac{i}{4}H_0^{(1)}(k|g-r|).$$

The spectra of the 2-D Green's function along the source line and receiver line can be given by

$$G(r,k_s)=\frac{i}{2\gamma_s}\exp(i\gamma_s x_s)\exp(ik\hat{s}\cdot r),$$

and

$$G(k_g,r)=\frac{i}{2\gamma_g}\exp(-i\gamma_g x_g)\exp(-ik\hat{g}\cdot r),$$

which are in the form of a plane wave. After plane wave decomposition, the spectrum representation of equation (3) take the form of

$$\begin{aligned}\Phi(x_g,k_g|x_s,k_s)=&\frac{\exp(-i\gamma_g x_g+i\gamma_s x_s)}{4\gamma_g\gamma_s}\int v(x,z)\exp\{-i[(\gamma_g-\gamma_s)x+(k_g+k_s)z]\}dxdz\\&-\frac{i\exp(-i\gamma_g x_g)}{2\gamma_g}\int v(x,z)\varphi(x,z|x_g,k_s)\exp[-i(\gamma_g x-k_g z)]dxdz\quad.\end{aligned}\tag{4}$$

The scattered field at the observation locations is expressed as $\phi(x_g,z_g|x_s,z_s)$, and its spectrum is denoted as $\Phi(x_g,k_g|x_s,k_s)$. For many situations where the inhomogeneity, i.e., the scatterers are local concentrations, we can extrapolate the wave field approximately with a constant background velocity, as in the case of Fourier phase migration (Stolt, 1978), to obtain the scattering field at an arbitrary location, i.e.

$$\Phi(x,z|x_s,k_s)=\frac{1}{2\pi}\int\Phi(x_g,k_g|x_s,k_s)e^{i(\gamma_g x+k_g z)}dk_g,\tag{5}$$

where $\gamma_g=\sqrt{k_0^2-k_g^2}$ is the horizontal wave number. By noticing that the integrals on the right side of equation (5) are Fourier transforms, and substituting equation (5) into (4), we have

$$\begin{aligned}&\Phi(x_g,k_g|x_s,k_s)=A(\gamma_g,\gamma_s)V(\gamma_g-\gamma_s,k_g+k_s)-\\&\frac{B(\gamma_g)}{2\pi}\int dk''\varphi(x_g,k''|x_s,k_s)e^{-i\gamma''x_g}\int v(x,z)e^{-i[(\gamma_g-\gamma'')x+(k_g-k'')z]}dxdz,\end{aligned}$$

or

$$\Phi(x_g,k_g|x_s,k_s)=A(\gamma_g,\gamma_s)V(\gamma_g-\gamma_s,k_g+k_s)+ \\ -\frac{B(\gamma_g)}{2\pi}\int dk''\varphi(x_g,k''|x_s,k_s)e^{-i\gamma''x_g}V(\gamma_g-\gamma'',k_g-k''), \tag{6}$$

where

$$A(\gamma_g,\gamma_s)=\frac{\exp(-i\gamma_g x_g+i\gamma_s x_s)}{4\gamma_g\gamma_s},$$

$$B(\gamma_g)=\frac{i\exp(-i\gamma_g x_g)}{2\gamma_g}.$$

By defining $D_{k_s}(k_g)=\frac{\Phi(x_g,x_g|x_s,k_s)}{A(\gamma_s,\gamma_g)}$, the notations in equation (6) can be simplified as

$$D_{k_s}(k_g)=V(\gamma_g-\gamma_s,k_g+k_s) \\ -\frac{i\gamma_s\exp(-i\gamma_s x_s)}{\pi}\int dk''\varphi(x_g,k''|x_s,k_s)e^{-i\gamma''x_g}V(\gamma_g-\gamma'',k_g-k''), \tag{7}$$

or further simplified as

$$D_{k_s}(k_g)=V_{k_s}(k_g)-\frac{i\exp(-i\gamma_s x_s)}{\pi}\int dk''\varphi_{k_s}(k'')V_{k_s}(k_g-k''), \tag{8}$$

where

$$V_{k_s}(k_g)=V(\gamma_g-\gamma_s,k_g+k_s),$$

$$V_{k_s}(k_g-k'')=V(\gamma_g-\gamma'',k_g-k''),$$

and

$$\Phi_{k_s}(k'')=\Phi(x_g,k''|x_s,k_s)e^{-i\gamma''x_g}.$$

Equation (8) is a convolution integral with the kennel of the scattered field spectrum. Notice that when the strength of the scatterer is weak, only the first term on the right side of the equation is used which is the Born approximation. However, for arbitrary scatterers, multiple scattering can be strong. The convolution integral in equation (8) can not be ignored and the linear relation under the Born approximation is broken. We will show in equation (8), V_{k_s} is a single diffracted projection for a fixed wavenumber k_s,. This is independent to other projections with different wavenumber k_s. Therefore, we can solve for them independently.

NONLINEAR DIFFRACTION PROJECTIONS

Equation (8) can be rewritten as

$$D_{k_s}(k_g) = V_{k_s}(k_g) - \frac{i\exp(-i\gamma_s x_s)}{\pi}\int dk''\,\varphi_{k_s}(k_g - k'')V_{k_s}(k''). \qquad (9)$$

For a fixed k_S, the above Toeplitz linear system can be solved for one trace of the scattering spectrum V as indicated in Figure 2a.

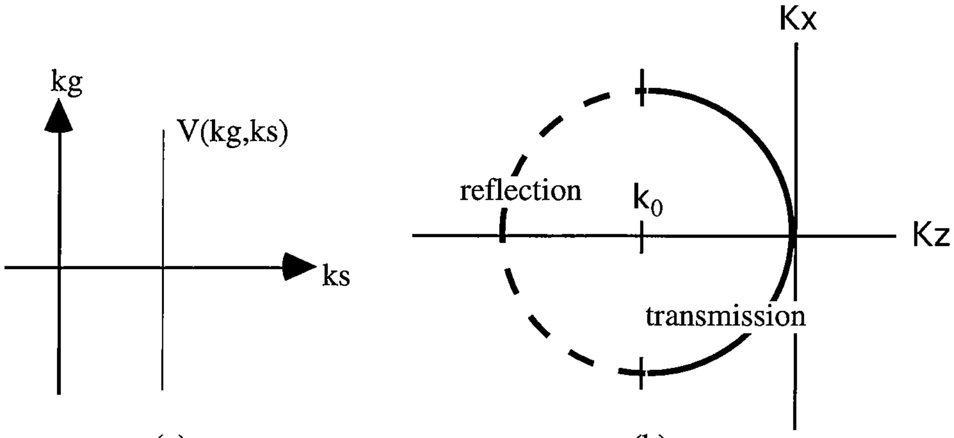

(a) (b)

Figure 2. Fourier transform of the nonlinear diffraction projection; (a) the projection in k_g–k_S domain, and (b) the projection in K_X-K_Z domain.

With a Jacobean transformation, the above linear trace of scatter spectrum in k_g–k_S becomes a curve in K_X-K_Z domain, see Figure 2 (b). We represent the discrete form of equation (13) as

$$D_{k_s}(m) = \sum_n \left[\delta(m-n) - \frac{i\exp(-i\gamma_s x_s)}{\pi}\varphi_{k_s}(m-n)\Delta k''\right]V_{k_s}(n). \qquad (14)$$

The system in equation (14) is a Toeplitz type and the matrix elements consist with Fourier coefficients of the observed scattered field, i.e.,

$$\begin{bmatrix} 1-i\Phi_{k_s}(0)/\pi & \Phi_{k_s}(-1) & \cdots & \Phi_{k_s}(-n) \\ \Phi_{k_s}(1) & 1-i\Phi_{k_s}(0)/\pi & & \Phi_{k_s}(1-n) \\ \vdots & & & \vdots \\ \Phi_{k_s}(n) & \Phi_{k_s}(n-1) & \cdots & 1-i\Phi_{k_s}(0)/\pi \end{bmatrix}.$$

NUMERICAL EXPERIMENTS

Figure 3a shows the velocity field used for the two-dimensional experiment: An anomalous circular region 20 m in diameter with a velocity of 5000 m/sec is located at the center of the medium. The background velocity is 3000 m/sec. The synthetic data are calculated with the analytical expression in Appendix B. The frequency used is 1000 Hz. The calculated scattering field is shown in figure 3b and we can see that the scattering field is stronger in the forward direction. The spectrum difference between the Born approximation and the nonlinear diffraction projection is shown in figure 4.

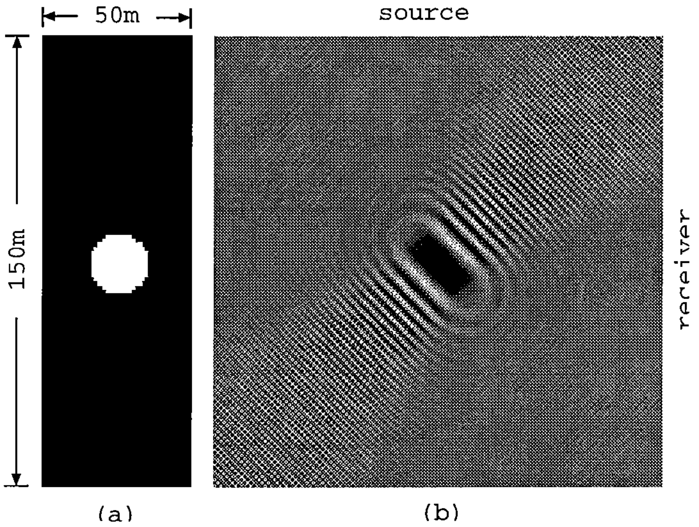

Figure 3. Synthetic data modeling using the analytical formula: a) a disk model; b) scattering data (real part). Frequency=1000Hz.

The largest difference (around ten percent) occurred at the highest frequency which is expected, Since the multiple scattering has the higher frequencies. It is shown in figure 5 that the shape reconstruction is quite good using both the Born approximation and nonlinear projection methods. Note that the disk is elongated in the x direction, both in figure 5b and 5c, as is expected since the resolution is poorer in that direction. Compared to the result using the Born approximation, the velocity reconstruction with the nonlinear projection algorithm has significantly improved (figure 5c).

In the second example, the model has a background velocity of 3500 m/sec and two linear velocity abnormal features of 5000 m/sec representing fracture zones (Figure 6a). The moment method is used to generate forward data (Appendix C). A 50 m horizontal by 150 m vertical area is considered with a sampling interval of 0.5 m. The frequency is 1000Hz.

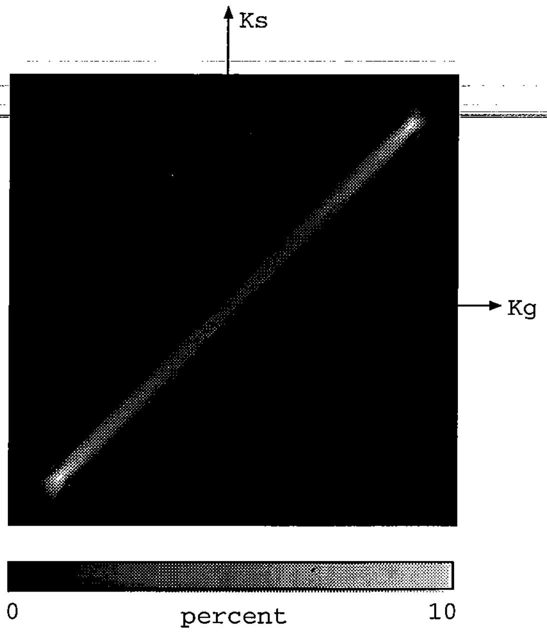

Figure 4. The spectrum difference between the linear and nonlinear projection. The largest difference occurred at high frequencies. The scattered field is from the synthetic data of the disk model.

The calculated scattering field (real part) is shown in figure 6b. The scattering spectra from the Born approximation and nonlinear diffraction projections are shown in figure 7. Once again we see the difference at high frequencies. The inversion results are shown in figure 8b and 8c. We can see that the diffractor lines are thicker comparing to input model and the

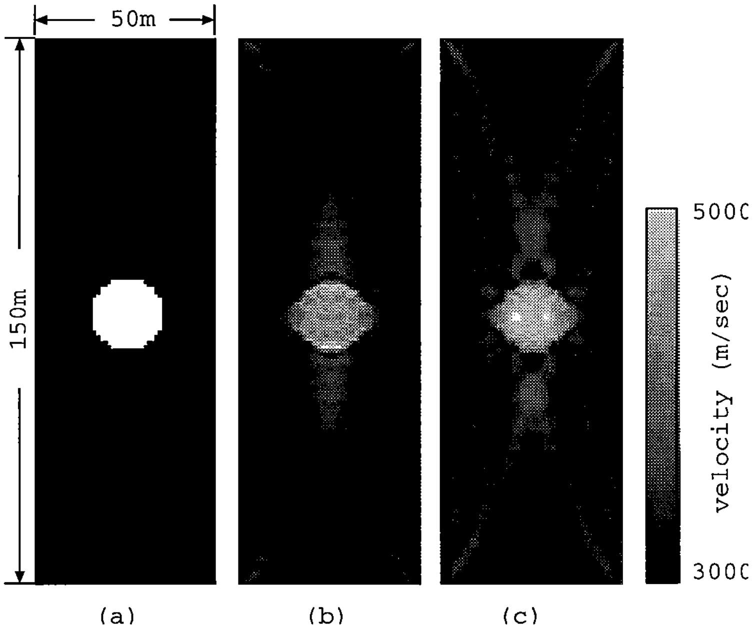

Figure 5. A comparison between the Born approximation and nonlinear projection diffraction tomography. a) A disk mode; b) the reconstruction with linear projection; c) the reconstruction with nonlinear projection.

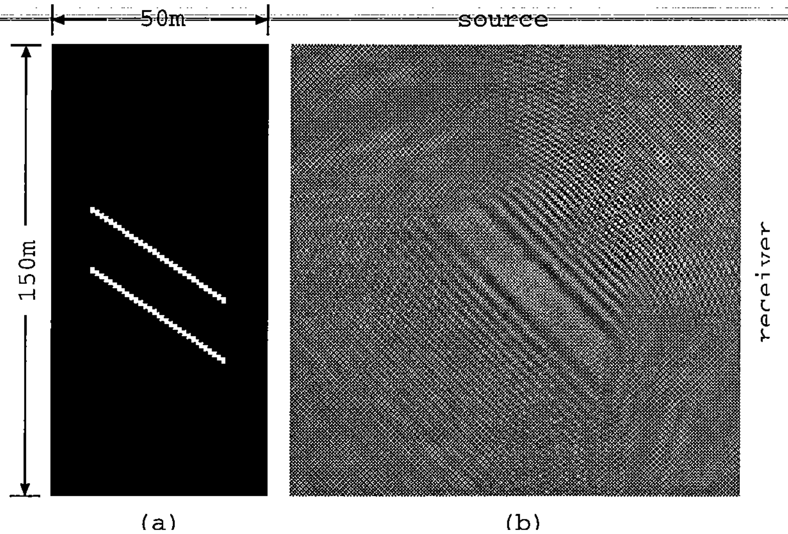

Figure 6. Synthetic data generated using the moment method: a) a fracture model; b) scattering data (real part). Frequency = 1000Hz.

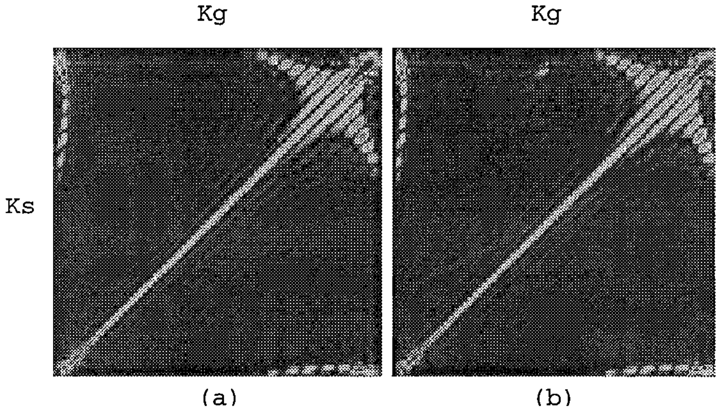

Figure 7. The spectrum of the scattered field with the linear and nonlinear diffraction projections. a) The spectrum with Born approximation; and b) the spectrum with nonlinear diffraction projection.

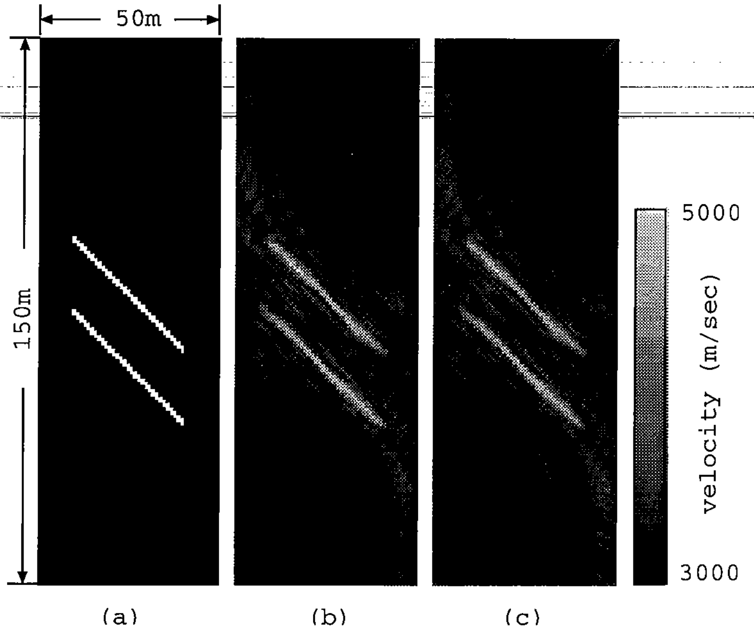

Figure 8. A comparison between the linear and nonlinear projection diffraction tomography. a) Fracture mode; b) the reconstruction with linear projection; and c) the reconstruction with nonlinear nonlinear projection.

diffractor lines are not as distinctly resolved in comparison with the original image. This is caused by the wavenumber domain coverage being constrained to low wavenumbers in the crosswell case. In this example, the reconstructed images with the Born approximation and nonlinear projection has little difference, since the multiple scattering is insignificant in the forward direction.

The last example is to test the quality of imaging for complex structure. The model consists three letters "STP" as the object to be reconstructed . The letters are consists of point scatters, see figure 9a. The sources and receivers are equally spaced at half wavelength intervals. Figure 9b shows the results from nonlinear projection diffraction tomography. The locations of the letters are correctly recovered. The distortion is possibly caused by inaccuracy of synthetic data modeling with the moment method at high frequencies (1500 Hz).

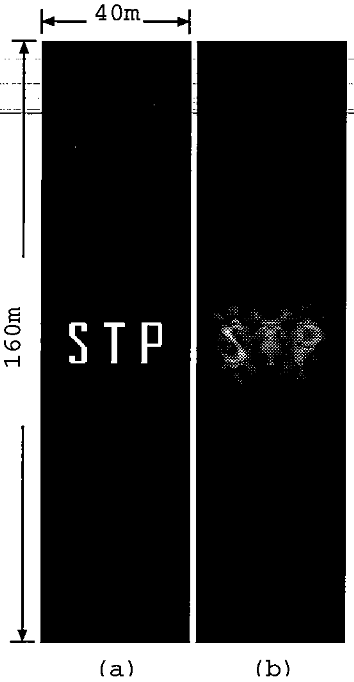

Figure 9. The reconstruction with nonlinear projection diffraction tomography. The synthetic data is calculated with the moment method at frequency = 1500 Hz.

CONCLUSIONS

It is possible that the computational efficiency and simplicity of the traditional diffraction tomography can be preserved while the nonlinear effects of multiple scattering are taken into account. Numerical results indicate the improvement to the Born approximation for the models have strong scatterers. However, when the scale of the scatterers significantly influence the propagation of the scattered field, the phase extrapolation breaks down. The method yields an algorithm of asymptotic order N^3logN, where N is the number of sources and receivers. Reconstruction is efficient on a IBM RS6000 workstation, requiring only approximately 2 minutes for a single frequency when N=150.

ACKNOWLEDGEMENTS

The author thanks Nick Smalley for editing this paper.

REFERENCES

A. J. Devaney, Geophysical diffraction tomography, IEEE Trans. Geosci. Remote Sensing GE-22, 3-13 (1984)

J. M. Harris, Diffraction tomography imaging with arrays of source and detectors, IEEE Trans. Geoscience Remote Sensing, vol. Ge-25, No. 4, 448-455, 1987

R. H. Stolt, Migration by Fourier transform, Geophysics, 43, 23-28.

R. S. Wu and M. N. Toksoz, Diffraction tomography and multi-source holography applied to seismic imaging, Geophysics 52, 11-25 (1987)

APPENDIX A

A DESCRIPTION OF THE BORN APPROXIMATION

The solution to Homholtz equation can be expressed as integral equation:

$$\psi(r) = \varphi(r) + \int dr' \, G(r - r')v(r')\psi(r'). \tag{A-1}$$

The asymptotic form of the wave function is

$$\psi(r) \to \varphi(r) + f(k,k')\frac{\exp(ikr)}{r} \tag{A-2}$$

$$f(k,k') = -\int dr' \, e^{-ik' \cdot r} v(r')\psi(r'), \tag{A-3}$$

Replacing the exact wave function $\psi(r')$ by the incident wave $\varphi(r)$ we find the scattering amplitude in the Born approximation:

$$f(k,k') = -\int dr' \, e^{-ik' \cdot r} v(r')\varphi(r'), \tag{A-4}$$

Choosing plane waves for $\varphi(r)$, we can represent the scattering amplitude in the form

$$f(k,k') = -\int dr' \, e^{-iq \cdot r} v(r'), \tag{A-5}$$

where q is the change in the particle momentum on the scattering

$$q = k - k'. \tag{A-6}$$

The absolute magnitude of the vector q is

$$q = 2k \sin\frac{\theta}{2}, \tag{A-7}$$

where θ is the scattering angle (the angle between the vector k' and k). We can see that the scattering amplitude in the Born approximation is determined by the Fourier component of the scattering field and depends only on the magnitude of the transferred momentum q.

The scattering potential function can be reconstructed by taking the inverse Fourier transform of equation (A-5). The conditions for Born approximation to be valid can be summarized as: For low frequencies

$$\bar{V} << 1/R^2, \quad kR << 1. \tag{A-8}$$

This condition implies that for perturbation theory to be applicable, the effective value of the potential must be small in comparison with the wave length localized in the region of the influence of the potential. For high frequencies

$$\overline{V} << \frac{1}{R^2} kR, \quad kR >> 1. \tag{A-9}$$

We note that the condition (A-9) is considerably weaker than the condition (A-8).

APPENDIX B

AN ANALYTICAL SOLUTION OF THE FIELD SCATTED FROM A DISK

We designate the source and receiver coordinates to be (r', θ') and (r, θ) (see figure B-1). The density and velocity inside and outside the disk are given by (ρ, v) and (ρ_0, v_0). Assuming the incident field is the Hankel function,

$$\varphi(|x' - x|) = \frac{i}{4} H_0^{(1)}(k_0 |x' - x|), \tag{B-1}$$

which can be expanded as, for r < r',

$$\varphi(|x' - x|) = \frac{i}{4} \sum_n e^{-in(\theta' - \theta)} H_n^{(1)}(k_0 r') J_n(k_0 r), \tag{B-2}$$

where $H_n^{(1)}$ is the Hankel function of the first kind and nth order.

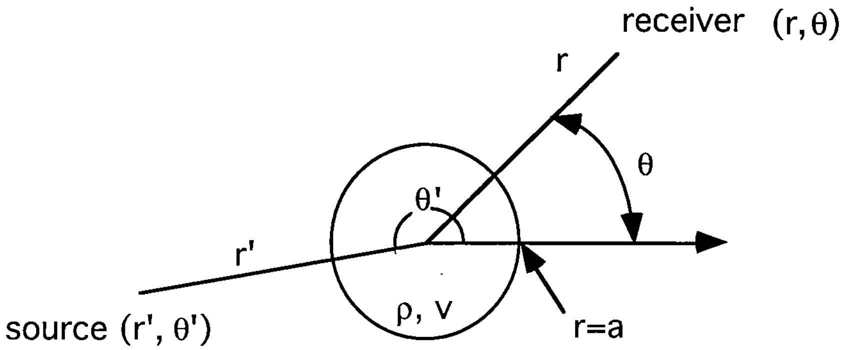

Figure A-1. The scattering geometry of a cylindrical disk.

The fields outside and inside the disk can be expressed as

$$\varphi_{out}(r) = \sum_n C_{out} e^{in\theta} H_n^{(1)}(k_0 r) \quad \text{and} \quad \varphi_{in}(r) = \sum_n C_{in} e^{in\theta} J_n(k_0 r) \tag{B-3}$$

The coefficients C_{in} and C_{out} are determined by using the boundary conditions for the problem, with require that $\rho\varphi$ and $\partial\varphi / \partial r$ be continuous at the surface of the disk. Applying these conditions we obtain the scattered field outside the disk:

$$\varphi_{out}(r) = \frac{i}{4} \sum_n e^{-in(\theta' - \theta)} H_n^{(1)}(k_0 r') H_n^{(1)}(k_0 r) A / B \tag{B-4}$$

where

$$A = \rho k_0 J_n(ka) \dot{J}_n(k_0 a) - \rho_0 k \dot{J}_n(ka) J_n(k_0 a),$$

$$B = \rho_0 k H_n^{(1)}(k_0 a) \dot{J}_n(ka) - \rho k_0 \dot{H}_n^{(1)}(k_0 a) J_n(ka).$$

The summation can be carry out over positive indices by using the index symmetry of the Bessel functions.

APPENDIX C

THE METHOD OF MOMENT

~~The moment method is often applied in calculation of the scattered field from the~~ two dimensional inhomogeneity (Bath, 1982, Chew, 1990), such as described by the following equation:

$$u(r) = u^i - \int u(r')e(r')G(r,r')d^2r' \qquad \text{(C-1)}$$

The method is straight forward and efficient when the size of the scatterer is small (i.e., the volume or area depending dimension of the problem is small.) The scattering region is region separated into N square cells (see figure C-1). Then, the scattering potential and wave field are represented as a summation of basis function over the N cells, i.e.,

$$e(r) = \sum_{j,k} e(r_{jk})b_{jk}(r)$$

$$\text{(C-2)}$$

$$u(r) = \sum_{j,k} a_{jk}b_{jk}(r)$$

where $b_{jk}(r)$ is the basis function, $e(r_{jk})$ and a_{jk} represent the coefficients describing the scattering potential and wave field over the basis function.

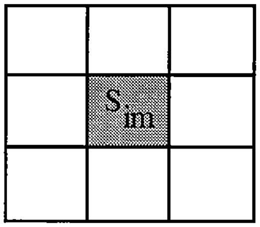

Figure C-1. Scattering potential is divided up into N square cells

We chose the same pulse basis function $b_{jk}(r)$ to discretize equation (C-1), i.e.,

$$b_{jk}(r) = \begin{cases} 1 & r \in s_{jk} \\ 0 & r \notin s_{jk} \end{cases} \qquad \text{(C-3)}$$

Applying the point-matching procedure, the equation (5) can be written as a linear algiboal system, i.e.,

$$u_{jk} + \sum_{i,m} g(j,k,i,m)f(r_{im})u_{im} = G(r_{jk}), \qquad \text{(C-4)}$$

where $g(j,k,i,m) = \int_{s_{im}} G(r_{jk})d^2r$.

DIFFRACTION TOMOGRAPHY OF STRONGLY SCATTERING MEDIA
PART II: USING FOURIER SERIES EXPANSION

Guan Y. Wang

ABSTRACT

To overcome the difficulty resulting from a strongly scattering medium, the total field in the integral equation is expanded as a Fourier series. The coefficients of the expansion are determined by the boundary values and the orthogonality of the Fourier series. The inverse Fourier transform applied to the filtered spectrum of the measurements is equivalently applied to each harmonic component in the series that results in multiscale images. The complete image is obtained, via Mobius transform, with those multiscale images.

INTRODUCTION

In anothe paper in this volume (Paper M, Diffraction tomography of Strongly scattering media part I: Using Phase Extrapolation,) referenced as paper I, the unknown total field in the integral equation is replaced by the extrapolation of the field at the boundary using the Fourier phase shift technique. The method works well for models where there are a few small scatterers. In this kind of model, multiple scattering can be strong but the propagation speed of the scattering fields is not significantly influenced by the inhomogeneities. Therefore, the field extrapolation is treated with a global dispersion relation. However, when the scatterers are more numerous or the scale of the scale of scatterers are larger both the field and propagation of the field are significantly modified by the presence of the scatterers. In this case, the scheme of phase shift extrapolation failed. The resultant image is distorted by the incorrect extrapolation.

In this study, the unknown total field is expanded as a Fourier series to avoid using the dispersion relation that is unknown or very complicated. The coefficients of the expansion are determined by the boundary values and the orthogonality of the Fourier series. The filtered spectrum of the measurement is related to multiscale spectra of the scattering potential resulting from the Fourier expansion of the imhomogeneous wave. The object function is recovered from multiscale components via Mobius inversion. As well as the applicability to strongly non-uniform medium, the method can be easily implemented and is computationally efficient, since the algorithm is similar to what is used in a constant background medium.

SPECTRUM OF THESCATTERED FIELD

Following the notation in the Paper I, the spectrum representation of the observed scattered field is written as

$$u^{sc}(k_g,k_s) = \frac{-ie^{i\gamma_g x_g}}{2\gamma_g} \int v(x,z) e^{-i\gamma_g x + ik_g z} u(x,z|k_s) dxdz, \qquad (1)$$

where the total field in the integrand is unknown and $\gamma_s = \sqrt{k_0^2 - k_s{}^2}$ .x_g is the separation between source and receiver well,

The total field in the integrand is known, but equation (1) is not a conventional Fourier type integral since the wave vector *k(r)* is spatially variant. We can not directly reconstruct the scattering potential function *v(r)* via the inverse Fourier transform. One way to overcome this difficulty is to expand the unknown inhomogenous field in terms of homogeneous field. That is,

$$u(x,z|k_s) = \sum_{n=-\infty}^{\infty} c_n e^{in\gamma_s(x-x_g)+ink_s z}. \qquad (2)$$

Comparing with the back extrapolation approach discussed in the Paper I

$$u(x,z|k_s) = \int u(x_g,k_g|k_s) e^{i\gamma_g(x-x_g)+ik_g z} dk_g$$

in which a globule dispersion relation is used and the relation is true only for homogeneous medium. The equation (2) states that the spectrum of the scattered field is generated equivalently by a series of multiple harmonic components. In other words, a field can be decomposed into harmonic components. The amplitude of each component is determined by the boundary value and the orthogrity of the Fourier base function. Notice that the wave vector in (2) consists with a series of multiplication of a homogeneous wave number. It is possible to reconstruct the scattering potential image with Fourier transforms.

At the observation well, Equation (2) can be expressed as

$$u(x_g,z|k_s) = \sum_{n=-\infty}^{\infty} c_n e^{ink_s z}, \qquad (3)$$

where the c_n is determined by virtue of the othogonality of the Fourier base function, i.e.,

$$c_n = \int u(x_g,z|k_s) e^{ink_s z} dz = u(x_g,nk_s|k_s). \qquad (4)$$

Substituting (4) in to (1) and changing the order of the summation and integration, one obtain

$$u^{sc}(k_g,k_s) = \frac{-i}{2\gamma_g} \sum_{n=-\infty}^{\infty} \frac{e^{i(\gamma_g - n\gamma_g)x_g}}{u(nk_s,k_s)} \int o(x,z) e^{i(n\gamma_s - \gamma_g)x + i(k_s + k_g)z} dxdz \qquad (5)$$

MULTI-SCALE RECONSTRUCTION

From equation (5) we can see that the filtered spectrum of the measurement on the left side of the equation is related to a series of weighted multiresolution potential spectra on the right side, i.e.,

$$2i\gamma_g u^{sc}(k_g,k_s) = \sum_{n=-\infty}^{\infty} \frac{e^{i(\gamma_g - n\gamma_s)x_g}}{u(nk_s,k_s)} V(n\gamma_s - \gamma_g, nk_s + k_g) \qquad (6)$$

The notation can be simplified as

$$D_{k_g}(k_s) = \sum_{n=-\infty}^{\infty} O_{k_g}(nk_s), \qquad (7)$$

where $D_{k_g}(k_s) = 2i\gamma_g u^{sc}(k_s,k_g)$ and $O_{k_g}(k_s) = \frac{e^{i(\gamma_g - n\gamma_s)x_g}}{u(nk_s,k_s)} V(n\gamma_s - \gamma_g, nk_s + k_g)$.

The equation (7) is rewritten as

$$\begin{aligned} D_{k_g}(k_s) &= \sum_{n=-\infty}^{\infty} O_{k_g}(nk_s) \\ &= \sum_{n=1}^{\infty} [O_{k_g}(nk_s) - O_{k_g}(-nk_s)] \end{aligned} \qquad (8)$$

where $n = 0$ term is dropped since the average value of the image is not computed correctly by the finite algorithm, since it will evaluate the spectrum at the origin as zero. The D.C. component of the image is restored by computing it directly form the data as $4u^{sc}(0,0)e^{-i\bar{k}L} / L \times H$, where LH is image area.

Applying the Mobius inversion to (8), we obtain

$$O_{k_g}(k_s) + O_{k_g}(-k_s) = \sum_{n=1}^{\infty} \mu(n) D_{k_g}(nk_s). \qquad (9)$$

or

$$\frac{e^{i(\gamma_g - \gamma_s)x_g}}{u(k_s,k_s)} V(\gamma_s - \gamma_g, k_s + k_g) + \frac{e^{i(\gamma_g + \gamma_s)x_g}}{u(-k_s,k_s)} V(-\gamma_s - \gamma_g, -k_s + k_g) = \sum_{n=1}^{\infty} \mu(n) D_{k_g}(nk_s) \qquad (10)$$

Notice that the first term on the left hand of (10) is ford scattering projection of potential function weighted by the spectrum of the forward field and the second term is the back scattering projection of the potential function weighted by the spectrum of the backward field. Unlike the situation in which the character of the angular dependence of the scattering amplitude in the Born approximation is determined by the wave energy. If the energy is sufficiently small the scattering is found to be isotropic and independent of energy. Otherwise, the scattering is sharply anisotropic and is principally in the forward direction. Since the total field including multiple scattering that is no longer only in the forward direction.

For the back scattering data, we can have similar results by repeating the above derivation, i.e.,

$$\frac{1}{u(k_s,k_s)}V(\gamma_s-\gamma_g,k_s+k_g)+\frac{1}{u(-k_s,k_s)}V(-\gamma_s-\gamma_g,-k_s+k_g)=\sum_{n=1}^{\infty}\mu(n)B_{k_g}(nk_s). \tag{11}$$

If we make the measurements at both of the source and receiver wells, we could separate forward and backward scattering projections by solve the 2 by 2 system consisting of equation (10) and (11). Then the scattering potential can be reconstructed via inverse Fourier transform. However, only crosswell data are available in practice. By noticing the complementary nature of the coverage of the forward and backward projections, we can design a filter to eliminate either one of them. For instance, a filter is designed to filt out backward projection $V(-\gamma_s-\gamma_g,-k_s+k_g)$, i.e.,

$$V(\gamma_s-\gamma_g,k_s+k_g)=\frac{e^{i(\gamma_g-\gamma_s)x_g}}{u(k_s,k_s)}f(k_g,k_s)\sum_{n=1}^{\infty}\mu(n)D_{k_g}(nk_s), \tag{12}$$

where the filter

$$f(k_g,k_s)=\begin{cases}1 & (\gamma_s-\gamma_g)^2+(k_s+k_g\pm k_0)^2\le k_0^2\\ 0\end{cases}$$

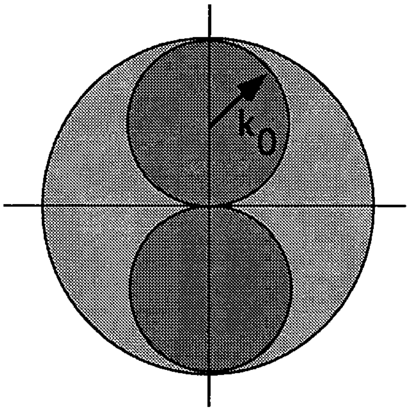

Figure 1. The coverage of the spectrum. The dark shadow is for forward scattering coverage and lighter shadow is for backscattering coverage.

In (12), we see that while the potential spectrum function is different from the result from the Born approximation but their theoretic coverage is the same. The potential function is then reconstructed via inverse Fourier transform. By doing so, the resolution of the reconstruction is degreased since the projection coverage is smaller after filtering operation. However, the non linearity due to multiple scattering in strongly scattering medium is still included in (12). Taking the inverse Fourier transform to both sides of equation () one obtain the reconstructed image, i.e.,

$$v(x,z)=\sum_{n=1}^{\infty}\mu(n)FT^{-1}\{\frac{e^{i(\gamma_g-\gamma_s)x_g}}{u(k_s,k_s)}f(k_g,k_s)D_{k_g}(nk_s)\} \tag{13}$$

In the case of the Born approximation, equation (13) would be one single term. ~~Now, after the inverse Fourier transform is applied to equation (13) a summation of multiscale components of the potential image is reconstructed. The role of the harmonic~~ indexes n is that of the scale lengths in the wavelet transforms. Consequently, a component $FT^{-1}\{\frac{e^{i(\gamma_g-\gamma_s)x_g}}{u(k_s,k_s)}f(k_g,k_s)D_{k_g}(nk_s)\}$ is an image with a specific scale. With large scale length, i.e., large n, $FT^{-1}\{\frac{e^{i(\gamma_g-\gamma_s)x_g}}{u(k_s,k_s)}f(k_g,k_s)D_{k_g}(nk_s)\}$ provides a global view. While small scales, i.e., small n, the component provides detailed views of smaller subsets of the image. The remaining problem is to combine those multiscale images into a complete image. The inverse Fourier transform is explicitly written as following:

$$\begin{aligned} &FT^{-1}\{\frac{e^{i(\gamma_g-\gamma_s)x_g}}{u(k_s,k_s)}f(k_g,k_s)D_{k_g}(nk_s)\} \\ &=\int \frac{e^{i(\gamma_g-\gamma_s)x_g}}{u(k_s,k_s)}f(k_g,k_s)D_{k_g}(nk_s)e^{i[(\gamma_s-\gamma_g)x+(k_s+k_g)z]}|J|dk_g dk_s \end{aligned} \tag{14}$$

where $|J|=\frac{|\gamma_g k_s+\gamma_s k_g|}{\gamma_s\gamma_g}$ is the Jacobean transformation from the coordinates (K_x,K_z) to the coordinates (k_s,k_g). Notice that in (13) as n is increased the data $D_g(nk_s)$provide the components with higher and higher frequency. After certain n, $D_g(nk_s)$ is replaced as zero to guarantee the resolution of the image is within the physical limitation. In another word, series (13) has only limit number of terms. This is not surprising because of the sinusoidal nature of propagating wave. A few terms of (2) are sufficient to reproduce the unknown total field.

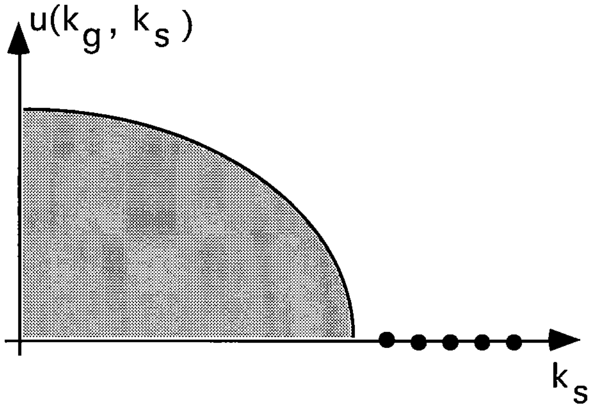

Figure 2. The spectrum response function is cut off at high frequencies.

CONCLUSIONS

We have presented a formulation of diffraction tomography, for strongly scattering medium, which relates the filtered spectrum of the measurement to multiscale spectra of the scattering potential resulting from the Fourier expansion of the imhomogeneous wave. The potential function is recovered from multiscale components via Mobius inversion. As well as the applicability to strongly non-uniform medium, the method can be easily implemented and is computationally efficient, since the algorithm is similar to what is used in a constant background medium.

REFERENCE

Chen, Nan-xian, 1989, Modified Mobius Inverse Formula and its application in physics, Physical review letters, 64, 11.

Hardy, G. H. and Wright, E. M., 1979, An introduction to the theory of numbers: Oxford University Press, Oxford, 5th ed.

Harris, J. M. 1987, Diffraction tomography with arrays of discrete sources and receivers: IEEE trans. Geosci. remote, GE-25(4), 448-455.

APPENDIX A

MOBIUS INVERSION THEOREM

According to Mobius inversion theorem (Hardy, 1979, Chen, N. 1989), if

$$F(x) = \sum_{n=1}^{\infty} f(nx) \tag{A-1}$$

then

$$f(x) = \sum_{n=1}^{\infty} \mu(n) F(nx), \tag{A-2}$$

provide $\sum_{m,n} |f(mnx)|$ converges.

where Mobius function

$$\mu(n) = \begin{cases} 1 & \text{n = 1} \\ (-1)^r & \text{n include r distinct prime factors} \\ 0 & \text{otherwise.} \end{cases}$$

Prove :

$$\begin{aligned} F(x) &= \sum_{n=1}^{\infty} \mu(n) f(nx) \\ &= \sum_{n=1}^{\infty} \mu(n) \sum_{m=1}^{\infty} F(mnx) \\ &= \sum_{k=1}^{\infty} \sum_{mn=k}^{\infty} \mu(n) F(mnx) \\ &= F(x) \end{aligned}$$

since $\sum_{mn=k} \mu(n) = \sum_{n|k} \mu(n) = \delta_{k,1}$.

Paper O

DIFFRACTION TOMOGRAPHY OF THE RANDOM ELASTIC MEDIUM

Guan Y. Wang

ABSTRACT

The diffraction tomography with backpropagation method is extended to the stochastic inversion of spatially random and time-independent elastic media. Within the accuracy of the first Born approximation, the spatial coherency of the field by such medium is related to the spatial coherency of the scattering potential and to its second moment respectively. By probing the random medium with multiple sources and receivers, the second order statistics of the medium can be recovered from the second order statistics of the perturbed field. For the forward modeling, the random distribution is characterized by an ellipsoidal autocorrelation function in the medium properties.

INTRODUCTION

It is important to determine the correlation properties of the randomly distributed heterogeneity or scattering centers from measurements of the scattered field in the reservoir characterization. From a typical sonic well-log we can see that the log curve is oscillating with a considerable number of phase-extreme and the phase periods are not constant. Comparing with other logs in the nearby locations, only relatively small number of phases can be correlated. The overwhelming majority of phases, their location, magnitudes, periods and number vary rapidly form well to well. This indicates that the real medium is a random one or, more precisely, the medium is consists of two components: regular and random components. The random heterogeneity of real media can be described in terms of random functions of position. The wave propagation can be studied with corresponding stochastic differential equations.

Despite extensive studies of the forward problem of wave propagation in random medium (Chernov, 1960; Tatarsky, 1961; Uscinski, 1979) progresses in inverse problem has been slow. There have been some efforts to determine the second-order moments of random scattering potentials, but these investigations have been confined to specific cases. In this study, we investigate the inverse scattering problem of the elastic random medium with a two dimensional model where the large scale inhomogeneities are represented by a homogeneous medium and small scale inhomogeneities are randomly distributed inside the homogeneous medium. The random distribution is characterized by an ellipsoidal autocorrelation function of the medium properties. Solutions of the problems are constructed as in the case of deterministic diffraction tomography. Since the scattering centers are randomly distributed in the medium, we describe it by the first and second moment. As we will show later, the first moment of the fluctuation of the elastic parameters gives the way that the incident wave is attenuated on passing through the medium. The second moment is the autocorrelation or crosscorrelation function of the fluctuation of the elastic parameters that are measures of the size and sharp of a typical irregularity in the medium. The resolved statistical quantities or combinations can be used in some other interpretation or simulation modalities.

SCATTERING FROM DETERMINISTIC ELASTIC MEDIA

We will first summarize the main formulas that we will need later, relating to scattering of elastic waves by deterministic media (Aki and Richards, 1980). The governing equation for an inhomogeneous elastic medium is

$$\rho \ddot{u}_i = (\lambda \nabla \cdot u)_{,i} + (\mu(u_{i,j} + u_{j,i}))_{,j}, \tag{1}$$

where u_i is the displacement in the i^{th} direction, λ and μ are Lamé parameters, and ρ is the density. Defining

$$\begin{aligned} \lambda &= \lambda_0 + \delta\lambda(r) \\ \mu &= \mu_0 + \delta\mu(r) \\ \rho &= \rho_0 + \delta\rho(r), \end{aligned} \tag{2}$$

where δ represents the perturbation to the homogeneous background. Substituting (2) into (1) results in

$$\begin{aligned} &\rho_0 \ddot{u}_i - (\lambda_0 + \mu_0)(\nabla \cdot u)_{,i} - \mu_0 \nabla^2 u_i = \\ &-\delta\rho \ddot{u}_i + (\delta\lambda + \delta\mu)(\nabla \cdot u)_{,i} + \delta\mu \nabla^2 u_i + (\delta\lambda)_{,i} \nabla \cdot u + (\delta\lambda)_{,j}(u_{i,j} + u_{j,i})_{,j}. \end{aligned} \tag{3}$$

The displacement in equation (3) can be represented as a superposition of the incident and scattered displacements, i.e.,

$$u_i = u_i^0 + u_i^{sc}. \tag{4}$$

Combining (3) and (4) we have

$$\begin{aligned} &\rho_0 \ddot{u}_i^{sc} - (\lambda_0 + \mu_0)(\nabla \cdot u^{sc})_{,i} - \mu_0 \nabla^2 u_i^{sc} = Q_i \\ &Q_i = -\delta\rho \ddot{u}_i + (\delta\lambda + \delta\mu)(\nabla \cdot u)_{,i} + \delta\mu \nabla^2 u_i + (\delta\lambda)_{,i} \nabla \cdot u + (\delta\lambda)_{,j}(u_{i,j} + u_{j,i})_{,j}, \end{aligned} \tag{5}$$

where Q_i is a secondary source. Using Green's theorem one obtain

$$u_i^{sc} = \int Q_j(r) *_t G_{ij}(r) d^2 r \tag{6}$$

where $*_t$ denotes convolution in time. Assuming the fluctuation of the physical parameters are small and applying the Born approximation, we have the integral representation

$$u_{lj}^{sc}(r_g, r_s, \omega) = -\int [-\omega^2 \delta\rho G_{li}^s G_{ij}^g + \delta\lambda G_{lk,k}^s G_{ij,i}^g + \delta\mu (G_{li,k}^s + G_{lk,i}^s) G_{ij,k}^g] dxdz, \tag{7}$$

in the frequency domain, where $G_{ij}^g = G_{ij}(r_g, r)$ and $G_{ij}^s = G_{ij}(r, r_s)$ are Green's functions. The displacement for a source in the l-direction and measurements in the j-direction can be represented as superposition of four wave types, i.e., P-to-P, P-to-S, S-to-P and S-to-S. Therefore

$$u_{lj}^{s} = u_{lj}^{PP} + u_{lj}^{PS} + u_{lj}^{SP} + u_{lj}^{SS}. \tag{8}$$

This representation is a direct consequence of the Green's function representation. The two dimensional Green's function for a homogeneous background is discussed in Appendix A. Here we give the results in the transform domain. For P-SV waves

$$\tilde{G}(r,k_s) = \frac{i}{2\rho\omega^2}\begin{bmatrix}(k_x^s)^2 & k_z^{\alpha s}k_x^s \\ k_z^{\alpha s}k_x^s & (k_z^{\alpha s})^2\end{bmatrix}\frac{e^{i\gamma_s^\alpha x_s - ik^\alpha \hat{s}\cdot r}}{\gamma_s^\alpha} + \frac{i}{2\rho\omega^2}\begin{bmatrix}(k_z^{\beta s})^2 & -k_z^{\beta s}k_x^s \\ -k_z^{\beta s}k_x^s & (k_x^s)^2\end{bmatrix}\frac{e^{i\gamma_s^\beta x_s - ik^\beta \hat{s}\cdot r}}{\gamma_s^\beta}. \tag{9}$$

SCATTERING FROM SPATIALLY RANDOM ELASTIC MEDIUM

If the medium is no longer deterministic, the fluctuations of the elastic parameters become, for each frequency, random function of the position vector r. These quantities must be then be characterized by appropriate statistical assembles (Uscinski, 1979). We assuming the regular part of the elastic parameters is constant and the perturbations are random functions of spatial variables, i.e.,

$$\begin{aligned} &\delta\lambda(r,\gamma) << \lambda_0 \qquad && <\delta\lambda(r,\gamma)>=0 \\ &\delta\mu(r,\gamma) << \mu_0 && <\delta\mu(r,\gamma)>=0 \\ &\delta\rho(r,\gamma) << \rho_0 && <\delta\rho(r,\gamma)>=0 \end{aligned} \tag{10}$$

For a spatially homogeneous process, the correlation function depends only on the coordinate differences $r = r_2 - r_1$, i.e., $N_{12} = N_{12}(r)$. For $r = 0$, the function N_{12} achieves its maximum N_{11}, equal to the mean square fluctuations. The correlation coefficient N is defined as the ratio of the correlation function N_{12} to the mean square fluctuation, i.e., $N = N_{12} / N_{11}$. As the distance between the points is increased, the correlation coefficient decreases from its maximum value of unity and becomes small compared to unity at a correlation distance. In other words, the statistical dependence between the fluctuations disappears. If the medium is not spatially homogeneous, the correlation function will depend not only on the coordinate difference but also on the coordinates themselves. However we shall consider only the statistically homogeneous case.

The forward problem of the scattering is investigated extensively. We consider the inverse problems of determine the two constituent factors of the two-point spatial correlation function of the scattering potential, i.e., its second moment and its degree of spatial correlation with the measured fluctuations of the scattered fields and their two-point correlation's. The stationary assumption is sufficient to write the autocorrelation of the medium as a function of the difference coordinates x_d and z_d:

$$R(x_d,z_d) =< p(x+x_d, z+z_d)p(x,z) >, \tag{11}$$

where $p(x,z)$ represents any one of the three elastic parameters. Obviously, it is convenient to calculate the statistical quantity in the transform domain. Substituting the appropriate parts of the Green's function in transform domain into (7) for each of the four waves, results in

$$\tilde{u}_{lj}^{pp}(k_s,k_g,\omega)=\frac{-1}{4\rho_0^2}\int\,[\frac{\delta\lambda}{\alpha_0^4}+\frac{\delta\rho}{\alpha_0^2}(\hat{i}\cdot\hat{g})+\frac{2\delta\mu}{\alpha_0^2}(\hat{i}\cdot\hat{g})^2]k_l^s k_j^g S^p R^p dxdz \tag{12}$$

$$\tilde{u}_{lj}^{ps}(k_s,k_g,\omega)=\frac{-1}{4\rho_0^2}\int\,[\frac{\delta\rho}{\alpha_0\beta_0}|\hat{i}\times\hat{g}|+\frac{2\delta\mu}{\alpha_0^2\beta_0^2}|\hat{i}\times\hat{g}|(\hat{i}\cdot\hat{g})]k_l^s k_J^g S^p R^s dxdz \tag{13}$$

$$\tilde{u}_{lj}^{sp}(k_s,k_g,\omega)=\frac{1}{4\rho_0^2}\int\,[\frac{\delta\rho}{\alpha_0\beta_0}|\hat{i}\times\hat{g}|+\frac{2\delta\mu}{\alpha_0^2\beta_0^2}|\hat{i}\times\hat{g}|(\hat{i}\cdot\hat{g})]k_L^s k_j^g S^s R^p dxdz \tag{14}$$

$$\tilde{u}_{lj}^{ss}(k_s,k_g,\omega)=\frac{-1}{4\rho_0^2}\int\,[\frac{\delta\rho}{\beta_0^2}(\hat{i}\cdot\hat{g})+\frac{\delta\mu}{\beta_0^4}((\hat{i}\cdot\hat{g})-|\hat{i}\times\hat{g}|)]k_L^s k_J^g S^s R^s dxdz \tag{15}$$

where

$$S^p=\frac{e^{i(\gamma_s^\alpha x_s+k^\alpha\hat{i}\cdot r)}}{\gamma_s^\alpha},$$

$$S^s=\frac{e^{i(\gamma_s^\beta x_s+k^\beta\hat{i}\cdot r)}}{\gamma_s^\beta},$$

$$R^p=\frac{e^{i(\gamma_g^\alpha x_g-k^\alpha\hat{i}\cdot r)}}{\gamma_s^\alpha},$$

and

$$R^s=\frac{e^{i(\gamma_g^\beta x_g-k^\beta\hat{i}\cdot r)}}{\gamma_g^\beta}$$

In (12)-(15), for the P-to-S and S-to-P modes, $k_J=k_L=k_z$ for $j=l=x$ and $k_J=k_L=-k_x$ for j=l=z. The convention for capital indexes given above holds for the S-to-S mode. Notice that

$$\begin{array}{ll}\hat{i}\cdot\hat{g}=1-(\hat{g}-\hat{i})/2=1-|K|^2/2k^2 & (\hat{i}\cdot\hat{g})^2=1+|K|^4/4k^4-|K|^2/2k^2 \\ |\hat{i}\times\hat{g}|=|K|\sqrt{1-|K|^2/4} & |\hat{i}\times\hat{g}|^2=|K|^2-|K|^4/4\end{array} \tag{16}$$

These operators represent the coverage's related to the observation geometry and the polarization, and (12) to (15) are all in the form of the Fourier transform. The spectral of the random perturbation of the l, r and m can be written as

$$[\frac{\delta\lambda(K^{pp})}{\alpha_0^4}+\frac{\delta\rho(K^{pp})}{\alpha_0^2}(\hat{i}\cdot\hat{g})+\frac{2\delta\mu(K^{pp})}{\alpha_0^2}(\hat{i}\cdot\hat{g})^2]k_l^s k_j^g=-4\rho_0^2\gamma_g^\alpha\gamma_s^\alpha e^{-i(\gamma_g^\alpha x_g+\gamma_s^\alpha x_s)}\tilde{u}_{lj}^{pp}$$

(17)

$$[\frac{\delta\rho(K^{ps})}{\alpha_0\beta_0}|\hat{i}\times\hat{g}|+\frac{2\delta\mu(K^{ps})}{\alpha_0^2\beta_0^2}|\hat{i}\times\hat{g}|(\hat{i}\cdot\hat{g})]k_l^s k_J^g=-4\rho_0^2\gamma_s^\alpha\gamma_g^\beta e^{-i(\gamma_g^\beta x_g+\gamma_s^\alpha x_s)}\tilde{u}_{lj}^{ps}$$

(18)

$$[\frac{\delta\rho(K^{sp})}{\alpha_0\beta_0}|\hat{i}\times\hat{g}|+\frac{2\delta\mu(K^{sp})}{\alpha_0^2\beta_0^2}|\hat{i}\times\hat{g}|(\hat{i}\cdot\hat{g})]k_L^s k_j^g=4\rho_0^2\gamma_s^\beta\gamma_g^\alpha e^{-i(\gamma_s^\beta x_s+\gamma_g^\alpha x_g)}\tilde{u}_{lj}^{sp}$$

(19)

$$[\frac{\delta\rho(K^{ss})}{\beta_0^2}(\hat{i}\cdot\hat{g})+\frac{\delta\mu(K^{ss})}{\beta_0^4}((\hat{i}\cdot\hat{g})-|\hat{i}\times\hat{g}|)]k_L^s k_J^g=-4\rho_0^2\gamma_s^\beta\gamma_g^\beta e^{-i(\gamma_g^\beta x_g+\gamma_s^\beta x_s)}\tilde{u}_{lj}^{ps}$$

(20)

where

$$K^{pp}=k^\alpha\hat{g}-k^\alpha\hat{i},$$

$$K^{ps}=k^\beta\hat{g}-k^\alpha\hat{i},$$

$$K^{sp}=k^\alpha\hat{g}-k^\beta\hat{i},$$

and

$$K^{ss}=k^\beta\hat{g}-k^\beta\hat{i}.$$

These equations indicate the spectrum relation between the physical parameters and the observed scattered field of four different modes. We define the power spectrum as the Fourier transform of the auto-correlation or cross-correlation. The auto-spectra or cross-spectra of the fluctuation of the elastic parameters is related to the power spectrum of the scattered fields, i.e.,

$$<m_{pp}^*m_{pp}>=(4\rho_0^2\gamma_g^\alpha\gamma_s^\alpha)^2<\tilde{u}_{lj}^{pp^*}\tilde{u}_{lj}^{pp}>, \tag{21}$$

$$<m_{ps}^*m_{ps}>=(4\rho_0^2\gamma_g^\beta\gamma_s^\alpha)^2<\tilde{u}_{lj}^{ps^*}\tilde{u}_{lj}^{ps}>, \tag{22}$$

$$<m_{sp}^*m_{sp}>=(4\rho_0^2\gamma_g^\alpha\gamma_s^\beta)^2<\tilde{u}_{lj}^{sp^*}\tilde{u}_{lj}^{sp}>, \tag{23}$$

and

$$<m_{ss}^*m_{ss}>=(4\rho_0^2\gamma_g^\beta\gamma_s^\beta)^2<\tilde{u}_{lj}^{ss^*}\tilde{u}_{lj}^{ss}>. \tag{24}$$

In expression (21) to (24), the random functions characterizing the medium appear by means of function m_{ij}. The mean value of the product $<m_{ij}{}^*m_{ij}>$ is combination of the auto-correlation and cross-correlation spectral of the physical parameters of the random medium. For instance,

$$<m_{pp}^{*}m_{pp}>=\frac{<\delta\lambda^{*}\delta\lambda>}{\alpha_0^8}+\frac{<\delta\rho^{*}\delta\rho>}{\alpha_0^4}(\hat{i}\cdot\hat{g})^2+4\frac{<\delta\mu^{*}\delta\mu>}{\alpha_0^8}(\hat{i}\cdot\hat{g})^4+$$

$$\frac{<\delta\lambda^{*}\delta\rho>}{\alpha_0^6}+2\frac{<\delta\lambda^{*}\delta\mu>}{\alpha_0^8}(\hat{i}\cdot\hat{g})^2+\frac{<\delta\rho^{*}\delta\lambda>}{\alpha_0^6}(\hat{i}\cdot\hat{g})+$$

$$2\frac{<\delta\rho^{*}\delta\mu>}{\alpha_0^6}(\hat{i}\cdot\hat{g})^3+2\frac{<\delta\mu^{*}\delta\lambda>}{\alpha_0^6}(\hat{i}\cdot\hat{g})^2+2\frac{<\delta\mu^{*}\delta\rho>}{\alpha_0^6}(\hat{i}\cdot\hat{g})^3 \tag{25}$$

We can invert individual correlation functions by using the scattering power spectrum at nine distinct frequencies, i.e.,

$$\begin{bmatrix} a_{11} & a_{12} & \cdot\;\cdot\;\cdot\;\cdot\;\cdot\;\cdot\;\cdot & a_{19} \\ a_{21} & a_{22} & \cdot\;\cdot\;\cdot\;\cdot\;\cdot\;\cdot\;\cdot & a_{29} \\ \cdot & \cdot & & \cdot \\ \cdot & \cdot & & \cdot \\ \cdot & \cdot & & \cdot \\ \cdot & \cdot & & \cdot \\ \cdot & \cdot & & \cdot \\ \cdot & \cdot & & \cdot \\ a_{91} & \cdot & \cdot\;\cdot\;\cdot\;\cdot\;\cdot\;\cdot\;\cdot & a_{99} \end{bmatrix} \begin{bmatrix} <\delta\lambda^{*}\delta\lambda> \\ <\delta\rho^{*}\delta\rho> \\ <\delta\mu^{*}\delta\mu> \\ <\delta\lambda^{*}\delta\rho> \\ <\delta\lambda^{*}\delta\mu> \\ <\delta\rho^{*}\delta\lambda> \\ <\delta\rho^{*}\delta\mu> \\ <\delta\mu^{*}\delta\lambda> \\ <\delta\mu^{*}\delta\rho> \end{bmatrix} = \begin{bmatrix} D(\omega_1) \\ D(\omega_2) \\ \cdot \\ \cdot \\ \cdot \\ \cdot \\ \cdot \\ \cdot \\ D(\omega_9) \end{bmatrix} \tag{26}$$

where the coefficients are

$$a_{i1}=1/\alpha_0^4 \qquad a_{i2}=(\hat{i}\cdot\hat{g})^2 \qquad a_{i3}=4(\hat{i}\cdot\hat{g})^2/\alpha_0^4$$

$$a_{i4}=1/\alpha_0^2 \qquad a_{i5}=2(\hat{i}\cdot\hat{g})^2/\alpha_0^4 \qquad a_{i6}=(\hat{i}\cdot\hat{g})/\alpha_0^2$$

$$a_{i7}=2(\hat{i}\cdot\hat{g})^3/\alpha_0^2 \qquad a_{i8}=2(\hat{i}\cdot\hat{g})^2/\alpha_0^2 \qquad a_{i9}=2(\hat{i}\cdot\hat{g})^3/\alpha_0^2,$$

and the subscript $i=1,\ldots,9$ represent nine distinct temporal frequencies. Notice that the operator $(\hat{i}\cdot\hat{g})$ is a function of the frequency. Therefore, the autopower spectrum and crosspower spectrum of the fluctuation of the individual physical parameter can be solved using system (26) and backpropagated to the spatial domain as in the case of deterministic diffraction tomography.

INITIAL RESULTS OF THE NUMERICAL EXPERIMENT

With figure 1, we show the random velocity field with an exponential autocorrelation function $f(x,z)=\exp(-\sqrt{(x/a)^2+(z/b)^2})$, where a and b is the horizontal and vertical autocorrelation length, respectively (see Appendix B). The inhomogeneities of the medium is described as isotropic or elongated in a direction parallel to either of the two Cartesian directions.

A random velocity field is shown in figure 2. λ is defined as the average wavelength occurred in regions of the medium where the fluctuations of elastic parameters are uncorrelated. $r_0 = b / a$ is defined as the aspect ratio. The weak scattering can be interpreted as $\lambda >> r_0$ which is used to gauge the wavefield modeling.

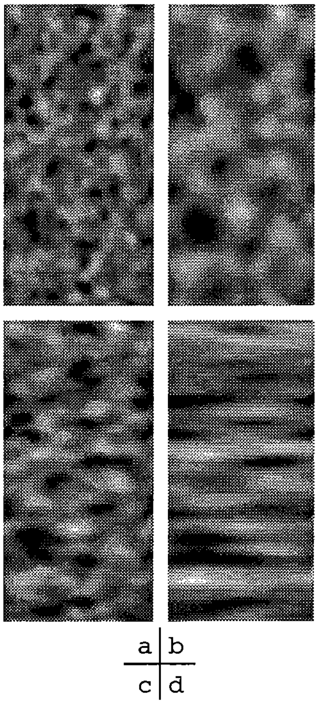

Figure 1. The random velocity field with different vertical and horizontal correlation length a's and b's. a) an isotropic model with a = b = 1; b) a = b = 2 ; c) a elliptical model with a = 2, b = 1; and d) a = 6, b = 1.

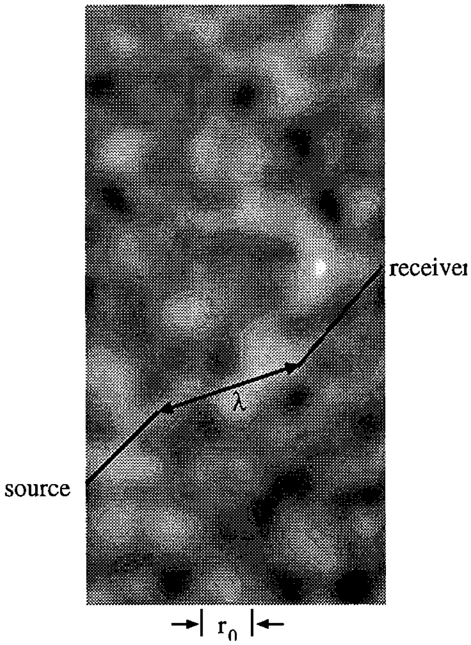

Figure 2. The weak scattering can be interpreted as $r_0 >> \lambda$, where λ is the average wavelength of the incident wave in the medium and r_0 is the aspect ratio ($r_0 = b/a$).

Two vertical slices of the velocity field are compared with the sonic well logs from McElroy near offset wells is shown in figure 3. We can see that the real medium has similar random characteristics.

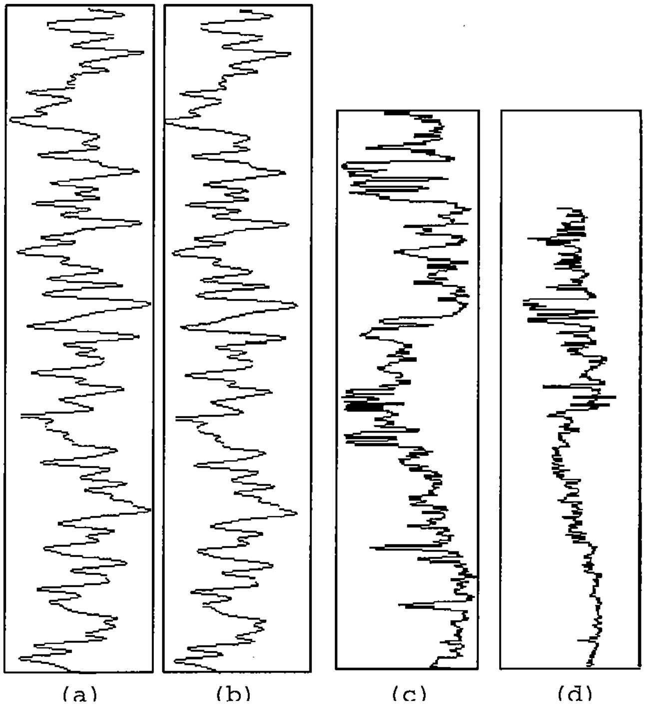

Figure 3. a) Two vertical slices of the random velocity field are compared with the sonic logs from McElroy near offset wells: a) a vertical slice of the velocity field at x=0; b) a vertical slice of the velocity field at x=100; c) McElroy 1068 log; and d) McElroy 1080 log.

In figure 4, the horizontal and vertical component seismograms obtained with finite difference scheme are shown. The autocorrelation lengths a and b is set 5m and 1m respectively. The grid size is chosen as $\Delta x = \Delta z = 0.15m$. The other elastic and statistical parameters are:

Central frequency of the source	$f_c = 400Hz$
P-wave velocity	$v_p = 3500m / \sec$
P-wave variance	$\sigma_p = 10\%$
P and s velocity ratio	$v_p / v_s = 1.65$
Variance of the ratio	$\sigma_{p/s} = 2\%$

From figure 4, we can see many weak scattering events after primary arrives in the seismogram that are due to small scale inhomogeneities.

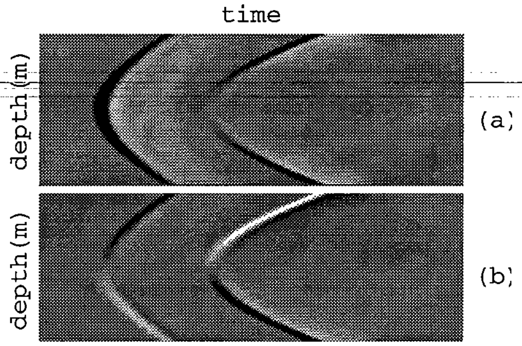

Figure 4. Finite difference simulation of the elastic wave propagation in random medium: a) horizontal component and b) vertical component.

For the real data, we use a similar a wavefield separation and processing scheme described in (Lazaratos, 1993), i.e.,

1) **2.5D Correction**

2) **Direct arrive removal**
    pick direct arrive
    align direct arrival
    subtract direct arrival
    dealign data

3) **Scattering enhancement and wove modes separation with F-K filters**

Using the above process flow, such as pp separation and enhancement, we processed a receiver gather of the McRlroy near offset data set which is shown in figure 5. We can see that there are many chaotic pp reflection/scattering features in the seismogram. Notice that the first p-wave arrival and firs s-wave arrive and thereafter have been eliminated. In figure 6, we show the power spectra of the processed data set at three distinct frequencies.

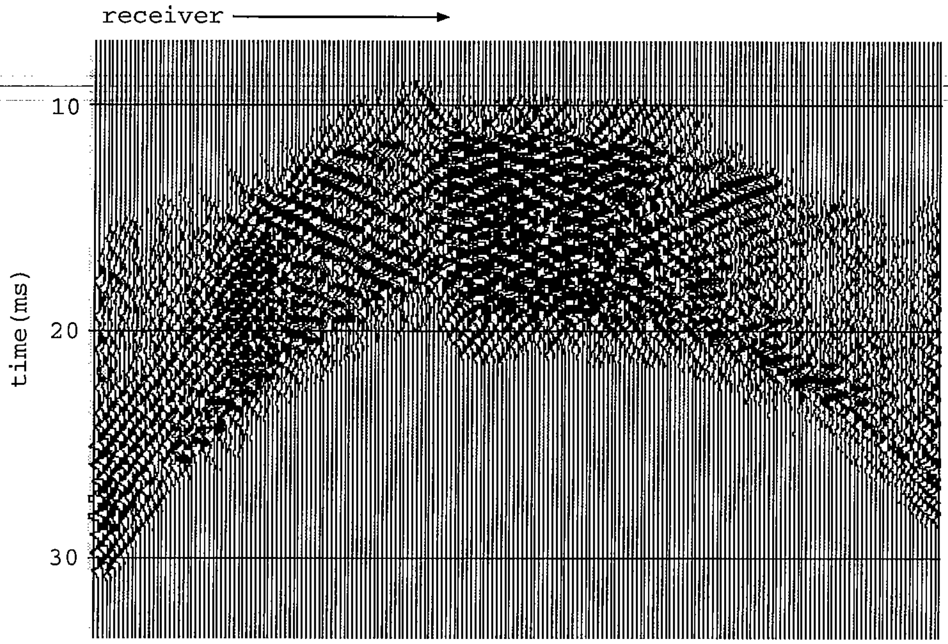

Figure 5. The processed wavefield from McElroy near-offset data set. The first p-arrival and first s-arrival and thereafter have been eliminated.

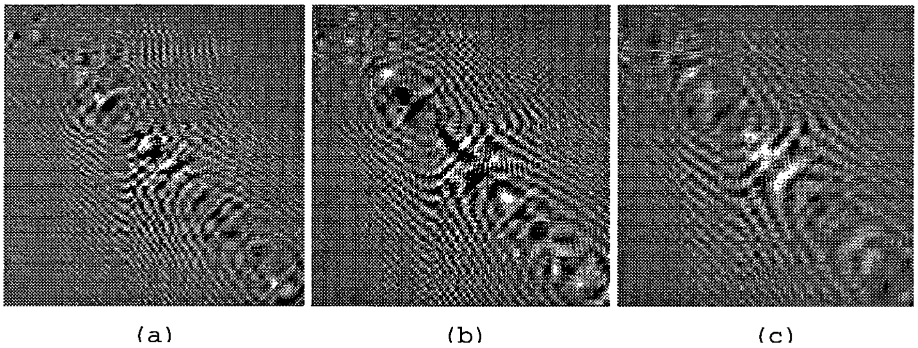

Figure 6. The spectra of the processed wavefield at three distinct frequencies: a), b) and c) is the spectrum at 1100 Hz; 1200 Hz; and 1600 Hz, respectively.

We invert the power spectra and get an autocorrelation function using diffraction tomographic technique discussed above. From figure 7, we can see that the auto correlation obtained is strongly aisotropical, i.e., the horizontal and vertical correlation lengths are different. This is expected since the other studies suggest the geology structure at the McElroy set are basically one dimensional. Note that the correlation function is not of a particular elastic parameters but of a m_{pp} function described in equation (21).

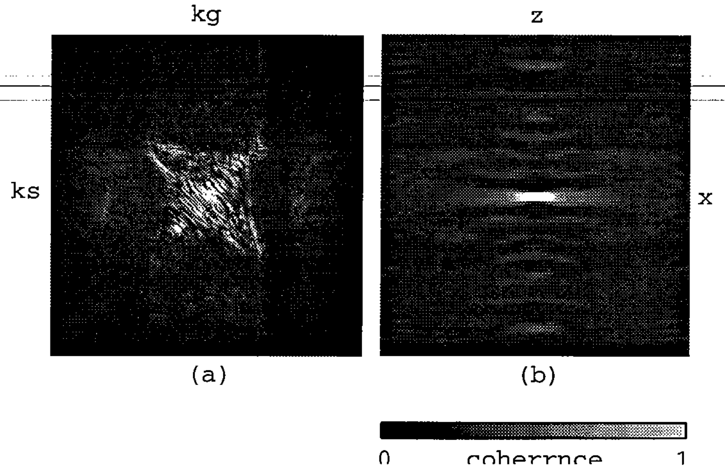

Figure 7. Diffraction tomographic inversion of the random medium: a) The spatial autopower spectrum of the processed wavefield of McElroynear-offset data set; and b) Inverted autocorrelation function of the m_{pp} function.

CONCLUSIONS

This is an on going research and the results shown are primary. One of the advantages of the method is that using resolved statistical quantities, such as the autopower and crosspower spectra. We can calculate the coherency between any two of the spectral that is a quantitative measure of the amount of linear relationship between two physical parameters. The may facilitate the study of the porosity or permeability of the medium or other simulation modalities. For the perturbation theory discussed above to be applicable it is necessary that the scattered field is small in comparison with the incident.

ACKNOWLEDGMENTS

I would like to thank Jessy Costa for many useful discussions and Lei-wei Mo for providing finite difference simulator.

REFERENCES

Aki, K., and Richard, P. G., Quantitative seismology, theory and methods: vol. 1 and 2, Freeman and Co., San Fransisco, 1980
Chernov, L. A., Wave propagation in a random medium (English translation R. A. Silverman), New York, McGraw-Hill, 1960
Ikelle, L. T., Yung, S. K. and Daube, F., 2-D random media with ellipsoidal autocorrelation functions, Geophysics, 58, 1359-1372, 1992
Lazaratos, S. K., Cross-well reflection imaging, Ph.D. thesis, Stanford University, 1993
Tatarsky, V. I., Wave propagation in a turbalent medium, New York, McGraw-Hill, 1961
Uscinski, B. J., The elements of wave propagation in random media, New York, McGraw-Hill, 1979

APPENDIX A

P-SV WAVE GREEN'S FUNCTION

The equation of motion in an elastic, isotropic medium is

$$\rho \ddot{u}_i - (\lambda u_{k,k})_{,i} - (\mu(u_{i,j} + u_{j,i}))_{,j} = F_i . \qquad \text{A-1}$$

For a two dimensional homogeneous background medium, in the x and z direction, we have

$$\rho \ddot{u}_x - \lambda(u_{x,xx} + u_{z,xz}) - 2\mu u_{x,xx} - \mu(u_{x,zz} + u_{z,xz}) = F_x , \qquad \text{A-2}$$

and

$$\rho \ddot{u}_z - \lambda(u_{x,xz} + u_{z,zz}) - 2\mu u_{z,zz} - \mu(u_{x,xz} + u_{z,zz}) = F_z . \qquad \text{A-3}$$

The displacements can be represented in terms of potentials (Aki and Richards, 1980) as

$$\begin{bmatrix} u_x \\ u_z \end{bmatrix} = \begin{bmatrix} \phi_{,x} \\ \phi_{,z} \end{bmatrix} + \begin{bmatrix} -\psi_{,z} \\ \psi_{,x} \end{bmatrix} \quad \text{and} \quad \begin{bmatrix} F_x \\ F_z \end{bmatrix} = \begin{bmatrix} \Phi_{,x} \\ \Phi_{,z} \end{bmatrix} + \begin{bmatrix} -\Psi_{,z} \\ \Psi_{,x} \end{bmatrix} \qquad \text{A-4}$$

where the potentials satisfy

$$\ddot{\phi} - \alpha^2 \nabla^2 \phi = \Phi / \rho \quad \text{and} \quad \ddot{\psi} - \beta^2 \nabla^2 \psi = \Psi / \rho , \qquad \text{A-5}$$

with $\alpha = \sqrt{(\lambda + 2\mu)/\rho}$ being the P-wave velocity and $\beta = \sqrt{\mu / \rho}$ the S-wave velocity of the medium. The upgoing and downgoing wavefields for the potentials in the Fourier transform domain are:

$$\phi^d = e^{ik_z^\alpha z} \quad \text{and} \quad \psi^d = e^{ik_z^\beta z} \quad \text{for } z > z_s , \qquad \text{A-6}$$

$$\phi^u = e^{-ik_z^\alpha z} \quad \text{and} \quad \psi^u = e^{-ik_z^\beta z} \quad \text{for } z < z_s . \qquad \text{A-7}$$

Rewriting the explicit form of A-2 and A-3 in the frequency domain

$$\begin{bmatrix} (\lambda + 2\mu)\partial_x^2 + \mu\partial_z^2 + \rho\omega^2 & (\lambda + \mu)\partial_x\partial_z \\ (\lambda + \mu)\partial_x\partial_z & (\lambda + 2\mu)\partial_z^2 + \mu\partial_x^2 + \rho\omega^2 \end{bmatrix} \begin{bmatrix} G_{xx} & G_{xz} \\ G_{zx} & G_{zz} \end{bmatrix} \qquad \text{A-8}$$

$$= - \begin{bmatrix} \delta(x - x_s)\delta(z - z_s) & 0 \\ 0 & \delta(x - x_s)\delta(z - z_s) \end{bmatrix} .$$

Taking the Fourier transform over x, A-8 becomes

$$\begin{bmatrix} -(\lambda+2\mu)k_x^2+\mu\partial_z^2+\rho\omega^2 & i(\lambda+\mu)k_x\partial_z \\ i(\lambda+\mu)k_x\partial_z & (\lambda+2\mu)\partial_z^2-\mu k_x^2+\rho\omega^2 \end{bmatrix} \begin{bmatrix} \tilde{G}_{xx} & \tilde{G}_{xz} \\ \tilde{G}_{zx} & \tilde{G}_{zz} \end{bmatrix} \qquad \text{A-9}$$

$$= -\begin{bmatrix} \delta(z-z_s) & 0 \\ 0 & \delta(z-z_s) \end{bmatrix} e^{-ik_x x_s}.$$

Using the potential and A-4, the solution of A-9 can be given as

$$\tilde{G}^d = \begin{bmatrix} ic_1 k_x \phi^d - c_3 \partial_z \psi^d & ic_5 k_x \phi^d - c_7 \partial_z \psi^d \\ c_1 \partial_z \phi^d + ic_3 k_x \psi^d & c_5 \partial_z \phi^d + ic_7 k_x \psi^d \end{bmatrix} \text{ for } z > z_s, \qquad \text{A-10}$$

and

$$\tilde{G}^u = \begin{bmatrix} ic_2 k_x \phi^u - c_4 \partial_z \psi^u & ic_6 k_x \phi^u - c_8 \partial_z \psi^u \\ c_2 \partial_z \phi^u + ic_4 k_x \psi^u & c_6 \partial_z \phi^u + ic_8 k_x \psi^u \end{bmatrix} \text{ for } z < z_s. \qquad \text{A-11}$$

Applying the conditions

$$\tilde{G}^d = \tilde{G}^u \qquad \text{and} \qquad \partial_z \tilde{G}^d - \partial_z \tilde{G}^u = -\begin{bmatrix} 1/\mu & 0 \\ 0 & 1/(\lambda+2\mu) \end{bmatrix} e^{-ik_x x_s}$$

the coefficients c1 to c8 is solved for

$$c_1 = c_8 = k_x / 2\rho\omega^2 k_z^\alpha$$

$$c_4 = -c_3 = c_5 = -c_6 = 1/2\rho\omega^2$$

$$c_7 = c_8 = k_x / 2\rho\omega^2 k_z^\beta.$$

Substituting the coefficients back we obtain

$$\tilde{G} = \begin{bmatrix} k_x^2 & sgn(z-z_s)k_x k_z^\alpha \\ sgn(z-z_s)k_x k_z^\alpha & (k_z^\alpha)^2 \end{bmatrix} \frac{ie^{ik_z^\alpha |z-z_s| - ik_x x_s}}{2\rho\omega^2 k_z^\alpha} \qquad \text{A-12}$$

$$+ \begin{bmatrix} (k_z^\beta)^2 & sgn(z_s-z)k_x k_z^\beta \\ sgn(z_s-z)k_x k_z^\beta & k_x^2 \end{bmatrix} \frac{ie^{ik_z^\beta |z-z_s| - ik_x x_s}}{2\rho\omega^2 k_z^\beta},$$

or equivalently

$$\tilde{G} = \begin{bmatrix} \dfrac{\partial^2}{\partial x^2} & \dfrac{\partial^2}{\partial x \partial z} \\ \dfrac{\partial^2}{\partial x \partial z} & \dfrac{\partial^2}{\partial z^2} \end{bmatrix} \frac{ie^{ik_z^\alpha |z-z_s| - ik_x x_s}}{2\rho\omega^2 k_z^\alpha} + \begin{bmatrix} \dfrac{\partial^2}{\partial x^2} & -\dfrac{\partial^2}{\partial x \partial z} \\ -\dfrac{\partial^2}{\partial x \partial z} & \dfrac{\partial^2}{\partial z^2} \end{bmatrix} \frac{ie^{ik_z^\beta |z-z_s| - ik_x x_s}}{2\rho\omega^2 k_z^\beta}. \qquad \text{A-13}$$

Taking the inverse Fourier transform on A-13 we arrive

$$G = \begin{bmatrix} \dfrac{\partial^2}{\partial x^2} & \dfrac{\partial^2}{\partial x \partial z} \\ \dfrac{\partial^2}{\partial x \partial z} & \dfrac{\partial^2}{\partial z^2} \end{bmatrix} \int \frac{ie^{ik_z^\alpha |z-z_s| - ik_x x_s}}{2\rho\omega^2 k_z^\alpha} dk_x + \begin{bmatrix} \dfrac{\partial^2}{\partial x^2} & -\dfrac{\partial^2}{\partial x \partial z} \\ -\dfrac{\partial^2}{\partial x \partial z} & \dfrac{\partial^2}{\partial z^2} \end{bmatrix} \int \frac{ie^{ik_z^\beta |z-z_s| - ik_x x_s}}{2\rho\omega^2 k_z^\beta} dk_x .$$

A-14

The individual components of the plane wave decomposition of the Green's function along the source line can be written as

$$\tilde{G}(r,k_s) = \frac{i}{2\rho\omega^2} \begin{bmatrix} (k_x^s)^2 & k_z^{\alpha s} k_x^s \\ k_z^{\alpha s} k_x^s & (k_z^{\alpha s})^2 \end{bmatrix} \frac{e^{i\gamma_s^\alpha x_s - ik^\alpha \hat{s}\cdot r}}{\gamma_s^\alpha} + \frac{i}{2\rho\omega^2} \begin{bmatrix} (k_z^{\beta s})^2 & -k_z^{\beta s} k_x^s \\ -k_z^{\beta s} k_x^s & (k_x^s)^2 \end{bmatrix} \frac{e^{i\gamma_s^\beta x_s - ik^\beta \hat{s}\cdot r}}{\gamma_s^\beta},$$

A-15

where $k^\alpha = \omega / \alpha$, $k^\beta = \omega / \beta$ and $k_z^{\alpha s}$, $k_z^{\beta s}$ are the vertical wavenumbers over the source line for P and S waves respectively. The decomposition along the receiver line can be obtained by replacing the s's with g's in A-15.

APPENDIX B

TWO DIMENSIONAL RANDOM MEDIUM MODELING

In this appendix, we present a scheme of generating a two dimensional random velocity field following Ikelle (1992). Assuming the random velocity field has a exponential autocorrelation function:

$$auto(x,z) = \exp(-\sqrt{x^2 / a^2 + z^2 / b^2}), \qquad \text{B-1}$$

where a and b are the autocorrelation lengths. The correlation function is considered ellipsoidal because the variables a and z have different scaling factor a and b. A distribution of uncorrelated random number $\theta \subset [0, 2\pi)$ is defined as the phase of the random velocity field. In the Fourier transform domain, the random velocity field has the form of

$$Rand(k_x, k_z) = \sqrt{auto(k_x, k_z)} \cdot \exp[i\theta(k_x, k_z)] \qquad \text{B-2}$$

Obviously, the velocity field

$$rand(x,z) = FT_{2d}\{Rand(k_x, k_z)\} \qquad \text{B-3}$$

has a autocorrelation function described above.

In the implantation, we make sure that the first two statistical moments are correct. To satisfy the finite difference's condition of stability and dispersion, the limits to p-wave velocity and s-wave velocity variations are imposed. These limits are large enough so that statistical parameters do not change.

PAPER P

POST-CDP-MAPPED MIGRATION IN VERTICAL SEISMIC PROFILE

Le-Wei Mo

ABSTRACT

In this paper, I investigate the post-CDP-mapped migration of dipping reflectors. VSP-CDP maps reflection of a dipping reflector into a third-order polynomial. Under certain conditions, this third-order polynomial can be approximated by a line. Under the guidance of forward modeling linear regression, this line is rotated in slant-stack tau-p space. Inverse slant stack gives the correctly imaged dipping reflector in space. This VSP post-CDP-mapped migration scheme is designed to be accurate from 0 to +/- 15 degrees.

INTRODUCTION

In vertical seismic profiling (VSP), a source is placed at the Earth surface and a string of receivers are placed in the borehole to record both the downgoing direct arrival and the upgoing reflections, Figure 1. The advantages of vertical seismic profiling over the conventional surface seismic reflection surveys are many. Since the receivers are buried in the borehole within the earth rather than on the earth surface, the source excited seismic waves propagate only once through the severe attenuating near-surface weathered zone.. The frequency contents of the seismic waves as recorded are richer than in surface seismic reflection survey. As VSP data are recorded inside the earth during the wave propagation process, VSP data are in-situ recorded data. VSP data has been used for correlating seismic and well log data, for identifying multiple reflections, for analyzing source signature effects, and for studying the effects of attenuation. As in surface seismic reflection survey, vertical seismic profiling data can also provide structural information of the earth subsurface, in partilcular near the borehole. Since the receivers are placed within the earth and the resulting recorded frequency bandwidth is wide, vertical seismic profiling data can provide higher resolution structural images in the vicinity of the borehole, revealing small features otherwise unseen in conventional surface seismic reflection survey images. High resolution structural images near the boreholes are very useful in reservoir characterizations. It has been reported vertical seismic profiling can detect waterflooding and CO2 injection fluid fronts. However, the vertical seismic profiling can only provide high resolution information in the vicinity of the boreholes, it is a complementary survey method to the convential surface seismic method which provide low resolution information but over a large area.

The methodology of structural imaging in vertical seismic profiling has largely been influenced by surface seismic reflection data processing. For example, in migration imaging, many authors have reported applying pre-stack depth profile migration methods. These pre-stack migration methods, e.g., Kirchhoff migration, reverse-time, phase-shift plus interpolation, are equivalent, they only differ in the way wavefields are extrapolated. In surface seismic reflection surveys, pre-stack depth migration has been popularly applied to all survey areas, and it has enjoyed many successes in subsurface structure imaging in the complexity of 3-D saltdomes. The success of pre-stack depth migration in surface seismic survey lies in the wide recording aperture and that there are many shots and receivers in surface seismic survey. In vertical seismic profiling, there is usually only shot gather data or in a better survey there are a few shot gathers,; and in each common shot gather there are usually less than 100 receiver traces data. This means the surveying aperture in VSP is very small, there are not enough pre-stack profile migration images to stack to attenuate out the edge diffractions and increase signal/noise level. Thus, even though pre-stack depth profile migration is a powerful imaging method, when applied to vertical seismic profiling where the conditions for its utilizations are not met, the results might not be satisfactory. In surface seismic survey, a less sophisticated structural imaging method is the sequence of CDP stack and post-stack migration, which has a better noise tolerance even though suffering in some lower accuary than the pre-stack depth migration.

Wyatt et al (1981) introduced the CDP technique of surface seismic reflection survey into vertical seismic profiling. In surface seismic reflection data processing, CDP stack is followed by a post-stack migration. because CDP stacking does not place the dipping reflectors at the correct positions. As noted in Wyatt et al (1981), post-CDP migration is an indispensible step in VSP-CDP structural imaging. But, this post-CDP migration has been lacking for more than a decade. In migration, curves are correctly migrated by migration operating on lines as a curve is the envelope of lines of various dips.

VSP reflection traveltime from a dipping interface

The VSP geometry for a single dipping interface at an angle θ is shown in Figure 1. In this survey geometry, L is the well-to-shot offset; d is the depth to the geophone receiving the reflected ray; and h is the depth to the point where the dipping interface intercepts the well.

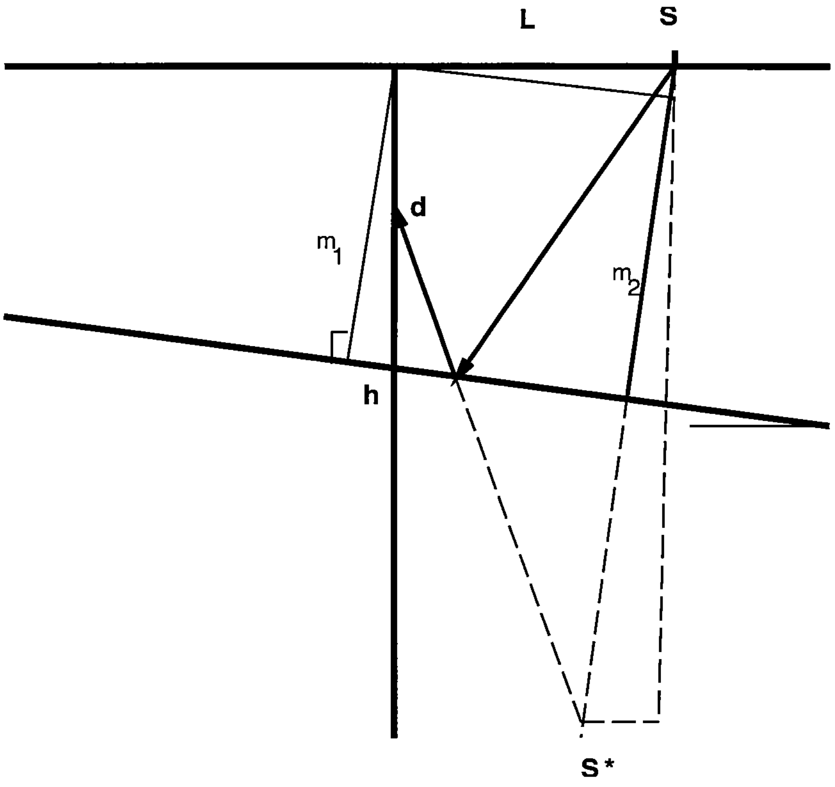

Figure 1: VSP reflection survey and traveltime

In deriving traveltime equation for the reflected ray, m_1 is the perpendicular distance from the top of the well to the interface, m_2 is the perpendicular distance from the shot to the interface. The following relationships follow from this figure:

$$m_1 = h\cos\theta$$

$$m_2 = m_1 + L\sin\theta$$

$$m_2 = h\cos\theta + L\sin\theta$$

The Cartesian coordinates at the image source $S*$ are:

$$x_{S*} = L - 2m_2\sin\theta$$

$$x_{S*} = L - 2(h\cos\theta + L\sin\theta)\sin\theta$$

$$z_{S*} = 2(h\cos\theta + L\sin\theta)\cos\theta$$

If the layer velocity is v and the reflection event traveltime is t,

$$v^2t^2 = x_{S*}{}^2 + [z_{S*} - d]^2$$

$$v^2t^2 = [L - 2(h\cos\theta + L\sin\theta)\sin\theta]^2 + [2(h\cos\theta + L\sin\theta)\cos\theta - d]^2$$

After some algebraic simplications, we arrive at:

$$v^2t^2 - L^2 = 4(h-d)(h\cos^2\theta + L\cos\theta\sin\theta) + d^2$$

When $d=0$ and $\theta = 0$, that is for flat reflector and the receivers being located at the earth surface, it reduces to the NMO traveltime equation for surface seismic reflection survey.

VSP reflection CDP depth mapping

The CDP mapping algorithm assumes flat reflectors, Figure 2. The reflection point coordinates are related by

$$\frac{x}{z-d} = \frac{L-x}{z}$$

From this equation we obtain

$$d = z - \frac{xz}{L-x}$$

The CDP mapping traveltime equation is

$$v^2t^2 = L^2 + (2z-d)^2$$

$$z = \frac{\sqrt{v^2t^2 - L^2} + d}{2}$$

Using the traveltime equation (A-6), we get

$$z = \frac{\sqrt{4(h-d)(h\cos^2\theta + L\sin\theta\cos\theta) + d^2} + d}{2}$$

Plug in the CDP mapping relation for d, we obtain

$$xz^2 = [(L-x)h + (2x-L)z](h\cos^2 + L\sin\theta\cos\theta)$$

This is a third-order nonlinear equation.

Let $\delta = h\cos^2 + L\sin\theta\cos\theta$, and fix x, it becomes a second-order equation for z,

$$z = \frac{(2x-L)\delta + \sqrt{(2x-L)^2\delta^2 + 4x(L-x)h\delta}}{2x}$$

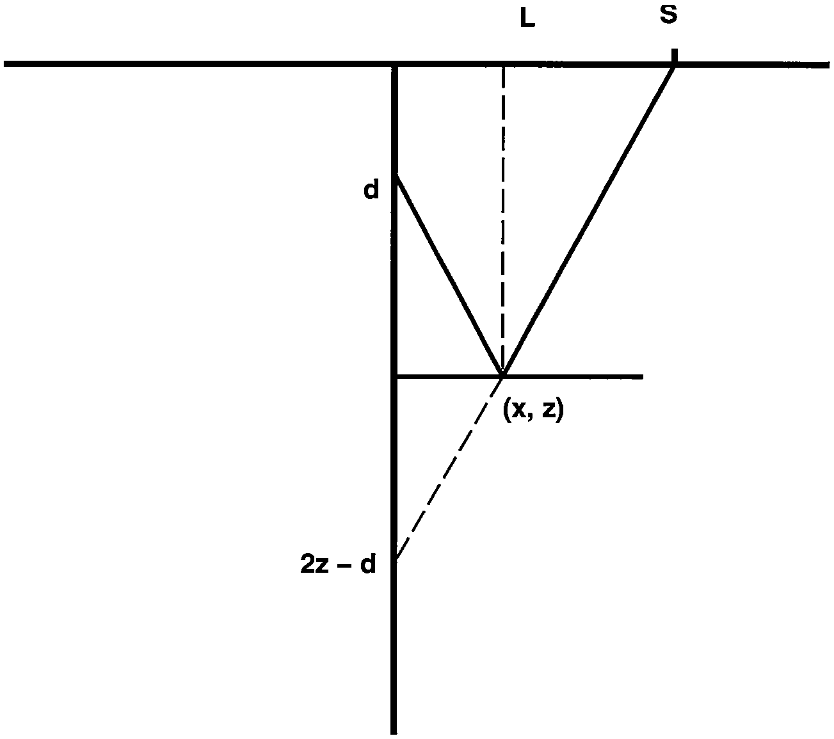

Figure 2: VSP reflection CDP mapping.

REFERENCES

Cassell, B. R., Alam, M. A., and Millahn, K. O., 1984, Interactive VSP-CDP mapping in complex media: 54th Ann. Internat. Mtg., Soc. Explor. Geophys., Expanded Abstracts, 842-845.

Chang, W. F., and McMechan, G. A., 1986, Reverse-time migration of offset vertical seismic profiling data using the excitation-time imaging conditions: Geophysics, 51, 67-84.

Dillon, P. B., and Thomson, R. C., 1984, Offset source VSP surveys and their image reconstruction: Geophysical Prospecting., 32, 790-811.

Dillon, P. B., 1988, Vertical seismic profile migration using the Kirchhoff integral: Geophysics, 53, 786-799.

Hardage, B.A., 1983, Vertical seismic profiling part A -- principles: Geophysical Press.

Wiggins, J. W., Ng, P., and Manzur, A., 1986 The relation between the VSP-CDP transformation and VSP migration: 56th Ann. Internat. Mtg., Soc. Explor. Explo.,Geophys., Expanded Abstract, 564-568.

Wyatt, K. D., and Wyatt, S. B., 1981, Determinating subsurface structure using the vertical seismic profiling: 51st Ann. Internat. Mig., Soc. Expl. Geophys., Expanded Abstracts, 99-102.

PAPER Q

EVALUATING THE EFFECT OF REFLECTION VELOCITY ANALYSIS BEFORE STACK ON THE WIDE OFFSET MRGP DATA SET

Nicholas Smalley

ABSTRACT

In this paper we consider the effect of reflection velocity analysis on reflection coherency before stack at several lateral point locations on the wide offset MRGP data set. We use the full range of angles or radial distances that the velocity analysis suggests can be stacked to give the most coherent reflection image possible at that particular lateral location. This approach has the advantage of giving the optimum stack possible for a localized lateral location. However, since the range of optimum angles changes greatly from the wells to the middle of the survey, it has the disadvantage of a change in the vertical spatial wavelength as a function of lateral location. We examine this approach at five lateral locations (CLP gathers) starting near the source well and going towards the middle of the data set. We see data that is well aligned for stack at each lateral location for all depths for three different bandpass filters.

INTRODUCTION

Crosswell reflection velocity analysis (Smalley, 1993) is based on the CLP sorting of crosswell data and the crosswell polar coordinate stacking system (Smalley, 1992). The objective of reflection velocity analysis is to find the stacking velocities that will maximize the coherency of the reflection data. After velocity analysis, we do CLP imaging using the stacking velocities determined from velocity analysis to map the reflection data from time to space. Reflection velocity analysis is more difficult for reflection points in the middle of the survey compared to reflection points at the wells due to the poorer signal to noise ratio. Consequently, the optimum range of angles or radial distances that can be used for the stack are fewer and at larger angles in the middle of the survey than at the wells.

VELOCITY ANALYSIS RESULTS

In figure 1 we see CLP - VLMO gathers for reflection points near the source well and in the middle of the survey after velocity analysis. We see two key differences in these gathers:

1) The signal to noise ratio is greater at the source well as opposed to the middle of the survey.

2) The range of angles or radial distances over which there is coherent reflection energy is larger at the source well as opposed to the middle of the survey.

Figure 2 shows the location of reflection velocity analysis nodes used on this survey. At each one of these nodes we performed reflection velocity analysis. The average range of angles used for all reflection depths at the source well and in the middle of the survey is shown in figure 3.

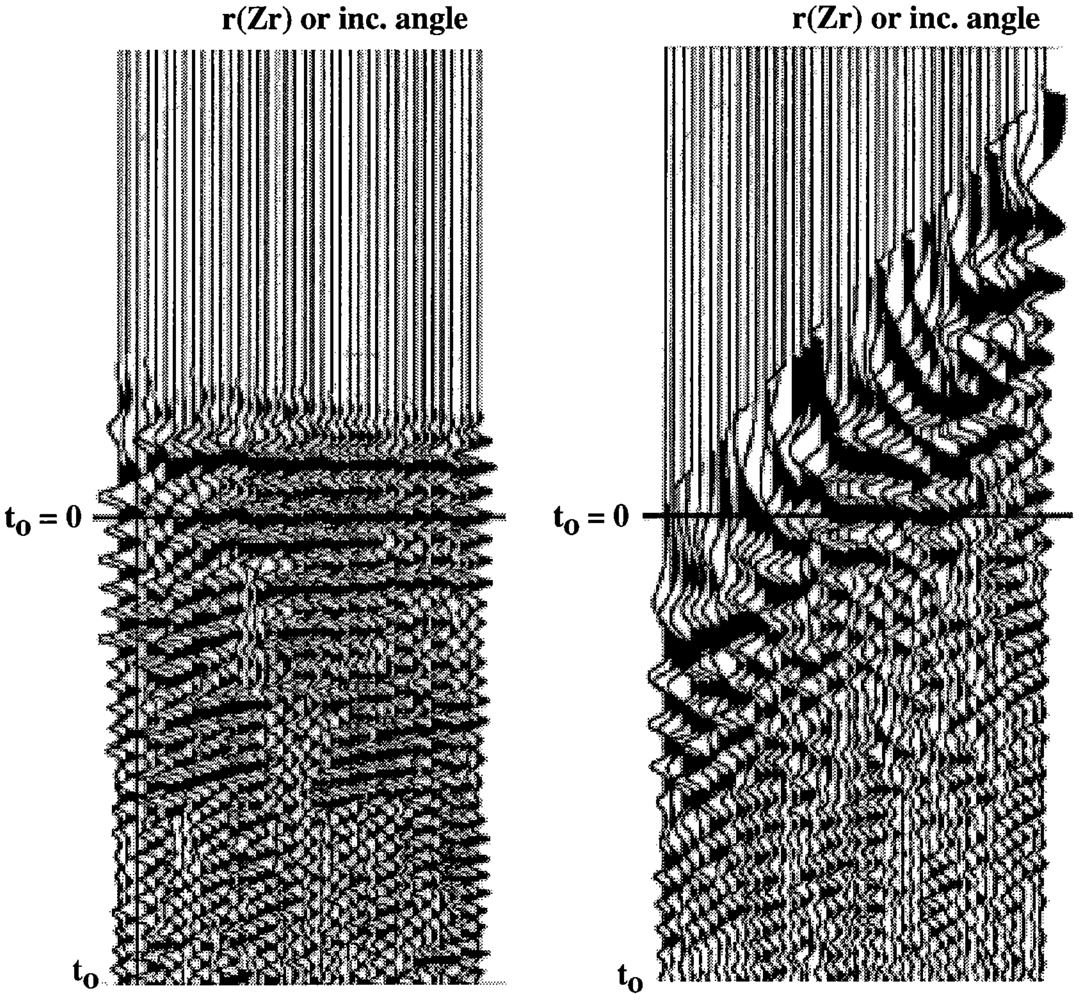

Figure 1. CLP - VLMO gathers for a reflection point near the source well (left) and a reflection point in the middle of the survey (right).

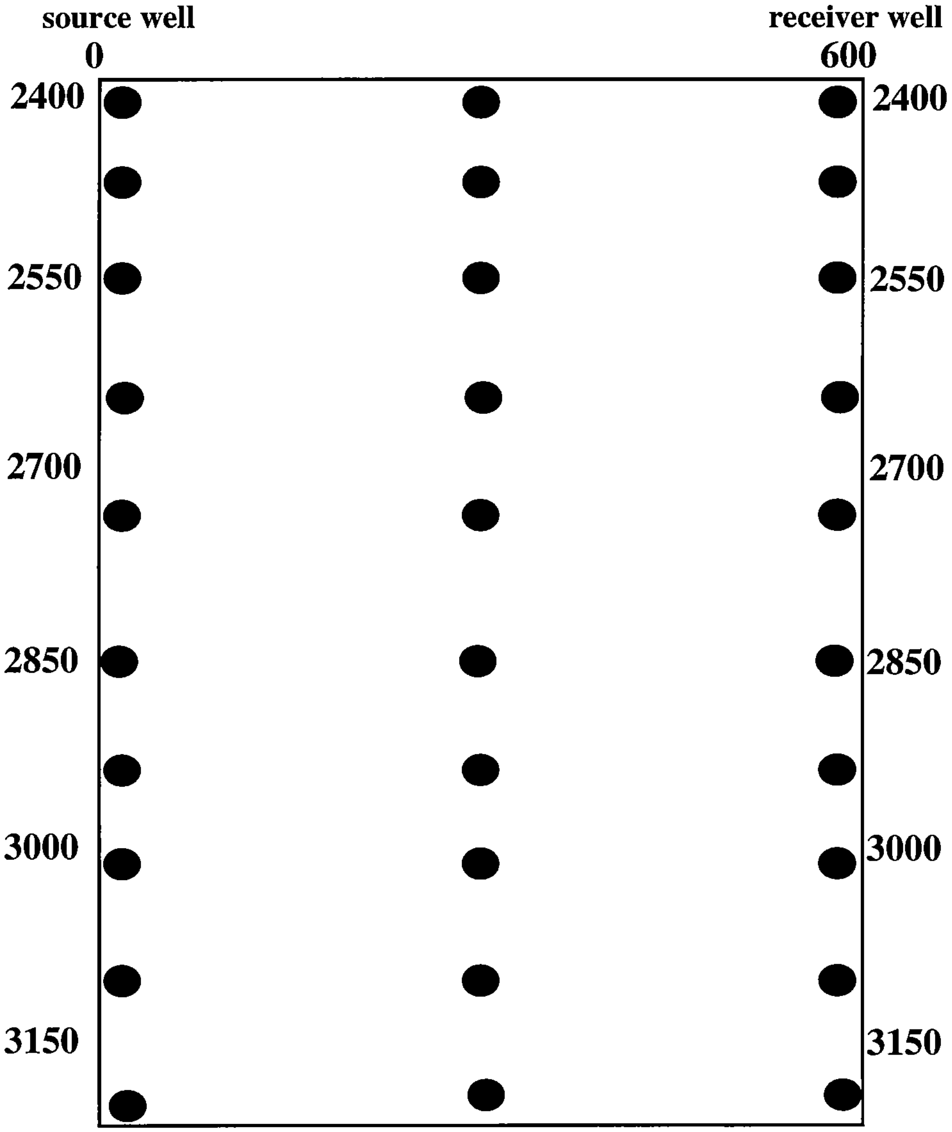

Figure 2. Location of nodes for reflection velocity analysis (units are feet).

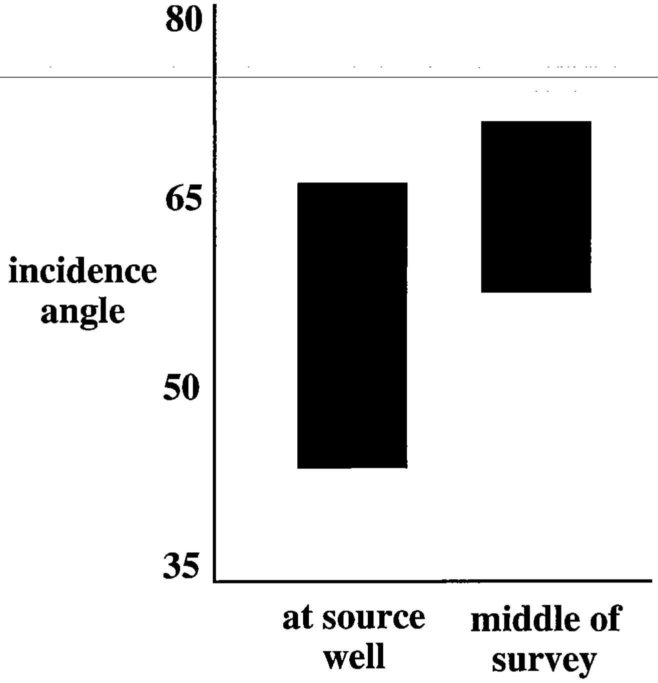

Figure 3. Average range of incidence angles used in the survey.

EVALUATING THE VELOCITY ANALYSIS ON REFLECTION ALIGNMENT

The reflection results using the velocity analysis and CLP imaging (Smalley, 1994) for five lateral point gathers (CLP gathers) are shown in figure 4. The lateral locations are 30, 90, 150, 210, and 270 feet from the source well. They are shown after additional wavefield separation and application of a bandpass filter. We show the same CLP gathers after a low bandpass filter is applied (figure 5), and after a high bandpass filter is applied (figure 6). We see the desired zero moveout for almost all of the events for the full range of depths for all three bandpass filters. Due to the different range of angles used near the source well as opposed to the middle of the wells, we see more reflection events for the CLP locations at 30 and 90 feet from the source well than for CLP locations at 210 and 270 feet from the source well. The benefit to using the full range of angles that velocity analysis suggests will give a coherent stack is a better stack for a localized lateral region. The CLP reflection imaging technique discussed in a previous paper (Smalley, 1994) kept a constant range of angles in the reflection imaging. This resulted in a consistent wavelet going from the source to receiver well. However, by forcing the range of angles used in the stack to stay constant throughout the survey, we don't get to keep all the angles or radial distances that can contribute constructively to the stack.

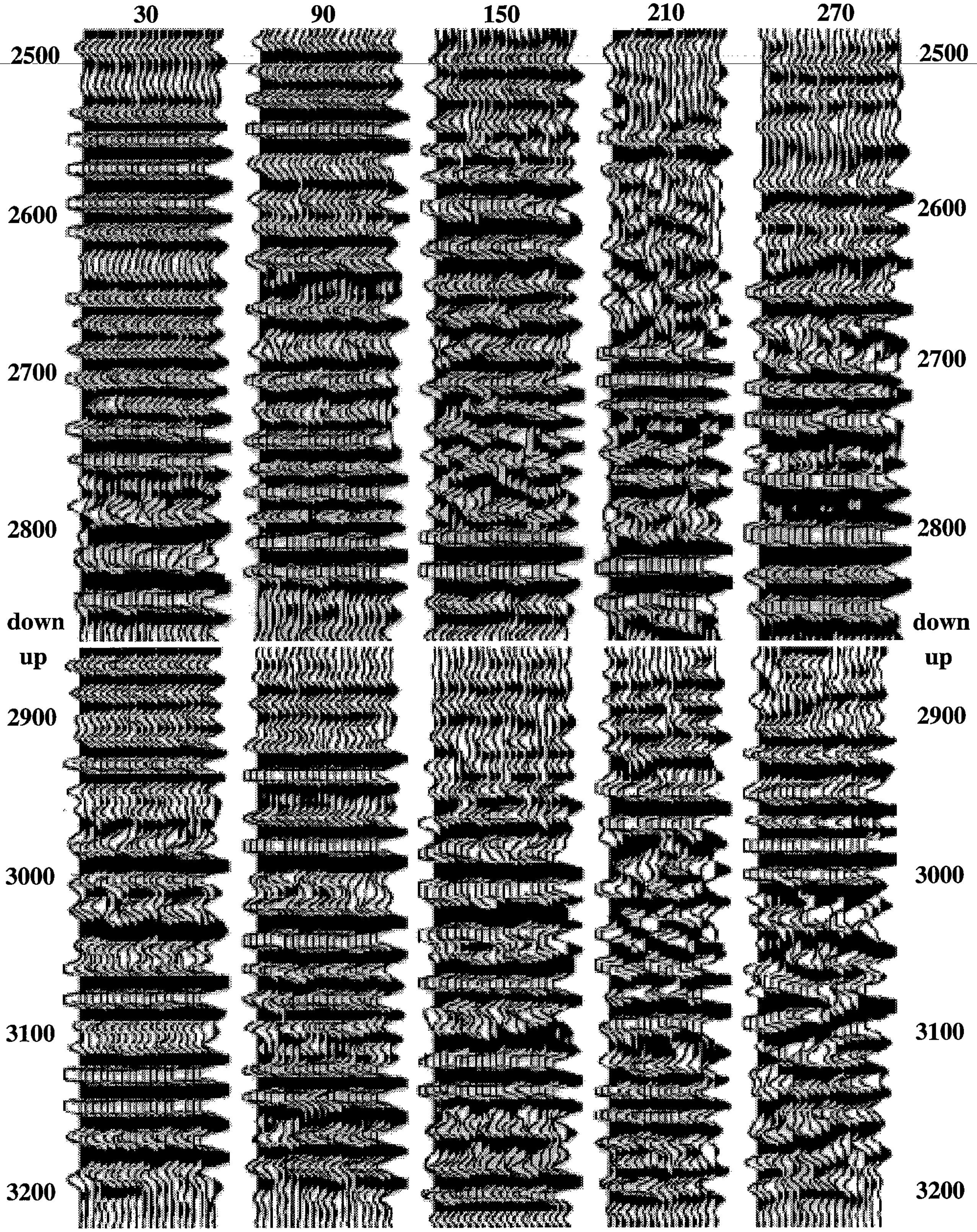

Figure 4. Five CLP gathers after velocity analysis and before stack with a bandpass filter.

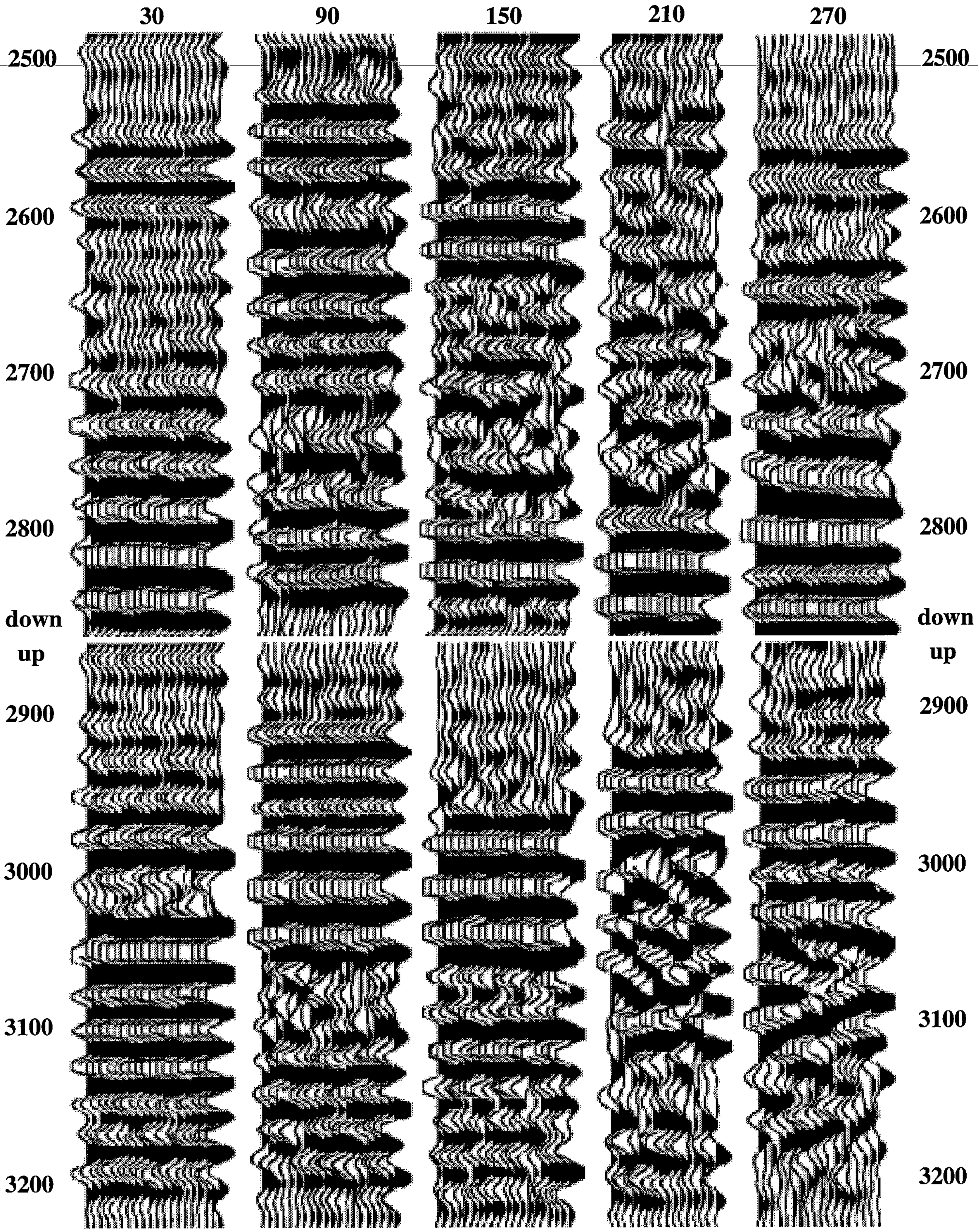

Figure 5. Five CLP gathers after velocity analysis and before stack with a low pass filter.

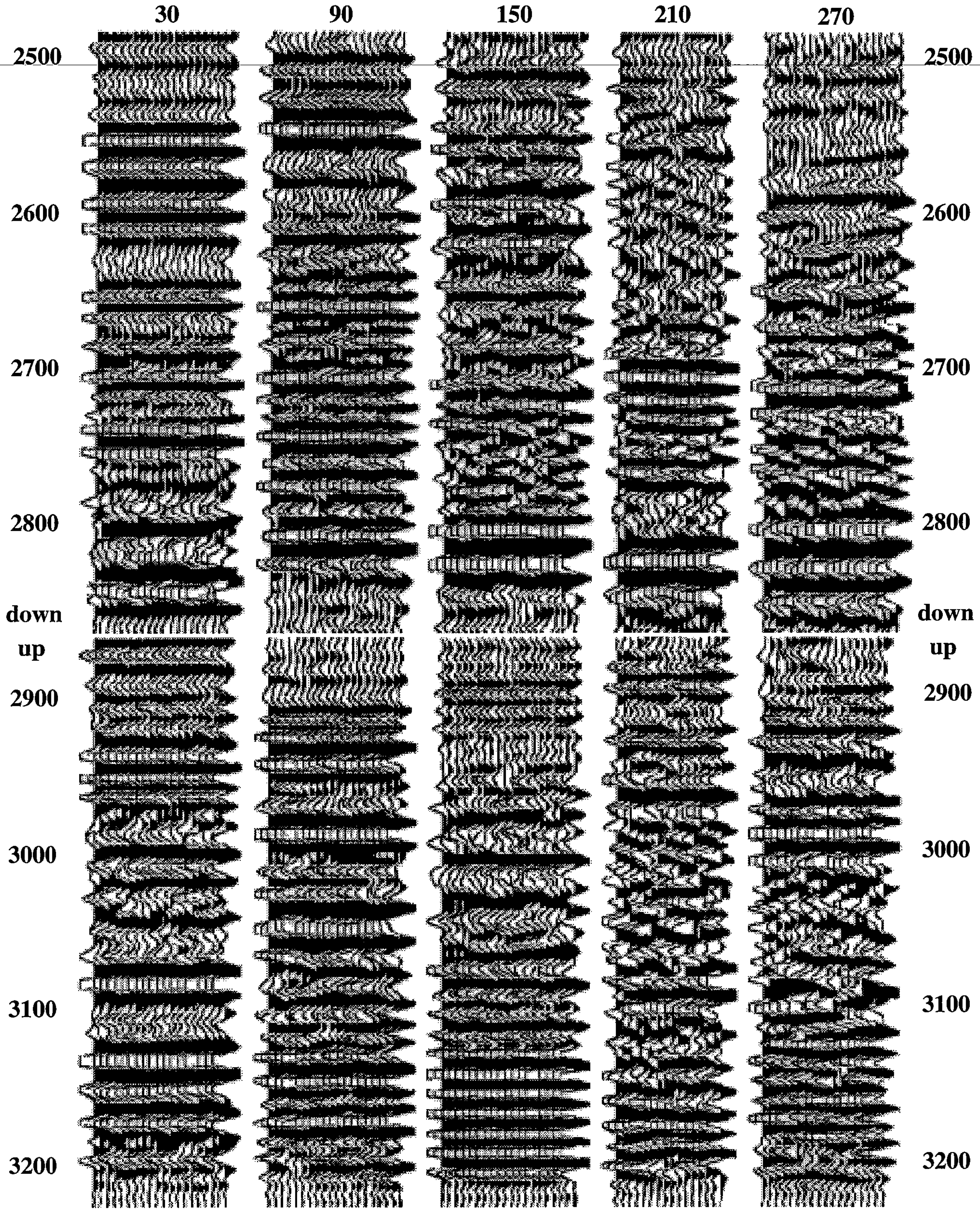

Figure 6. Five CLP gathers after velocity analysis and before stack with a high pass filter.

CONCLUSIONS

We have shown CLP gathers after velocity analysis for five lateral locations from near the source well to near the middle of the survey. We used the full range of angles or radial distances suggested by the velocity analysis for maximizing coherency in the CLP imaging on these five gathers. We see excellent alignment of the reflection data, and a change in the spatial wavelength as a function of CLP location. The potential benefits of using the full range of optimum angles in the stack would be a better stack at a specific lateral location as opposed to a better overall stack.

ACKNOWLEDGMENTS

The author thanks Jerry Harris and Bob Langan for their support, and the sponsors of the STP project at Stanford for their financial support.

REFERENCES

Lazaratos, S., 1993, Crosswell Reflection Imaging, Ph. D. Thesis.

Smalley, N., 1992, Crosswell Pre-Stack Partial Migration (Theory): STP vol. 3 No. 1, Paper M.

Smalley, N., 1993, Crosswell Reflection Velocity Analysis: STP vol. 4 No. 1 Paper G.

Smalley, N., 1994, Crosswell Common Lateral Point Reflection Imaging, STP vol. 5 No. 1, Paper E.

PAPER R

INVERTING FOR INTERVAL VELOCITIES FROM REFLECTION VELOCITY ANALYSIS ON THE WIDE OFFSET MRGP DATA SET

Nicholas Smalley

ABSTRACT

In this paper we describe a method for inverting for interval velocities from the stacking velocities determined from reflection velocity analysis for CLP (Common Lateral Point) reflection imaging. The results show finely detailed interval velocity profiles. We do this for a full range of reflection depths for three reflection point locations: at the source and receiver wells, and in the middle of the survey.

INTRODUCTION

One of the principle components of the CLP reflection imaging method is the reflection velocity analysis. This procedure consists of finding the stacking velocities that will optimize the stack of the reflection data. The stacking velocities are the rms. or average velocities used in the HNMO and VLMO (Smalley, 1992) moveout corrections. The determination of stacking velocities for reflection imaging is the forward problem. The determination of interval velocities from the stacking velocities is the inverse problem.

FORMULATION OF STACKING VELOCITIES AND INTERVAL VELOCITIES

The concept of stacking velocities for crosswell data is taken from the variable velocity HNMO and VLMO moveout equations (Smalley, 1993). The variable velocity HNMO equation is:

$$t^2 = t_{ho}^2 + C_1 f^2, \tag{1}$$

where

$$C_1 = \frac{\sum\limits_{Z=Zs}^{Z=Zr} s_i \Delta z_i + \sum\limits_{Z=Zg}^{Z=Zr} s_i \Delta z_i}{\sum\limits_{Z=Zs}^{Z=Zr} \frac{\Delta z_i}{s_i} + \sum\limits_{Z=Zg}^{Z=Zr} \frac{\Delta z_i}{s_i}}, \tag{2}$$

and

$$t_{ho} = \sum\limits_{Z=Zs}^{Z=Zr} s_i \Delta z_i + \sum\limits_{Z=Zg}^{Z=Zr} s_i \Delta z_i, \tag{3}$$

where s_i is the interval slowness, f is the horizontal well offset, Zs is the source depth, Zg is the geophone or receiver depth, Zr is the reflection depth, and Δz_i is the interval layer thickness. C_1 is equivalent to the inverse of the rms. velocity squared of the transversed layers. We can rewrite equation (3) in the crosswell reflection polar coordinates (Smalley, 1992):

$$t_{ho} = \bar{s} \cdot [1 + \sin 2\alpha(Zr)]^{\frac{1}{2}} \cdot r(Zr), \tag{4}$$

where $\bar{s}$ is the average slowness, defined by

$$\bar{s} = \frac{1}{\left[|Zr - Zs| + |Zr - Zg|\right]} \left(\sum_{Z=Zs}^{Z=Zr} s_i \Delta z_i + \sum_{Z=Zg}^{Z=Zr} s_i \Delta z_i \right). \tag{5}$$

Equation (4) is the VLMO equation in variable velocity media. We have written the HNMO and VLMO moveout equations in terms of the rms. velocity and average of the slownesses of the transversed layers. As we see in equations (2) and (3), and in figure 1, the HNMO and VLMO stacking velocities or slownesses are a function of the source and receiver pair. While this makes the forward problem of determining stacking velocities more complicated, it gives us additional information about the interval velocities which make up the stacking velocities.

VELOCITY ANALYSIS PROCEDURE (FORWARD PROBLEM)

The reflection velocity analysis procedure is shown in figure 2, and detailed in a previous paper (Smalley, 1993). The data set used in this paper is the wide offset MRGP. The location of velocity analysis nodes (Smalley, 1994) for this survey is shown in figure 3 . In doing the velocity analysis, we assumed that the HNMO and VLMO stacking velocities are equal. Determining a different HNMO and VLMO stacking velocity for a given source - receiver pair and reflector depth would be very impractical. Additionally, we quantify these values in terms of velocities instead of slownesses. Figures 4, 5, and 6 show the stacking velocities for reflection depths 2410, 2560, and 2660 feet. Figures 4 and 5 are for a reflection lateral location at the source well. Figure 6 is for a reflection lateral location in the middle of the survey.

SOLVING FOR INTERVAL VELOCITIES (INVERSE PROBLEM)

The matrix inversion formulation to find the interval velocities or slownesses is given by

$$\begin{pmatrix} \Delta z_w & & & \\ \Delta z_w & \Delta z_1 & & \\ \Delta z_w & \Delta z_1 & \Delta z_2 & \\ \Delta z_w & \Delta z_1 & \Delta z_2 & \Delta z_3 \end{pmatrix} \begin{pmatrix} s_w \\ s_1 \\ s_2 \\ s_3 \end{pmatrix} = \begin{pmatrix} S_w \\ S_1 \\ S_2 \\ S_3 \end{pmatrix},$$

where Δz_w is the thickness of the wide angle reflection layer where no velocity analysis is performed, Δz_i is the thickness of the layers over which velocity analysis is performed, s_w and S_w is the slowness of the wide angle reflection layer, s_i is the slowness of the i th layer, and S_i is the stacking slowness from the reflection depth to the i th layer. The thickness of the layers Δz_i is determined from the velocity analysis procedure (figure 1). This system of equations is most easily solved by Gaussian elimination.

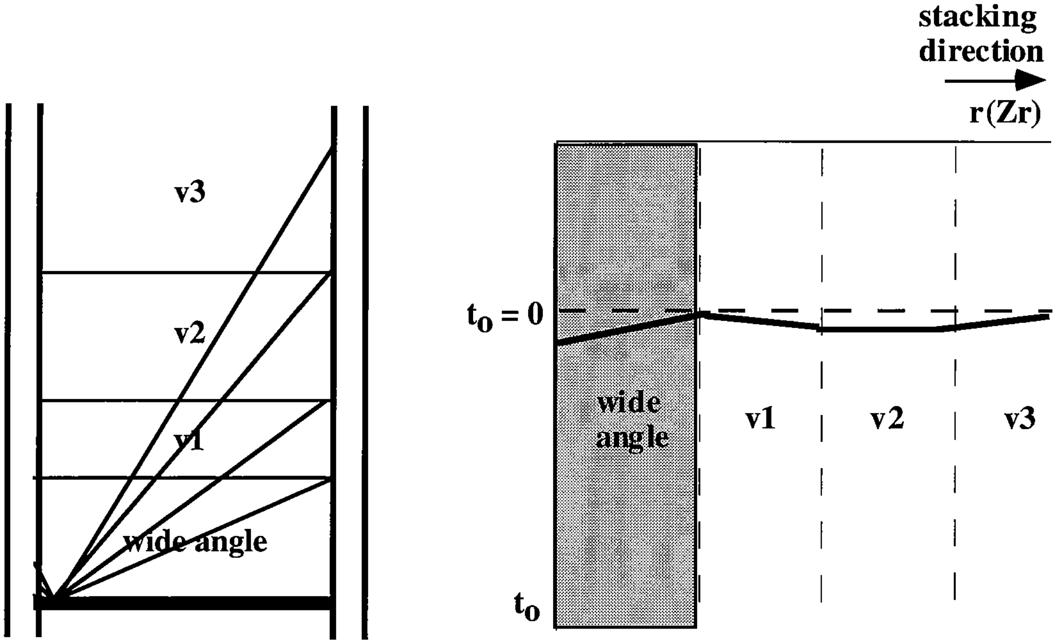

Figure 1. Raypaths for a CLP transcending different layers (left), and the corresponding CLP-VLMO gather before velocity analysis.

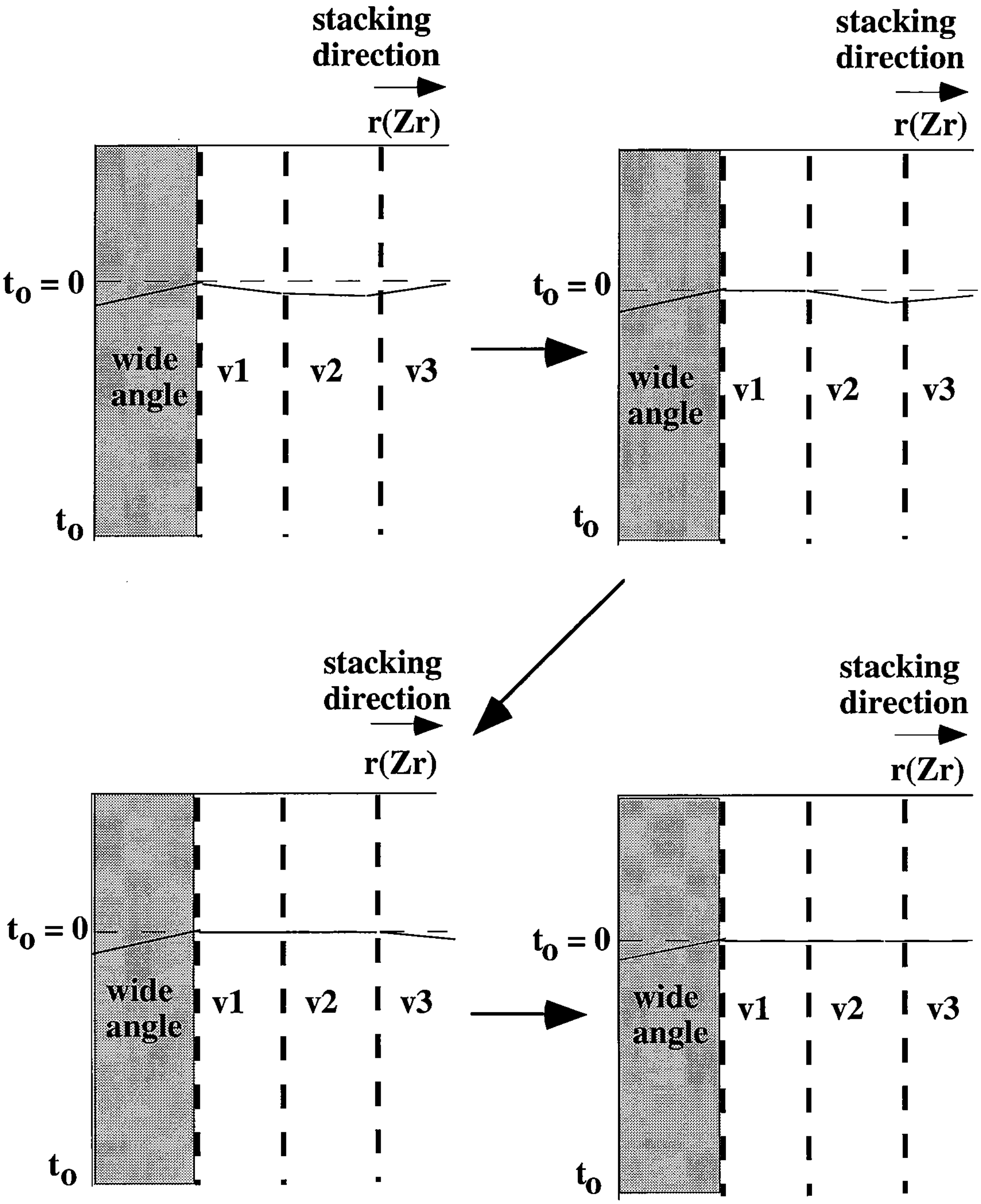

Figure 2. Reflection velocity analysis sequence.

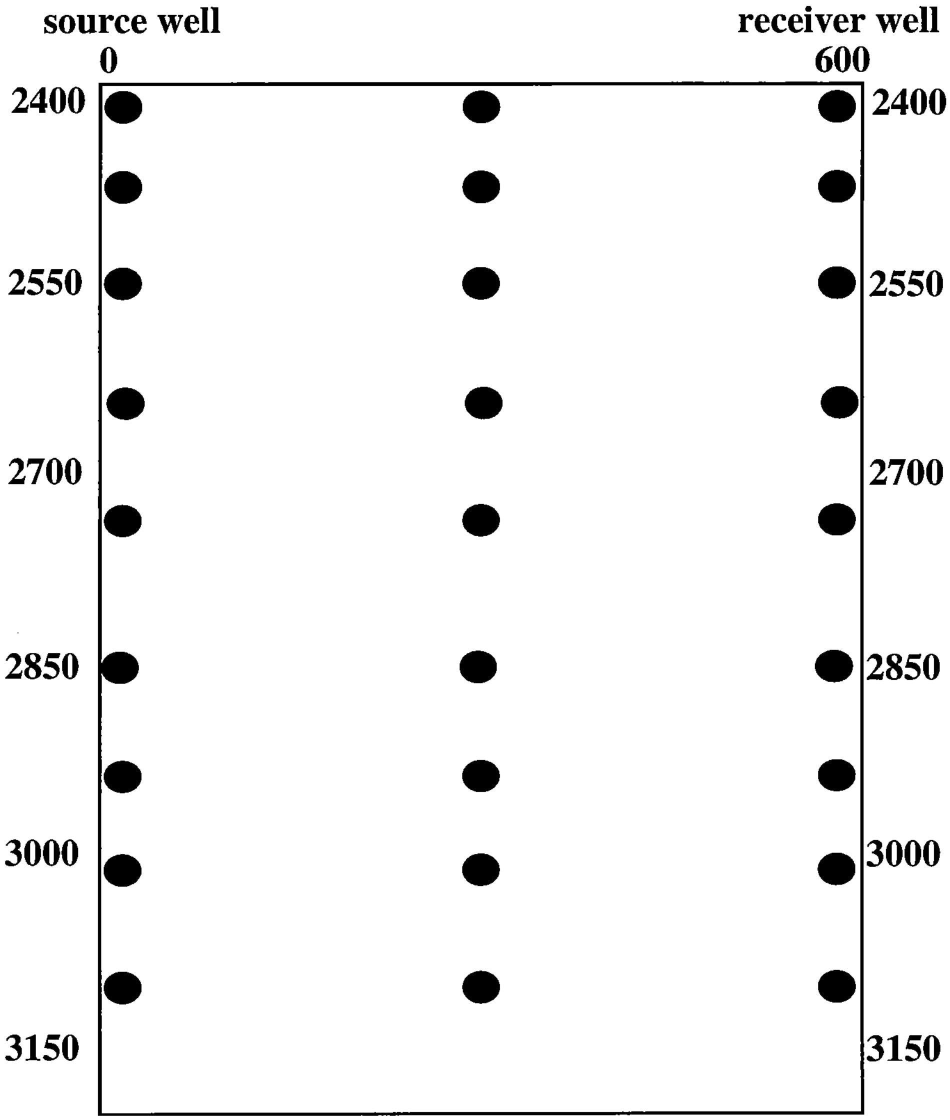

Figure 3. Location of reflection velocity analysis nodes (units are feet).

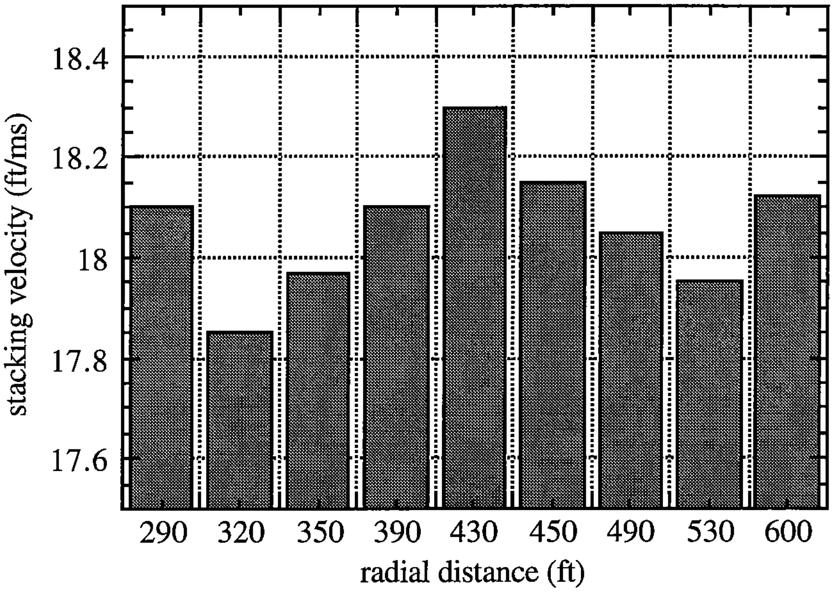

Figure 4. Stacking velocities for reflection depth 2410 feet at the source well.

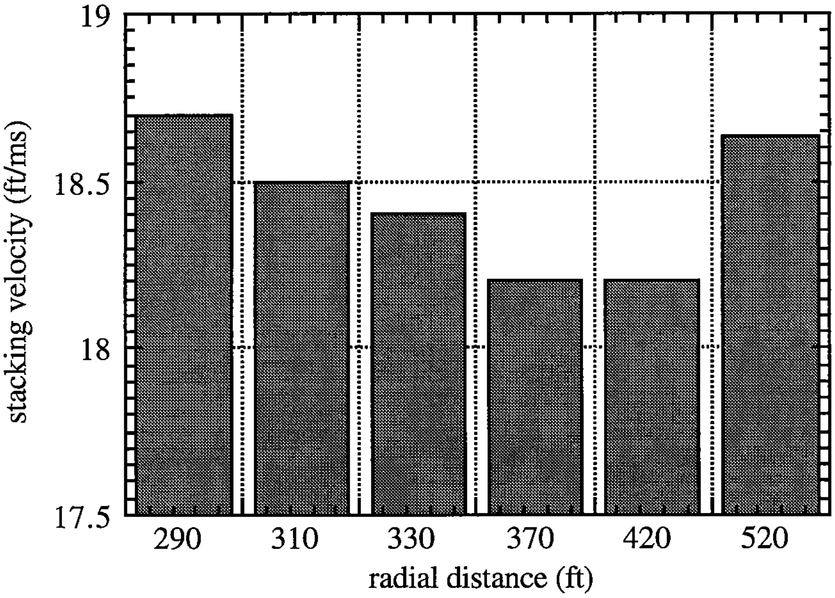

Figure 5. Stacking velocities for reflection depth 2560 feet at the source well.

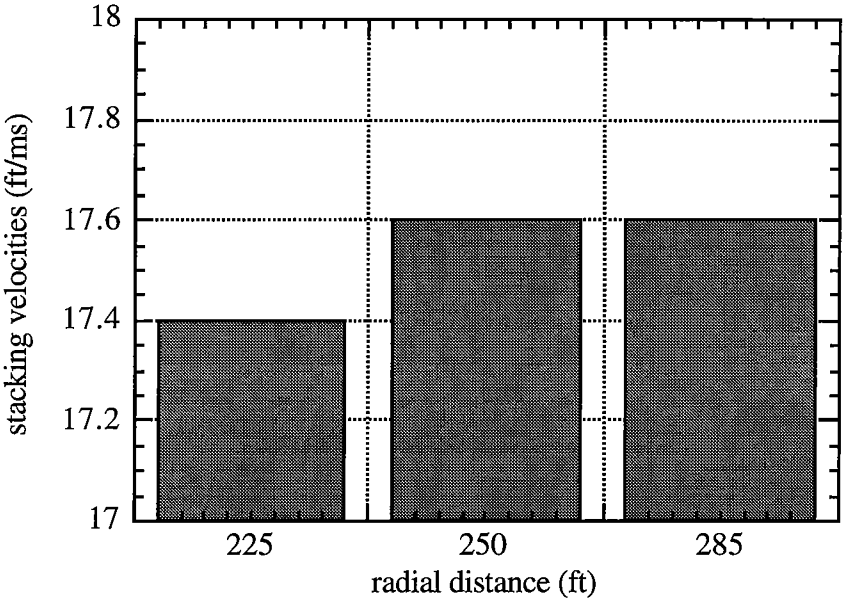

Figure 6. Stacking velocities for reflection depth 2660 feet in the middle of the survey.

INVERSION RESULTS

In figures 7, 8, and 9 we see the interval velocity inversion results from the stacking velocities for reflections points at the source well for reflection depths of 2410 feet and 2560 feet, and in the middle of the wells at 2660 feet respectively. We see an interval velocity structure from each of these inversions.

Combining the inversions - imaging

In order to combine the inversions from all reflection depths for a given reflection lateral point location, we define a bin region of 10 ft thick vertically going from the source to receiver well. Within each bin we average the interval velocities determined from all the reflection depth inversions for that depth. In figures 10, 11, and 12 we see the combined inversions for the reflection lateral locations at the source well, in the middle of the survey, and at the receiver well . We see a well defined velocity profile for each of these inversions. We see more variation and depth range for the inversion at the source and receiver wells than in the middle of the survey. The range of radial distances used in velocity analysis in the middle of the wells is much smaller than the range at the wells due to the poorer signal to noise ratio.

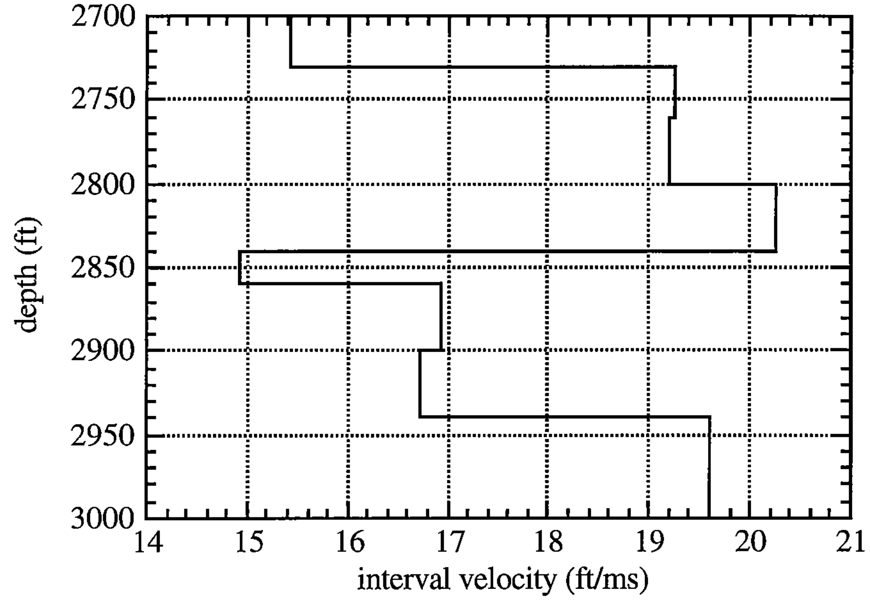

Figure 7. Interval velocities for reflection depth 2410 feet at the source well.

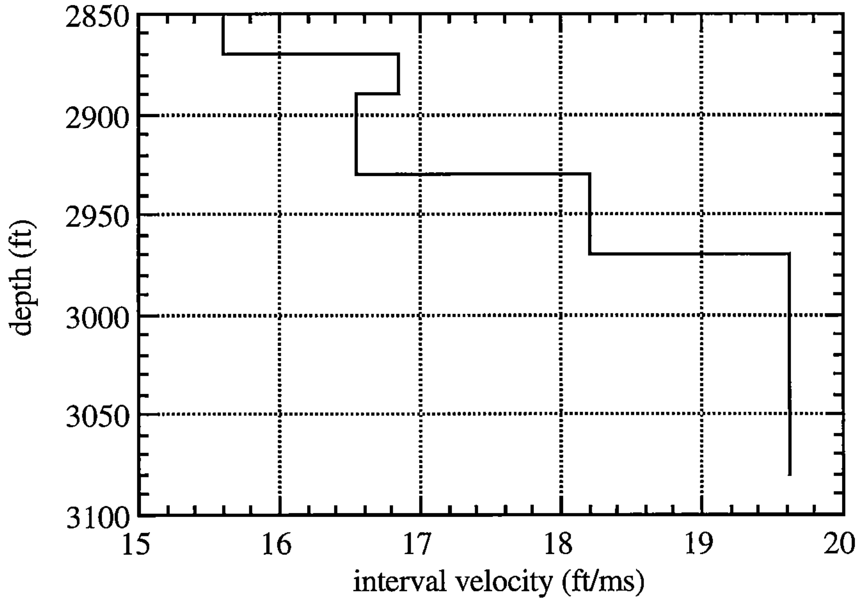

Figure 8. Interval velocities for reflection depth 2560 feet at the source well.

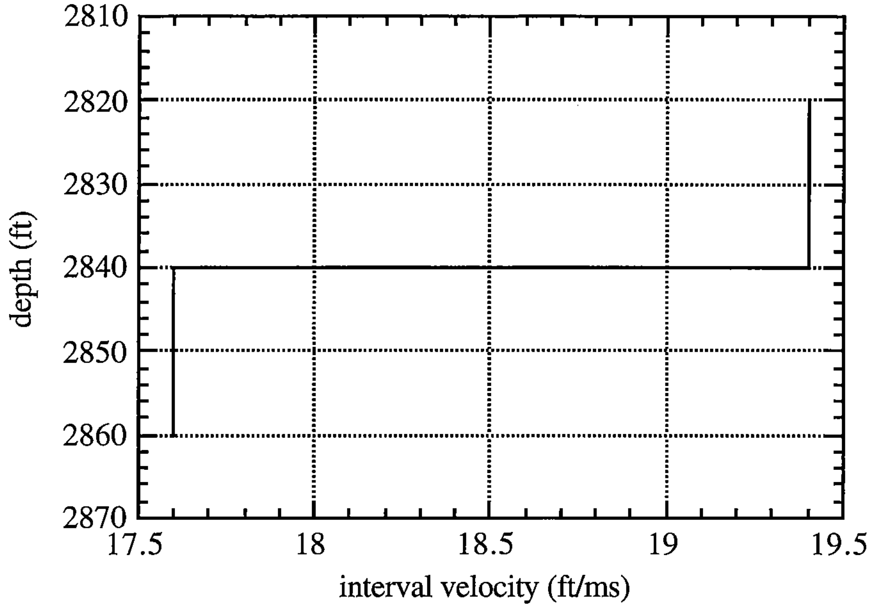

Figure 9. Interval velocities for reflection depth 2660 feet in the middle of the survey.

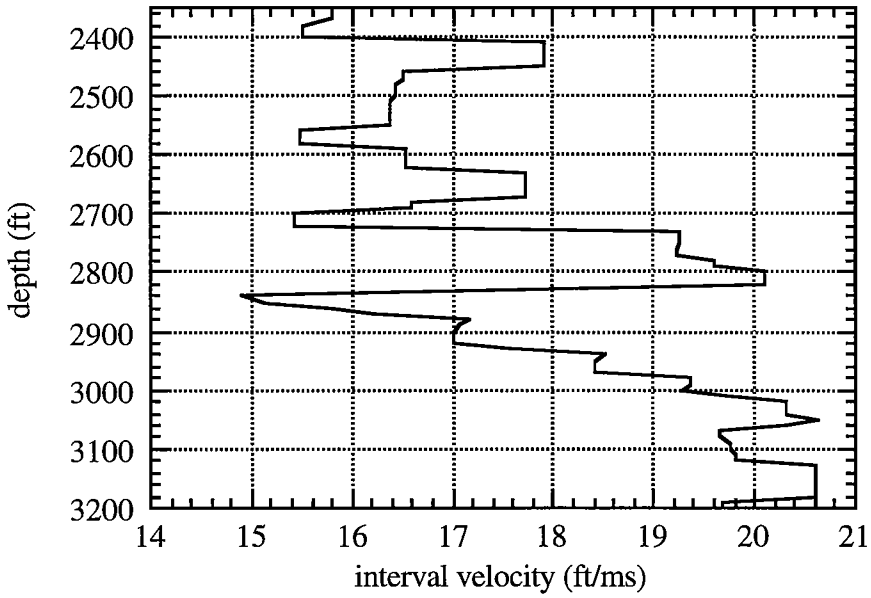

Figure 10. Final interval velocity profile from reflection points at the source well.

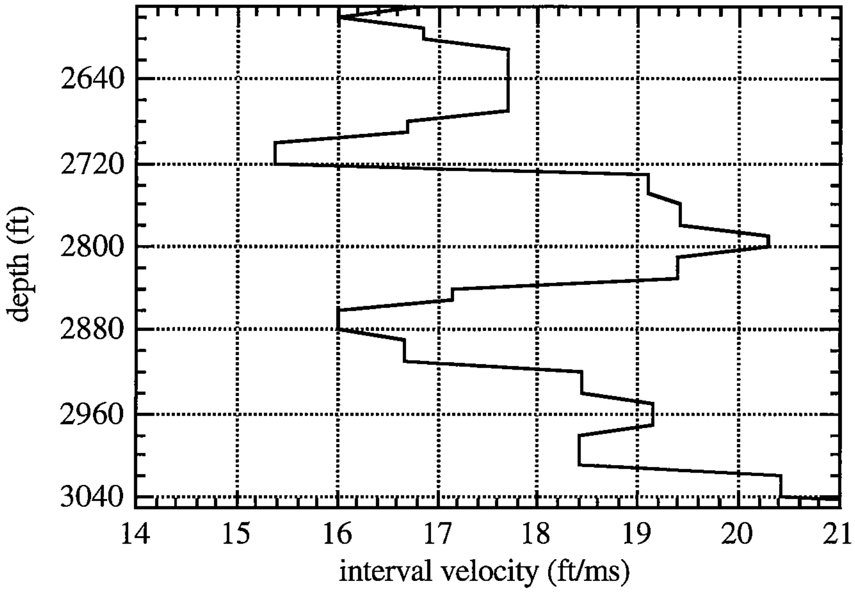

Figure 11. Final interval velocity profile from reflection points in the middle of the survey.

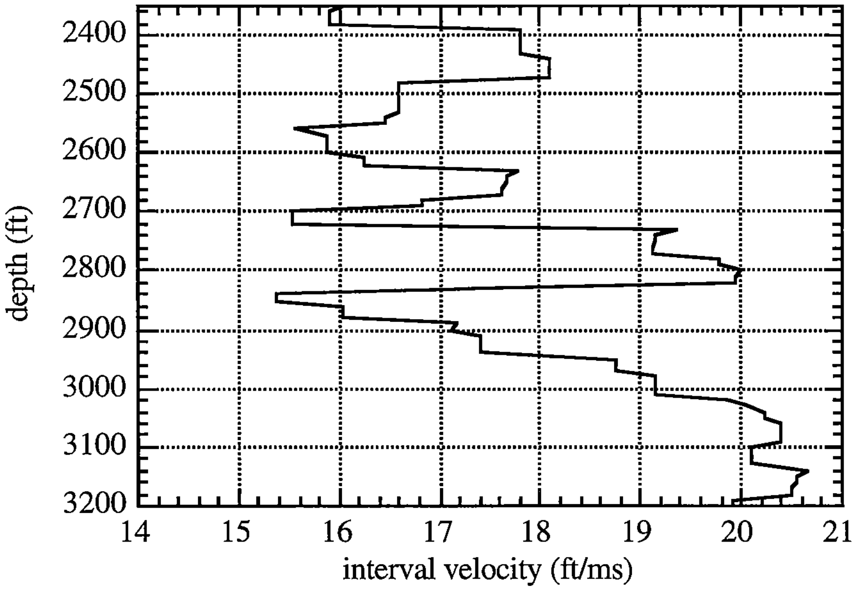

Figure 12. Final interval velocity profile from reflection points at the receiver well.

CONCLUSIONS

We have presented a method for inverting for interval velocities from stacking velocities determined from reflection velocity analysis. The interval velocity profiles are characterized by a well defined velocity structure and sharp boundaries for reflection points at both the source and receiver wells, and in the middle of the survey.

ACKNOWLEDGMENTS

The author thanks Jerry Harris and Bob Langan for their support, and the sponsors of the Seismic Tomography Project at Stanford University for the financial support.

REFERENCES

Smalley, N., 1992, Cross-well Pre-Stack Partial Migration (Theory): STP vol. 3 No. 1, Paper M.

Smalley, N., 1993, Cross-well Reflection Velocity Analysis: STP vol. 4 No. 1, Paper G.

Smalley, N., 1994, Common Lateral Point (CLP) Reflection Imaging, STP vol. 5 No.1 Paper E.

PAPER S

ANALYSIS OF NOISES AFTER PRESTACK MIGRATION IN CROSSWELL SEISMIC PROFILING

Le-Wei Mo

ABSTRACT

Pre-stack Kirchhoff migration equations for cross-well seismic survey in medium with arbitrary velocity variations are derived. Migration operation increases signal/noise ratio. We show that S/N ratio is much higher in migration images than in common shot gather data.

Radiation angle transformation helps separating signal from noise in pre-stack migration images. We show that channel wave events in common angle images dip at the radiation angle. Transmission multiple reflection events in common angle images appear vertical. Slant stack dip filtering is used to attenuate these two kinds of noises.

KIRCHOFF MIGRATION

In this section, I derive the Kirchhoff migration integral for a medium with arbitrary velocity variations, for prestack migration of single source and multiple receiver multichannel data. The application is for prestack migration of cross-well seismic data, in particular. Begin with the Helmholtz equation,

$$(\nabla^2 + \omega^2 / v^2)G = \delta(r - r_1) \qquad (1)$$

G is the function which solves equation (1) and satisfies the radiation conditions (Goodman, 1970); ∇^2 is the Laplacian operator, ω is frequency, $v(x,z)$ is acoustic velocity, and δ is the Dirac delta function. Later, r and r_1 will turn out to be the position vectors of the source/receiver pair and point scatterer, respectively. The wave field $P(r,\omega)$ satisfies the equation

$$(\nabla^2 + \omega^2 / v^2)P(r,\omega) = 0 \qquad (2)$$

inside the source-free volume V. To obtain the Kirchhoff integral, we use the Green's second theorem,

$$\int_V (\phi_1\nabla^2\phi_2 - \phi_2\nabla^2\phi_1)dV = \int_S (\phi_1\partial_n\phi_2 - \phi_2\partial_n\phi_1)dS \qquad (3)$$

where n denotes the outward normal direction to the surface *S,* and substitute $\phi_1 = P(r,\omega)$, and $\phi_2 = G$ to obtain

$$P(r_1,\omega) = \int_S (P(r,\omega)\partial_n G - G\partial_n P(r,\omega))dS \qquad (4)$$

which is the Kirchhoff integral.

In the Kirchhoff integral equation (4), both the wave field records $P(r,\omega)$ and its gradient are required. But in actual seismic profiling, only the wave fields $P(r,\omega)$ are recorded. French (1975) and Schneider (1978) showed that if the data are collected in a flat plane, the second term in the integrand of the Kirchhoff equation is the negative of the first term. This condition is approximately valid for borehole profiling, since any change of borehole direction must proceed gradually and may be assumed negligible for typical seismic wavelengths. We therefore replace the second term containing the normal derivative of the data with the negative of the first term. Also, we extend the boundary ofthe integration surface to infinite distance, where there is no back-scattered energy as governed by the radiation conditions, so the only remaining contribution to the integral comes from the recording surface *S*. Equation (4) becomes

$$P(r,\omega) = 2\int_S P(r_g,\omega)\partial_n G dS \qquad (5)$$

We now write $G = A(r|r_g)e^{-i\omega\tau(r|r_g)}$ and use the geometrical optics approximation for the amplitude $A(r|r_g)$ and phase $\tau(r|r_g)$. The negative sign in the phase of G is taken because we shall be extrapolating backward in time. Along a ray path, the variation in $e^{-i\omega\tau}$ is much larger than the variation in A. Thus the first term in the derivative of G

$$\partial_n G = (\partial_n A)e^{-i\omega\tau} - Ae^{-i\omega\tau}i\omega(\partial_n\tau) \qquad (6)$$

is small compared to the second term and is neglected. The Kirchhoff integral (5) can now be written in the form

$$P(r,\omega) = -2\int_S P(r_g,\omega)A\, e^{-i\omega\tau}i\omega(\partial_n\tau)dS \qquad (7)$$

in which

$$\partial_n\tau = n\cdot\partial\tau = n\cdot t/v_g = \cos\theta_g / v_g \qquad (8)$$

where t is the unit tangent vector for the emerging ray, and θ_g is the angle of emergence, and v_g is the acoustic velocity at the receiver. The amplitude term $A(r|r_g)$ can be obtained from the transport equation.

The reflectivity function $R(r,\omega)$ is defined as the ratio of the back-propagated field from the receivers $P(r,\omega)$ to the incidence field from the source $P_s(r,\omega)$ (Claerbout, 1970),

$$R(r,\omega)=\frac{P(r,\omega)}{P_s(r,\omega)} \qquad (9)$$

The incidence source field is approximated by the WKBJ Green's function

$$P_s(r,\omega)=A(r|r_s)e^{i\omega\tau(r|r_s)} \qquad (10)$$

Combining equations (7) and (9) gives the holographic (i.e., frequency-domain) form of Kirchhoff migration. The time-space domain reflectivity is obtained by an inverse Fourier transform,

$$R(r)=-2\int_S \frac{A(r|r_g)}{A(r|r_s)}\frac{\cos\theta_g}{v_g}\partial_t P(r_g,\tau(r|r_s)+\tau(r|r_s))dS \qquad (11)$$

TRANSMISSION MULTIPLE REFLECTIONS AND CHANNEL WAVES

In this study, I use an earth section model 600 ft in depth and 184 ft in horizontal separation, Figure 1. The medium has a constant reference acoustic velocity of 18000 ft/s. At the depth of 300 ft and 400 ft, there are two thin low velocity layers of acoustic velocity 10000 ft/s, the thickness is 2.5 ft or two grid points in discrete representation.

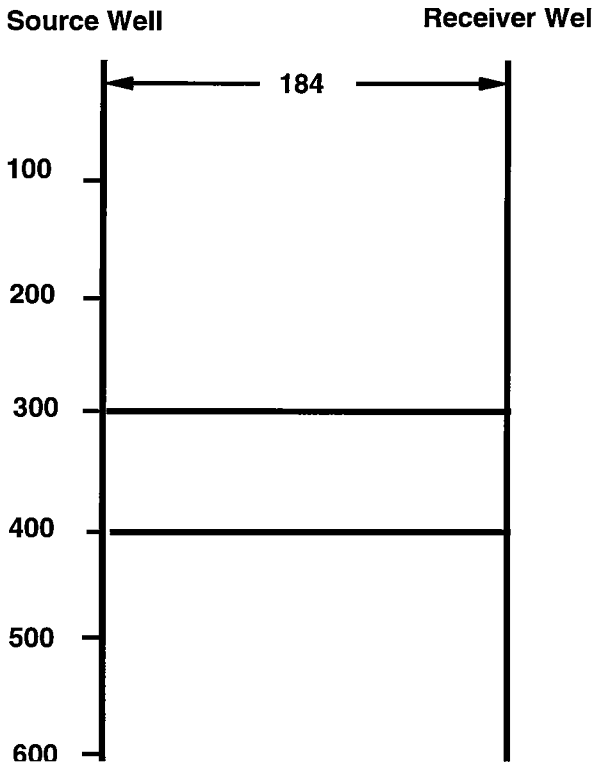

Figure 1: Cross well earth model

Figure 2 shows two finite-difference modeling common shot gather data. In the first gather, the source is above the two reflectors at 140 ft. The data shows distinct direct arrival, primary upgoing reflections from the two reflectors, transmission multiple and much weaker upgoing multiple. The upgoing multiple undergoes one more reflection than the transmission multiple, so that its amplitude is an order of magnitude weaker. In this modeling the record length of 50 ms is the record length of an actual field survey. As a result, higher order multiples are not recorded. Thus, we focus our analysis at the transmission multiples.

In the second gather, the source is located in the low velocity layer at 300 ft, so that channel waves are generated. The reflection event of the upper reflector coalesces into the direct arrival.

Figure 3 shows the pre-stack Kirchhoff migration images of the previous two common shot gather data. According to the analysis of multiples in (Mo, 1995), the equivalence of transmission multiples and primary reflections.

$$H = S - n(H_2 - H_1) \qquad (12)$$

where S is the source depth, H_2 and H_1 are the depths of two reflectors, n is the order of transmission multiples, and then H is the depth of the equivalent primary reflection.

In Figure 3 (a) the source at 140 ft, the speudo-primary reflection image event of the first order transmission multiple appears at the depth of 40 ft. In Figure 3 (b) the source at 300 ft, the speudo-primary reflection image event of the first order transmission multiple appears at the depth of 200 ft. The imaging events of the channel waves appear as horizontal ellipses.

Figure 4 shows some common radiation angle images. The image events of the transmission multiples appear as the vertical events. And the image events of the channel waves align along the radiation directions.

Figures 5, 6, and 7 show common shot gather data, pre-stack migration images, and common radiation angle images for a complicated reflector model.

RANDOM NOISES

Random noise data are modeled by

$$n(t) = f(t) * w(t) \qquad (13)$$

where $f(t)$ is modeled as Gaussian distribition random signal, the mean of which is zero and the standard variation equals to the amplitude of the reflection signal, and $w(t)$ is the same as the source wavelet function.

Figure 8 shows a common shot gather data with Gaussian random noises. The signal/noise ratio is 1 in the data. Figure 9 shows the corresponding pre-stack Kirchhoff migration image, the signal/noise ratio increases greatly as compared to the data. It is convincing by comparing this image of noisy input data with the image Figure 6 of input data without noises. The pre-stack migration is performed by applying the Kirchhoff migration integral equation (11). Figure 10 shows some common radiation angle images.

CONCLUSIONS

Imaging effects of transmission multiples are equivalent to primary reflectins. And their imaging speudo-depths have linear relationship with the source depth. As a result, after radiation angle transformation on the prestack image volume the image events of the transmission multiples appear vertically in common radiation angle images.

Channel waves in cross-well seismic survey appear in the receiver traces horizontally across the source. Imaging effects of channel waves in pre-stack migration appear as ellipses with the locations of the source and the hirozontal receiver as the foci. As a result, the image events of the channel waves align along the radiation angle direction in common radiation angle images.

By definition, in pre-stack migration operation signals are summed constructively and random noises are summed distructively. Pre-stack migration increases signal/noise ratio. Signal/noise ratio is higher in pre-stack migration images than in common shot gather data.

REFERENCES

Goodman, J., 1970,
Introduction to Fourier Optics.

Mo, L., and Harris, J. M., 1995,
Travel time equations in cross-well seismic profiling: STP-5.

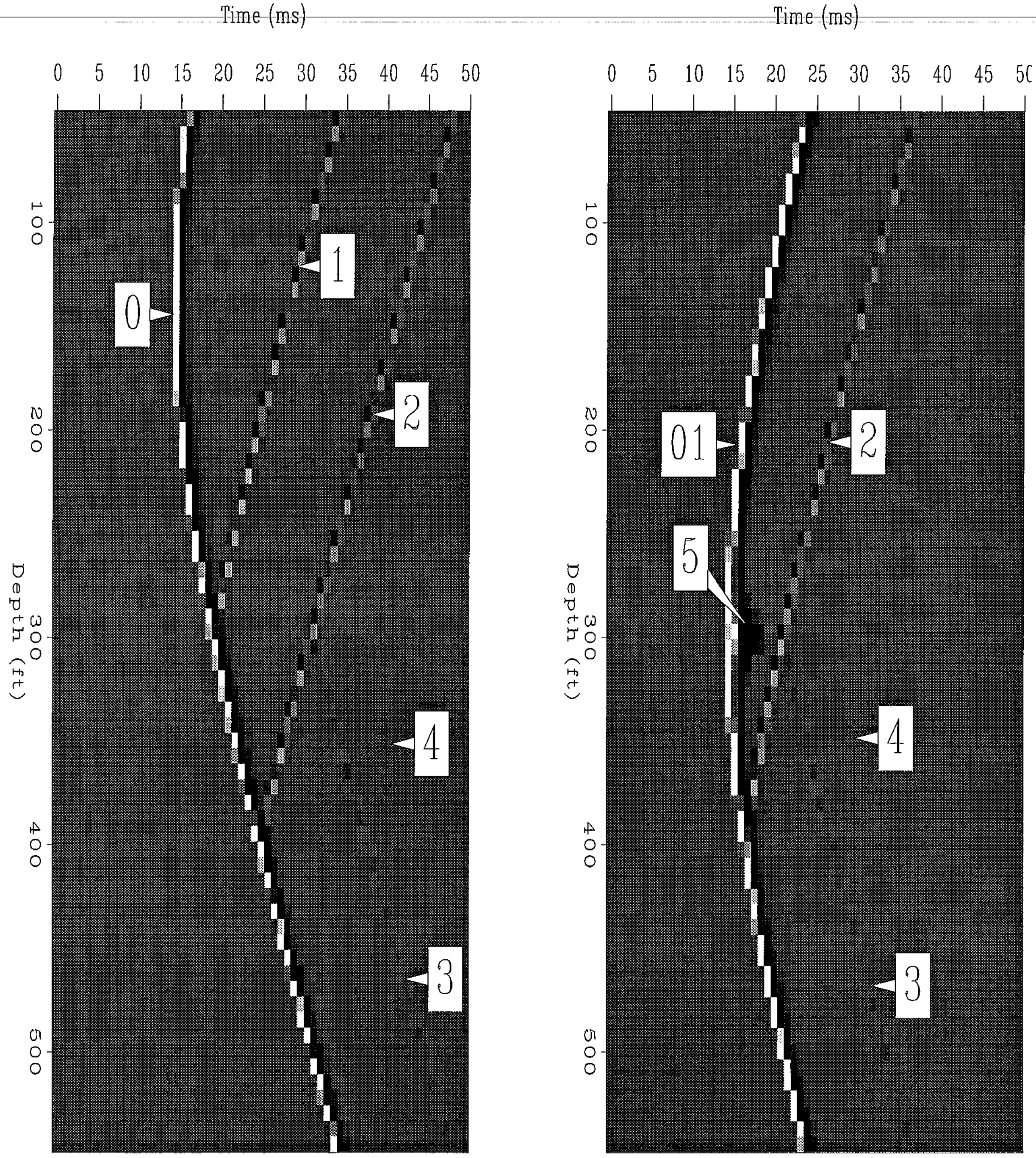

(a) Source at 140 ft

(b) Source at 300 ft

Figure 2: Common shot gather data in model with two reflectors. 0 is the direct arrival, 1 primary reflection from the upper reflector, 2 primary reflection from the lower reflector, 3 transmission multiple, 4 upgoing multiple, and 5 channnel wave.

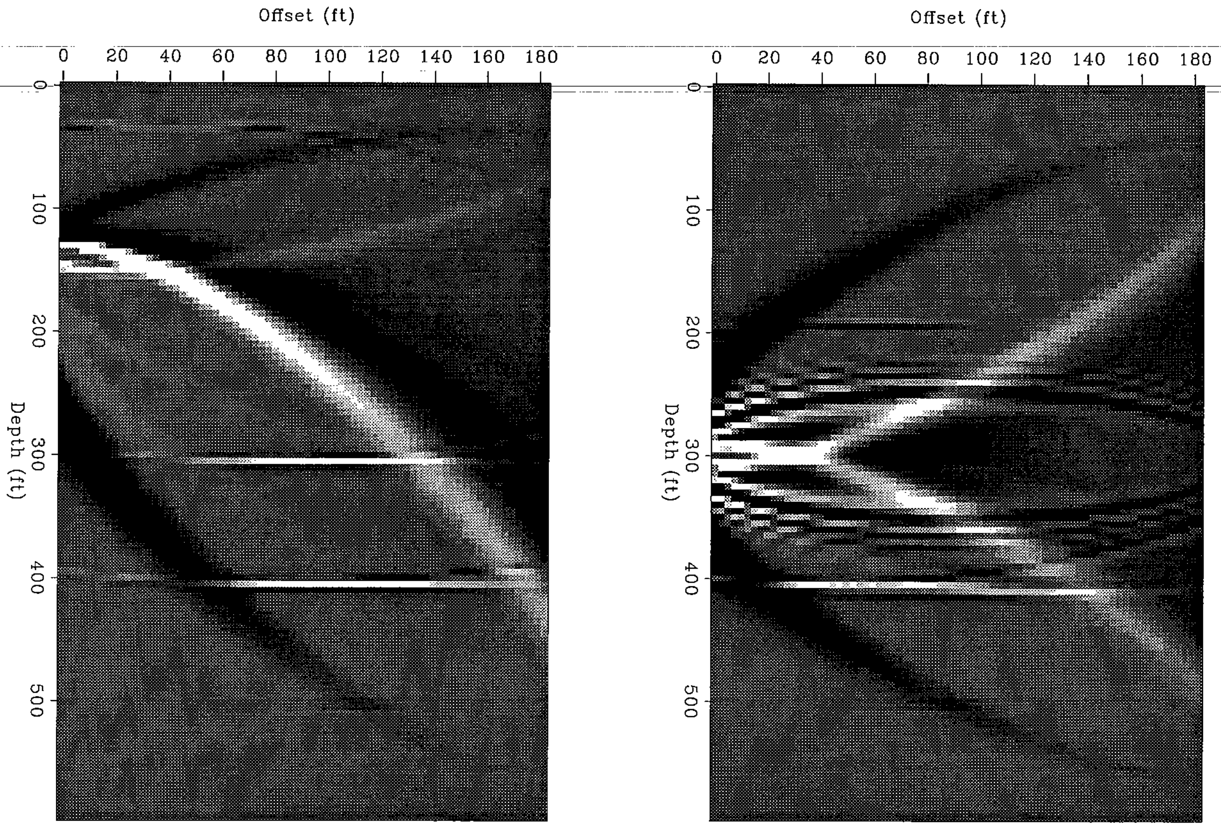

(a) Source at 140 ft

(b) Source at 300 ft

Figure 3 : Prestack migration images.

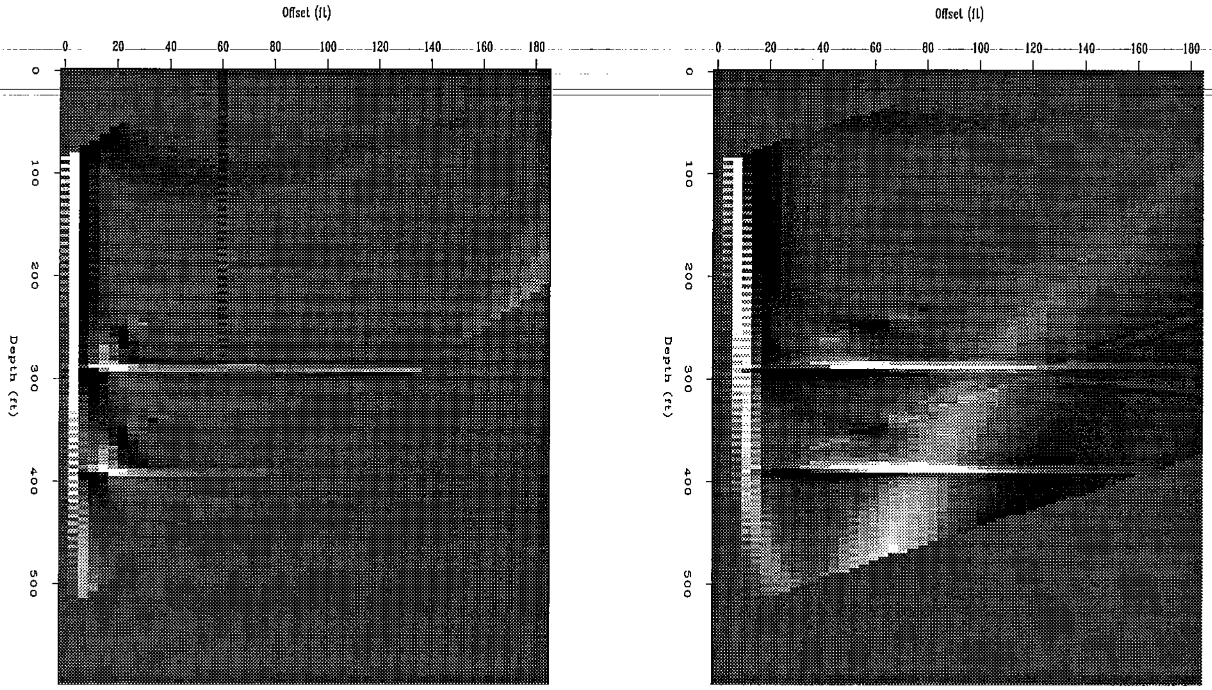

(a) -60 degrees (b) -40 degrees

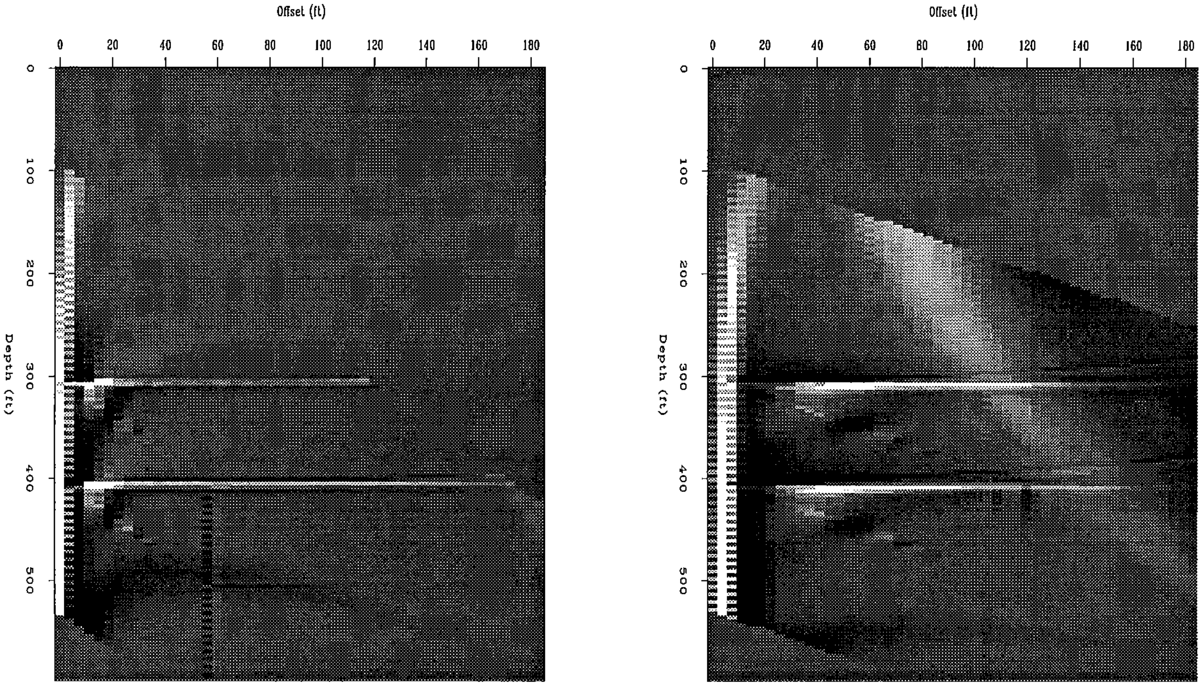

(c) 60 degrees (d) 40 degrees

Figure 4: Common radiation angle images.

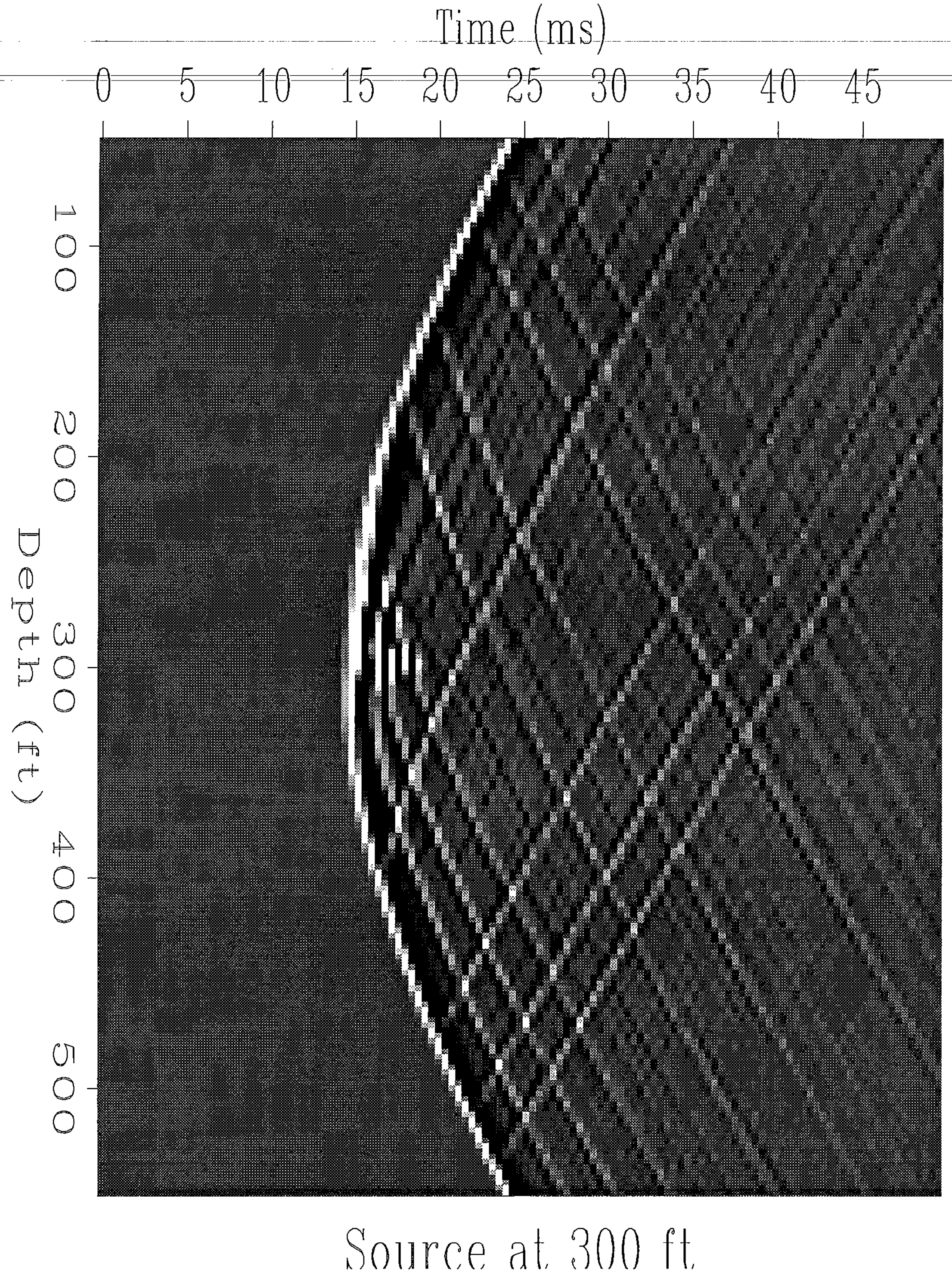

Figure 5: Common shot gather data.

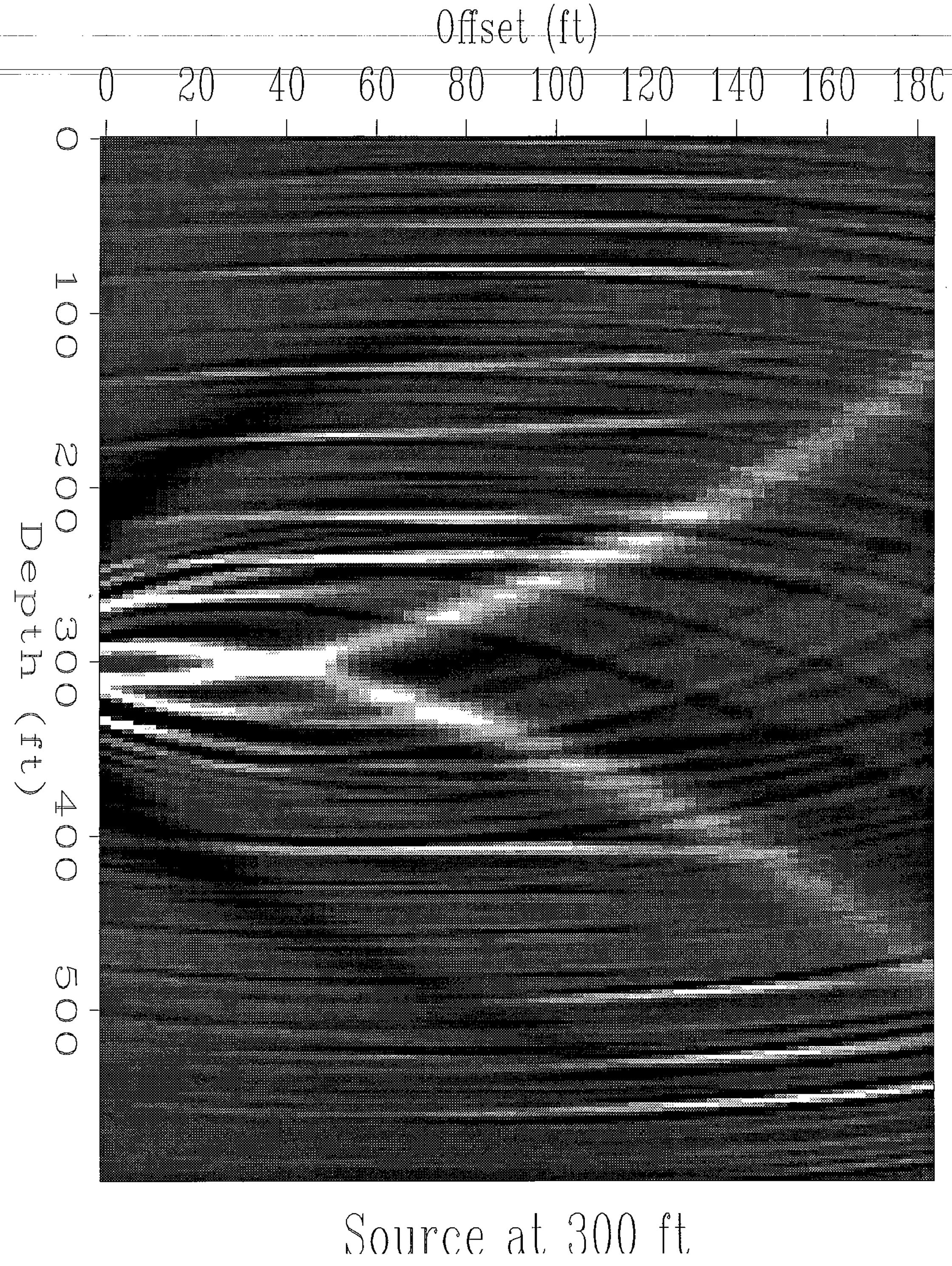

Figure 6: Prestack migration image.

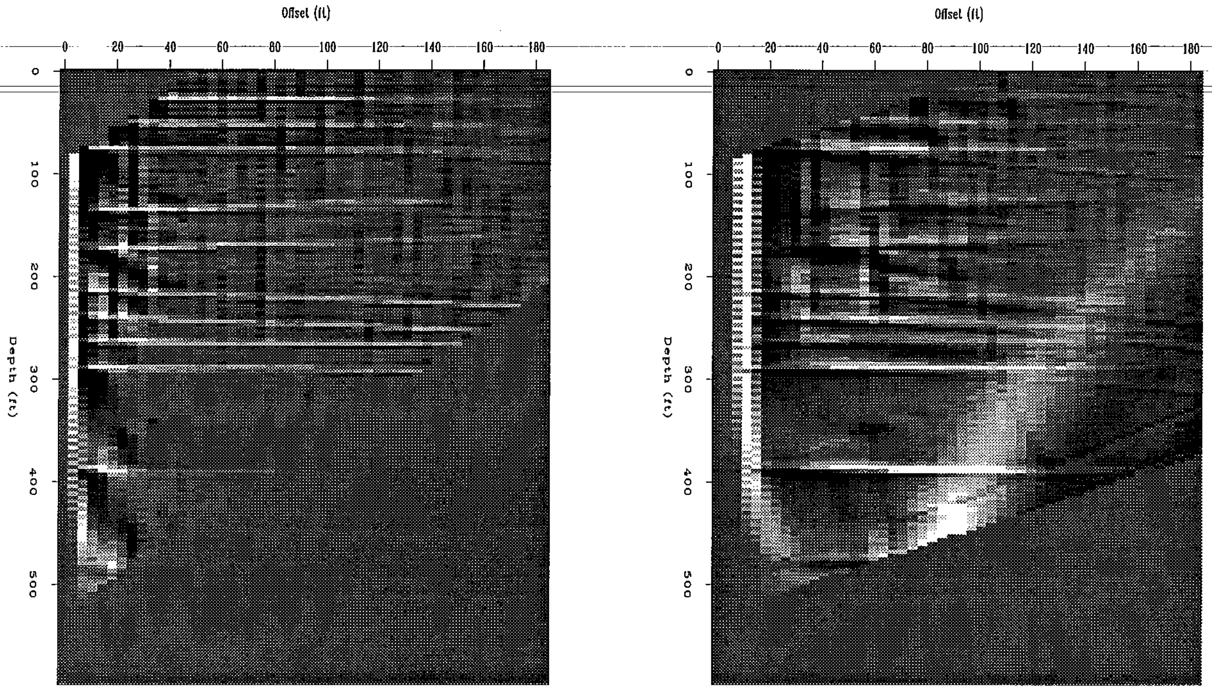

(a) -60 degrees

(b) -40 degrees

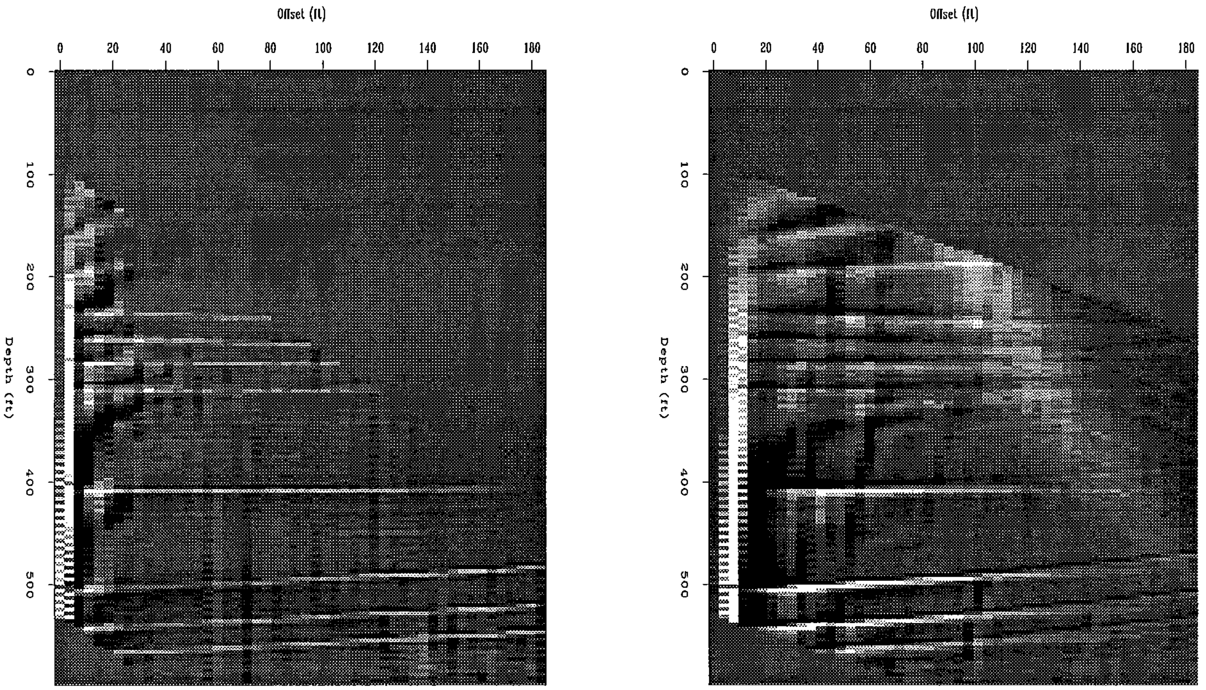

(c) 60 degrees

(d) 40 degrees

Figure 7: Common radiation angle images.

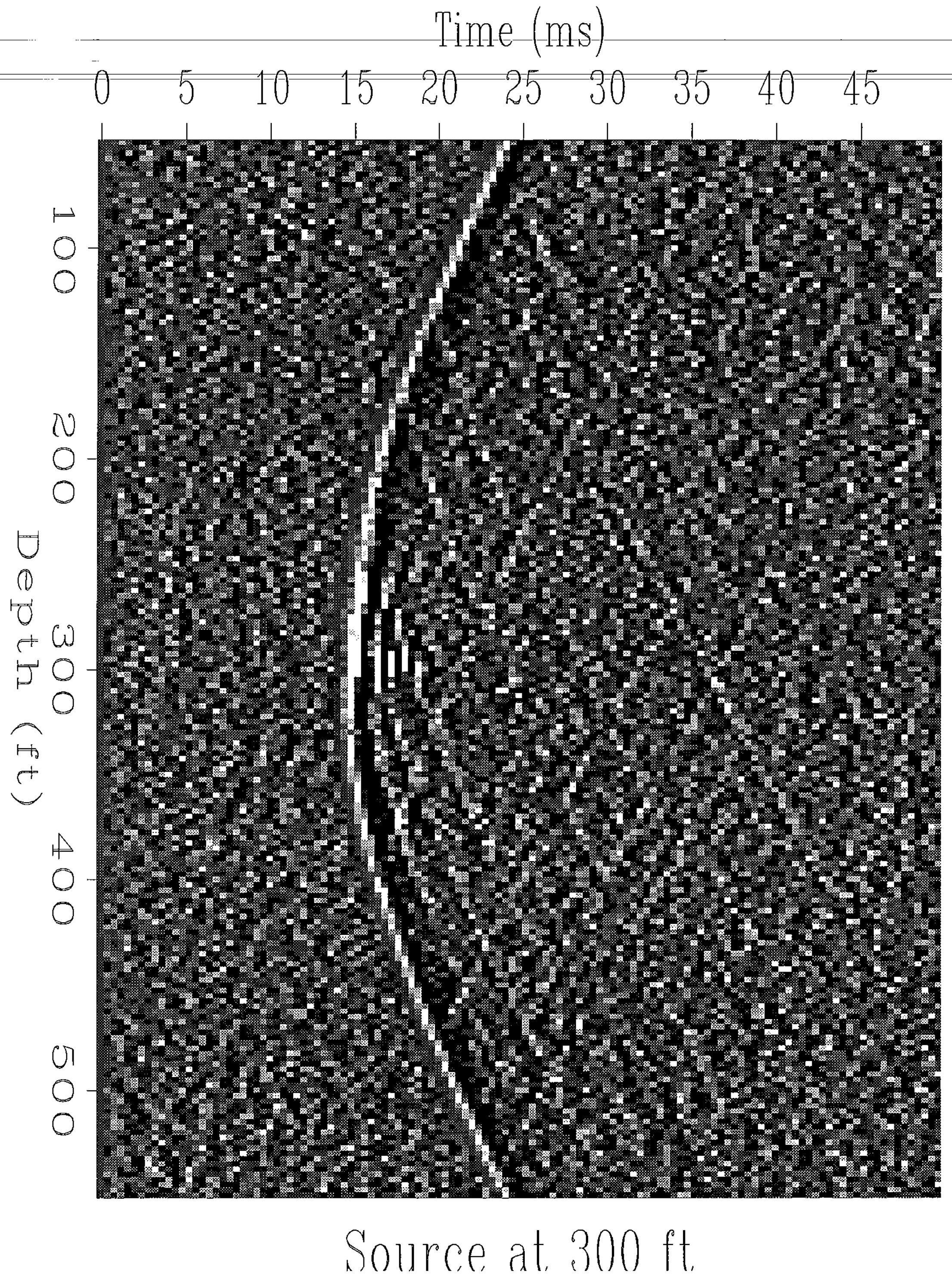

Figure 8: Common shot gather data.

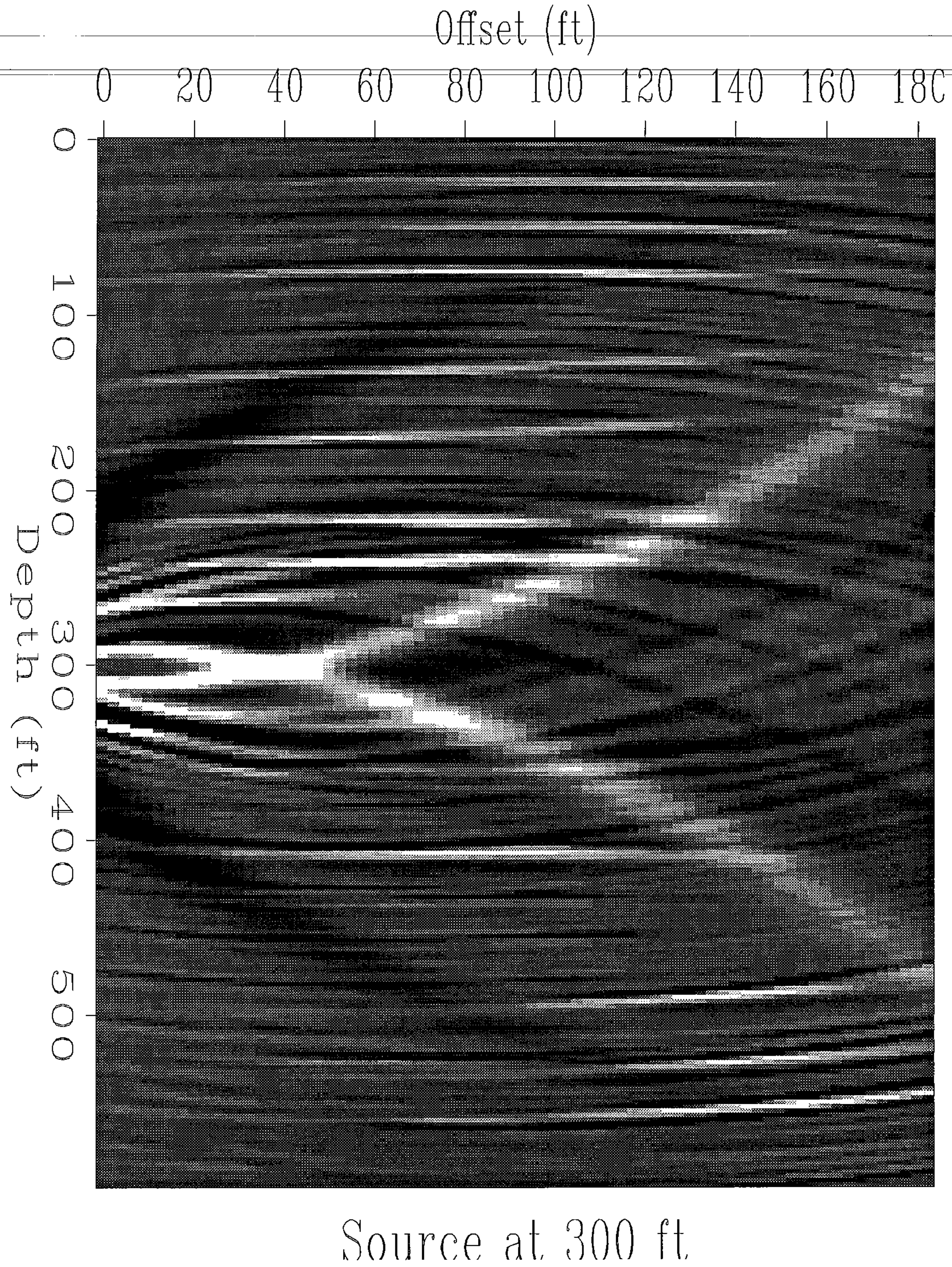

Figure 9: Prestack migration image.

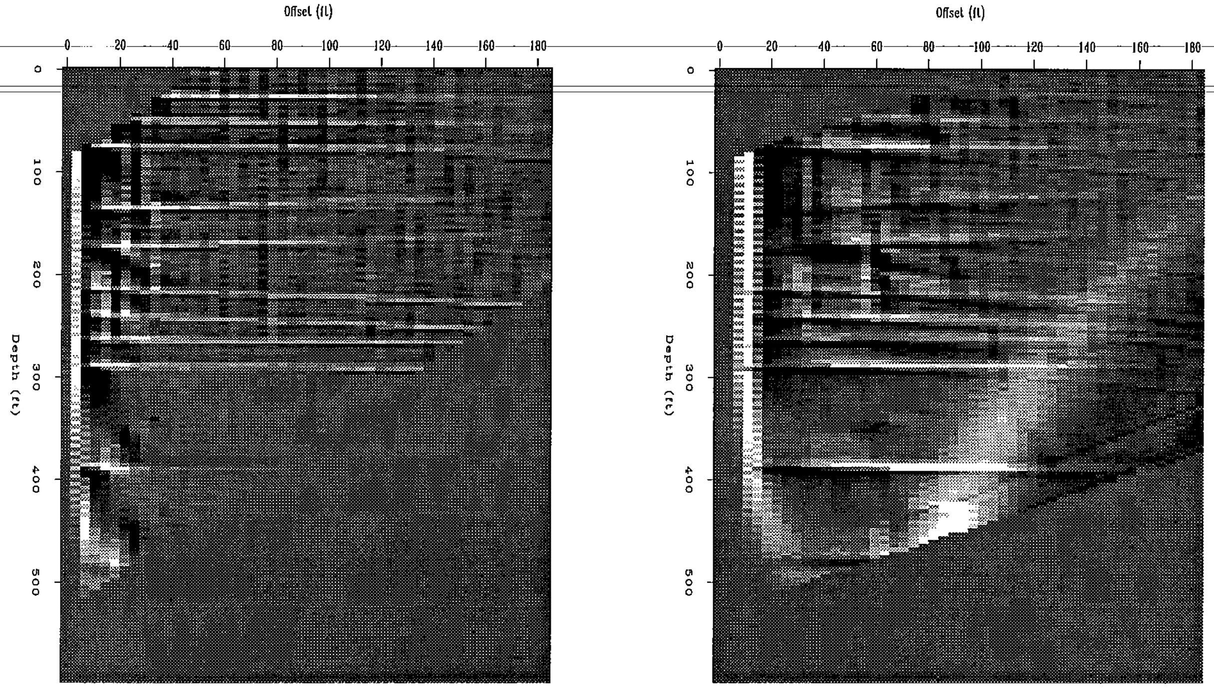

(a) -60 degrees (b) -40 degrees

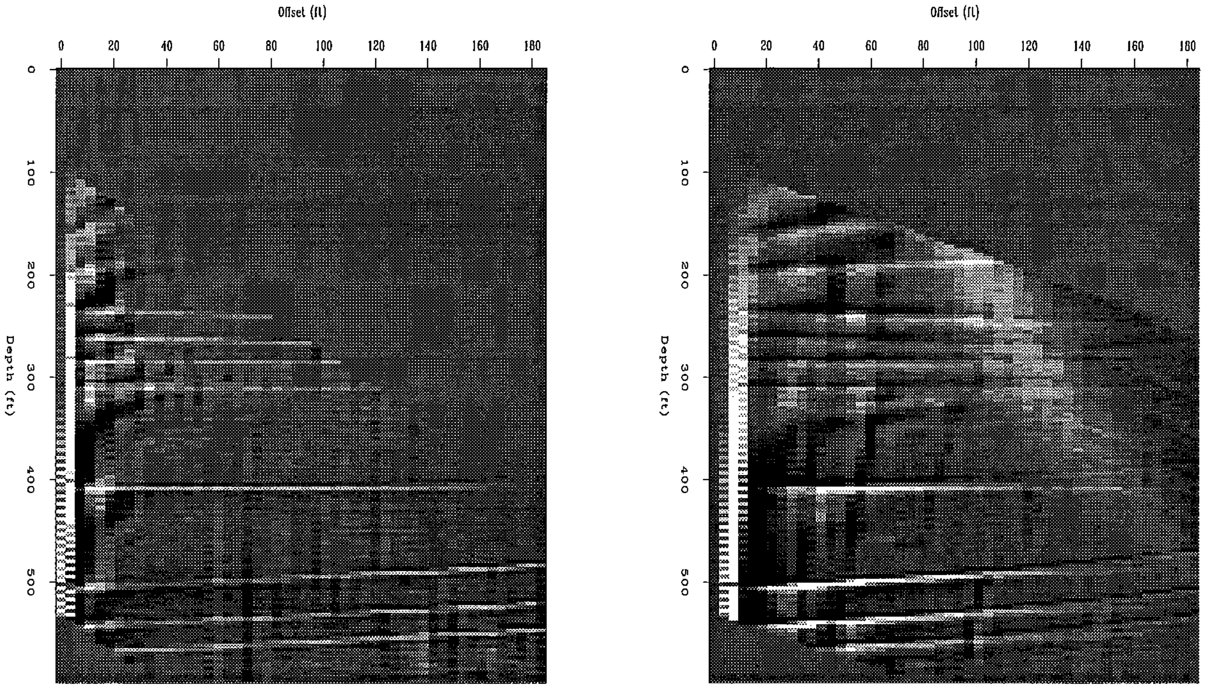

(c) 60 degrees (d) 40 degrees

Figure 10: Common radiation angle images.

PAPER T

TRAVELTIME EQUATIONS IN CROSSWELL SEISMIC PROFILING

Le-Wei Mo

ABSTRACT

The traveltime equations for direct arrival, primary reflections, and multiple reflections are derived. When the depth of the source approaches the depth of the reflector, the traveltimes of the direct arrival and primary reflection coalesce into each other. Transmission multiple reflections are equivalent to primary reflections, whose virtual depths have a linear relationship with the source depth.

INTRODUCTION

In this paper, we first derive the traveltime equations for direct arrival and primary reflections in cross-well seismic profiling. Then we derive the traveltime equations for multiple reflections.

Finally, we analyse the kinematic relationships of these different arrivals, and their effects in seismic imaging.

DIRECT ARRIVAL

In the following study of deriving traveltime equations for cross-well seismic survey profiling, I assume that the two boreholes are straightly vertical and the lateral separation distance is L. A single source is placed in one borehole, the legend and the depth of the source are denoted by S. A series of receivers are placed in another borehole, the legend and the depth of a receiver are denoted by R. I further assume the interwell medium has a constant velocity v.

The ray path linking the source S and the receiver R is straight, Figure 1. The traveltime for the direct arrival is:

$$t = \frac{1}{v}\sqrt{(S-R)^2 + L^2} \qquad (1)$$

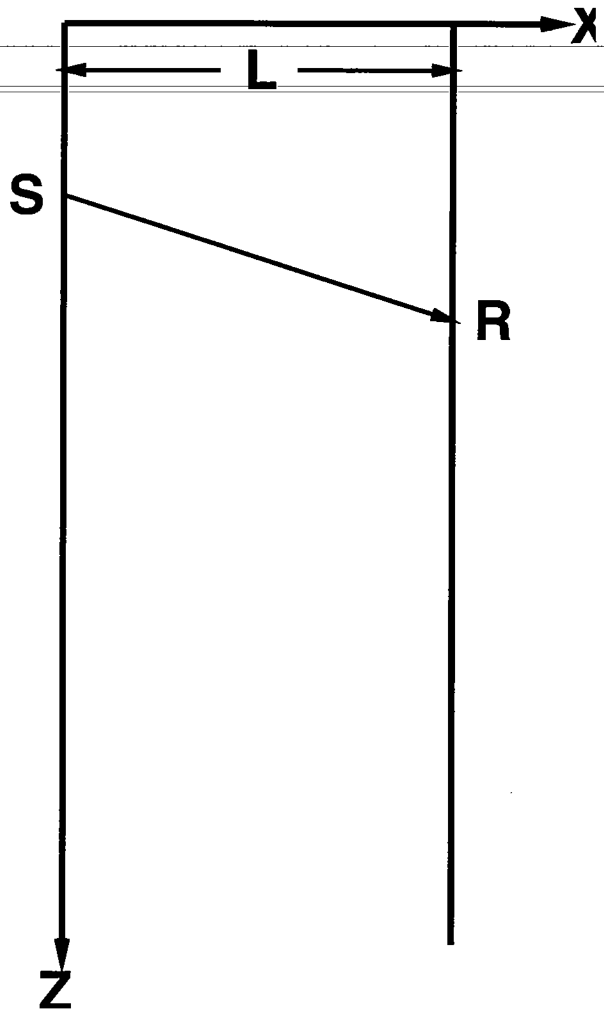

Figure 1: Direct arrival

PRIMARY REFLECTIONS

There are two cases of primary reflections, i.e., upgoing primary reflection when both the source and the receiver are above the reflector (Figure 2), and downgoing primary reflection when both the source and the receiver are below the reflector (Figure 3). When the reflector is flat at a depth of H, the image source is in the source borehole. In both cases the depth of the image source $S*$ could be described by $H+(H-S)=2H-S$. Employing the traveltime equation of direct arrival, the traveltime equation for the primary reflection is:

$$t = \frac{1}{v}\sqrt{(2H - S - R)^2 + L^2}, \text{ for } S < H, R < H; \text{ or } S > H, R > H \tag{2}$$

For a common shot profiling with S as a constant, it is hyperbola with the apex at H=2H-S. For R<H or R>H , the traveltime equation represents only a far limb of the hyperbola.

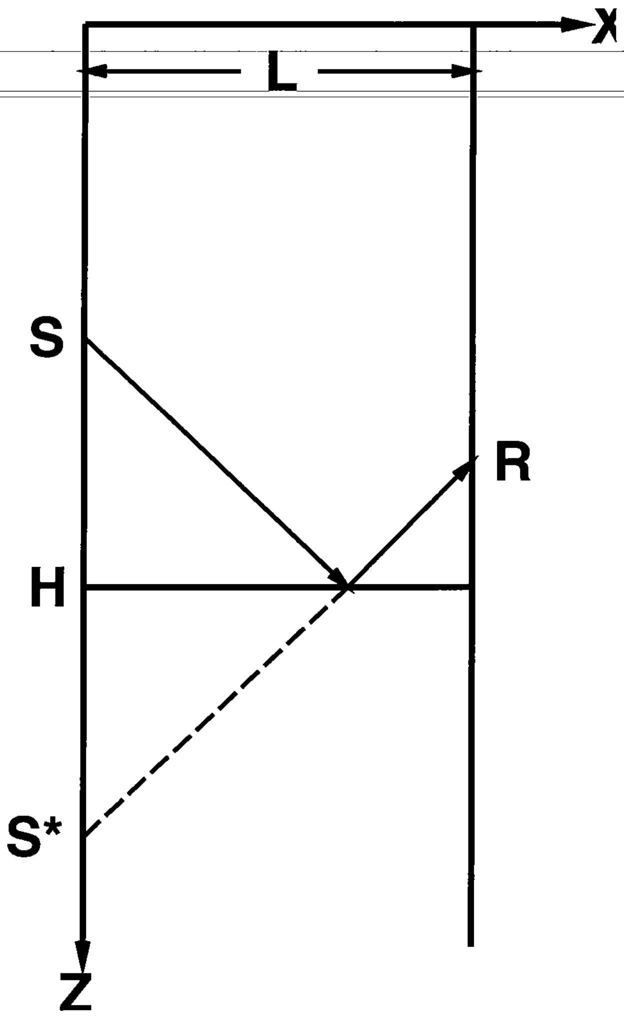

Figure 2: Primary upgoing reflection.

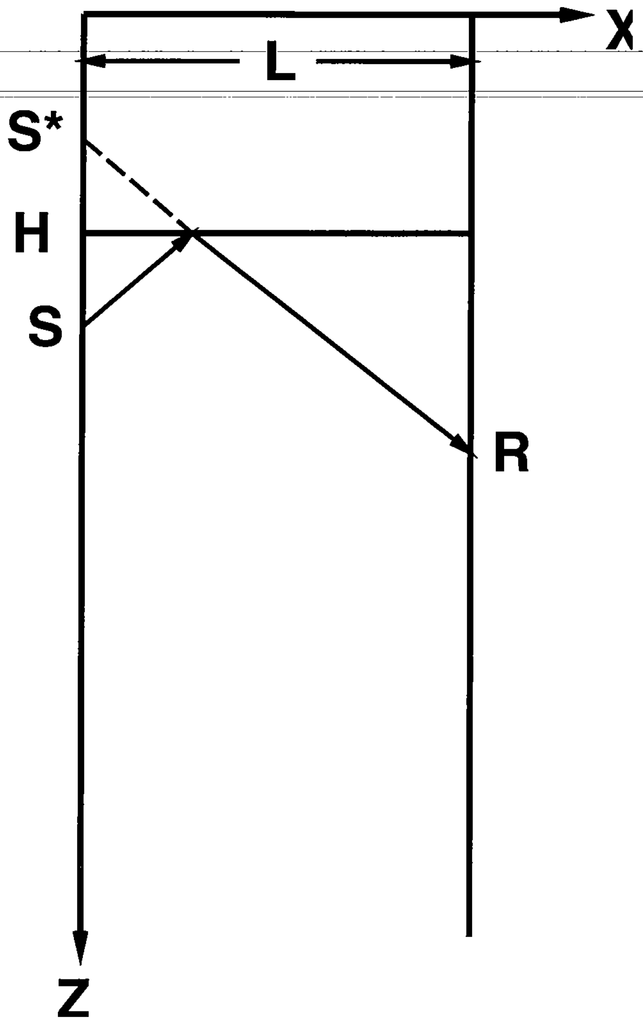

Figure 3: Primary downgoing reflection.

DOWNGOING (TRANSMISSION) MULTIPLE REFLECTIONS

First order transmission multiple reflection

The depth of the upper reflector is H_1, that of the lower reflector H_2, $H_2 > H_1$. For first order transmission multiple reflection, there are two cases, i.e., the receiver is located between the two reflectors or the receiver is located below the lower reflector.

When the receiver is located between the two reflectors (Figure 4), the depth of the equivalent primary reflector is $H_2 + (H_2 - H_1) = 2H_2 - H_1$. The depth of the image receiver $R*$ is $2H_2 - H_1 - (R - H_1) = 2H_2 - R$. Employing the traveltime equation of primary reflection, the traveltime equation for the first order transmission multiple reflection is:

$$t = \frac{1}{v}\sqrt{\left(2(2H_2 - H_1) - S - (2H_2 - R)\right)^2 + L^2}$$

$$= \frac{1}{v}\sqrt{\left(2(H_2 - H_1) - S + R\right)^2 + L^2}, \text{ for } S < H_2, R > H_1 \qquad (3)$$

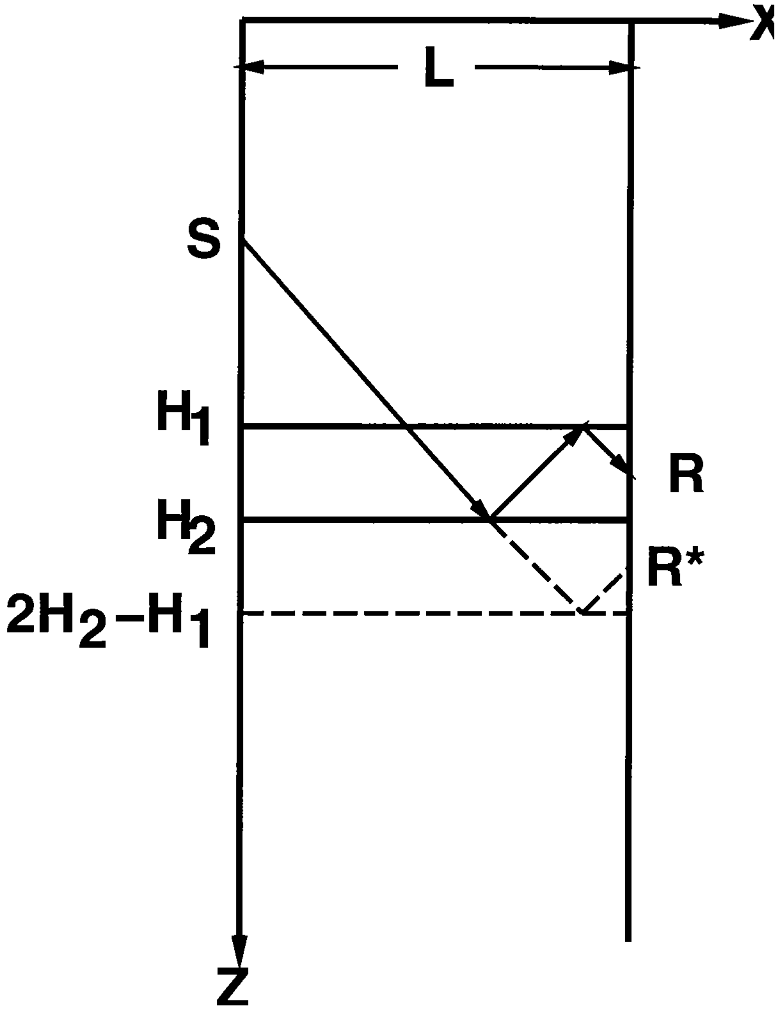

Figure 4: First order downgoing multiple reflection.

When the receiver is located below the lower reflector (Figure 5), the depth of the equivalent primary reflector is $H_2 + 2(H_2 - H_1) = 3H_2 - 2H_1$. The depth of the image receiver R^* is $3H_2 - 2H_1 - (R - H_2) = 4H_2 - 2H_1 - R$. The traveltime equation is:

$$t = \frac{1}{v}\sqrt{\left(2(3H_2 - 2H_1) - S - (4H_2 - 2H_1 - R)\right)^2 + L^2}$$

$$= \frac{1}{v}\sqrt{\left(2(H_2 - 2H_1) - S + R\right)^2 + L^2}, \text{ for } S < H_2, R > H_1 \qquad (4)$$

We see that it is the same as equation (3).

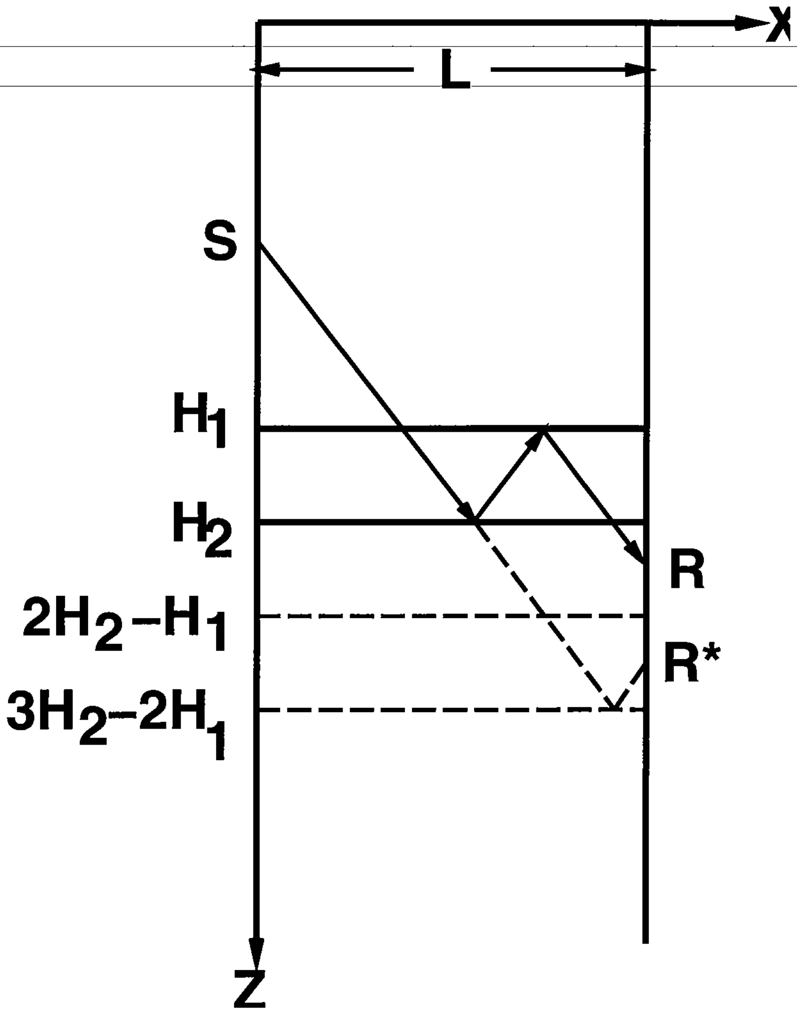

Figure 5: First orderdowngoing multiple reflection.

Second order transmission multiple reflection

The depth of the equivalent primary reflector is $H_2 + 3(H_2 - H_1) = 4H_2 - 3H_1$, Figure 6. The depth of the image receiver is $4H_2 - 3H_1 - (R - H_1) = 4H_2 - 2H_1 - R$. The traveltime equation is:

$$t = \frac{1}{v}\sqrt{\left(2(4H_2 - 3H_1) - S - (4H_2 - 2H_1 - R)\right)^2 + L^2}$$

$$= \frac{1}{v}\sqrt{\left(4(H_2 - H_1) - S + R\right)^2 + L^2}, \text{ for } S < H_2, R > H_1 \qquad (5)$$

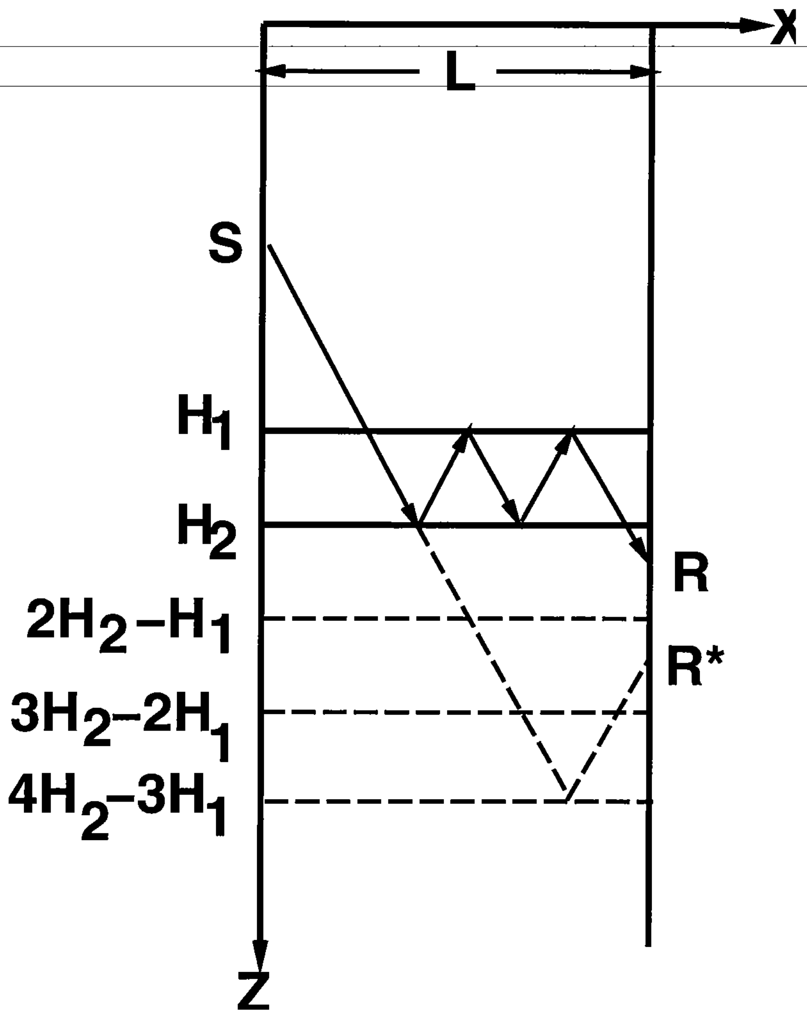

Figure 6: Second order downgoing multiple reflection.

n-th order transmission multiple reflection

We can generalize the above traveltime equations of low order transmission multiple reflections to the n-th order. The traveltime of the n-th order transmission multiple reflection is

$$t=\frac{1}{v}\sqrt{\left(2n\left(H_2-H_1\right)-S+R\right)^2+L^2},\ \text{for } S<H_2, R>H_1 \tag{6}$$

UPGOING (TRANSMISSION) MULTIPLE REFLECTIONS

When the source is deeper than the two reflectors, the equations (3), (4), (5), and (6) are still valid under the different conditions $H_2 < H_1, S > H_2$ and $R < H_1$.

UPGOING MULTIPLE REFLECTIONS

First order upgoing multiple reflection

For the first order upgoing multiple reflection, Figure 7, the depth of the equivalent primary reflector is $H_2 + (H_2 - H_1) = 2H_2 - H_1$. The traveltime equation is:

$$t = \frac{1}{v}\sqrt{\left(2(2H_2 - H_1) - S - R\right)^2 + L^2}, \text{ for } S < H_2, R < H_2 \qquad (7)$$

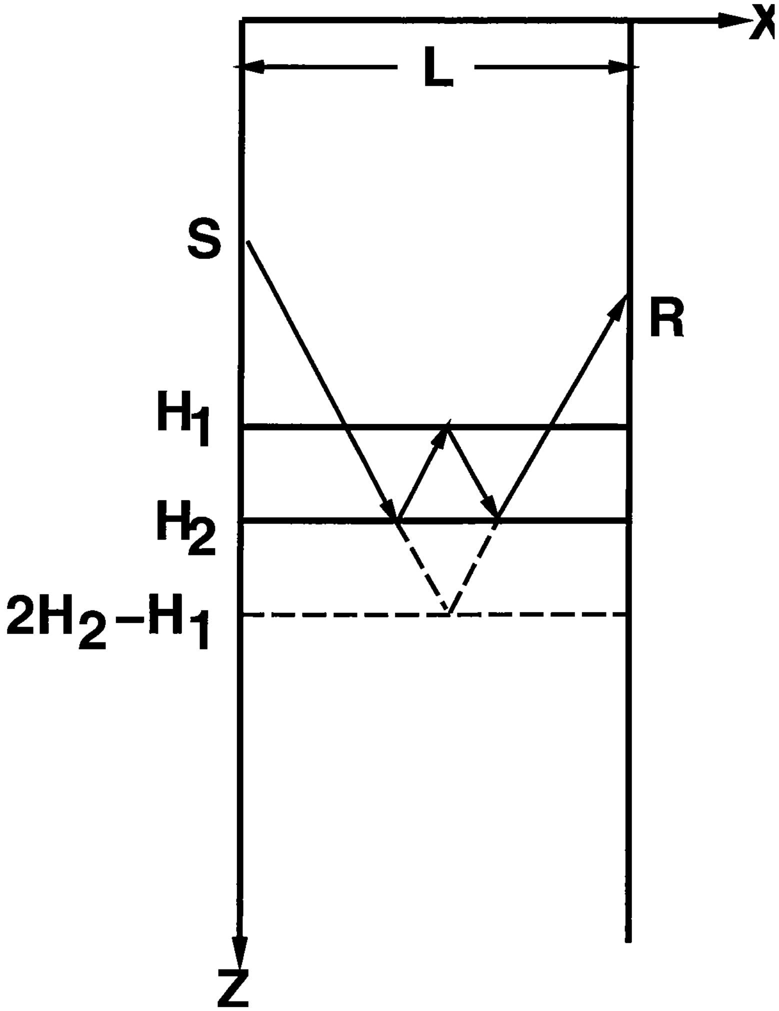

Figure 7: First order upgoing multiple reflection.

Second order upgoing multiple reflection

For the second order upgoing multiple reflection, Figure 8, the depth of the equivalent primary reflector is $H_2 + 2(H_2 - H_1) = 3H_2 - 2H_1$. The traveltime equation is:

$$t = \frac{1}{v}\sqrt{\left(2(3H_2 - 2H_1) - S - R\right)^2 + L^2}, \text{ for } S < H_2, R < H_2 \qquad (8)$$

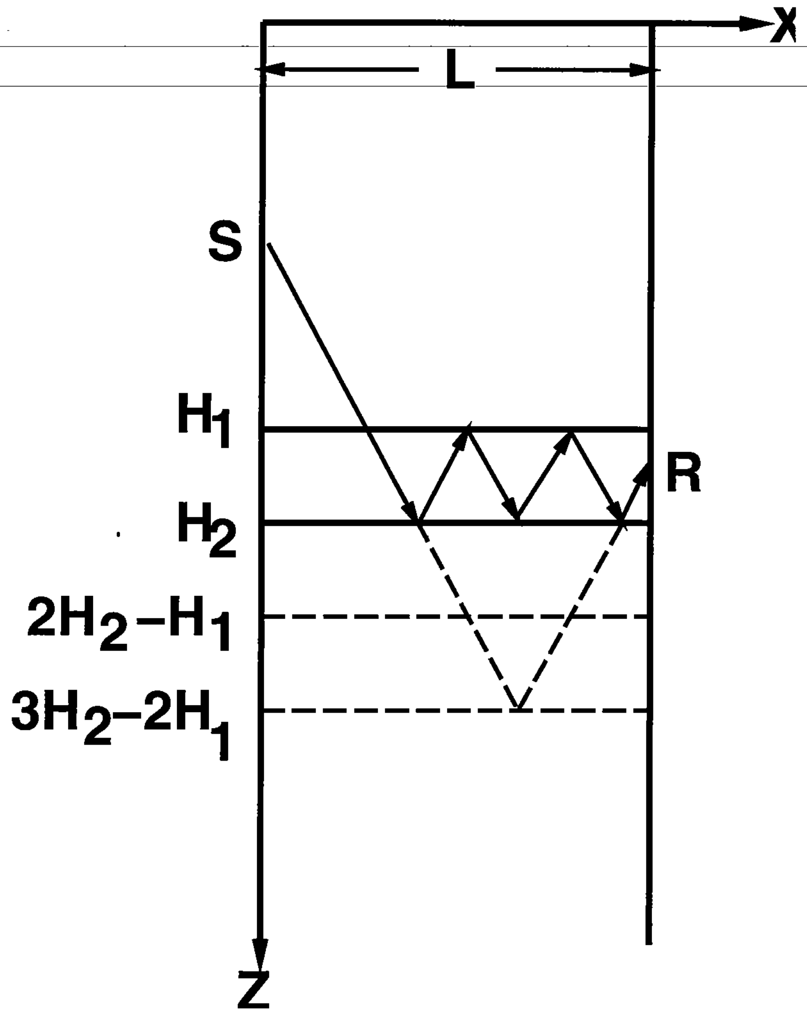

Figure 8: Second order upgoing multiple reflection.

n-th order upgoing multiple reflection

As after any one additinal reflection between the two reflectors, the depth of the equivalent primary reflector increases by $H_2 - H_1$. For the n-th order upgoing multiple reflection, the traveltime equation is:

$$t = \frac{1}{v}\sqrt{\left(2((n+1)H_2 - nH_1) - S - R\right)^2 + L^2}, \text{ for } S < H_2, R < H_2 \tag{9}$$

DOWNGOING MULTIPLE REFLECTIONS

When the source is deeper than the two reflectors, the equations (7), (8), and (9) are still valid under the conditions $H_2 < H_1, S > H_2$ and $R > H_2$.

DIRECT ARRIVAL AND PRIMARY REFLECTIONS

The traveltime equation (2) for the primary reflection can be rewritten as:

$$t = \frac{1}{v}\sqrt{(H + H - S - R)^2 + L^2} \qquad (10)$$

Comparing this equation to the traveltime equation (1) for direct arrival shows that when the depth of the source approaches the depth of the reflector, these two traveltime equations coalesce into each other. Taking wave propagation directions into account, we know that when the depth of the source approaches the depth of the reflector from above (below),the traveltime of the upgoing (downgoing) primary reflection approaches that of the upgoing (downgoing) direct arrival.

MULTIPLE REFLECTIONS

Travel time equations (2) and (9) shows that the multiple reflection is equivalent to a primary reflection from a virtual depth, and as the source depth S changes the virtual depth stays fixed. This is detrimental to seismic imaging. Before using the data for seismic imaging, a multiple attenuation scheme, e.g., predictive deconvolution should be applied to attenuate the multiples. But multiple reflections are orders of magnitude weaker than transmission multiple reflections. So we will concentrate on studying and attenuating transmission multiple reflections.

DOWNGOING (TRANSMISSION) MULTIPLE REFLECTIONS AND DOWNGOING PRIMARY REFLECTION

Travel time equations (2) and (6) shows that for

$$2H - S = -(2n(H_2 - H_1) - S)$$

$$H = S - n(H_2 - H_1) \qquad (11)$$

Downgoing transmission multiple reflection is equivalent to a downgoing primary reflection from the depth $H = S - n(H_2 - H_1)$, which has a linear relationship with the source depth S. For downgoing transmission multiples that $S < H_2, H < H_1$; for upgoing transmission multiples that $S > H_2, H > H_1$.

REFERENCES

Mo, L., and Harris, J. M., 1995, Analysis of noises after prestack migration in cross-well seismic profiling: STP-5.

PAPER U

CROSSWELL SEISMIC IMAGING IN THE PERMIAN BASIN: TWO CASE HISTORIES

R. T. Langan, J. M. Harris, S. K. Lazaratos, and T. L. Jensen‡

ABSTRACT

Crosswell seismic imaging technology has advanced rapidly over the last three years as the processing methods have become more robust, the cost of data acquisition has fallen, and the interwell distances of operation have increased. The Permian Basin of West Texas is proving to be an ideal environment in which to develop this technology because of the relatively low seismic attenuation of the carbonate-dominated lithology, the moderate well spacings in the large number of mature fields, and the unusually high number of reflecting horizons. Current technology permits us to operate in carbonates at well spacings on the order of 2000 ft (650 m) and to image *P*- and *S*-wave reflecting horizons on a scale of 8 to 25 ft (2.4 to 7.6 m). Crosswell technology is not limited to carbonates, although the majority of recent applications have been in this environment.

In this paper we discuss two different crosswell experiments in the Permian Basin, each with unique objectives. The first experiment deals with a waterflood in a Middle Clearfork Formation reservoir on the Eastern Shelf, where we are trying to explain the erratic response of adjacent wells to water injection. In the second project we are trying to image the structure and stratigraphy associated with subtle "anomalies" in 3-D surface seismic images of the Wolfcamp Formation. Figure 1 shows the general location of the Midland Basin (where the lithologies are presumably consistent with deeper water) and the Eastern Shelf, relative to the location of the well-known Grayburg Formation reservoirs (e.g., McElroy) of the Central Basin Platform.

INTRODUCTION

Two recent innovations have had a major impact on crosswell seismic technology. The first is the acquisition method of "shooting on the fly". In this method the downhole source is fired at preset depth intervals as it moves continuously up the borehole, while the receivers are fixed in position (Harris et al., 1995). This technique permits an acquisition rate of more than 20,000 seismic traces in one day, which results in sharply reduced costs and minimizes the disruption of field operations.

The second innovation is the implementation of a true interwell reflection imaging algorithm for real data (Lazaratos et al., 1995) capable of imaging reflectors from one well to the other. This algorithm is a variant of methods used to image offset VSP's, except the number of traces in our crosswell data sets is many times greater than those collected with offset VSP's.

We have been pursuing a variety of applications in the mature oil fields of the Permian Basin in West Texas in order to drive the development of the technology. The Permian Basin provides an environment that has made it easier to overcome many prior problems associated with data acquisition and processing. For example, even though our source is of

---

‡Chevron USA, Midland, Texas

relatively low power, the transmissive carbonates (high Q) of this region combined with the relatively close well spacings permit the collection of high signal-to-noise ratio data. Secondly, the high P- and S-wave velocities of these carbonates relative to water velocity make it possible to separate the components of the reflected wavefield from coherent noise associated with tube waves. Finally, the highly variable velocity and density structure of these carbonates gives rise to wavefields rich in reflected energy, which has been helpful in developing imaging algorithms suitable for crosswell geometries.

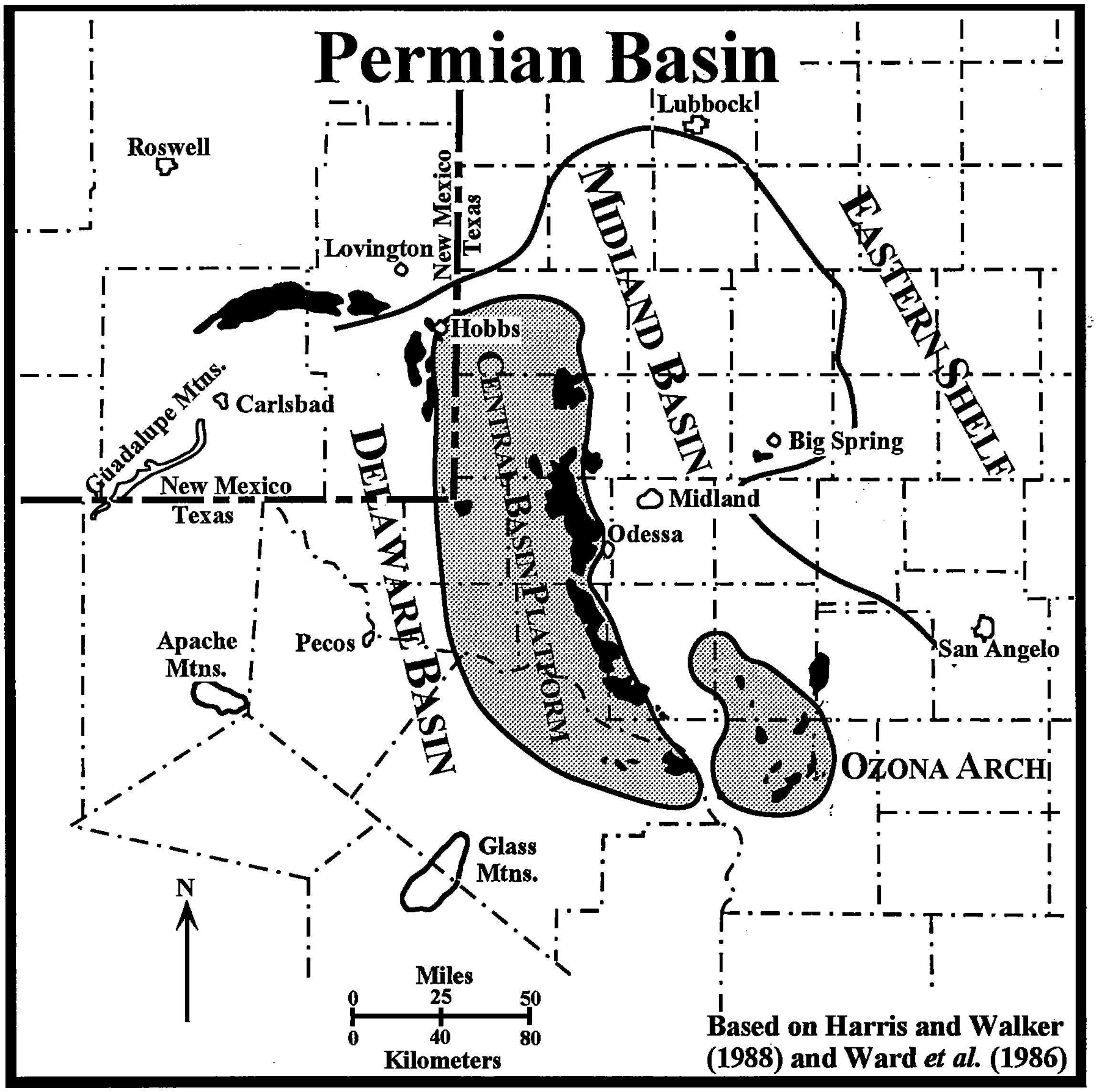

Figure 1. The main paleogeographic provinces of the Permian Basin of West Texas are outlined in relation to major oil fields producing from the Grayburg Formation (black regions).

The geophysical conditions in the Permian Basin are not the only reason for developing the technology in this location. The large reserves still remaining in many of the mature oil fields require increasingly sophisticated techniques to extract. These techniques may be more effectively designed and implemented using information available from crosswell seismic technology.

The two case histories summarized in this paper are still active research projects. We have provided interpretations, some speculative, based upon the crosswell images in order to demonstrate the potential of their unusually high resolution. This resolution is possible because the data were collected using a relatively high frequency source (the piezoelectric element was swept in frequency from 200 Hz to 2000 Hz in most cases) and a closely spaced, five-level hydrophone string.

CASE STUDY I: WATERFLOOD PROJECT

Our first example is from a waterflood project in an oil field on the western edge of the Eastern Shelf (see Figure 1). The reservoir is a 300-ft-thick (91 m) interval in the Middle Clearfork Formation, also a carbonate. The injection rates are unpredictable from one well to the next, which is difficult to explain from the information available from the well logs. The 3-D surface seismic data suggest a slight westward dip of the strata towards the Midland Basin, but the seismic resolution is on the order of the half-thickness of the producing interval itself. We collected three crosswell profiles between four water injectors as shown in Figure 2. We chose this layout in order to obtain a 3-D perspective around a well that was not accepting water. The average injection rate for water at each well is shown in gallons per day (1 gallon = 3.785 liters).

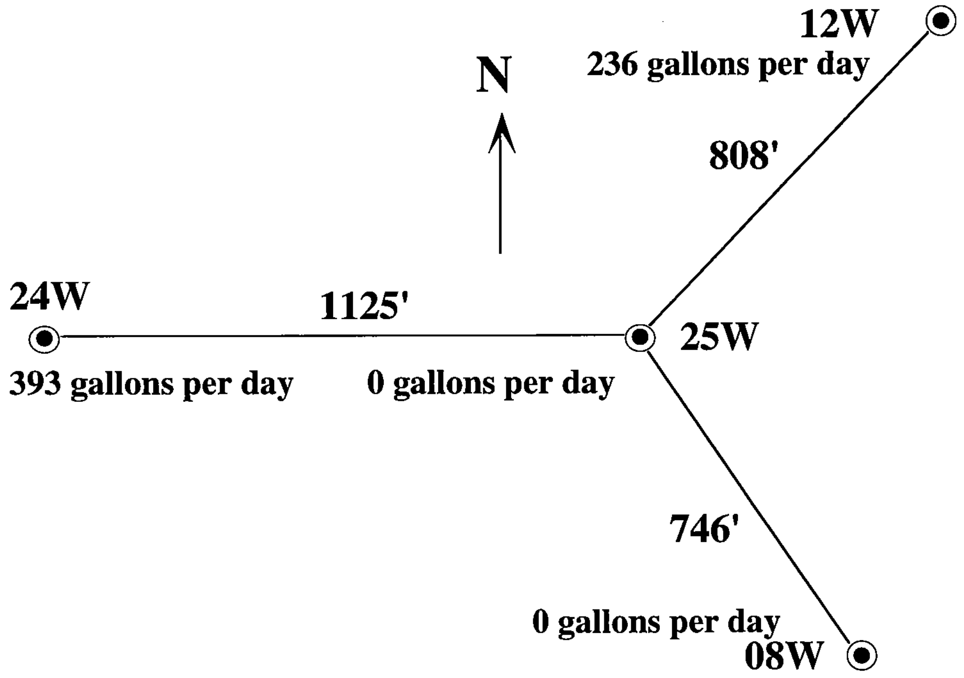

Figure 2. An outline of the three crosswell profiles which tie together four water injectors in our waterflood study.

The reflection images for two of the profiles are shown in Figure 3. These two profiles are nearly orthogonal, but give a dominantly north-south regional perspective. The top of the reservoir is at a depth of about 2840 ft and is characterized by thin laminations. The characteristic wavelength in this zone is on the order of 15 ft (4.6 m).

At these well spacings, 752 ft (229 m) and 802 ft (244 m), the energy propagation distances are at the upper limit of what was detectable for the tools available when we collected these data in late 1993. This results in the poor signal-to-noise ratio seen in the center of the sections, and elsewhere.

These reflection images suggest there may be some eastwardly dipping faults near injector Well 25W with displacements on the order of 10 ft (3.0 m). These faults could disrupt flow in various horizons, which might explain why this well will not take water. Some of these interpreted faults are indicated by the white lines superposed on the section. There is difficulty in tying the faults at the well, which may be in part due to our current processing methods--reflections within a few feet of the source and receiver wells are unintentionally removed by filters used to remove the transmitted arrivals. Another explanation is that we have "over-interpreted" the image. The true dip of these faults is probably greater than the apparent dip on each section. Both lines appear to be oblique to the dip of the fault planes.

There also appears to be a westwardly dip on the order of 1° in many of the reflecting horizons and there is a hint of several stratigraphic pinchouts. These features may also affect the waterflood response.

Figure 4 shows the reflection image from the remaining profile, but it is of poorer quality because of the greater propagation distances involved. However, one can see a slight westwardly dip of many strata and the presence of pinchouts in this section. The frequency content of the reflections is lower and the noise level is greater. The resolution is such that we are unable to see the continuation of the faults interpreted in Figure 3. However, improved wavefield separation and mapping methods developed since these data were processed may improve the image if it is reprocessed.

CASE STUDY II: IMAGING AN "ANOMALY"

Modern 3-D surface seismic data collected in the Midland Basin have revealed subtle amplitude anomalies in the carbonate-rich Wolfcamp Formation. These anomalies are at the threshold of seismic resolution and sometimes contain reservoir-quality carbonates. Information from wells that either penetrate or narrowly miss these anomalies gives only a partial explanation. One well which penetrated an "anomaly" encountered a massive limestone unit, while a nearby well encountered siliciclastic-rich carbonates at the same depth, which one could interpret as debris. Of interest is the internal structure of these "anomalies", their stratigraphic relationship with adjacent strata, and the depositional environment. An opportunity to address these questions with a crosswell survey occurred because there were two wells available for study, one that had penetrated the anomaly, the other which missed, and they were separated by only about 640 ft (195 m).

Some of the operational aspects of this survey are still proprietary, but we can discuss the imaging results and their interpretation in a general sense.

A velocity tomogram computed from the transmitted energy is presented in Figure 5a. It was constructed using the adaptive-gridding technique of Harris (1994). The basis of this algorithm is the definition of velocity through the use of a sparse grid of nodes.

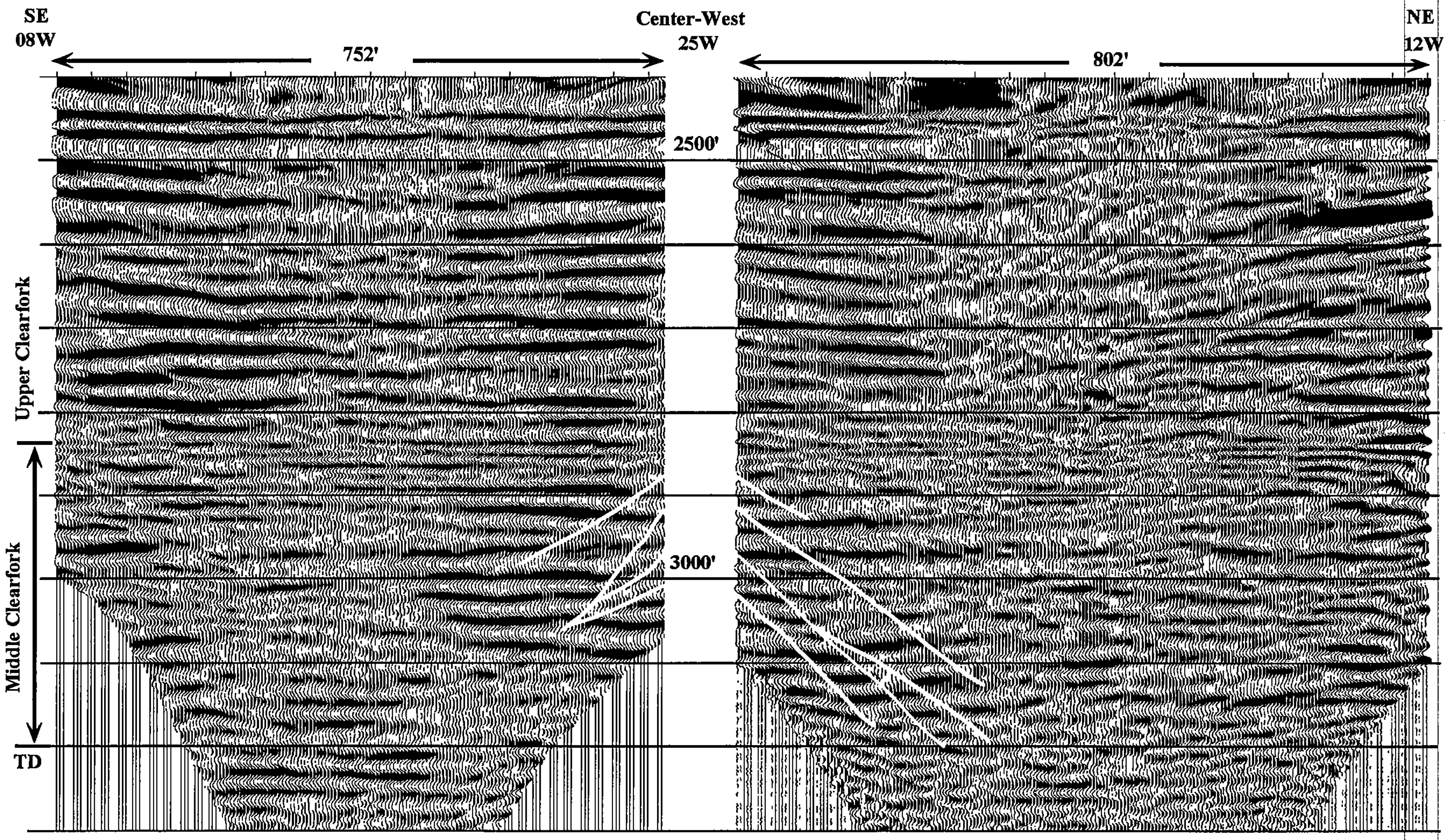

Figure 3. P-wave reflection images for two profiles around a central water injector. We have speculated on the existence of some faults near this injector that are within the reservoir zone. They are indicated by the white lines.

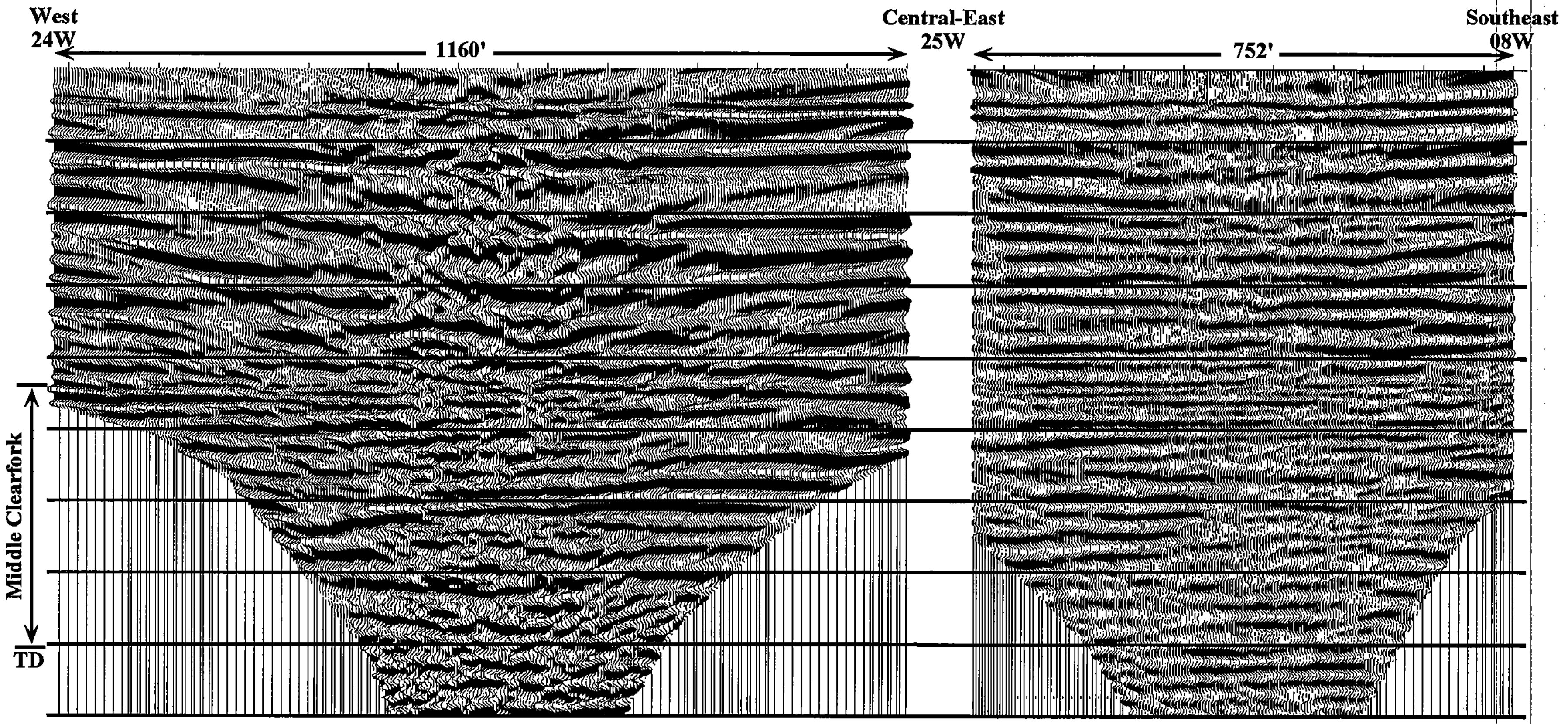

Figure 4. The east-west line on the left has the greatest well spacing (1160' nominal distance) and the poorest resolution. Therefore, we have not interpreted it. The profile on the right is from the previous figure, but flipped from left to right in order to make the tie at the well.

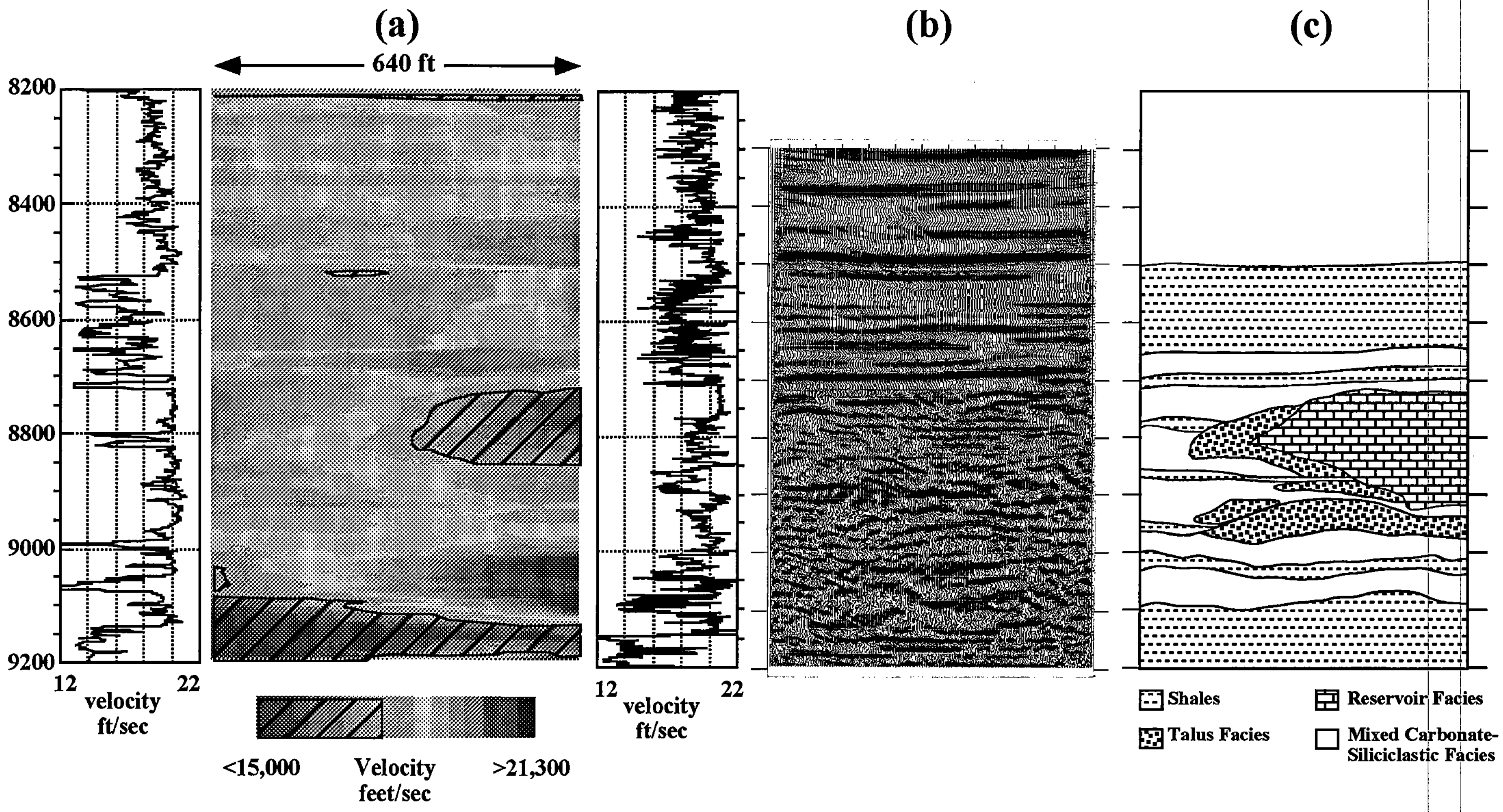

Figure 5. A crosswell tomographic velocity image, crosswell reflection image, and subsequent interpretation of the data associated with subtle anomalies present in surface seismic data.

Formulation of the inversion problem in terms of node-type models provides the capability to use adaptive gridding to address the problems of non-uniform ray coverage and inhomogeneous resolution. The spacing and density of nodes are adaptively selected to provide more uniform ray density per node or to match the geometrical pattern of the geological structure being imaged. In this way, reconstruction artifacts may be reduced, while velocity estimates are made more reliably. Also, "unknowns" are not wasted on homogeneous zones, but may be concentrated in heterogeneous regions of the image. Values of velocity at any point can be derived by interpolating the values at nearby nodes.

We have shown the sonic logs from each of the wells along the side of the tomogram. The anomaly from the surface data corresponds to the region between 8700 ft in depth and 9000 ft in depth in Well B.

The tomogram delineates an oval-shaped, low velocity zone extending from Well B to about the midpoint between the wells. Lower velocities in these carbonates often correlate with higher porosities. The corresponding crosswell reflection image, shown in Figure 5b, shows flat-lying internal structure or stratigraphy within this low velocity zone, and relatively flat-lying structure externally and to the left, but with some discontinuity in strata across the boundary. Below the low velocity region and between about 8900 ft and 8850 ft in depth are two small features about 300 ft apart. They consist of curved and dipping reflections, but with some flat-lying events in between.

This reflection image was obtained using the current wavefield separation and time-to-depth mapping methodologies of TomoSeis. An earlier generation of processing (circa early 1993) contained considerable tube wave energy and poorer bedding continuity, but the reflections we could see are consistent with the image presented here.

An interpretation of the reflection image, which incorporates knowledge obtained from the tomogram, the well logs, and core from Well B, is shown in Figure 5c. The reservoir facies is characterized by discontinuous reflections and low interval velocities, the talus facies by more continuous reflections and intermediate interval velocities, and the mixed carbonate-silicilastic facies by continuous events and fast interval velocities. The data suggest that the reservoir facies in Well B grade laterally into the talus facies, and then into the mixed carbonate-siliciclastic facies found in Well A.

CONCLUSIONS

Crosswell seismology is similar to other seismic techniques in that it includes both velocity estimation (i.e., tomographic imaging) and reflection imaging (i.e., VSP-CDP mapping and migration). Reflection imaging provides more resolution and is finding applications in reservoir delineation and characterization.

These images fill a resolution "gap" between surface seismic data and well log data. The surface seismic data can have a great deal of volumetric coverage of a reservoir, but have relatively poor resolution. Well log and core data have a high degree of resolution, but relatively poor volumetric coverage. One of our hopes for crosswell imaging is that by filling this resolution "gap", it will help us tie together the wide range of more traditional data types, while giving us an understanding of reservoir behavior at a unique scale of resolution.

Crosswell reflection imaging is in its infancy. The first reflection image obtained from data collected in the Permian Basin of West Texas dates back to only 1992 and significant strides have since been made in the imaging technology. The images shown in this paper are likely to change as they benefit from improvements in processing.

The interpretation of some of the features we see in these reflection images is speculative because of our limited experience with them. However, clearly it is unlikely we could obtain these subtle features from more traditional data types such as 3-D surface seismic data or well logs.

More powerful sources with greater bandwidths have been deployed since we collected the data in these case histories. These tools should result in higher quality data sets and greater well spacings then we have shown. In addition, multiple hydrophone strings are now being used to collect several profiles simultaneously, which has reduced acquisition costs.

ACKNOWLEDGMENTS

We would like to thank the Gas Research Institute for its financial support of the waterflood project, without which we would have been able to take the risk of acquiring the data over greater distances than were considered "safe" in 1993.

REFERENCES

Harris, J.M., 1994, An approach to adaptive gridding for traveltime tomography: Annual Report, Seismic Tomography Project, Stanford University.

Harris, J.M., Nolen-Hoeksema, R.C., Langan, R.T., Van Schaack, M.A., Lazaratos, S.K., and Rector, J.W., 1995, High-resolution crosswell imaging of a west Texas carbonate reservoir: Part 1-Project summary and interpretation, *Geophysics*, **60**, 667-681.

Harris, P.M., and Walker, S.D., 1988, McElroy Field, Central Basin Platform, U.S. Permian Basin, *in* Petroleum Geologists Treatise of Petroleum Geology: Atlas of Oil and Gas Fields, No. 1, Beaumont, E.A., and Foster, N. H., (ed.), 32 p.

Lazaratos, S.K., Harris, J.M., Rector, J.W., and Van Schaack, M.A., 1995, High-resolution crosswell imaging of a west Texas carbonate reservoir: Part 4-Reflection imaging, *Geophysics*, **60**, 702-711.

Ward, R.F., Kendall, C.G.ST.C., and Harris, P.M., 1986, Upper Permian (Guadalupian) facies and their association with hydrocarbons-Permian Basin, west Texas and New Mexico, *Am. Assoc. Petrol. Geol. Bull.*, **70**, 239-262.

STP INFORMATION

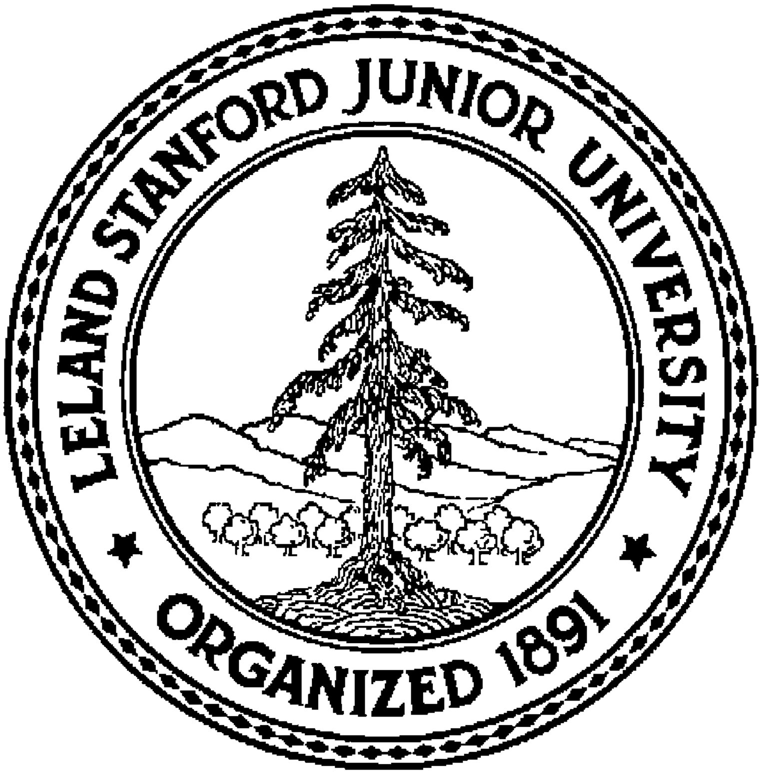

STP COMPUTER HARDWARE RESOURCES

WORKSTATIONS, TERMINALS and MACINTOSHES

DECalpha station 3000/400	96 Mb RAM, 1.0 Gb disk
DECalpha station 3000/400 (2)	48 Mb RAM, 1.0 Gb disk
DECstation 5000/240	80 Mb RAM, 1.0 Gb disk
DEC station 5000/240	64 Mb RAM, 6.1 Gb disk
DECstation 5000/240	48 Mb RAM, 3.0 Gb disk
DECstation 5000/200	32 Mb RAM, 2.0 Gb disk
DECstation 3100	24 Mb RAM, 200 Mb disk
Sun 4/150	8 Mb RAM, 200 Mb disk
Sun 3/60	8 Mb RAM, 200 Mb disk

2 - 14" color NCD X terminals
3 - 16" monochrome NCD X terminals
1 - 16" NH color terminal
3 - Macintoshes

PERIPHERALS

2 - 8mm Exabyte tape drives
1 - TK50 tape drive
1 - HP ScanJet Plus
2 - Laserwriter Plus
1 - HP Deskjet color printer

STP DIRECTORY

Name:	Phone:	Electronic Mail: (@pangea.stanford.edu)
Faculty:		
Jerry M. Harris	(415) 723-0496	harris
Post Docs:		
Jesse Costa	(415) 723-4469	costa
Feng Yin	(415) 725-4369	feng
Graduate Students:		
Le-wei Mo	(415) 725-1331	mo
Youli Quan	(415) 725-6524	quan
Nicholas Smalley	(415) 725-6524	smalley
Mark Van Schaack	(415) 723-4469	mvs
Guan Wang	(415) 725-1331	gywang
STP Administrator		
Sonya N. Williams	(415) 723-1099	sonya
Seismic Tomography Fax	415) 725-2032	
Stanford University Fax	(415) 723-0010	
Stanford University Telex	348402 STANFORD STNU	

RESEARCH PERSONNEL

Jerry M. Harris received his M.S. degree (1974) in electrical engineering from the California Institute of Technology. From 1974 to 1977, he was with the Communications Satellite Corporation working millimeter wave scattering and attenuation in the troposphere. He returned to Caltech and finished the Ph.D. in 1980. After graduation from Caltech, he joined Exxon Production Research Company where he worked on adaptive signal processing and scattering of seismic waves. In 1982, he initiated Exxon's crosswell tomography project in Long Range Research. In 1984, he joined the Standard Oil Company to lead development of the seismic tomography project. Dr. Harris joined the faculty at Stanford University in 1988 as Associate Professor of Geophysics. His current research interests include experimental methods in seismology and electromagnetics for imaging and measurement of in-situ rock properties, crosswell tomography, and general topics involving wave physics and signal processing.

Jesse C. Costa received the B.S. Physics 1983, M.S. in 1987 and Doctorate in Geophysics in 1993 all from the Universidade Federal do Para. He was a summer student at Schumberger Cambridge Research in 1991 and 1992, and an adjunct Professor at the Department of Physics at Universidade Federal do Para since 1989.

Bob Langan received his B.S. degree in Electrical Engineering (1971), an M.S. degree in Geological Sciences (1974), an M.S. in Civil Engineering (1979), and a Ph.D. in Geological Sciences (1980), all from Northwestern University. After completing a Postdoctoral Fellowship in Civil Engineering at Northwestern, he joined Gulf Research and Development in Pittsburgh in 1981. At Gulf he worked on the development of seismic reflection traveltime tomography and associated problems such as raytracing in heterogeneous media, and the resolution and uniqueness of surface sesimic data. He joined Chevron Oil Field Research Company in La Habra in 1985 at the time of the Chevron-Gulf merger. At Chevron he joined Bjorn Paulsson in working on crosswell imaging, and he began to apply the knowledge he gained from working on surface seismic tomography to the crosswell problem. Bob joined the Seismic Tomography Project in October 1993 as a Visiting Scholar and Consulting Associate Professor in order topursue STP's and Chevron's mutual desire to advance crosswell imagingtechnology. Dr. Langan's current interests are in the application of crosswell reflection and velocity images.

Le-Wei Mo received a B.A. in applied geophysics from Changchun College of Geology in 1985. From 1986 to 1987 he studied in the Master's program, Computer Science Department, at Fudan University. From 1988 to 1999, he worked for the Beijing Computer Center, Ministry of Geology and Mineral Resources. He received his M.S. in computer application from Fudan University in 1990. He worked for Stanford Exploration Project as a research assistant from February 1991 to September 1992. He joined the Seismic Tomography Project in September 1992 and is currently working towards a Ph.D. in geophysics. His research interests include signal processing, seismic wave modeling and imaging.

Youli Quan received his B.S. in 1982 from the University of Science and Technology of China, and his M.S. in 1986 from the Institute of Geophysics, Chinese Academy of

Sciences, and is presently a Ph.D. student at Stanford University. He worked for the Institute of Geophysics, Chinese Academy of Sciences from 1986 to 1989.

Nicholas Smalley received his B.S. in Geophysics from Texas A&M in 1989. He is a Ph.D. candidate in Geophysics. His research interests are crosswell reflector imaging and migration. He is a member of the Society of Exploration Geophysicists.

Mark Van Schaack received his B.S. in geophysical engineering from the Colorado School of Mines in 1985. He joined Schlumberger Wireline Services in 1985 and spent his next four years working in Syria, Egypt, and Sudan as a Field Engineer. In 1989, Mark went to work as a Research Associate for the University of California, Santa Barbara's Institute for Crustal Studies. His work at ICS included the processing of several surface seismic lines shot in the Southeastern Sierra Nevada's. He has been a graduate student at Stanford University since 1990 and is currently working toward his Ph.D. in geophysics.

Guan Yong Wang received his B.S. in geophysics from the Geological Institute of Changchun. From 1982 to 1983, he worked as a geophysicist for Shanxi Geological Survey (China). He received his M.S. in geophysics from the Graduate School of Academia Sinica in 1986. From 1986 to 1989, he was a research geophysicist with the Institute of Geology, State Seismological Bureau in China. He received a M.E. in engineering geoscience in 1991 from the University of California at Berkeley. He joined the Seismic Tomography Project in September 1991, and is currently working towards a Ph.D. in geophysics.

Feng Yin received his B.S. degree (1982) and M.S. (1984) in electrical engineering from the Nanjing Institute of Technology. From 1984 to 1986, he was with Beijing Vacuum Electronics Institute working with laser scattering and spectroscopy technology. He received his Ph.D in electrical engineering from Southeast University (China). After graduation from SU, he joined their Department of Physics as an associate professor from 1990 to 1993. In 1993, he worked as a visiting scholar in geophysics at the Institute of Karlsruhe University (Germany). In October of 1993, he joined the Seismic Tomography project as a post-doctoral fellow. His current research interests include seismic tomography, migration and wave propagation in inhomogeneous media, and inverse scattering problems.

STP 1995 Sponsors

Dennis O'Brien
Advance Geophysical Corporation
7409 Alton Court, Suite 100
Englewood, CO 80111
(303) 779-8080

Henry Tan
Amoco Production Company
P.O. Box 3385
Tulsa, OK 74102
(918) 660-3845

Robert Langan
Chevron Petroleum Technology Company
P.O Box 446
La Habra, CA 90633-0446
(310) 694-7394

John Queen
Conoco Inc.
P.O. Box 1267
Ponca City, OK 74602-1267
(405) 767-5015

Sen T. Chen
Exxon Production Research Co.
P.O. Box 2189
Houston, TX 77252
(713) 966-6053

Sergio Zarantonello
Fujitsu America
3055 Orchard Drive
San Jose, CA 95134-2022
(408) 456-7216

Timothy Fasnacht
Gas Research Institute
8600 West Bryn Mawr Avenue
Chicago, IL 60631
(312) 399-8221

Yoshiro Ishii
Japan National Oil Corporation
1-2-2 Hamada, 1- Chome
Mihama, Chiba City
260 Japan
043 (276) 9254

R. L. LeRoy
Noranda Technology Centre
240 boulevard Hymus
Pointe-Claire, Quebec
Canada H9R 1G5
(514) 630-9300

Djamla Manuel Soares Filho
Petrobras America Inc.
CENPES/DIVEX/SEGEF
Cidade Universitaria Quadra 7
Ilha do Fundao
21910 Rio de Janeiro RJ Brazil
5521 598-6441

Joseph Gallagher
Phillips Petroleum Company
570G Plaza Office Building
Bartlesville, OK 74004
(918) 661-9715

William Bashore
Reservoir Characterization
Research & Consulting, Inc.
2524 Monterey Place
Fullerton, CA 92633
(714) 871-0237

Danny R. Melton
Texaco Inc.
P.O. Box 770070
Houston, TX 77215-0070
(713) 954-6065

James L. Peters
Union Pacific Resources Co.
P.O. Box 7
Fort Worth, TX 76101-0007
(817) 877-6717